Electron Selective Contact in Perovskite Solar Cells



Konrad Wojciechowski

St Cross College

University of Oxford

A thesis submitted in fulfilment of the requirements for the degree of

Doctor of Philosophy at the University of Oxford

February 2016

Declaration

This thesis is a result of my own work and includes nothing which is the result of collaboration except where explicitly indicated in the text.

I declare that no part of this work has been submitted for a degree or any other qualification at this or any other university.

Konrad Wojciechowski, February 2016

Electron Selective Contact in Perovskite Solar Cells

Konrad Wojciechowski, St Cross College, University of Oxford

Thesis submitted in fulfilment of the requirements for the degree of Doctor of Philosophy at the University of Oxford. Hilary Term, 2016

Abstract

Over the last 4 years, perovskite solar cells emerged as an attractive, highly efficient, and low-cost alternative to established, conventional photovoltaic technologies. The power conversion efficiency of these devices recorded an unprecedented rise, currently exceeding certified values of 20%. This thesis covers a number of technological advancements which lead to improved photovoltaic performance, as well as vital insight into some more fundamental aspects of the perovskite device operation. The focus of this body of work is primarily directed towards the electric contact in the PV stack which is responsible for electron collection.

The motivation of the study presented here is given in Chapter 1, and includes a brief summary of the current energy landscape. Chapter 2 introduces the theoretical background of photovoltaic technology, starting from the basics of semiconductor physics, through to the principles of solar cell operation, as well as some characteristic properties of the perovskite materials. Details of the experimental methods used in this study are reported in Chapter 3.

Chapter 4 reports the development of a low temperature process (sub-150 °C) for the manufacture of perovskite solar cells. Dispersions of pre-synthesised, highly crystalline TiO_2 nanoparticles were used as an electron selective contact, which eliminated the high temperature sintering step.

Chapters 5, 6 and 7, report the interface modification of an n-type contact, resulting in a substantially improved device operation and suppression of hysteresis phenomenon which is characteristic of perovskite photovoltaics. Fullerene-based materials have been found to make excellent electronic contact with halide perovskite materials, and are shown to be far superior to commonly used metal oxides. The facilitated electron collection allows enhancements in the photovoltaic performance of these devices. Furthermore, the organic layers used in this study can be processed at low temperatures.

Finally, the development of transparent conductive electrodes based on silver nanowires is presented in Chapter 8. The fabricated electrodes exhibit low sheet resistance, high degree of transparency, and can be processed at low temperatures, allowing them to be compatible with processing on flexible substrates and multi-junction architectures. The application of silver nanowires in different perovskite solar cell architectures is also reported.

Acknowledgements

Foremost, I would like to thank my supervisor, prof. Henry Snaith, who has been a true inspiration from the very first day of my DPhil course. His enthusiasm and passion for science were absolutely contagious, his scientific thinking and incredible creativity something to look up to. It's been a great honour to be part of his research team.

Great thanks go to all the collaborators I was lucky to work with, both in Oxford and elsewhere. Special thanks to Dr. Tomas Leijtens, Dr. Sandeep Pathak, Dr. Sam Stranks, Ivan Ramirez, Dr. Nakita Noel, Dr. Michael Saliba, Dr. Pabitra Nayak, Dr. Antonio Abate, Dr. Christoph Schlueter, Dr. Svetlana Siprova, Dr. Nikos Kopidakis, Dr. Olivier Dautel, Dr. Therese Gorisse who substantially contributed to the study presented in this thesis, either experimentally or through endless discussions.

Big thanks to all the Snaithlings, for making incredibly stimulating and fun work environment, for the never-ending scientific and philosophical discussions in the lab and after hours over many pints. Special thanks to Kita for a great moral support, keeping me sane and all the food. To Martina for feeding me and being an organisational guru. To Max, Derek, David, Tomas, Severin, James, Mike and Jacob and for sharing so many fantastic memories and being true friends.

Very special thanks to all the Aston family, Boozey, Andrea, Max, Matz, Matt, Milena and Severin. You guys are the best! It's been an unforgettable time in the old and new Aston, a real home!

To my parents, for being constantly supportive throughout my entire life. I have made it here thanks to you!

Special thanks to Karolina who has been my inspiration and motivation for the doctoral studies, and has always given me a great support.

General thanks to everyone I met during my studies in Oxford. Thank you for all the great memories and many friendships. You all have made this time and this place very special to me.

Abbreviations

AM1.5	Air Mass 1.5
AFM	Atomic Force Microscope
AgNW	Silver Nanowire
ALD	Atomic Layer Deposition
C_{60}-SAM	Pyrrolidine Derivative of C_{60}
CB	Conduction Band
ClB	Chlorobenzene
DOS	Density of States
DMF	N,N-Dimethylformamid
DSSC	Dye-sensitised Solar Cell
EL	Electroluminescence
EtOH	Ethyl Alcohol
FB	Forward Bias
FF	Fill Factor
FTIR	Fourier Transform Infrared
FTO	Fluorine-doped tin Oxide
HAXPES	Hard X-ray Photoelectron Spectroscopy
HOMO	Highest Occupied Molecular Orbital
HTM	Hole Transport Material
Ht-TiO_2	High Temperature Processed TiO_2
IPA	Isopropyl Alcohol
ITO	Indium Tin Oxide
J_{SC}	Short-circuit Current Density

JV	Current density-Voltage
Li-TFSI	Bis(trifluoromethane)sulfonimide lithium
Lt-TiO_2	Low Temperature Processed TiO_2
LUMO	Lowest Unoccupied Molecular Orbital
MAI	Methylammonium Iodide
MSSC	Meso-superstructured Solar Cell
NP	Nanoparticle
OFET	Organic Field-effect Transistor
PCBM	[6,6]-phenyl-C_{61}-butyric acid methyl ester
PCBCB	PCBM derivative with benzocyclobutene
PCE	Power Conversion Efficiency
PDS	Photothermal Deflection Spectroscopy
PEDOT:PSS	Poly(3,4-ethylenedioxythiophene) polystyrene sulfonate
PEIE	Polyethylenimine, ethoxylated
Perov	perovskite
PL	Photoluminescence
PLQE	Photoluminescence Quantum Efficiency
PMMA	Poly(methyl methacrylate)
PV	Photovoltaics
PVA	Polyvinyl alcohol
PVP	Polyvinylpyrrolidone
SC	Short-circuit
SCLC	Space-charge Limited Current
SAM	Self-assembled Monolayer
SEM	Scanning Electron Microscope
Sol-gel C_{60}	(N-[3-(Triethoxysilyl)propyl]-2-carbomethoxy-3,4-fulleropyrrolidine)

Spiro-OMeTAD	2,2′,7,7′-tetrakis(N,N′-di-p-methoxyphenylamine)-9,9′-spirobifluorene
SPO	Stabilised Power Output
tBP	*tert*-butyl pyridine
TCSPC	Time-Correlated Single Photon Counting
TiAcAc	Titanium diisopropoxide bis(acetylacetonate)
TRMC	Time-resolved Microwave Conductivity
UV-Vis	Ultraviolet-Visible
VB	Valence Band
V_{OC}	Open-circuit Voltage
WF	Work Function
XRD	X-ray Diffraction

Table of Contents

Chapter 1 Introduction 1

1.1 Context and motivation 1

1.2 PV technologies 3

1.3 Emergence of perovskite solar cells 5

1.4 Aim of the thesis 6

1.5 References 8

Chapter 2 Theoretical background 13

2.1 Principles of the photovoltaic device 13

2.1.1 Basics of semiconductors 13

2.1.2 Solar cell operation 15

2.1.3 Solar cell characterisation 23

2.2 Perovskite solar cell 26

2.2.1 What is perovskite? 26

2.2.2 Operating principles of perovskite solar cells 29

2.2.3 Principles of the heterojunction interface 34

2.3 References 37

Chapter 3 Experimental methods 45

3.1 Synthesis of materials 45

3.1.1 TiO_2 nanoparticles 45

3.1.2 Silver nanowires 46

3.1.2.1 Filtration of AgNWs 47

3.2 Sample preparation 47

3.2.1 Perovskite solar cell fabrication 47

3.2.1.1 Substrate preparation 48

3.2.1.2 Electron selective contact 48

3.2.1.3 Planar perovskite layer 51

3.2.1.4 Meso-superstructured perovskite layer 52

3.2.1.5 Hole transport layer 52

3.2.1.6 Top metal electrode 53
3.2.1.7 Encapsulation layer 53
3.2.2 Organic field-effect transistors (OFETs) 53
3.2.3 Samples for different characterisation 54
3.2.3.1 Conductivity measurements 54
3.2.3.2 Hard X-ray photoelectron spectroscopy measurements 55
3.2.3.3 Photoluminescence measurements 55
3.2.4 Silver nanowire-based electrodes 55
3.3 Electrical characterisation 57
3.3.1 Solar cell characterisation 57
3.3.2 Conductivity measurement 59
3.3.3 Impedance spectroscopy 61
3.3.4 Transient photocurrent and photovoltage decay 62
3.3.5 Electron mobility measurement 64
3.4 Spectroscopic characterisation 65
3.4.1 Optical absorption 65
3.4.2 X-ray diffraction 65
3.4.3 Photoluminescence measurements 65
3.4.4 Photoluminescence quantum efficiency 67
3.4.5 Electroluminescence 68
3.4.6 Time-resolved microwave conductivity 68
3.4.7 Photothermal deflection spectroscopy 69
3.4.8 Hard X-ray photoelectron spectroscopy 70
3.4.9 Fourier transform infrared spectroscopy 71
3.5 Microscopy 71
3.5.1 Scanning electron microscopy 71
3.5.2 Atomic force microscopy 71
3.6 References 72

Chapter 4 Sub 150 °C Processed Meso-superstructured Perovskite Solar Cells with Enhanced Efficiency 75

4.1 Context 76

4.2 Introduction 76
4.3 Results and discussion 78
4.3.1 Low temperature TiO_2 films 78
4.3.2 Solar cell performance 81
4.3.3 Electronic characterisation 87
4.4 Conclusions 90
4.5 References 91

Chapter 5 Heterojunction Modification for Highly Efficient Organic-Inorganic Perovskite Solar Cells 97

5.1 Context 98
5.2 Introduction 99
5.3 Results and discussion 102
5.3.1 Photoinduced charge extraction at perovskite interfaces 102
5.3.2 Density of states in TiO_2 106
5.3.3 Device performance 110
5.4 Conclusions 115
5.5 References 116

Chapter 6 C_{60} as an Efficient n-Type Compact Layer in Perovskite Solar Cells 121

6.1 Context 122
6.2 Introduction 123
6.3 Results and discussion 124
6.3.1 Compact layer-perovskite interface 124
6.3.2 Device performance 129
6.3.3 Charge extraction study 135
6.3.3.1 Hysteresis mechanism 138
6.3.4 Stability measurements 140
6.4 Conclusions 143
6.5 References 144

Chapter 7 Cross-linkable Fullerene Derivatives for Solution-processed n–i-p Perovskite Solar Cells 149

7.1 Context 150
7.2 Introduction 150
7.3 Results and discussion 152
7.3.1 Properties of cross-linkable fullerene derivatives 152
7.3.2 Electron extraction with crosslinked fullerenes 157
7.3.3 Photovoltaic performance 158
7.3.4 Hysteresis consideration 161
7.3.5 Stability measurements 165
7.4 Conclusions 169
7.5 References 170

Chapter 8 Transparent Electrodes Based on Silver Nanowires 175
8.1 Context 176
8.2 Introduction 177
8.3 Results and discussion 179
8.3.1 Synthesis of silver nanowires and film fabrication 179
8.3.2 Removal of PVP shell 184
8.3.2.1 Methanol washing 184
8.3.2.1 Nitrogen plasma etching 188
8.3.3 Silver nanowires embedded in a matrix 190
8.3.4 Silver nanowires in perovskite solar cells 192
8.4 Conclusions 195
8.5 References 197

Chapter 9 Conclusions 203
9.1 Summary of the key results 203
9.2 Outlook 207
9.3 References 209

Appendix 213
1. Publications 213
2. Conferences 215
3. Posters 217

Chapter 1

Introduction

1.1 Context and motivation

The worldwide energy consumption rate is growing at an exponential rate, currently exceeding 15 TW.[1] It is estimated that the global energy demand in 2040 will be 56% bigger than it was in 2010.[2] As such, energy supply and energy security will be one the biggest challenges that human civilization will have to face. Currently, nearly 80% of the world's energy is provided from burning fossil fuels.[3] The process of converting the chemical energy stored in these materials into thermal energy, is accompanied by the emission of greenhouse gases into the atmosphere. This fact has very important repercussions, specifically with respect to climate change and the global warming effect. In order to avoid catastrophic environmental consequences, increased diversification of the energy supply is essential. Legislative steps, such as 2008 Climate Change Act, have been taken in order to tackle the environmental crisis.[4] Technological advances in clean, renewable energy sources have to follow if the objectives undertaken in this agreement are to be met.

The main renewable energy sources include biomass, hydropower, wind, sunlight, and geothermal heat. All these renewables combined satisfied around 19% of the final global energy consumption in 2012, and 22% of the electricity generation in 2013; but modern, sustainable renewable sources provided only around 10% of the energy consumption.[3] The detailed breakdown based on the 2015 report from Renewable Energy Policy Network for the 21st Century (REN21) is shown in Figure 1.1. Solar energy is arguably the most abundant energy source on planet earth, with the theoretical potential of solar power being estimated at 89,300 TW.[5] At the moment, only a scant portion of the global energy supply comes from sunlight, so there is much scope for development in this area. Large-scale deployment of solar PV technologies has been hindered by production costs, material availability, material toxicity, or combinations of these. Thanks to a number of advancements in the past several years, solar PV has reached the fastest annual capacity growth of all renewables in the year of 2011.[6]

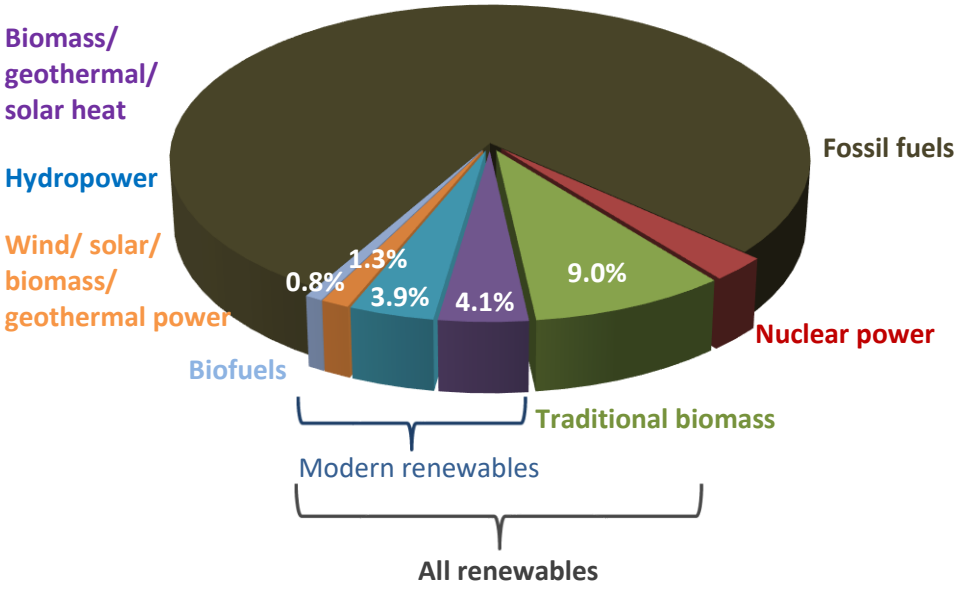


Figure 1.1 Estimated share of final global energy consumption in 2013. The data was obtained from the Renewable Energy Policy Network for the 21st Century.[3]

1.2 PV technologies

PV is an abbreviation for photovoltaics, the technology utilizing solar energy by converting sunlight directly into electricity. The photovoltaic device, also known as a solar cell, employs a semiconducting material capable of absorbing a selected part of the solar spectrum. The part of the spectrum which is absorbed by a given material is defined by its bandgap (energy range in the solid where no electronic states can exist). Upon interaction with photons and the absorption of their energy, a population of free charge carriers – electrons and holes – is created in the semiconductor. The electrochemical potential difference due to photoexcitation defines the magnitude of the electrical voltage generated. This phenomenon is called photovoltaic effect.

The most commonly applied material in commercial solar cells is crystalline silicon (mono- or polycrystalline), constituting over 90% of annual PV production.[7] The power conversion efficiencies (PCEs) of polycrystalline silicon modules are currently approaching 20% (over 22% for monocrystalline modules).[8] Historically, the cost of fabricating highly crystalline wafers for efficient solar cells was very high due to the complicated manufacturing process. This disparity enabled extensive research into finding cheaper alternatives over the last few decades. Currently, the cost of solar energy from silicon-based modules is very low. The new lowest price bid record – 3 U.S. cents per kilowatt-hour – was set in May 2016 for the solar plant in Abu Dhabi.[9]

The second generation PV materials, which encompasses thin-film technology with materials such as Gallium Arsenide (GaAs), Copper Indium Gallium Selenide (CIGS), Cadmium Telluride (CdTe), and amorphous silicon (a-Si) delivered new solutions. The cost of the energy produced by some of these technologies, especially CIGS and CdTe,

has become very competitive. Increasing commercial manufacturing of thin-film solar modules can be observed, overall constituting about 9% of the annual PV production.[7]

The use of toxic (cadmium) or rare (indium) elements constituted some of the limitations in the thin film approaches. For the last 25 years there has been an increased effort to find even cheaper alternatives, made primarily of abundant and non-toxic materials. Organic PV (OPV), dye-sensitized solar cells (DSSC), or quantum dot solar cells (QDSC) have been developed, but the efficiencies of these technologies still fall short compared to the more mature and established ones.[8]

Meanwhile, there has been a dramatic drop in the price of silicon, mainly due to both increased demand, and technological advances in the manufacturing process. Obtaining 'grid parity' (cost of electricity from alternative source levels the existing electricity prices) with silicon technology has recently become achievable.[10] Despite unprecedented low prices of silicon modules, there is still tremendous scope for alternatives, especially in flexible PV applications, an area which is of rapidly growing interest, and where conventional crystalline silicon technology cannot be utilized. Furthermore, fabrication of multi-junction architectures is a very attractive concept. In such structures the silicon cell is combined with another PV junction to increase the overall efficiency, and further reduce the cost of energy.

At the end of last decade a new class of materials stemming from the research on DSSCs has arisen – organic-inorganic lead halide perovskites.[11–14] Perovskites have attracted an explosion of interest in the research community, mainly due to the incredibly fast development of the technology (achieved also by the proximity to DSSC and OPV research) and a very broad range of potential applications, including flexible solar cells and multi-junction devices.[15–17]

1.3 Emergence of perovskite solar cells

Organic-inorganic metal halide perovskite solar cells were reported for the first time between 2006 and 2009 by the work of Miyasaka and co-workers,[18,11] when they employed small $CH_3NH_3PbX_3$ (where X is I or Br) nanocrystals replacing the ruthenium complex dyes in a dye-sensitized solar cell architecture, containing either a liquid electrolyte redox couple or polypyrrole carbon black composite solid-state hole conductor. However, significant research into these materials didn't occur until breakthroughs occurred three years later with the use of the molecular solid state hole transporting material, spiro-OMeTAD (2,2',7,7'-Tetrakis-(N,N-di-4-methoxyphenylamino)-9,9'-spirobifluorene), producing much more efficient and more stable devices;[13,14] even enabling completely new device architectures to be realised with the absence of mesoporous TiO_2.[14] Since then, metal-halide perovskite materials have garnered an explosion of interest due to their remarkable photovoltaic performance, low temperature and facile processing,[14,19–21,16,22–24] and even have even been shown to exhibit efficient light emission and lasing properties.[25–27] Verified solar cell PCEs exceeding 20% have also been achieved,[28,29] a feat which gives perovskite PV a place as one of the most promising and fastest growing of all photovoltaic technologies.

The high performance and rapid development of the technology is attributed to the favourable optoelectronic properties of the perovskite material, such as broad absorption, appropriate and tunable bandgap, high crystallinity, very low defect density, and excellent charge transport properties with long electron and hole diffusion lengths.[26,30–33] The chemistry and crystallography of the organic-inorganic lead halide perovskites, as well as the main principles governing the operation of solar cells employing these materials, are presented in Chapter 2.

1.4 Aim of the thesis

With the booming power conversion efficiencies of perovskite solar cells, it is important to understand the physical phenomena and existing limitations occurring in these devices. A better understanding of the system can achieved by carrying out fundamental studies of the physical processes taking place in a device, which should lead to a more systematic improvement of the device operation. In Chapter 4 certain limitations in the PV performance of a device arising at the n-type interface are identified and discussed. The quality of the electronic contact between the perovskite material and an electron selective layer is further elaborated in Chapters 5-7 by using a range of spectroscopic tools. Significantly improved solar cell performance with an optimised fullerene-based contact is demonstrated.

The hysteresis phenomenon occurring in current-voltage characteristics of perovskite solar cells has recently become a subject of intense debate within the community.[34] Understanding this process and finding a way to eliminate its effects is one of the challenges to the commercial viability of the perovskite technology. The influence of the electron selective contact on the magnitude of hysteretic behaviour is presented in Chapters 5-7. It is found that the ease of collection of the photogenerated charges plays a significant role in suppressing the hysteresis; and hence suitable engineering of the charge selective contacts can dramatically improve the device operation. The origin of the hysteretic effect is elaborated upon in Chapter 6.

Flexible, lightweight and portable electronics, including solar cells, are of increasing demand, with a wide range of applications opening up.[35,36] In order to fabricate a device stack on a flexible polymeric substrate, low temperature processing (below 150 °C) is required, due to the low glass transition point of the polymers. Furthermore, the ability to process the entire PV junction at low temperatures will allow the fabrication of monolithic, multi-junction stacks

without compromising the integrity of the underlying materials. A reduction of high energy procedures during the manufacturing process also directly translates to the lower fabrication costs.

Metal-halide perovskites typically crystallize at temperatures ranging between 100 and 150 °C. Nevertheless, most device architectures use crystalline titanium oxide as a bottom electron selective contact, which typically involves high temperature sintering step. In Chapters 4, 6 and 7 the development of low temperature, solution-processed n-type compact layers is presented, which enables fabrication of the entire perovskite PV device in a process below 150 °C.

The realisation of efficient, flexible perovskite solar cells requires advancements in the field of transparent electrodes. Transparent conductive oxides (TCOs) are commonly used as a bottom electrode in PV applications. This class of materials has a number of disadvantages when processed on flexible substrates, including significant brittleness and lower conductivities when deposited at low temperatures.[37,38] In the past decade silver nanowires have emerged as a promising transparent conductor for optoelectronic applications.[39] Chapter 8 focuses on the development of silver nanowire-based, transparent electrodes. These nanowires can be fabricated at room temperature, and display the high conductivity and transparency typically required from a TCO. The applicability of such electrodes in perovskite solar cells is also discussed.

In summary, this thesis is primarily aimed at identifying and understanding the physical processes occurring at the electron selective contact of the perovskite solar cell, and applying a suitable interface engineering in order to improve the device operation. Additionally, addressed in this work is the development of low temperature processing of the perovskite photovoltaic stack and transparent conductive electrode, as a step forward in the fabrication of a highly efficient, flexible solar cell.

1.5. References

(1) International Energy Agency. 2014 Key World Energy Statistics.

(2) U.S. Energy Information Administration. Annual Energy Outlook 2015.

(3) Renewable Energy Policy Network for the 21st Century. Renewables 2015 - Global Status Report.

(4) Parliament of the United Kingdom. Climate Change Act 2008. *HM Gov.* **2008**, 1–103.

(5) Tsao, J. Y.; Waide, P. The World's Appetite for Light : Empirical Data and Trends Spanning Three Centuries and Six Continents. *Leukos* **2010**, *6*, 259–281.

(6) Renewable Energy Policy Network for the 21st Century. Renewables 2013 - Global Status Report.

(7) Fraunhofer Institute for Solar Energy Systems, P. A. Photovoltaics Report - November 2015.

(8) Green, M. A.; Emery, K.; Hishikawa, Y.; Warta, W.; Dunlop, E. D. Solar Cell Efficiency Tables (version 46). *Prog. Photovoltaics Res. Appl.* **2015**, *23*, 805–812.

(9) Anna Hirtenstein. New Record Set for World's Cheapest Solar, Now Undercutting Coal http://www.bloomberg.com/news/articles/2016-05-03/solar-developers-undercut-coal-with-another-record-set-in-dubai.

(10) Saga, T. Advances in Crystalline Silicon Solar Cell Technology for Industrial Mass Production. *NPG Asia Mater.* **2010**, *2*, 96–102.

(11) Kojima, A.; Teshima, K.; Shirai, Y.; Miyasaka, T. Organometal Halide Perovskites as Visible-Light Sensitizers for Photovoltaic Cells. *J. Am. Chem. Soc.* **2009**, *131*, 6050–6051.

(12) Im, J.-H.; Lee, C.-R.; Lee, J.-W.; Park, S.-W.; Park, N.-G. 6.5% Efficient Perovskite Quantum-Dot-Sensitized Solar Cell. *Nanoscale* **2011**, *3*, 4088–4093.

(13) Kim, H.-S.; Lee, C.-R.; Im, J.-H.; Lee, K.-B.; Moehl, T.; Marchioro, A.; Moon, S.-J.; Humphry-Baker, R.; Yum, J.-H.; Moser, J. E.; et al. Lead Iodide Perovskite Sensitized

All-Solid-State Submicron Thin Film Mesoscopic Solar Cell with Efficiency Exceeding 9%. *Sci. Rep.* **2012**, *2*, 591.

(14) Lee, M. M.; Teuscher, J.; Miyasaka, T.; Murakami, T. N.; Snaith, H. J. Efficient Hybrid Solar Cells Based on Meso-Superstructured Organometal Halide Perovskites. *Science* **2012**, *338*, 643–647.

(15) Green, M. A.; Ho-Baillie, A.; Snaith, H. J. The Emergence of Perovskite Solar Cells. *Nat. Photonics* **2014**, *8*, 506–514.

(16) Snaith, H. J. Perovskites: The Emergence of a New Era for Low-Cost, High-Efficiency Solar Cells. *J. Phys. Chem. Lett.* **2013**, *4*, 3623–3630.

(17) Stoumpos, C. C.; Kanatzidis, M. G. Halide Perovskites: Poor Man's High Performance Semiconductors. *Adv. Mater.* **2016**, *28*, 5778–5793.

(18) Kojimaa, A.; Teshimac, K.; Miyasakab, T.; Shirai, Y. Novel Photoelectrochemical Cell with Mesoscopic Electrodes Sensitized by Lead-Halide Compounds. *210th ECS Meet. Cancun, Mex. Oct. 29−Nov. 3* **2006**, No. 2, 2014.

(19) Liu, M.; Johnston, M. B.; Snaith, H. J. Efficient Planar Heterojunction Perovskite Solar Cells by Vapour Deposition. *Nature* **2013**, *501*, 395–398.

(20) Burschka, J.; Pellet, N.; Moon, S.-J.; Humphry-Baker, R.; Gao, P.; Nazeeruddin, M. K.; Grätzel, M. Sequential Deposition as a Route to High-Performance Perovskite-Sensitized Solar Cells. *Nature* **2013**, *499*, 316–319.

(21) Jeon, N. J.; Lee, H. G.; Kim, Y. C.; Seo, J.; Noh, J. H.; Lee, J.; Seok, S. Il. O-Methoxy Substituents in Spiro – OMeTAD for Efficient Inorganic – Organic Hybrid Perovskite Solar Cells O-Methoxy Substituents in Spiro – OMeTAD for Efficient Inor- Ganic – Organic Hybrid Perovskite Solar Cells. *J. Am. Chem. Soc.* **2014**, *136*, 7837–7840.

(22) Park, N.-G. Organometal Perovskite Light Absorbers Toward a 20% Efficiency Low-Cost Solid-State Mesoscopic Solar Cell. *J. Phys. Chem. Lett.* **2013**, *4*, 2423–2429.

(23) Kim, H. S.; Im, S. H.; Park, N.-G. Organolead Halide Perovskite: New Horizons in Solar Cell Research. *J. Phys. Chem. C* **2014**, *118*, 5615–5625.

(24) Gao, P.; Grätzel, M.; Nazeeruddin, M. K. Organohalide Lead Perovskites for

Photovoltaic Applications. *Energy Environ. Sci.* **2014**, *7*, 2448–2463.

(25) Tan, Z.-K.; Moghaddam, R. S.; Lai, M. L.; Docampo, P.; Higler, R.; Deschler, F.; Price, M.; Sadhanala, A.; Pazos, L. M.; Credgington, D.; et al. Bright Light-Emitting Diodes Based on Organometal Halide Perovskite. *Nat. Nanotechnol.* **2014**, *9*, 687–692.

(26) Deschler, F.; Price, M.; Pathak, S.; Klintberg, L. E.; Jarausch, D.; Higler, R.; Hu, S.; Leijtens, T.; Stranks, S. D.; Snaith, H. J.; et al. High Photoluminescence Efficiency and Optically Pumped Lasing in Solution-Processed Mixed Halide Perovskite Semiconductors. *J. Phys. Chem. Lett.* **2014**, *5*, 1421–1426.

(27) Xing, G.; Mathews, N.; Lim, S. S.; Yantara, N.; Liu, X.; Sabba, D.; Grätzel, M.; Mhaisalkar, S.; Sum, T. C. Low-Temperature Solution-Processed Wavelength-Tunable Perovskites for Lasing. *Nat. Mater.* **2014**, *13*, 476–480.

(28) NREL. http://www.nrel.gov/ncpv/images/efficiency_chart.jpg.

(29) Kim, C.; Ryu, S.; Seo, J.; Seok, S. Il. High-Performance Photovoltaic Perovskite Layers Fabricated through Intramolecular Exchange. *Science (80-.).* **2015**, *348*, 1234–1237.

(30) Stranks, S. D.; Eperon, G. E.; Grancini, G.; Menelaou, C.; Alcocer, M. J. P.; Leijtens, T.; Herz, L. M.; Petrozza, A.; Snaith, H. J. Electron-Hole Diffusion Lengths Exceeding 1 Micrometer in an Organometal Trihalide Perovskite Absorber. *Science* **2013**, *342*, 341–344.

(31) Xing, G.; Mathews, N.; Sun, S.; Lim, S. S.; Lam, Y. M.; Grätzel, M.; Mhaisalkar, S.; Sum, T. C. Long-Range Balanced Electron- and Hole-Transport Lengths in Organic-Inorganic CH3NH3PbI3. *Science* **2013**, *342*, 344–347.

(32) Wehrenfennig, C.; Eperon, G. E.; Johnston, M. B.; Snaith, H. J.; Herz, L. M. High Charge Carrier Mobilities and Lifetimes in Organolead Trihalide Perovskites. *Adv. Mater.* **2013**, *26*, 1584.

(33) Stranks, S. D.; Snaith, H. J. Metal-Halide Perovskites for Photovoltaic and Light-Emitting Devices. *Nat. Nanotechnol.* **2015**, *10*, 391–402.

(34) Snaith, H. J.; Abate, A.; Ball, J. M.; Eperon, G. E.; Leijtens, T.; Noel, N. K.; Stranks, S. D.; Wang, J. T.; Wojciechowski, K.; Zhang, W. Anomalous Hysteresis in Perovskite

Solar Cells. *J. Phys. Chem. Lett.* **2014**, *17*, 1511–1515.

(35) Shahi, S. Photovoltaics: Flexible Optoelectronics. *Nat. Photonics* **2010**, *4*, 506–506.

(36) Wong, W. S.; Salleo, A. *Flexible Electronics*; Wong, W. S., Salleo, A., Eds.; Electronic Materials: Science & Technology; Springer US: Boston, MA, 2009; Vol. 11.

(37) Eisa, M. H.; Faraj, M. G.; Azhari, F. Deposited Indium Tin Oxide (ito) Thin Films by Dc- Magnetron Sputtering on Polyethylene Terephthalate Substrate (pet). *Film* **2011**, *56*, 730–741.

(38) Olle Inganäs. Organic Photovoltaics: Avoiding Indium. *Nat. Photonics* **2011**, *5*, 201–203.

(39) Langley, D.; Giusti, G.; Mayousse, C.; Celle, C.; Bellet, D.; Simonato, J.-P. Flexible Transparent Conductive Materials Based on Silver Nanowire Networks: A Review. *Nanotechnology* **2013**, *24*, 452001.

Chapter 2

Theoretical background

2.1 Principles of the photovoltaic device

2.1.1 Basics of semiconductors

When atoms are brought together in a solid material of periodic structure, atomic orbitals are split into a large number of closely-spaced levels, forming a continuum of energy states, otherwise known as a band.[1] Semiconducting materials constitute the principal building blocks of solar cells, and their band structure is comprised of two regions which contain many electronic states. These two regions are separated by an energetic gap where no energy states exist. This gap is commonly known as the bandgap of a material. Electrons in a semiconductor are primarily located in the lower band, termed the valence band (VB), where they have very limited freedom of movement due to a high occupation of states. When an energy equal to or higher than the bandgap is delivered to the system, an electronic transition to the higher band, or conduction band (CB), is possible. In the CB, the occupation of electronic states is low, and therefore electrons can freely move between many unoccupied states.

In metallic materials, in contrast to semiconductors, the Fermi level (E_f), which is defined as the electrochemical potential of the electrons, or the electronic state which has 50% probability of being occupied by an electron, lies within the conduction band.[2] In metals the band structure often forms a continuum of electronic states with no distinguishable bandgap. As a consequence, electrons can be easily excited between these states and have high freedom of movement. These materials typically have high conductivity values due to large density of mobile carriers, and are excellent conductors of both charge and heat. Insulators are materials which have a very large energetic gap, typically beyond 4 eV,[2] and very low conductivities. A schematic representation of the energetic states for all three types of materials is shown in Figure 2.1. The dotted line represents the Fermi level in each material.

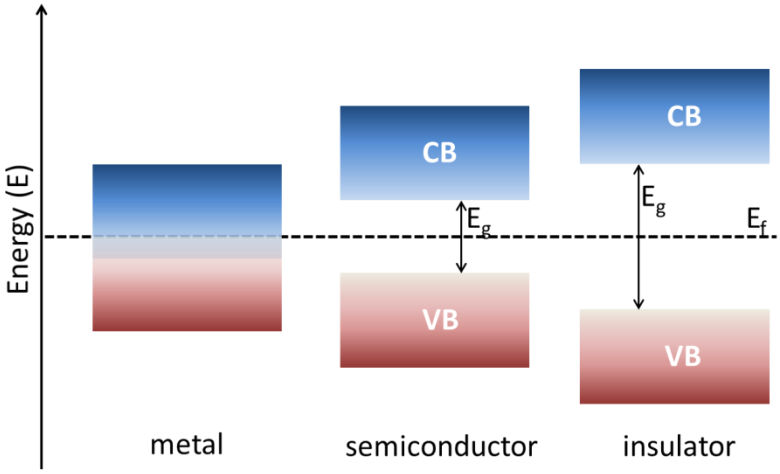


Figure 2.1. Schematic representation of electronic states in metals, semiconductors and insulators. Semiconducting and insulating materials have characteristic energetic gap (E_g) between conduction band (CB) and valence band (VB), where there are no electronic states. It is significantly larger for insulators. Dotted line represents the Fermi level (E_f) of each material.

The Fermi level is an intrinsic property of a given material. It can be modified by the addition of electrons or holes through a process called doping. Adding electrons (n-type doping), raises the Fermi level such that it is closer to the conduction band. Conversly, introducing holes (p-type doping), shifts the Fermi level closer to the

valence band. Doping is commonly used in semiconductors to modify their optoelectronic properties and improve their conductivities by increasing the carrier concentration. Chemical doping involves the introduction of impurity atoms into the crystal lattice. These atoms can donate additional electrons or holes to the semiconductor's conduction band or valence band, respectively. A typical illustration of chemical doping is the case of silicon (Si), which is the most widely used semiconducting material. Silicon is a group IV element and has four valence electrons. In order to p-dope this material, a small concentration of atoms of group III elements such as boron, gallium or indium, are introduced into the material. These elements have only three valence electrons, and as such, have the effect of increasing the hole density, or making the material electron deficient. Conversely, in order to n-dope Si, atoms of group V elements, such as phosphorus are introduced into the material. These elements have five valence electrons, and when introduced into Si, increase its electron density, effectively n-doping it.

2.1.2 Solar cell operation

A solar cell is a device which directly converts sunlight into electrical energy. There are three main principles which govern the operating of a photovoltaic device: light harvesting (generation of charges), separation and transport of photogenerated charges, and collection of these charges at the respective electrodes.

Photons of energy equal to or higher than a material's bandgap can interact with electrons in the valence band. As a result they can get absorbed, giving away their energy and triggering the excitation of an electron into the conduction band. The maximum number of excited electrons

and hence the maximum photocurrent achievable for a given semiconducting material is directly related to its absorption onset, which occurs at a wavelength defined by the material's bandgap. The standard solar spectrum at the earth's surface (AM1.5) used for characterisation of solar cells is shown in Figure 2.2. The attenuation by the atmosphere is quantified by the air mass (AM) factor. AM of 1.5 corresponds to the sun's elevation angle of 42 º.[1] The sun's spectrum (AM1.5) can approximated to the black body radiation at 5760 K. The AM1.5 is normalised to match the irradiance of 1000 W/m^2.[1]

The shaded areas in Figure 2.2 correspond to the fractions of the solar spectrum available for absorption for silicon and the metal-halide perovskite ($CH_3NH_3PbI_3$). The theoretical maximum current density (J_{max}) achievable by each absorbing material can be derived from Equation 2.1 (calculated values are presented in Table 2.1):[1]

$$J_{max} = q \int_{E_g}^{\infty} \emptyset_{ph}^{AM1.5}(E) dE \quad (2.1)$$

where q is elemental charge and $\emptyset_{ph}^{AM1.5}(E)$ is photon flux density at a given wavelength.

In Figure 2.2 J_{max} is plotted as a function of the material's band gap. It should be noted that this is the current density under the assumption of perfect generation (no optical losses) and collection of charges, i.e. when external quantum efficiency is 100%.

Table 2.1. Theoretical maximum current density calculated from Equation 2.1.

Material	Bandgap, E_g (eV)	Maximum current density, J_{max} (mA/cm^2)
Silicon (Si)	1.11[3]	43.5
Perovskite ($CH_3NH_3PbI_3$)	1.55[4]	27.1

There is a trade-off between the number of photons available for absorption and the fraction of the photon's energy which is used in a solar cell. Both are limited by the semiconductor's bandgap. Photogenerated charges are extracted at a potential smaller than the bandgap

(difference between electrochemical potential of electrons in CB and holes in VB after photoexcitation), so the excess of energy from absorbing high energy photons (so called hot carriers) is usually lost *via* thermalisation processes. As such, the smaller bandgap the higher the maximum achievable current density. At the same time however, lower photovoltages are delivered by such semiconductor. Shockley and Queisser calculated that for a single junction solar cell the ideal bandgap for a semiconductor is 1.1 eV, and that such a device can deliver 30% power conversion efficiency.[5] The calculation was done at the radiative limit, assuming no non-radiative recombination losses, and taking sun's spectrum as the radiation of a black body at 6000 K.

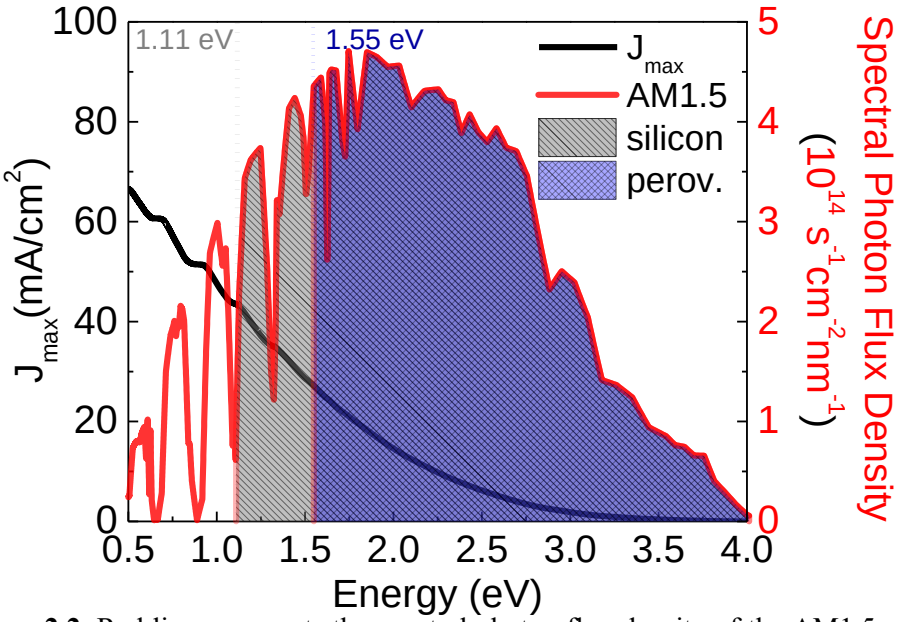


Figure 2.2. Red line represents the spectral photon flux density of the AM1.5 sunlight. Shaded areas indicate the amount of spectrum which is available for absorption for each semiconducting material (silicon and perovskite). Black line is a plot of maximum current density available for a given semiconductor (calculated by Equation 2.1) as a function of its bandgap.

The bandgap of a semiconductor determines what fraction of the solar spectrum is available for absorption, while the probability of each electronic transition happening at a given wavelength is described by material's absorption coefficient. The absorption coefficient is a very important

parameter in the characterisation of photoactive materials in solar cells. It determines the thickness of a semiconductor layer that is required in order to completely absorb all the photons which have an energy equal to or higher than the semiconductor bandgap. The higher the absorptivity, the thinner the semiconductor films that can be used. Increasing the thickness of a material introduces additional challenges to efficient transport and collection of photogenerated charges.

Following light absorption, an excited electron in the conduction band can remain bound *via* Coulombic attraction to the hole created in the valence band. Such electron-hole pair is known as exciton.[2,6] The Binding energy of the coupled charges varies between materials and primarily depends on the dielectric constant of the semiconductor.[1,2]

Organic semiconductors typically have low dielectric constants (on the order of 3), and as such, form excitonic solar cells. Upon photoexcitation Frenkel-like excitons are created, which exhibit binding energies of around 0.5 eV – a value too large to facilitate spontaneous dissociation into free carriers at room temperature.[1,7] The use of a heterojunction of an electron donor and an acceptor material, with an appropriate difference in electron affinities and ionisation potentials has been shown to efficiently split bound charges.[8] This separation occurs only at the junction, with the diffusion length of excitons being only about 10 nm – an order of magnitude lower than the absorption length.[7] The solution to this limitation was a distributed interface, where donor and acceptor molecules were mixed in a blend, forming the so-called bulk heterojunction architecture.[9] The development of this concept has led to single-junction organic solar cells exceeding 10% power conversion efficiency.[10]

Inorganic crystalline semiconductors, such as silicon, or gallium arsenide (GaAs) have high dielectric constants (11.9 and 13.1 for Si and GaAs, respectively),[11] which allows for effective screening of the electrostatic attraction between bound electron and hole.[12]

Wannier-Mott type excitons are typically associated with this class of materials. Here, the binding energy of the excitons is at the level of kT (26 meV), such that at room temperature these excitons are predominantly dissociated into highly mobile free carriers.[1]

A crystalline silicon solar cell, the most established PV technology, embodies two doped (p- and n-type) silicon slabs brought in contact. The schematic diagram of such a cell and its operating principles are shown in Figure 2.3a-d.[1,13] When two semiconductors are brought into contact, free electrons from the n-doped side and holes from the p-doped side diffuse towards the interface and recombine with each other. This leads to the formation of a depletion region at the p-n junction. Immobile dopant core ions are left behind, positive on n-side and negative on p-side, and an electric field is formed across the junction. The magnitude of the built-in potential (V_{bi}) set by an electric field depends on the doping density and is equal to the difference between the Fermi levels of the two semiconductors. The field keeps the carriers on the opposite sides of the junction. When the incident light is absorbed, an increased concentration of both carriers causes displacement from thermal equilibrium, and the Fermi level is split into two quasi-Fermi levels, one for electrons and one for holes. The difference between the quasi-Fermi levels gives the magnitude of the open-circuit voltage.

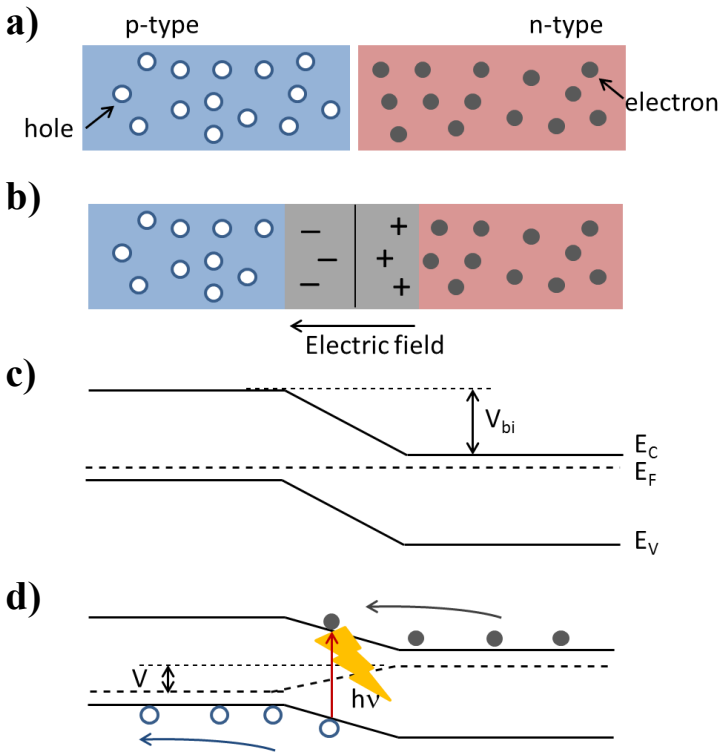


Figure 2.3. (a) Schematic diagram of two semiconductors, p- and n-type doped, put together in direct contact; **(b)** creation of the depletion region and p-n junction at the vicinity of the contact, exposed dopant core ions are marked at the junction; **(c)** energy band diagram of the p-n junction in dark, with a built-in potential (V_{bi}), and **(d)** the junction under working conditions (irradiation and forward bias) generating voltage (V), with marked electron and hole drift.

Upon photoexcitation, photogenerated free carriers move towards the charge collecting contacts. This charge transport occurs via a combination of drift (driven by an electric field) and diffusion (driven by concentration gradient) currents. This relation is described by Equation 2.2:[1]

$$J = (n\mu_n + p\mu_p)qF + (D_n\Delta n - D_p\Delta p)q \tag{2.2}$$

where J is net current, n and p are electron and hole concentrations, F is electric field across the material, and D is diffusion constant for electrons (D_n) and holes (D_p). Diffusion constant can be related with carrier mobility by Einstein relation (2.3):

$$D_x = \frac{\mu_x k_B T}{q} \tag{2.3}$$

where μ_x is carrier (electron or hole) mobility, k_B is Boltzmann's constant, and T is temperature.

Charge extraction at the electrodes should happen selectively for one type of carrier, electron collection at the n-type contact, and hole collection at the p-type contact. In conventional silicon devices this is achieved by putting into contact two oppositely doped wafers. The n-type layer does not allow for holes to permeate due to the low conductivity for this type of carrier. This results from a low concentration of holes in the material. Analogous situation occurs for the p-type layer which blocks electrons. Doping must occur at a level such that the number of majority carriers in the dark is equal to or higher than the concentration of additional carriers generated by light.[13] In many different PV technologies a heterojunction with a uniform layer of a charge selective material is used. The selectivity is provided by choosing a material of appropriate energy bandgap and electron affinity, which allows only one type of carriers to be efficiently transferred across the interface towards the electrode, while blocking the other type of carrier, such that it cannot be extracted. This mechanism of charge collection is common in the devices where diffusion component is more prominent in charge transport.[1,14,15]

The loss of photogenerated electrons or holes, which are not extracted from the device as a photocurrent, is known as recombination and is a limiting factor to performance of solar cells. There are several mechanisms of carrier annihilation. Recombination processes can be divided into two groups: unavoidable ones, which are related to the thermodynamic principles of the solar cell and are also present in an ideal device, and avoidable ones, which originate from imperfections of the semiconducting material.[1] The main mechanism of the first category is direct recombination between an electron

in the conduction band and a hole in the valence band The excess energy produced by this interaction is usually released as a photon, through a process termed photoluminescence. This is an example of radiative recombination. Another intrinsic process is Auger recombination, where electron and hole interact with each other, resulting in annihilation of both carriers and an increase in the kinetic energy of a third carrier. Auger recombination becomes more dominant at high charge densities, and it is more important for low bandgap materials.[1]

The second category of recombination processes is usually related to the existence of electronic trap states either within the absorber, or at the interfaces between the absorber and charge extraction layers.[1] Trap states originate from various crystallographic defects (uncoordinated atoms, vacancies, grain boundaries) or surface states.[16] Charge carriers trapped in shallow sites can be thermally excited and still contribute to the photocurrent. However, a large number of trapping and detrapping cycles, can heavily influence the effective mobility of the carriers, and the efficiency of charge extraction.[1,15] Deeply trapped carriers are permanently immobilised, and eventually recombine with oppositely charged carriers in a non-radiative process, giving away the excess of energy as heat. Solution-processed semiconductors typically exhibit a high level of defect states and electronic disorder, which is mainly attributed to the character of the crystallisation process, typically involving thermal annealing.[17,18] For a good solar cell operation non-radiative recombination should be limited to the minimum.

2.1.3 Solar cell characterisation

A solar cell in the dark acts like a diode. It displays rectifying behaviour, which means that the current flow only occurs in one direction, i.e. when forward bias is applied (V is higher than 0), and it is blocked under reverse bias conditions (V is less than 0). The dark current in an ideal case is described by ideal diode equation given below:[1]

$$J_d(V) = J_0\left(e^{qV/k_BT} - 1\right) \tag{2.4}$$

where J_0 is a saturation current (a temperature-dependant recombination parameter, in an ideal case where there is no non-radiative recombination it's a constant for a given device stack[19]), and V is a voltage bias applied to the electrodes.

Under illumination, when a load is applied to the cell terminals, the potential difference between the electrodes opposes the electrochemical potential gradient coming from the photogeneration. The reverse current driven by the potential bias can be approximated to the diode's dark current. Therefore, the net current produced by the solar cell is the difference between the photocurrent and the dark current (superposition approximation), and for an ideal diode model, this is given by Equation 2.5:[1]

$$J = J_{sc} - J_d(V) = J_{sc} - J_0\left(e^{qV/k_BT} - 1\right) \tag{2.5}$$

where J_{sc} is a short-circuit current density.

When there is no load applied (V=0 and J_d=0), the net current of the device comes only from the photogenerated charges, and this is called the short-circuit current density (J_{sc}). When the applied bias is high enough, i.e. when there is no charge flowing out of the device (the terminals are isolated), the photocurrent is equal to the dark current, and

the cell is in open-circuit condition. The voltage required to cancel out the electrochemical potential gradient of charge carriers in the device induced by illumination is termed open-circuit voltage (V_{oc}), and can be described by Equation 2.6:[1]

$$V_{oc} = \frac{k_B T}{q} ln\left(\frac{J_{sc}}{J_0} - 1\right) \tag{2.6}$$

where J_{sc} is short-circuit current density.

An example of the solar cell's current density-voltage (JV) characteristics, in dark and under illumination, is shown in Figure 2.4a. The parameters that are used for assessing photovoltaic performance, and that can be extracted from the JV curve include: J_{sc}, V_{oc}, fill factor (FF), and power conversion efficiency (PCE). The FF and PCE are described by Equations 2.7 and 2.8, respectively:

$$FF = \frac{J_{max}V_{max}}{J_{sc}V_{oc}} \tag{2.7}$$

where J_{max} is current density at maximum power point, and V_{max} is voltage at max power point.

$$PCE = \frac{P_{max}}{P_i} = \frac{J_{sc}V_{oc}FF}{P_i} \tag{2.8}$$

where P_{max} is device's maximum power, and P_i is a power of incident light.

The shape of the JV curve and magnitude of the FF is influenced by the loss mechanisms which occur in the device. A silicon solar cell can be described by a simple circuit model where a diode, which generates photocurrent, is connected in parallel with a shunt resistor (representing leakage losses), and another resistor connected in series (representing resistive losses that come from non-ideal contacts and transport issues).[1] The scheme of such circuit is shown in Figure 2.4b.

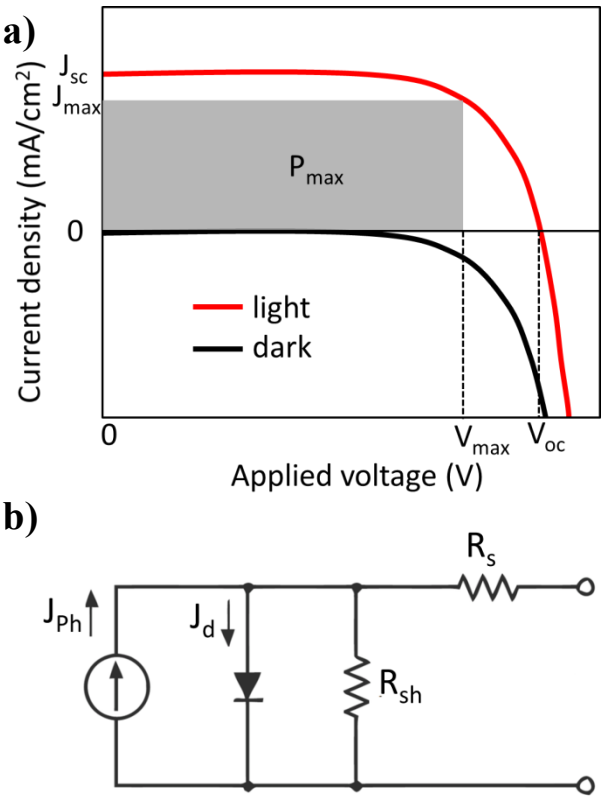


Figure 2.4. (a) Current density-voltage characteristics of a solar cell in dark (black curve) and under illumination (red curve). Photovoltaic parameters which can be extracted from the curve include: short-circuit current density (J_{SC}), open-circuit voltage (V_{OC}), current density and voltage at the maximum power point (J_{max} and V_{max}); **(b)** equivalent circuit model representing a silicon solar cell containing a photocurrent source (J_{Ph}) connected in parallel with a diode (J_d), and two resistors, one connected in parallel (R_{sh}) and one in series (R_s).

2.2 Perovskite solar cell

2.2.1 What is perovskite?

The term perovskite refers to any material which has the crystal structure of calcium titanate ($CaTiO_3$) and the general formual ABX_3. It is a very broad family of materials, encompassing conductors, insulators, superconductors, materials with thermoelectric, piezoelectric, and ferroelectric properties.[20] The compounds of interest for photovoltaic applications are organic-inorganic lead halide perovskites. Originally devices were primarily based on $CH_3NH_3PbX_3$ films, where X is I, Br, Cl, or a combination of halides.[21–23] The lattice arrangement of methylammonium lead triiodide ($CH_3NH_3PbI_3$) representing cubic structure is shown in Figure 2.5.[24]

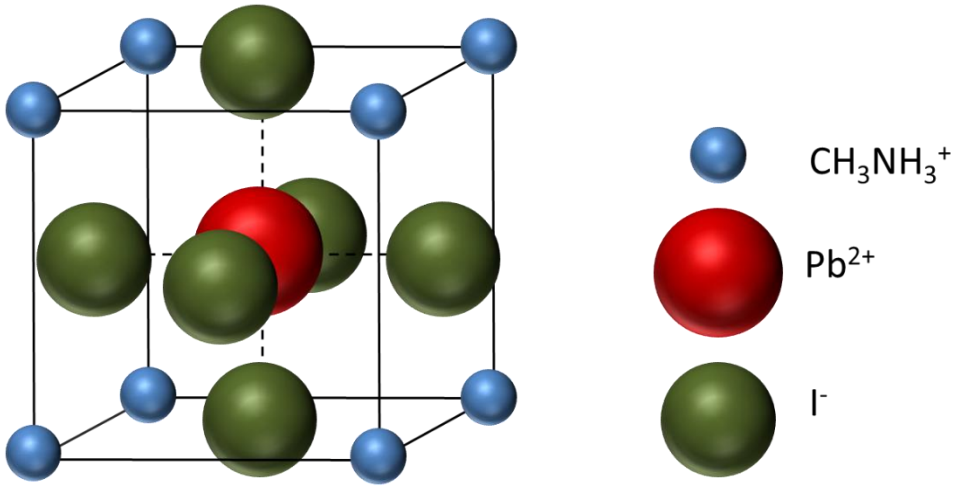


Figure 2.5. Crystal structure of the perovskite material of the general formula ABX_3, where A is organic cation ($CH_3NH_3^+$), B is metal cation (Pb^{2+}), and X is halide anion (I^-).

Perovskite solar cells have recorded exceptionally fast increases in power conversion efficiencies.[23,25,26] It took only few years of research to start competing in photovoltaic performance with well established, mature technologies, such as crystalline silicon, CIGS or CdTe, at least with regards to laboratory-scale devices. The high photovoltaic performance of solar cells employing perovskites is attributed to their favourable optoelectronic properties. $CH_3NH_3PbI_3$ is an excellent absorber with a bandgap of of 1.55 eV, which is very close to that of GaAs, currently the most efficient photovoltaic material.[1,4,25] The perovskite material has been shown to be predominantly non-excitonic at room temperatures, and it displays very long electron and hole diffusion lengths, which has direct influence on the device operation principles.[27–29] Recently, the exciton binding energy has been found to be at the level of a few meV at room temperature, *via* direct, magnetic field-assisted spectroscopic measurement, which corroborates previous findings about the generation of free charges.[30] As a result of this and its ambipolar characteristics, the perovskite can assume both the role of light absorber, and long range charge transporter in a simple thin-film configuration.[31–34] Furthermore, high crystallinity, and low non-radiative decay rates yield a very high ratio of bandgap to open-circuit voltage, a feat which is quite remarkable for a solution-processed material.[23,35,36] All these properties are complemented with the exceptional ease with which the materials crystallise, and its favourable defect chemistry, which is only just starting to be understood.[35,37,38]

Another great advantage of these materials is the tunability of the optical bandgap. It has been shown that the bandgap is strongly correlated with the metal-halide-metal bond angle.[39] Therefore, by changing a halide atom in the crystal lattice, the optical properties of the material can be adjusted.[21,40–42] When iodine is gradually replaced by bromine, films of a broad range of colours can be achieved, reaching a bandgap of up to 2.2 eV for the tribromide perovskite ($CH_3NH_3PbBr_3$).[21] The A-site cation in the

perovskite lattice can also be intermixed. The methylammonium group has been interchanged with organic cations of different sizes (formamidinium, guanidinium),[40,42–44] inorganic cations (caesium),[45,46] or a combination of both.[47–49] The last approach has been recently shown to improve the stability of the structure. The parameter which describes the possibility of forming a three-dimensional perovskite lattice from a combination of given atoms, is the Goldschmidt tolerance factor (t), given by Equation 2.9:[39]

$$t = \frac{r_A + r_X}{\sqrt{2}(r_B + r_X)} \tag{2.9}$$

where r_A is the radius of the A-cation, r_B is the radius of the B cation, and r_X is the radius of the X anion.

The value of t has to be in the range from around 0.8 to 1 in order for the formation of a 3D perovskite to occure.[39,49] When the tolerance factor is higher than 1, this results in the formation of distorted, or layered (two-dimensional) structures. Values of the tolerance factor which are closer to the lower boundary often indicate the likelihood of there being stronger bonding between the cation and halide anion, preventing the perovskite formation.

The emergence of all solid-state perovskite solar cell architectures, where liquid electrolyte was replaced with a solid-state hole transporting material, provided dramatically improved structural stability of the perovskite layer.[4,50,51] Since then, the chloride-containing precursor solution ($PbCl_2$ used instead of PbI_2) has been a popular route for fabricating highly efficient devices.[4,31] The optical bandgap and X-ray diffraction pattern of $CH_3NH_3PbI_{3-x}Cl_x$ material is the same as $CH_3NH_3PbI_3$, but the film formation and certain optoelectronic properties are superior for the chloride-derived films.[27,52,53] This fact raised many questions about the role of chlorine in the

crystallisation of these films, i.e. whether these ions are incorporated into the crystal lattice forming a mixed halide perovskite, and what mechanism governs these improved optoelectronic properties. Recent studies suggest that lattice incorporation of Cl ions is thermodynamically unfavourable due to the large difference in ionic radii between Cl and I.[54] The material is predominantly composed of $CH_3NH_3PbI_3$, with trace amounts of Cl, that have been detected by spectroscopic techniques.[55,56] Furthermore, it has been postulated that chloride ions assist favourable nucleation and easier release of the excess of organic component, leading to a better film morphology.[57,58] The majority of the Cl is removed from the film during annealing as MCl. The exact role of chlorine is still yet to be fully understood, as well as the precise location where residual ions reside, or the degree of their lattice incorporation, if any. In this thesis, the formula $CH_3NH_3PbI_{3-x}Cl_x$ is used to denote methylammonium lead iodide perovskite derived from the chloride-based precursor (CH_3NH_3I : $PbCl_2$, 3:1 molar ratio, N,N-Dimethylformamide as solvent), in order to highlight the processing route, which has strong influence on some electronic properties of the material.

2.2.2 Operating principles of perovskite solar cells

The perovskite material ($CH_3NH_3PbI_3$) was used for the first time in photovoltaic applications as a sensitizer for mesoporous TiO_2 (m-TiO_2).[50,59] The cell was operating in the traditional dye-sensitised solar cell architecture.[60] In this case, nanocrystalline perovskite was embedded in the m-TiO_2 and took on the role of a dye, in that it was responsible for light harvesting. The porosity of the oxide provides a large surface area for absorber loading.[60] With this configuration, photoexcited electrons in perovskite are injected into TiO_2, and are transported through the mesoporous structure towards the electrode. In the first embodiment of the perovskite cell, a liquid electrolyte was used

as a redox couple to regenerate holes in the valence band. The corrosive electrolyte solution (based on the iodide/triiodide redox couple) was a major drawback of these cells, causing rapid degradation of the perovskite material.[50,61]

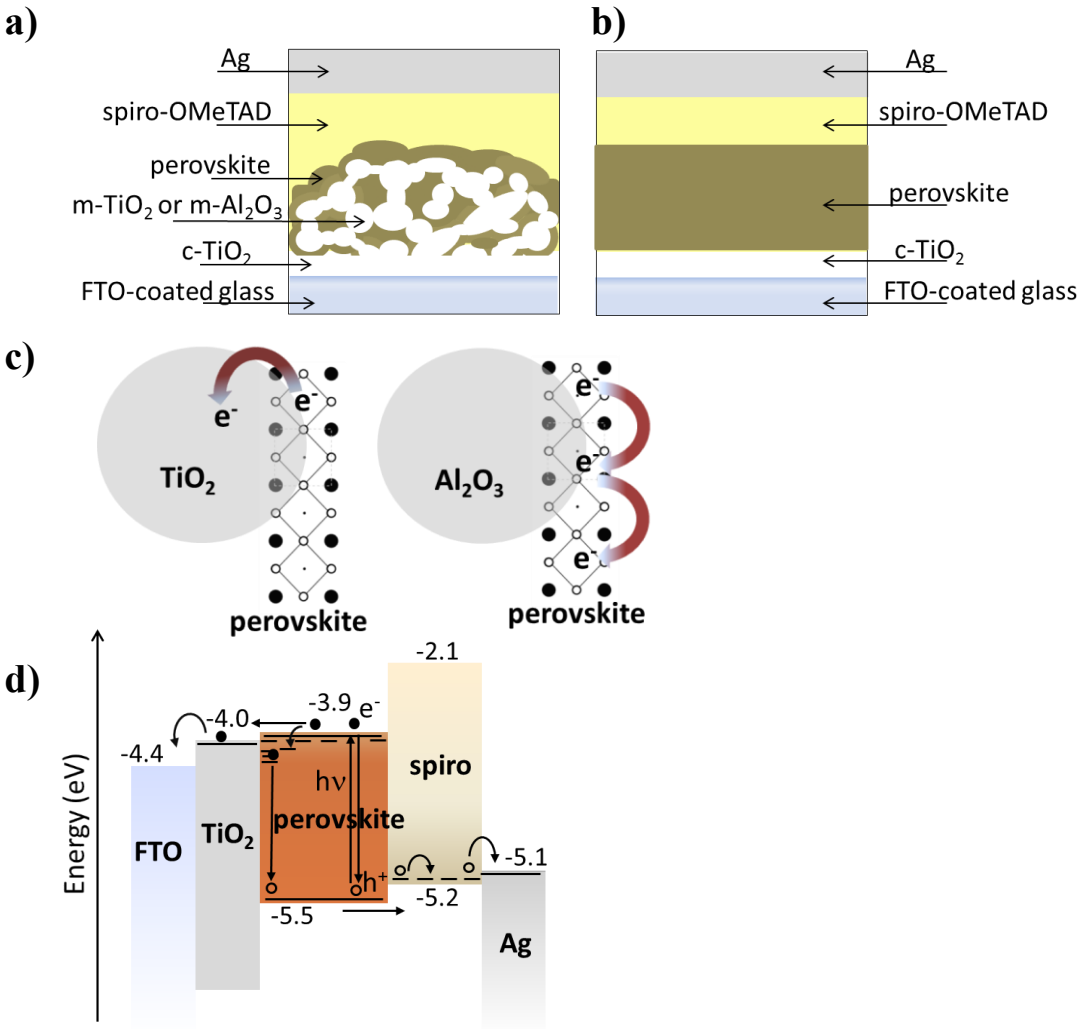


Figure 2.6. Diagram of all solid-state perovskite solar cell in **(a)** a mesoscopic architecture (porous Al_2O_3 or TiO_2 infiltrated by perovskite), and **(b)** a planar heterojunction architecture (n-i-p configuration employing flat perovskite film); **(c)** schematic representation of the difference in electron transport mechanism between meso-TiO_2 perovskite solar cell (the electron is injected into the oxide) and meso-Al_2O_3 device (the alumina acts as a scaffold, and the electron is transported within the perovskite film); **(d)** the principal electronic processes occurring in a planar heterojunction perovskite solar cell, including: photoexcitation, charge transport, electron trapping, radiative and non-radiative recombination, electron and hole injection into n- and p-type contact, respectively.

The big breakthrough was achieved three years later when the liquid electrolyte was replaced with a solid-state hole transporting material, 2,2',7,7'-Tetrakis-(N,N-di-4-methoxyphenylamino)-9,9'-spirobifluorene (spiro-OMeTAD).[51] The operating principles of the device remained the same, with photogenerated charges in the perovskite being extracted at the heterojunctions with TiO_2 (electron transfer) and spiro-OMeTAD (hole transfer), and subsequently transported towards their respective electrodes.

Independently to Park, a solid-state HTM in combination with perovskite ($CH_3NH_3PbI_{3-x}Cl_x$) was used in the Snaith group.[4] The biggest revelation in this work was a replacement of mesoporous TiO_2 with mesoporous Al_2O_3, an insulator which cannot accept nor transport charges. Surprisingly, the solar cells exhibited high efficiencies, making it apparent that perovskite can also efficiently transport both types of carriers. The aluminium oxide added as a scaffold for perovskite crystallisation, and this architecture became known as the meso-superstructured solar cell (MSSC).[4] In such a device, photogenerated charges are transported within the absorbing material towards the charge selective contacts. As an n-type contact (electron collection), a thin and compact film of crystalline TiO_2 is typically used. Spiro-OMeTAD is most often employed as a p-type contact (hole collection).[26]

The ambipolar nature of the perovskite material has quickly led to thin-film architectures, where a semiconductor slab is sandwiched between the charge selective contacts.[31,32] The polarity of the contacts processed on either side of the perovskite layer can be reversed. Planar heterojunction (PHJ) devices have been fabricated in both, the n-i-p and p-i-n configurations.[32–34,62,63] In the first case, the intrinsic perovskite layer is sandwiched between the n-type electron-selective material from the

substrate side and p-type hole-selective material from the top side. In the p-i-n architecture the charge collection is reversed – holes are collected at the bottom and electrons at the top. The diagrams of flat and mesoscopic perovskite architectures are shown in Figure 2.6a-b. The principle processes occurring during device operation are schematically depicted in Figure 2.6c-d.

The thin-film device operation is enabled by certain optoelectronic properties of the perovskite material. The low exciton binding energy, as discussed in the previous section, results in a rapid dissociation of the photogenerated electron-hole pairs (within 2 ps), and predominantly free charges at room temperature.[28,64] The perovskite's electron and hole mobilities can be in the range of 10-30 $cm^2/V{\cdot}s$.[64,65] The crucial aspect for a given semiconductor to efficiently operate in a planar heterojunction architecture is how its absorption depth (optical length within the material where light's intensity drops to 1/e of the initial intensity, before entering the material[1]) compares with carriers' diffusion length (average distance a charge can travel before it recombines). Due to the high absorption coefficient in $CH_3NH_3PbI_3$ (5.7×10^4 cm^{-1} at 600 nm)[29], the absorption depth is relatively short, around 400 nm at a wavelength of 700 nm.[23] The diffusion lengths of electrons and holes were reported to exceed 1 μm for the chloride-derived perovskite ($CH_3NH_3PbI_{3-x}Cl_x$), when determined from time-resolved photoluminescence (TRPL) measurements.[27] Such long diffusion lengths enable the use of film which is thick enough to absorb all the incident sunlight, and at the same time provide efficient transport of photogenerated charges out of the perovskite layer. Diffusion lengths measured by other methods (values from TRPL may be underestimated due to assumption of perfect charge extraction at the interfaces[23]), such as electron beam-induced current (EBIC) or terahertz spectroscopy, are even higher, yielding over 2 microns.[65,66]

Favourable recombination dynamics results in long photoluminescence lifetimes (microseconds have been reported[27,67]) and long diffusion lengths of the free carriers. At high charge densities, the PL decay is bimolecular, which suggests the radiative pathways to be the dominant ones.[28] It is corroborated by very high photoluminescence quantum yield (PLQE), approaching 70% (even higher values at lower temperatures).[36] At lower excitation fluences, including under solar cell operating conditions, trap-assisted non-radiative recombination becomes a significant factor, and the decay dynamics are monomolecular. Limiting the non-radiative pathways can bring the device operation closer to the Shockley-Quiesser limit. The density and nature of the electronic trap states are important factors which influence the recombination dynamics.[1]

Various defects in a semiconductor's lattice can act as trap states or recombination centres by increasing the level of non-radiative recombination, which in turn, limits the photovoltaic performance. Polycrystalline perovskite films exhibit a relatively low level of electronic disorder. The Urbach energy – a measure of this disorder – is around 15 meV, very similar to that of crystalline silicon (11 meV).[23,35] The defect density in $CH_3NH_3PbI_3$ films is estimated to be on the order of 10^{16} cm^{-3}, which is uncharacteristically low for a solution-processed material. Despite the low level of traps, it is apparent that these defects can significantly influence the device operation. Grain boundaries are one of the potential recombination sites, contributing to the operational losses. The inter-grain potential barrier on the perovskite surface, measured in dark, was determined to be at the level of only 45 meV.[66] On the other hand, it has been shown that the optoelectronic properties of the material can significantly improve with larger crystals and fewer grains. Single crystals of $CH_3NH_3PbI_3$ and $CH_3NH_3PbBr_3$ have been recently grown, with estimated diffusion length of 175 μm

and trap density of 10^{10} cm^{-3}.[68] Furthermore, trap states can originate from various lattice defects or surface states. Chemical passivation can be applied to inactivate some of these centres.[67,69,70]

The most efficient perovskite solar cells still employ a thin, m-TiO_2 layer (about 200 nm).[71,72] These cells have a thick perovskite capping layer (typically thicker than m-TiO_2 film), which makes them resemble a planar n-i-p architecture. The porous oxide facilitates crystallisation of the perovskite film with superior properties. Furthermore, m-TiO_2 seems to be making excellent electronic contact, where charges are efficiently collected across the interface with minimal resistive losses. Planar heterojunction cells devoid of metal oxide are not lagging far behind,[73,74] but more work on interfacial engineering (finding ideal contacts on both sides) and structural optimisation of the perovskite layer is required to achieve PCEs exceeding 20%.

2.2.3 Principles of the heterojunction interface

The architecture of perovskite solar cells evolved from mesostructured into planar heterojunction thin-films.[75] The physical processes occurring at the interfaces with the perovskite material have a major impact on the photovoltaic performance of these cells.[76] The work presented in this thesis largely focuses on what is happening at these junctions and how the use of different extraction layers affects device operation.

When two semiconductors are put in contact their Fermi levels need to align.[1] Intrinsic carriers present in either material will start flowing across the contact in order to establish the equilibration and unification of the Fermi levels on both sides of the interface. This theorem is known as Anderson's rule.[76,77] When charges diffuse to align

the Fermi levels, depletion and band bending appears in the vicinity of the contact.[1] A build-in potential is set up across the junction. One can easily distinguish between different types of junctions. When two semiconductors made of the same material are put together they form a homojunction, when the materials are different it is known as a heterojunction.[1] Two crystalline silicon wafers with different doping characteristics (p- and n-type) form a p-n homojunction, which has been discussed in more detail in the section 2.1.2. Examples of the energy diagrams for homo-, hetero-, and metal-semiconductor (Schottky) junctions are shown in Figure 2.7.[76]

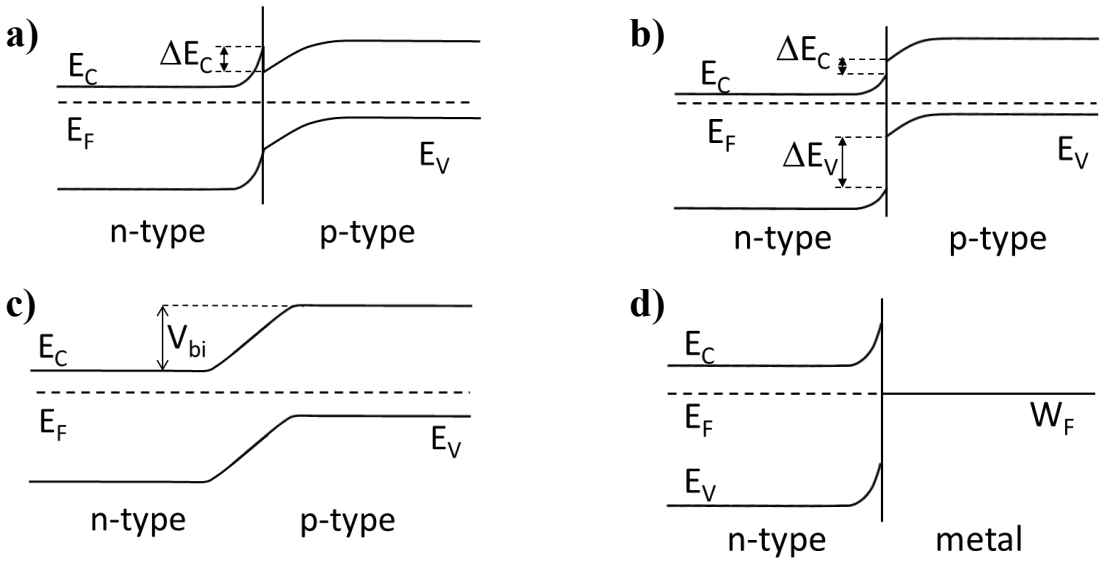


Figure 2.7. Interfacial energy band diagram of semiconductors forming **(a)** n-p heterojunction with a positive conduction band offset (ΔE_C) – a 'notch', and **(b)** negative offset – a 'cliff'; **(c)** n-p homojuction with a built-in potential, V_{bi}; **(d)** Schottky junction of n-type semiconductor and a metal of a work function, W_F.

The efficient transfer of photogenerated charges across the interface has a significant influence on a device's photovoltaic performance. A cliff or a notch at the heterojunction (as shown in Figure 2.7a-b) can lead to the accumulation of carriers, and in turn pronounced recombination. Furthermore, numerous electronic defects arising at the interface (lattice mismatch, vibronic states, uncoordinated atoms) can trap the

charges before they get extracted, contributing to the operational losses (trap-assisted non radiative recombination).[1,76]

Carrier transport in the absorber layer is described by Equation 2.2. In a heterojunction device, both the electric field in the depletion region (band bending at the interface) and the diffusion component play a significant role in transporting charges.[1,15] The carrier distribution in a semiconductor depends on the generation rate under illumination, carrier concentration at the vicinity of the contact, and the interfacial charge transfer rate. When the extraction velocity is higher than the diffusion rate, the density of carriers at the interface is very low. This in turn creates a concentration gradient, which helps the charges diffuse towards the appropriate contact where they are collected. If charge extraction is not very effective, carriers build up at the interface, which leads to increased recombination. Therefore, efficient charge transfer at the heterojunction is vital to minimise charge losses.

The control of the defect density and the quality of the electronic contact at the charge extraction heterojunctions can significantly improve the device operation. Detailed investigations of the structural and electronic interactions between the materials is necessary, in order to find an optimal contact. Theoretical calculations can provide very useful tools in addressing these tasks. There is large scope for research into charge selective materials for planar heterojunction perovskite solar cells, especially for n-type materials. Advancements in this field could lead to further enhancements of power conversion efficiencies, as well as resolve some stability issues present in these devices.

2.3 References

(1) Nelson, J. *The Physics of Solar Cells*; Series on Properties of Semiconductor Materials; Imperial College Press, 2003.

(2) Kittel, C. *Introduction to Solid State Physics*, 8th ed.; Wiley, 2004.

(3) Streetman, B. G.; Banerjee, S. *Solid State Electronic Devices*; Prentice-Hall series in solid state physical electronics; Pearson Prentice Hall, 2006.

(4) Lee, M. M.; Teuscher, J.; Miyasaka, T.; Murakami, T. N.; Snaith, H. J. Efficient Hybrid Solar Cells Based on Meso-Superstructured Organometal Halide Perovskites. *Science* **2012**, *338*, 643–647.

(5) Shockley, W.; Queisser, H. J. Detailed Balance Limit of Efficiency of P-N Junction Solar Cells. *J. Appl. Phys.* **1961**, *32*, 510.

(6) Koch, S. W.; Kira, M.; Khitrova, G.; Gibbs, H. M. Semiconductor Excitons in New Light. *Nat. Mater.* **2006**, *5*, 523–531.

(7) Leo, K. Organic Photovoltaics. *Nat. Rev. Mater.* **2016**, *1*, 1–2.

(8) Tang, C. W. Two-Layer Organic Photovoltaic Cell. *Appl. Phys. Lett.* **1986**, *48*, 183.

(9) Hiramoto, M.; Fujiwara, H.; Yokoyama, M. Three-Layered Organic Solar Cell with a Photoactive Interlayer of Codeposited Pigments. *Appl. Phys. Lett.* **1991**, *58*, 1062.

(10) Zhao, W.; Qian, D.; Zhang, S.; Li, S.; Inganäs, O.; Gao, F.; Hou, J. Fullerene-Free Polymer Solar Cells with over 11% Efficiency and Excellent Thermal Stability. *Adv. Mater.* **2016**, *28*, 4734–4739.

(11) Sze, S. M.; Ng, K. K. *Physics of Semiconductor Devices*; Wiley, 2006.

(12) Aspnes, D. E.; Studna, A. A.; Kinsbron, E. Dielectric Properties of Heavily Doped Crystalline and Amorphous Silicon from 1.5 to 6.0 eV. *Phys. Rev. B* **1984**, *29*, 768–779.

(13) Würfel, P.; Würfel, U. *Physics of Solar Cells: From Principles to New Concepts*;

Physics textbook; Wiley, 2005.

(14) Peng, B.; Jungmann, G.; Jäger, C.; Haarer, D.; Schmidt, H.-W.; Thelakkat, M. Systematic Investigation of the Role of Compact TiO_2 Layer in Solid State Dye-Sensitized TiO_2 Solar Cells. *Coord. Chem. Rev.* **2004**, *248*, 1479–1489.

(15) Nelson, J. Continuous-Time Random-Walk Model of Electron Transport in Nanocrystalline TiO_2 Electrodes. *Phys. Rev. B* **1999**, *59*, 374–380.

(16) Queisser, H. J. Defects in Semiconductors: Some Fatal, Some Vital. *Science* **1998**, *281*, 945–950.

(17) Diao, Y.; Tee, B. C.-K.; Giri, G.; Xu, J.; Kim, D. H.; Becerril, H. A.; Stoltenberg, R. M.; Lee, T. H.; Xue, G.; Mannsfeld, S. C. B.; et al. Solution Coating of Large-Area Organic Semiconductor Thin Films with Aligned Single-Crystalline Domains. *Nat. Mater.* **2013**, *12*, 665–671.

(18) Graetzel, M.; Janssen, R. A. J.; Mitzi, D. B.; Sargent, E. H. Materials Interface Engineering for Solution-Processed Photovoltaics. *Nature* **2012**, *488*, 304–312.

(19) Cuevas, A. The Recombination Parameter J0. *Energy Procedia* **2014**, *55*, 53–62.

(20) Snaith, H. J. Perovskites: The Emergence of a New Era for Low-Cost, High-Efficiency Solar Cells. *J. Phys. Chem. Lett.* **2013**, *4*, 3623–3630.

(21) Noh, J. H.; Im, S. H.; Heo, J. H.; Mandal, T. N.; Seok, S. Il. Chemical Management for Colorful, Efficient, and Stable Inorganic− Organic Hybrid Nanostructured Solar Cells. *Nano Lett.* **2013**, *13*, 1764–1769.

(22) Ryu, S.; Noh, J. H.; Jeon, N. J.; Kim, Y. C.; Yang, W. S.; Seoa, J.; Seok, S. Il. Voltage Output of Efficient Perovskite Solar Cells with High Open-Circuit Voltage and Fill Factor. *Energy Environ. Sci.* **2014**, *7*, 2614–2618.

(23) Stranks, S. D.; Snaith, H. J. Metal-Halide Perovskites for Photovoltaic and Light-Emitting Devices. *Nat. Nanotechnol.* **2015**, *10*, 391–402.

(24) Baikie, T.; Fang, Y.; Kadro, J. M.; Schreyer, M.; Wei, F.; Mhaisalkar, S. G.; Graetzel, M.; White, T. J. Synthesis and Crystal Chemistry of the Hybrid Perovskite

(CH_3NH_3)PbI_3 for Solid-State Sensitised Solar Cell Applications. *J. Mater. Chem. A* **2013**, *1*, 5628.

(25) NREL. http://www.nrel.gov/ncpv/images/efficiency_chart.jpg.

(26) Green, M. A.; Ho-Baillie, A.; Snaith, H. J. The Emergence of Perovskite Solar Cells. *Nat. Photonics* **2014**, *8*, 506–514.

(27) Stranks, S. D.; Eperon, G. E.; Grancini, G.; Menelaou, C.; Alcocer, M. J. P.; Leijtens, T.; Herz, L. M.; Petrozza, A.; Snaith, H. J. Electron-Hole Diffusion Lengths Exceeding 1 Micrometer in an Organometal Trihalide Perovskite Absorber. *Science* **2013**, *342*, 341–344.

(28) Stranks, S. D.; Burlakov, V. M.; Leijtens, T.; Ball, J. M.; Goriely, A.; Snaith, H. J. Recombination Kinetics in Organic-Inorganic Perovskites: Excitons, Free Charge, and Subgap States. *Phys. Rev. Appl.* **2014**, *2*, 034007.

(29) Xing, G.; Mathews, N.; Sun, S.; Lim, S. S.; Lam, Y. M.; Grätzel, M.; Mhaisalkar, S.; Sum, T. C. Long-Range Balanced Electron- and Hole-Transport Lengths in Organic-Inorganic $CH_3NH_3PbI_3$. *Science* **2013**, *342*, 344–347.

(30) Miyata, A.; Mitioglu, A.; Plochocka, P.; Portugall, O.; Wang, J. T.-W.; Stranks, S. D.; Snaith, H. J.; Nicholas, R. J. Direct Measurement of the Exciton Binding Energy and Effective Masses for Charge Carriers in Organic–inorganic Tri-Halide Perovskites. *Nat. Phys.* **2015**, *11*, 582–587.

(31) Ball, J. M.; Lee, M. M.; Hey, A.; Snaith, H. J. Low-Temperature Processed Meso-Superstructured To Thin-Film Perovskite Solar Cells. *Energy Environ. Sci.* **2013**, *6*, 1739.

(32) Liu, M.; Johnston, M. B.; Snaith, H. J. Efficient Planar Heterojunction Perovskite Solar Cells by Vapour Deposition. *Nature* **2013**, *501*, 395–398.

(33) Docampo, P.; Ball, J. M.; Darwich, M.; Eperon, G. E.; Snaith, H. J. Efficient Organometal Trihalide Perovskite Planar-Heterojunction Solar Cells on Flexible Polymer Substrates. *Nat. Commun.* **2013**, *4*, 2761.

(34) Malinkiewicz, O.; Yella, A.; Lee, Y. H.; Espallargas, G. M.; Graetzel, M.; Nazeeruddin, M. K.; Bolink, H. J. Perovskite Solar Cells Employing Organic Charge-Transport Layers. *Nat. Photonics* **2013**, *8*, 128–132.

(35) De Wolf, S.; Holovsky, J.; Moon, S.-J.; Löper, P.; Niesen, B.; Ledinsky, M.; Haug, F.-J.; Yum, J.-H.; Ballif, C. Organometallic Halide Perovskites: Sharp Optical Absorption Edge and Its Relation to Photovoltaic Performance. *J. Phys. Chem. Lett.* **2014**, *5*, 1035–1039.

(36) Deschler, F.; Price, M.; Pathak, S.; Klintberg, L. E.; Jarausch, D.; Higler, R.; Hu, S.; Leijtens, T.; Stranks, S. D.; Snaith, H. J.; et al. High Photoluminescence Efficiency and Optically Pumped Lasing in Solution-Processed Mixed Halide Perovskite Semiconductors. *J. Phys. Chem. Lett.* **2014**, *5*, 1421–1426.

(37) Stranks, S. D.; Burlakov, V. M.; Leijtens, T.; Ball, J. M.; Goriely, A.; Snaith, H. J. Recombination Kinetics in Organic-Inorganic Perovskites: Excitons, Free Charge, and Subgap States. *Phys. Rev. Appl.* **2014**, *2*, 034007.

(38) Kim, J.; Lee, S.; Lee, J. H.; Hong, K. The Role of Intrinsic Defects in Methylammonium Lead Iodide. *J. Phys. Chem. Lett.* **2014**, *5*, 1312−1317.

(39) Filip, M. R.; Eperon, G. E.; Snaith, H. J.; Giustino, F. Steric Engineering of Metal-Halide Perovskites with Tunable Optical Band Gaps. *Nat. Commun.* **2014**, *5*, 5757.

(40) Eperon, G. E.; Stranks, S. D.; Menelaou, C.; Johnston, M. B.; Herz, L. M.; Snaith, H. J. Formamidinium Lead Trihalide: A Broadly Tunable Perovskite for Efficient Planar Heterojunction Solar Cells. *Energy Environ. Sci.* **2014**, *7* (3), 982.

(41) Jang, D. M.; Park, K.; Kim, D. H.; Park, J.; Shojaei, F.; Kang, H. S.; Ahn, J.-P.; Lee, J. W.; Song, J. K. Reversible Halide Exchange Reaction of Organometal Trihalide Perovskite Colloidal Nanocrystals for Full-Range Band Gap Tuning. *Nano Lett.* **2015**, *15*, 5191–5199.

(42) Jeon, N. J.; Noh, J. H.; Yang, W. S.; Kim, Y. C.; Ryu, S.; Seo, J.; Seok, S. Il. Compositional Engineering of Perovskite Materials for High-Performance Solar Cells. *Nature* **2015**, *517*, 476–480.

(43) Pellet, N.; Gao, P.; Gregori, G.; Yang, T.-Y.; Nazeeruddin, M. K.; Maier, J.; Grätzel, M. Mixed-Organic-Cation Perovskite Photovoltaics for Enhanced Solar-Light Harvesting. *Angew. Chemie Int. Ed.* **2014**, *53*, 3151–3157.

(44) Boix, P. P.; Agarwala, S.; Koh, T. M.; Mathews, N.; Mhaisalkar, S. G. Perovskite Solar Cells: Beyond Methylammonium Lead Iodide. *J. Phys. Chem. Lett.* **2015**, *6* (5), 898–907.

(45) Kulbak, M.; Cahen, D.; Hodes, G. How Important Is the Organic Part of the Lead Halide Perovskite Photovoltaic Cells? Efficient $CsPbBr_3$ Cells. *J. Phys. Chem. Lett.* **2015**, *6*, 2452–2456.

(46) Eperon, G. E.; Paternò, G. M.; Sutton, R. J.; Zampetti, A.; Haghighirad, A. A.; Cacialli, F.; Snaith, H. J. Inorganic Caesium Lead Iodide Perovskite Solar Cells. *J. Mater. Chem. A* **2015**, *3*, 19688–19695.

(47) Lee, J.-W.; Kim, D.-H.; Kim, H.-S.; Seo, S.-W.; Cho, S. M.; Park, N.-G. Formamidinium and Cesium Hybridization for Photo- and Moisture-Stable Perovskite Solar Cell. *Adv. Energy Mater.* **2015**, *5*, 1501310.

(48) Yi, C.; Luo, J.; Meloni, S.; Boziki, A.; Ashari-Astani, N.; Grätzel, C.; Zakeeruddin, S. M.; Rothlisberger, U.; Grätzel, M. Entropic Stabilization of Mixed A-Cation ABX_3 Metal Halide Perovskites for High Performance Perovskite Solar Cells. *Energy Environ. Sci.* **2016**, *9*, 656–662.

(49) Li, Z.; Yang, M.; Park, J.-S.; Wei, S.-H.; Berry, J.; Zhu, K. Stabilizing Perovskite Structures by Tuning Tolerance Factor: Formation of Formamidinium and Cesium Lead Iodide Solid-State Alloys. *Chem. Mater.* **2015**, *28*, 284–292.

(50) Kojima, A.; Teshima, K.; Shirai, Y.; Miyasaka, T. Organometal Halide Perovskites as Visible-Light Sensitizers for Photovoltaic Cells. *J. Am. Chem. Soc.* **2009**, *131*, 6050–6051.

(51) Kim, H.-S.; Lee, C.-R.; Im, J.-H.; Lee, K.-B.; Moehl, T.; Marchioro, A.; Moon, S.-J.; Humphry-Baker, R.; Yum, J.-H.; Moser, J. E.; et al. Lead Iodide Perovskite Sensitized All-Solid-State Submicron Thin Film Mesoscopic Solar Cell with Efficiency Exceeding 9%. *Sci. Rep.* **2012**, *2*, 591.

(52) Eperon, G. E.; Burlakov, V. M.; Docampo, P.; Goriely, A.; Snaith, H. J. Morphological Control for High Performance, Solution-Processed Planar Heterojunction Perovskite Solar Cells. *Adv. Funct. Mater.* **2013**, *24*, 151.

(53) Colella, S.; Mosconi, E.; Fedeli, P.; Listorti, A.; Gazza, F.; Orlandi, F.; Ferro, P.; Besagni, T.; Rizzo, A.; Calestani, G.; et al. $MAPbI_{3-X}Cl_X$ Mixed Halide Perovskite for Hybrid Solar Cells: The Role of Chloride as Dopant on the Transport and Structural Properties. *Chem. Mater.* **2013**, *25*, 4613–4618.

(54) Chen, Q.; Zhou, H.; Fang, Y.; Stieg, A. Z.; Song, T.-B.; Wang, H.-H.; Xu, X.; Liu, Y.; Lu, S.; You, J.; et al. The Optoelectronic Role of Chlorine in $CH_3NH_3PbI_3$(Cl)-Based Perovskite Solar Cells. *Nat. Commun.* **2015**, *6*, 7269.

(55) Unger, E. L.; Bowring, A. R.; Tassone, C. J.; Pool, V. L.; Gold-Parker, A.; Cheacharoen, R.; Stone, K. H.; Hoke, E. T.; Toney, M. F.; McGehee, M. D. Chloride in Lead Chloride-Derived Organo-Metal Halides for Perovskite-Absorber Solar Cells. *Chem. Mater.* **2014**, *26*, 7158–7165.

(56) Colella, S.; Mosconi, E.; Pellegrino, G.; Alberti, A.; Guerra, V. L. P.; Masi, S.; Listorti, A.; Rizzo, A.; Condorelli, G. G.; Angelis, F. De; et al. Elusive Presence of Chloride in Mixed Halide Perovskite Solar Cells. *J. Phys. Chem. Lett.* **2014**, *5*, 3532–3539.

(57) Williams, S. T.; Zuo, F.; Chueh, C.-C.; Liao, C.-Y.; Liang, P.-W.; Jen, A. K.-Y. Role of Chloride in the Morphological Evolution of Organo-Lead Halide Perovskite Thin Films. *ACS Nano* **2014**, *8*, 10640–10654.

(58) Yu, H.; Wang, F.; Xie, F.; Li, W.; Chen, J.; Zhao, N. The Role of Chlorine in the Formation Process of "$CH_3NH_3PbI_{3-X}Cl_X$ " Perovskite. *Adv. Funct. Mater.* **2014**, *24*, 7102–7108.

(59) Kojimaa, A.; Teshimac, K.; Miyasakab, T.; Shirai, Y. Novel Photoelectrochemical Cell with Mesoscopic Electrodes Sensitized by Lead-Halide Compounds. *210th ECS Meet. Cancun, Mex. Oct. 29−Nov. 3* **2006**, No. 2, 2014.

(60) O'Regan, B.; Grätzel, M. A Low-Cost, High-Efficiency Solar Cell Based on Dye-Sensitized Colloidal TiO_2 Films. *Nature* **1991**, *353*, 737–740.

(61) Im, J.-H.; Lee, C.-R.; Lee, J.-W.; Park, S.-W.; Park, N.-G. 6.5% Efficient Perovskite Quantum-Dot-Sensitized Solar Cell. *Nanoscale* **2011**, *3*, 4088–4093.

(62) Jeng, J.-Y.; Chiang, Y.-F.; Lee, M.-H.; Peng, S.-R.; Guo, T.-F.; Chen, P.; Wen, T.-C. $CH_3NH_3PbI_3$ Perovskite/Fullerene Planar-Heterojunction Hybrid Solar Cells. *Adv. Mater.* **2013**, *25*, 3727–3732.

(63) Liu, D.; Kelly, T. L. Perovskite Solar Cells with a Planar Heterojunction Structure Prepared Using Room-Temperature Solution Processing Techniques. *Nat. Photonics* **2014**, *8*, 133–138.

(64) Ponseca, C. S.; Savenije, T. J.; Abdellah, M.; Zheng, K.; Yartsev, A.; Pascher, T.; Harlang, T.; Chabera, P.; Pullerits, T.; Stepanov, A.; et al. Organometal Halide Perovskite Solar Cell Materials Rationalized: Ultrafast Charge Generation, High and Microsecond-Long Balanced Mobilities, and Slow Recombination. *J. Am. Chem. Soc.* **2014**, *136*, 5189–5192.

(65) Wehrenfennig, C.; Eperon, G. E.; Johnston, M. B.; Snaith, H. J.; Herz, L. M. High Charge Carrier Mobilities and Lifetimes in Organolead Trihalide Perovskites. *Adv. Mater.* **2013**, *26*, 1584.

(66) Edri, E.; Kirmayer, S.; Henning, A.; Mukhopadhyay, S.; Gartsman, K.; Rosenwaks, Y.; Hodes, G.; Cahen, D. Why Lead Methylammonium Tri-Iodide Perovskite-Based Solar Cells Require a Mesoporous Electron Transporting Scaffold (but Not Necessarily a Hole Conductor). *Nano Lett.* **2014**, *14*, 1000–1004.

(67) Noel, N. K.; Abate, A.; Stranks, S. D.; Parrott, E. S.; Burlakov, V. M.; Goriely, A.; Snaith, H. J. Enhanced Photoluminescence and Solar Cell Performance via Lewis Base Passivation of Organic-Inorganic Lead Halide Perovskites. *ACS Nano* **2014**, *8*, 9815–9821.

(68) Dong, Q.; Fang, Y.; Shao, Y.; Qiu, J.; Cao, L.; Huang, J. Electron-Hole Diffusion Lengths > 175 μm in Solution-Grown $CH_3NH_3PbI_3$ Single. *Science* **2015**, *347*, 967–970.

(69) Xu, J.; Buin, A.; Ip, A. H.; Li, W.; Voznyy, O.; Comin, R.; Yuan, M.; Jeon, S.; Ning, Z.; McDowell, J. J.; et al. Perovskite–fullerene Hybrid Materials Suppress Hysteresis in Planar Diodes. *Nat. Commun.* **2015**, *6*, 7081.

(70) Shao, Y.; Xiao, Z.; Bi, C.; Yuan, Y.; Huang, J. Origin and Elimination of Photocurrent Hysteresis by Fullerene Passivation in $CH_3NH_3PbI_3$ Planar Heterojunction Solar Cells. *Nat. Commun.* **2014**, *5*, 5784.

(71) Kim, C.; Ryu, S.; Seo, J.; Seok, S. Il. High-Performance Photovoltaic Perovskite Layers Fabricated through Intramolecular Exchange. *Science* **2015**, *348*, 1234–1237.

(72) Kim, Y. C.; Jeon, N. J.; Noh, J. H.; Yang, W. S.; Seo, J.; Yun, J. S.; Ho-Baillie, A.; Huang, S.; Green, M. A.; Seidel, J.; et al. Beneficial Effects of PbI_2 Incorporated in Organo-Lead Halide Perovskite Solar Cells. *Adv. Energy Mater.* **2016**, *6*, 1502104.

(73) Bi, C.; Wang, Q.; Shao, Y.; Yuan, Y.; Xiao, Z.; Huang, J. Non-Wetting Surface-Driven High-Aspect-Ratio Crystalline Grain Growth for Efficient Hybrid Perovskite Solar Cells. *Nat. Commun.* **2015**, *6*, 1–7.

(74) Correa Baena, J. P.; Steier, L.; Tress, W.; Saliba, M.; Neutzner, S.; Matsui, T.; Giordano, F.; Jacobsson, J.; Srimath Kandada, A. R.; Zakeeruddin, S. M.; et al. Highly Efficient Planar Perovskite Solar Cells through Band Alignment Engineering. *Energy Environ. Sci.* **2015**, *8*, 2928–2934.

(75) Snaith, H. J. Perovskites: The Emergence of a New Era for Low-Cost, High- Efficiency Solar Cells. *J. Phys. Chem. Lett.* **2013**, *4*, 3623.

(76) Shi, J.; Xu, X.; Li, D.; Meng, Q. Interfaces in Perovskite Solar Cells. *Small* **2015**, *11*, 2472–2486.

(77) Anderson, R. L. Experiments on Ge-GaAs Heterojunctions. *Solid. State. Electron.* **1962**, *5*, 341–351.

Chapter 3

Experimental methods

3.1 Synthesis of materials

3.1.1 TiO_2 nanoparticles

TiO_2 anatase nanoparticles were synthesised in ambient conditions following a previously reported method.[1] In a typical synthesis, 2 ml of anhydrous $TiCl_4$ (99.9%, Sigma-Aldrich) was added dropwise with stirring, into a vial containing 8 ml of anhydrous ethanol (Sigma-Aldrich 200 proof). The contents of this vial was transferred into a 100 ml flask containing 40 ml anhydrous benzyl alcohol (Sigma-Aldrich, 99.8% purity). The solution was heated to 80 °C and stirred for 9 hours. After that time, the reaction was arrested by cooling down the solution, which contained a translucent dispersion of very fine TiO_2 nanoparticles. Subsequently. 4 ml of the above solution was mixed with 36 ml of diethyl ether (Fisher Scientific, >99%), causing the precipitation of the TiO_2. The precipitate was centrifuged, washed in acetone (Fisher Scientific) and redispersed in anhydrous ethanol, resulting in a colloidal solution with a concentration of ca. 28 mg/ml (3.54 wt% of TiO_2). The formulation was then diluted

(down to 1.18 wt% of TiO_2) in anhydrous ethanol, and the appropriate amount (10-20 mol% with respect to TiO_2 content) of titanium diisopropoxide bis(acetylacetonate) (TiAcAc, 75 wt% in isopropanol, Sigma-Aldrich) was added directly to the mixture. The solution was left to stand for at least 2 hours before use.

3.1.2 Silver nanowires (AgNWs)

Silver nanowires were synthesized *via* a modified polyol method reported elsewhere.[2] For the optimised reaction conditions 32 ml of ethylene glycol (EG, Sigma-Aldrich 99.8% purity) was added into a 100 ml flask. The solvent was heated at 120 °C for 1 hour in an oil bath. Then, 40 μl of pre-prepared 0.22 M solution of NaCl (Sigma-Aldrich) in EG was added, followed by 20 μl of 0.020 M $Fe(NO_3)_3$ (Sigma-Aldrich) in EG and 4.152 ml of 0.378 M polyvinylpyrrolidone (PVP, Mw = 55000, Sigma-Aldrich) in EG. At the end 4.152 ml of 0.247 M $AgNO_3$ (Sigma-Aldrich) in EG was added at the rate of ca. 0.5 ml/min. The temperature of the oilf bath was kept at 120 °C for another 10 minutes after the addition of $AgNO_3$, and subsequently increased to 130 °C, after which the reaction was allowed to progress for a further 5 hours. An excess of acetone was used to cause the precipitation of the nanowires, after which the supernatant was discarded and the precipitate redispersed in 40 ml of methanol (Fisher Scientific). When acetone is introduced into the solution, the nanowires settle out of the solution fairly rapidly, whereas smaller nanoparticles remain dispersed for a longer period of time. As such, by utilising this acetone wash, the wire to particle ratio is greatly improved after each acetone wash. The concentration of the resulting nanowire disperion was ca. 5 mg/ml.

3.1.2.1 Filtration of AgNWs

The dispersion of AgNWs in methanol was vacuum filtered using a polypropylene filter of 5 μm pore size. The filter was immersed in a solution of fresh methanol. The nanowires were redispersed by short sonication (20-40 seconds) in an ultrasonic bath. This filtration step was repeated 4 times. After the last filtration, AgNWs were redispersed in isopropyl alcohol (IPA, Fisher Scientific). The schematic diagram of the process is shown in Figure 3.1

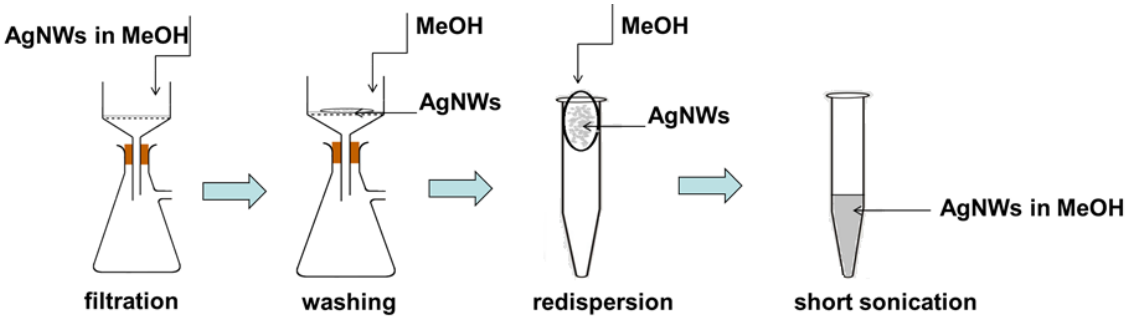


Figure 3.1. Schematic diagram of the vacuum filtration method.

3.2 Sample preparation

3.2.1 Perovskite solar cell fabrication

The perovskite solar cells (PSCs) presented in this thesis were fabricated in accordance with standard procedures reported in literature.[3–5]

3.2.1.1 Substrate preparation

All the photovoltaic devices described herein were fabricated on fluorine-doped tin oxide (FTO)-coated glass substrates, supplied by Hartford Glass (TEC15 of 15 Ω/sq or TEC7 of 7 Ω/sq).

The FTO coating was etched with zinc powder (Alfa Aesar) and 2M HCl (Fisher Scientific). In order to achieve the desired pattern, stripes of scotch tape were placed over the area where the FTO coating was required. The substrates were subsequently washed with a Hellmanex solution (ca. 2 wt% in water), and then sonicated in acetone and isopropanol, for a duration of 10 minutes per solvent. The substrate preparation was completed by oxidising organic residues present on the FTO surface by one of the three methods: the samples were either subjected to 10 minutes of oxygen plasma etching (used for the cells employing TiO_2 compact layer), sintered at 500 °C for 45 minutes (cells with C_{60} compact layer), or treated with a piranha solution (cells with cross-linked fullerenes as a bottom contact). For piranha etching, the substrates were immersed in the piranha solution (sulphuric acid (Fisher Scientific) : hydrogen peroxide (Sigma-Aldrich), 2:1 v/v), and heated at 150 °C for 2 hours. The solution was then allowed to naturally cool to room temperature after which the samples were thoroughly rinsed with deionised water, and sonicated in acetone and IPA.

3.2.1.2 Electron selective contact

As an electron selective material the following materials have been used: TiO_2 (three different types), fullerene-functionalised TiO_2, C_{60}, cross-linkable fullerene derivatives: fulleropyrrolidine derivative containing a triethoxysilane moiety (N-[3-

(Triethoxysilyl)propyl]-2-carbomethoxy-3,4-fulleropyrrolidine (sol-gel C_{60}, chemical structure given in Figure 3.2a) and phenyl-C61-butyric acid benzocyclobutene ester (PCBCB, chemical structure give in Figure 3.2b).

The low temperature TiO_2 compact layer (lt-TiO_2, nanoparticles from section 3.1.1) was prepared by spin-coating (spinning rate: 2000 rpm) the colloidal dispersion of anatase nanoparticles in anhydrous ethanol (formulated with TiAcAc on top of a plasma-cleaned FTO substrate, followed by drying at 150 °C for 30 minutes. The thickness of the compact layer was determined by the concentration of TiO_2 nanoparticles (3.54 – 0.24 wt% of TiO_2).

The amorphous TiO_x compact layer was prepared by spin-coating (spinning rate: 2000 rpm) the precursor solution (titanium isopropoxide, TTIP, Sigma-Aldrich) in anhydrous ethanol (concentration: 0.254 M), with the addition of 2 M HCl solution, on top of plasma-cleaned FTO substrate, followed by annealing at 150 °C for 30 min.

The standard high temperature TiO_2 blocking layer (ht-TiO_2) was prepared from the same TTIP precursor solution (spinning rate: 2000 rpm), where annealing at 150 °C was additionally followed by a sintering step of 500 °C for 45 minutes.

The fullerene-functionalization of the compact layer was achieved by immersing hot TiO_2 substrates (when they were cooling down after sintering, temperature around 120 °C) in the C_{60}-SAM solution (0.1 mg/ml in chlorobenzene, filtered with 0.2 μm PTFE filter) for 24-36 hours, followed by rinsing with chlorobenzene and drying for 10 min at 120 °C. The C_{60}-SAM molecule was received from the group of Alex-Jen (University of Washington, US) and used without further purification. Benzoic acid assembling was done by immersing the warm

substrates in a solution of benzoic acid (0.06 mg/ml in a 1:1 mixture of acetonitrile (Sigma-Aldrich) and tert-butanol (Sigma-Aldrich)) for 4 hours, followed by rinsing in acetonitrile.

For the C_{60} (Solenne) compact layer deposited on top of sintered FTO glass, the optimised spin coating speed of the solution (concentration: 10 mg/ml) in anhydrous 1,2-dichlorobenzene (Sigma-Aldrich) was 1500 rpm, yielding a film thickness of 37 nm (as determined by atomic force microscopy), followed by drying at 60 °C for 2 minutes.

The compact layer made of a sol-gel C_{60} was spin-coated on top of piranha-cleaned FTO substrates from a solution in 1,2-dichlorobenzene (concentration: 2, 4 or 6 mg/ml, spinning rate: 2000 rpm). After spin-coating, the film was held in trifluoacetic acid (Fisher) vapour for 60 seconds in order to trigger the crosslinking reaction. The sample was then transferred into a nitrogen-filled glovebox and annealed at 130 °C for 30 minutes to complete the crosslinking process. Subsequently, the sample was taken out of the glovebox and rinsed with methanol. The sol-gel C_{60} molecule was received from Olivier Dautel (Laboratory of Macromolecular Chemistry, Charles Gerhardt Institute, France) and used without further purification.

For the modification of the FTO work function, an aqueous solution of polyethylenimine, 80% ethoxylated (PEIE, Sigma-Aldrich) (concentration: 0.4 wt%) was spin-coated (spinning rate: 5000 rpm) on top of piranha-cleaned FTO, and then dried at 80 °C for 2 minutes. Subsequently, a sol-gel C_{60} compact layer was processed according to the above description.

The PCBCB was spin-coated on top of piranha-cleaned FTO substrate from a solution in 1,2-dichlorobenzene (concentration: 5 or 10 mg/ml, spinning rate: 2000 or 3000 rpm). After spin-coating, the sample was transferred into a nitrogen-filled glovebox and annealed at 200 °C for 10 minutes to crosslink the fullerene. The sample was then taken out of the glovebox and

rinsed with methanol. The PCBCB molecule was received from Raghunath Dasar (research group of Prof. Seth Marder, Georgia Institute of Technology, US), and used without further purification. The synthesis of the molecule was reported by Deb *et al.*[6]

a) **b)**

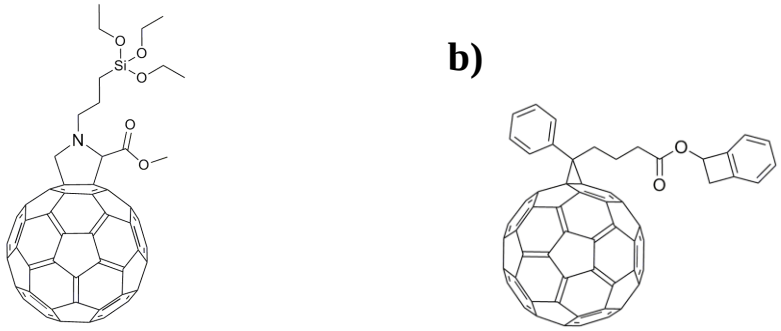


Figure 3.2. Chemical structure of **(a)** the sol-gel C_{60} molecule, and **(b)** PCBCB.

3.2.1.3 Planar perovskite layer

For one-step solution-processed perovskite films, the samples with compact layers (deposition methods described above) were transferred into a nitrogen-filled glovebox. A precursor solution of the concentration of 360-400 mg/ml (CH_3NH_3I (Oxford PV) and $PbCl_2$ (98%, Sigma-Aldrich), 3:1 molar ratio in anhydrous dimethylformamide (DMF, Sigma-Aldrich)) was spin-coated (spinning rate: 2000 rpm) at room temperature, followed by drying at room temperature for 30 min and annealing at 90 °C for 150 min, and 120 °C for 15 minutes, according to the procedure reported elsewhere.[5]

For the two-step perovskite deposition, 110 nm of PbI_2 (99%, Sigma-Aldrich) was thermally evaporated directly on top of the compact layer. The samples were subsequently transferred into a nitrogen-filled glovebox, where a solution of methylammonium iodide (MAI) (concentration: 20 mg/ml) in anhydrous IPA (Sigma-Aldrich) was spin-coated (spinning rate: 5000 rpm) on the samples, followed by annealing at 100 °C for 120 minutes to form

a perovskite film. The two-step deposition was carried out by Svetlana Siprova at the Department of Physics, University of Oxford.

3.2.1.4 Meso-superstructured perovskite layer

The alumina scaffold was deposited by spin-coating (rate: 2500 rpm) from a solution of Al_2O_3 nanoparticles (Sigma-Aldrich, 50 nm in diameter, concentration: ca. 6.7 wt% in IPA), and the resulting film was annealed at 120-150 °C for 15 minutes, according to a previously reported method.[4] The samples were then transferred into a nitrogen-filled glovebox for the deposition of the perovskite layer. The perovskite precursor solution of concentration of 350-400 mg/ml (CH_3NH_3I and $PbCl_2$, 3:1 molar ratio in dimethylformamide (DMF)) was spin-coated (spinning rate: 2000 rpm) at room temperature, followed by annealing at 100 °C for 90 minutes, and 120 °C for 10 minutes.

3.2.1.5 Hole transport layer

Following the annealing of the perovskite, either iodopentafluorobenzene (IPFB, Sigma Aldrich) or thiophene (Sigma Aldrich) was spin-coated (spinning rate: 2000rpm) on top of the perovskite in order to passivate any surface defects.[7,8]

For all the devices presented in this thesis, 2,2',7,7'-tetrakis-(N,N-di-pmethoxyphenylamine)9,9-spirobifluorene (spiro-OMeTAD) was used as a hole transporting material (HTM). The spiro-OMeTAD layer was deposited by spin-coating (spinning rate: 2000 rpm) a solution of spiro-OMeTAD (Lumtec or Borun Chemicals) in chlorobenzene onto the surface of the perovskite layer after passivation. The solution consisted of 8 wt % spiro-OMeTAD in chlorobenzene, doped with *tert*-butyl pyridine

(*t*BP, Sigma Aldrich) and lithium bis(trifluoromethanesulfonyl)imide (Li-TFSI, Sigma-Aldrich) at a concentration of 80 mol % and 30 mol % respectively.

3.2.1.6 Top metal electrode

Following the deposition of the HTM, the samples were taken out of the glovebox and left in dry air overnight to for the oxidation of the spiro-OMeTAD . As a top electrode, 50 nm of gold or 120 nm of silver was deposited on top of the device by thermal evaporation at the rate of ~2 Å/s, base pressure of ~10^{-6} bar, through a shadow mask, using a Kurt Lesker Nano36 thermal evaporator.

3.2.1.7 Encapsulation layer

The devices which were used for the stability measurements presented in Chapter 6 (meso-superstructured architecture) were encapsulated with a hot-melt polymer foil, which was processed in a nitrogen filled glovebox. Encapsulation of the devices was done at Oxford Photovoltaics Ltd.

3.2.2 Organic field-effect transistors (OFETs)

Commercial, highly doped Si/SiO_2 substrates were cleaned in an ultrasonic bath, sequentially in acetone, ethanol and isopropanol (10 minutes in each solvent), and subjected to 10 minutes of UV-ozone cleaning. A 15 nm thick layer of poly(1-vinyl-1,2,4-triazole) (PVT) was spin-coated onto the pre-cleaned substrates. The samples were then transferred into a nitrogen-filled glovebox. The PCBM or sol-gel C_{60} films were processed directly on top of the PVT coated substrates by spin-coating the desired solution (40 mg/ml in chlorobenzene) at

1000 rpm. The sol-gel C_{60} layer was cross-linked by exposure to a trifluoroacetic acid (TFA) vapour for 1 min, followed by annealing at 130°C for 30 min. The top electrode contact, a 70 nm-thick layer of aluminium, was deposited by thermal evaporation. The schematic diagram of the sample is presented on Figure 3.3. All OFET devices were fabricated by Therese Gorisse at the Bordeaux Institute of Technology (IMS), France.

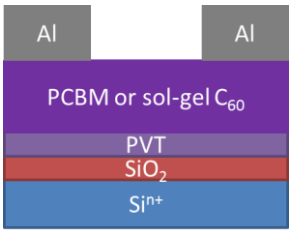


Figure 3.3. Schematic diagram of the OFET device. Transistor samples were fabricated by Therese Gorisse at the Bordeaux Institute of Technology (IMS), France.

3.2.3 Samples for different characterisation

3.2.3.1 Conductivity measurements

For the conductivity measurements of different TiO_2 layers, the films were deposited on glass substrates, processed in the same manner as for the photovoltaic devices. The thickness of the channel (TiO_2 layer) was determined from an SEM cross-sectional image. The gold electrodes (50 nm-thick films) were thermally evaporated (base pressure: ~10^{-6} bar, Kurt Lesker Nano36 thermal evaporator) onto the spin-coated films through a shadow mask designed for a four-point probe conductivity set-up.

3.2.3.2 Hard X-ray photoelectron spectroscopy measurements

For the hard X-ray photoelectron spectroscopy (HAXPES) measurements, compact layers (TiO_2 or TiO_2 modified with C_{60}-SAM) were prepared in air, in the same manner as for

the PV devices. The samples were then transferred into a nitrogen-filled glovebox and perovskite films were deposited directly onto the compact layer from a diluted precursor solution, 30 mg/ml (CH_3NH_3I and $PbCl_2$, 3:1 molar ratio in DMF), followed by drying at room temperature for 30 minutes and annealing at 90 °C for 60 minutes. The perovskite film thickness was between 10-20 nm. Following the annealing, samples were mounted onto the sample holder for HAXPES measurement inside the glovebox and were kept in inert atmosphere throughout the duration of the experiment.

3.2.3.3 Photoluminescence measurements

For the photoluminescence measurements (time-resolved PL and PL quantum efficiency) of perovskite films with different quenchers, all the samples were deposited on glass substrates, in the same manner as for the PV devices. The perovskite layers were then sealed with a ~100 nm-thick layer of the inert polymer, poly(methylmethacrylate) (PMMA, spin-coated from a solution of 10 mg/ml in chlorobenzene at 1000 rpm) in order to protect the films from degradation in humid air.

For the photothermal deflection spectroscopy (PDS) and time-resolved microwave conductivity (TRMC) measurements all the films were deposited on IR-grade quartz substrates, and processing conditions were the same as for the films used in PV devices.

3.2.4 Silver nanowire-based electrodes

A filtered silver nanowire solution was spin-coated dynamically (the solution was being dispensed when the substrate was already spinning) on pre-cut and cleaned glass samples (ca. 0.8x0.8 cm^2). 100 µl per sample was deposited dropwise (2-3 seconds between drops), spinning rate: 2000-3000 rpm. The matrix materials were spin-coated in a similar manner

(volume: 10-60 μl, time between doses: 2-5 seconds). For the ZnO layer, a 2 M solution of $Zn(CH_3COO)_2.H_2O$ in methanol was used. ZnO was formed after drying the sample at 100 °C for 10 minutes. For the TiO_2 film, a 0.112 M solution of nanoparticles was dispersed in anhydrous ethanol with a TiAcAc addition (8.7 mol% in respect to TiO_2) was used. For the PEDOT:PSS layer, an aqueous dispersion (Clevios PH1000) diluted in IPA or methanol was used (concentration: 0.4 wt%). The aluminium-doped zinc oxide (AZO) layer was deposited in a home-made Atomic Layer Deposition (ALD) system. High purity diethylzinc, water and trimethylaluminium (dopant) were used as AZO precursors. Nitrogen was used as a carrier and purging gas, with the flow rate set to 20 sccm and controlled by a mass flow controller. The deposition was carried out at 150 ºC, base pressure of 0.3 mbar and growth rate of 1.9 Å per cycle.

For the deposition of AgNWs through stamping method, nitrocellulose membranes (pore size: 0.2 μm) were used as stamps.[9] The dispersion of AgNWs in IPA (concentration: 0.125 mg/ml, volume: 5-10 ml) was vacuum-filtered through the membrane. The filter coated with nanowire mesh was subsequently subjected to nitrogen plasma etching in order to remove the polyvinylpyrrolidone shell from the silver's surface. The AgNW mesh was transferred from the membrane onto a glass substrate coated with a layer of polyvinyl alcohol (PVA, spin-coated on glass from 5 wt% aqueous solution at 3000 rpm) by manual pressing.

3.3 Electrical characterisation

3.3.1 Solar cell characterisation

The current density-voltage characteristics of solar cells were measured under simulated AM1.5 100 mW·cm^{-2} sunlight (ABET Technologies Sun 2000) with a Keithley 2400 sourcemeter unit. The lamp was calibrated with an NREL-calibrated KG5 filtered silicon reference with a solar mismatch factor of 1.01.

The mismatch factor corrects the error originating from the difference in spectral responsivity of the test cell and the reference device, and the mismatch in spectral irradiance of the used light source and the reference spectrum (AM1.5). It can be expressed by Equation 3.1:[10]

$$M = \frac{\int_{\lambda_1}^{\lambda_2} E_{Ref}(\lambda) S_R(\lambda) d\lambda}{\int_{\lambda_1}^{\lambda_2} E_{Ref}(\lambda) S_T(\lambda) d\lambda} \frac{\int_{\lambda_1}^{\lambda_2} E_S(\lambda) S_T(\lambda) d\lambda}{\int_{\lambda_1}^{\lambda_2} E_S(\lambda) S_R(\lambda) d\lambda} \quad (3.1)$$

where $E_{Ref}(\lambda)$ is the reference spectral irradiance, $E_S(\lambda)$ is the light source spectral irradiance, $S_R(\lambda)$ is the spectral responsivity of the reference cell, $S_T(\lambda)$ is the spectral responsivity of the test cell, λ_1 and λ_2 define the spectral range where the reference and test cells respond.

Spectral responsivities of the devices are derived from external quantum efficiency measurement (EQE), which defines how many carriers are generated per incident photon of a given wavelength. To minimise the mismatch factor, the reference cell should have the spectral response as close to the test device as possible.

Thee mismatch factor for the perovskite device based on $CH_3NH_3PbI_{3-x}Cl_x$ which was used in this study was derived by Henry Snaith at the Department of Physics, University of Oxford. The active area of the device was defined by a metal mask with square aperture of the area of 0.0625 (or 0.0919) cm^2. The pre-masked active area of the solar cells was approximately 0.12

cm^2 nominally defined by the overlap area of the evaporated metal and FTO electrodes. Solar cells were masked for all the current-voltage measurements. The masking is essential to eliminate the edge effects, which causes overestimations of measured current densities.[11] The JV curves were typically scanned from 0 V (short-circuit) to 1.4 V (forward bias) and back to 0 V with a scan rate of 150 or 450 mV/s.

Due to the presence of hysteresis effects in perovskite solar cells and dependence of a JV curve on scanning conditions (scanning rate and scanning direction), the stabilised power output (SPO) measurement was developed by the author. In this measurement a current output was measured at the constant applied bias (voltage of the maximum power point from the reversely scanned JV curve) over a period of time until the stabilised current reading was reached (typically 30-50 seconds). The existing JV setup was used for these measurements.

The aging tests in Chapter 6 were done at the maximum power point (MPP tracker), under simulated AM1.5 76 $mW{\cdot}cm^2$ sunlight generated from an unfiltered Xenon lamp in a sun test CPS Plus aging box, at a temperature of 60 °C, with no active humidity control. Furthermore, JV curves were recorded every 65 minutes (voltage scanned from 1.2 V to 0 V, scan rate: 0.15 V/s). The measurements were performed at Oxford Photovoltaics Ltd.

The aging tests in Chapter 7 were carried out in a customised aging setup. Selected solar cells were put inside sealable aluminium boxes with glass windows, which were connected to a flow of nitrogen, used to maintain inert atmosphere during the aging process. All the cells in the box were connected to the external bias of 0.7 V (close to maximum power point) and were illuminated with the Atlas CPSPlus Xenon lamp (100 mW/cm^2 light intensity) during the entire stressing period. The aging was interrupted to test the photovoltaic performance (JV curves measured in the setup described above) every 20-40 hours. The customised aging setup (gas

flow, aluminium boxes with machined windows and electrical connections) was designed and constructed by Ivan Ramirez at the Department of Physics, University of Oxford.

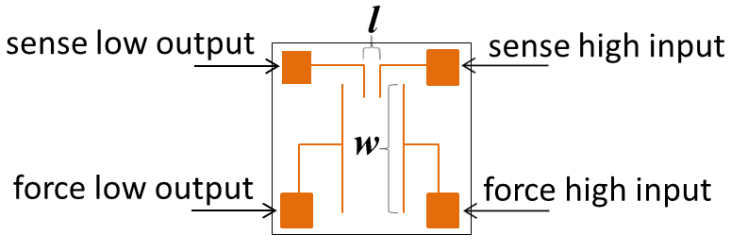
3.3.2 Conductivity measurement

Conductivity was measured using the existing four-point probe set-up, in order to eliminate the influence of the contact resistance between the material and evaporated electrode. The electrode pattern (see Figure 3.4a) is comprised of the two large outer electrodes and two short inner ones. The potential was applied from the Keithley 2400 sourcemeter between the outer electrodes (force channel) driving the current through the channel, and the voltage drop across the inner channel formed by the smaller electrodes (connected to the sense channel in the sourcemeter) was measured. The drop in potential in the channel as a function of current for different applied biases should give linear characteristic. The slope of the linear fit to the data points corresponds to the sample's resistance in the channel. Knowing the dimensions of the channel, the conductivity of the material (σ) can be derived, according to Equation 3.2:

$$\sigma = \frac{l}{Rwd} \tag{3.2}$$

where l is the length of the sense channel (distance between sense probes, 0.5 mm), R is sample's resistance (slope from the linear fit), w is the width of the channel where current is flowing (dimension of the big probe, 1 cm), and d is material's film thickness.

a)



b)

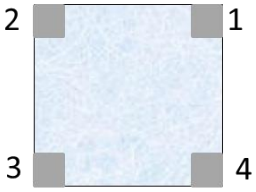


Figure 3.4. (a) Schematic diagram of the electrode's pattern used for four-point probe conductivity set-up; **(b)** sample for conductivity measurements according to the van der Pauw method. Silver electrodes are painted in the corners and numbered anti-clockwise.

Sheet resistance (R_S) of the silver nanowire electrodes was measured at the same four-point probe setup, and calculated from Equation 3.3:

$$R_S = \frac{Rw}{l} \tag{3.3}$$

The van der Pauw method was also used to derive R_S.[12] The measurement procedure was set up by the author. Silver paint (Electrodag) was placed in the four corners of the square sample (numbered counter-clockwise, as shown in Figure 3.4b) to make the contact with the probes connected to the Keithley sourcemeter. In this method, two current-voltage readings need to be taken. In the first one, voltage is applied between the electrodes on one side of the sample, forcing the flow of current (I_{12}). At the same time, the drop of voltage is sensed on the other side of the sample (V_{34}), giving the resistance value of $R_{12\text{-}34}$ (vertical reading). In the second reading, the neighbouring edge becomes the force channel, giving the current measurement (I_{23}), voltage drop (V_{41}), and resistance value ($R_{23\text{-}41}$) in horizontal arrangement. If the sample is

perfectly symmetrical and isotropic, the horizontal reading should be identical to the vertical value. The sheet resistance is given by Equation 3.4:,

$$R_S = \frac{\pi R}{ln2} \tag{3.4}$$

where $R = R_{12\text{-}34} = R_{23\text{-}41}$.

If vertical and horizontal resistances are not equal, the van der Pauw formula, given by Equation 3.5, has to be solved numerically for R_S.

$$e^{\frac{-\pi R_{12-34}}{R_S}} + e^{\frac{-\pi R_{23-41}}{R_S}} = 1 \tag{3.5}$$

3.3.3 Impedance spectroscopy

Impedance measurements of the diode samples (FTO/TiO_2 or modified-TiO_2/spiro-OMeTAD/gold) were carried out using a FRA-equipped PGSTAT-302N from Autolab. A 20 mV AC sinusoidal signal with the frequency ranging from 1 MHz to 0.1 Hz was applied for each voltage bias (forward bias changing from 0 V to 1.2 V). The real part of the capacitance for each data point was obtained by fitting the spectra with the equivalent circuit model comprised of a resistor (R_1, assigned to contact resistance) connected in series with an RC element, where second resistor (R_2, assigned to sample resistance) is connected in parallel with a capacitor (C, assigned to sample capacitance). At the intermediate frequency region, capacitance values significantly increase with increasing voltage bias under dark conditions, which is a signature of accumulation of charges in the material (chemical capacitance).[13] The capacitance-voltage curves were plotted for the data obtained at the AC frequency of 1 kHz.

The equivalent circuit is a theoretical model which simulates all the electrical characteristics of the measured circuit. Its formalism is based on Kirchoff's Law, Ohm's Law and the Principle

of Superposition.[14] It is used to simplify calculations and aid the analysis of the electrical properties of the measured system. All the elements in the model should have a physical meaning and choosing too many elements can increase the uncertainty of finding a final value for these elements.

3.3.4 Transient photocurrent and photovoltage decay

The technique of transient photovoltage and photocurrent decays was developed by O'Regan *et al.* to probe the dynamics of charge transport and recombination in solid-state dye-sensitised solar cells.[15,16] Perovskite devices can be also examined with this method, but the timescales on which the photophysical processes occur in PSCs, impose some limitations.[17]

In these measurements, a solar cell is kept at a constant white background illumination, which causes filling up of sub-bandgap trap states and sets a specific charge density level in the device, which in turn influences the dynamics of electronic processes. An array of diodes (Lumiled Model LXHL-NWE8 whitestar) was used as a background light, with the intensity varying from 1 to 100 mW/cm^2. The device was irradiated with a short pulse of light and the induced changes were recorded with an oscilloscope. In this study, the pulse was generated from the red light diodes (LXHLND98 redstar, 200 ms square pulse width, 100 ns rise and fall time). The perturbation pulse needs to be of a small enough intensity (less than 10% of the background's intensity), such that the steady-state dynamics is not significantly affected. Furthermore, the diode pulse profile and its relatively long fall time imposes limitations on the timescale of dynamics which can be probed by the setup (typically processes of lifetimes not shorter than microseconds).

The measurements were performed in two different modes, galvanostatic and potentiostatic. When a fixed current is set in the device by the sourcemeter (galvanostatic condition), charges

generated by the perturbation pulse cannot be extracted out of the device and they recombine within the cell. The response measured by the oscilloscope gives information about the recombination lifetime (τ_{rec}), and voltage perturbation can be extracted (ΔV). An example of this is shown in Figure 3.5.

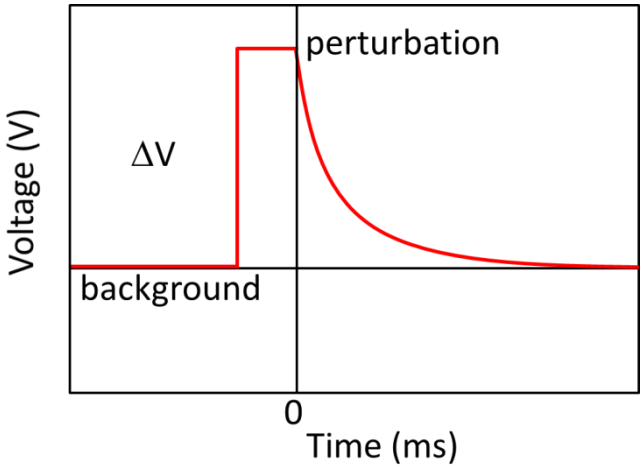


Figure 3.5. Schematic of a typical photovoltage decay measurement, where a sample is illuminated with a background light and a short pulse perturbates the signal from the steady-state level.

In potentiostatic mode, the cell is kept at short-circuit condition. The pulse-generated charge (ΔQ) can be directly extracted by integrating the photocurrent decay curve. The lifetime derived from this decay (τ_{mes}) contains information about both recombination and charge transport. The transport lifetime (τ_{trans}) can be calculated from Equation 3.6:

$$\tau_{trans} = \frac{1}{\frac{1}{\tau_{mes}} - \frac{1}{\tau_{rec}}} \tag{3.6}$$

where τ_{rec} is recombination lifetime measured in galvanostatic mode (derived from the voltage decay) at short-circuit condition.

Another important measurement is photovoltage decay. This is measured in galvanostatic mode at open-circuit (current is fixed at 0). It gives information about the dynamics of recombination

at its peak regime (open-circuit condition), which is very different to short-circuit recombination.

Furthermore, by measuring voltage perturbation (ΔV) at open-circuit for a range of different background intensities and perturbation charge (ΔQ) at short-circuit for the same intensity range, the differential capacitance (C) can be calculated, following the Equation 3.7:

$$C\ (V) = \frac{\Delta Q}{\Delta V} \tag{3.7}$$

The capacitance as a function of V_{OC}, which is proportional to the background illumination intensity, represents the distribution of density of states (DOS) in the device.[16]

Photocurrent and photovoltage decay measurements presented in this thesis were performed by Tomas Leijtens at the Department of Physics, University of Oxford.

3.3.5 Electron mobility measurement

The electron mobilities of the fullerene derivatives were determined by fabricating organic field-effect transistors (OFETs). The n-type semiconducting characteristics of the pristine films were studied in a bottom-gate/top-contact device configuration: Si^{n+}/SiO_2/PVT/material/Al (see Figure 3.3). The measurements were done in a linear regime, at source-drain voltage (V_{ds}) of 5 V. The electron mobility was extracted at the gate potential (V_{gs}) of 15 V. These measurements were done by Therese Gorisse at the Bordeaux Institute of Technology (IMS), France.

3.4 Spectroscopic characterisation

3.4.1 Optical absorption

UV-Vis absorption spectra were obtained using a Cary 300 Bio (Agilent Technologies) UV-Vis spectrophotometer, equipped with an integrating sphere accessory (Labsphere). The spectra were recorded either in absorbance (A) or transmittance (T) mode. The relation is given by Equation 3.8:

$$A\ (\lambda) = log\left(\frac{I_0(\lambda)}{I(\lambda)}\right) = log\left(\frac{1}{T(\lambda)}\right) \tag{3.8}$$

where I_0 is the intensity of the incident light, and I is the intensity of the light transmitted through the sample.

3.4.2 X-ray diffraction

X-ray diffractograms were obtained from powder samples or thin films deposited on glass using Panalytical X'Pert Pro X-ray diffractometer at the Department of Physics, University of Oxford.

3.4.3 Photoluminescence measurements

Time-resolved photoluminescence (TRPL) measurements were acquired using a time-correlated single photon counting (TCSPC) setup (FluoTime 300, PicoQuant GmbH). The schematic diagram of the TCSPC setup is shown in Figure 3.6. The method is based on the repetitive registration of single photons emitted by the sample, which are precisely timed. When a laser pulse excites the sample, the signal is synced by the electronics recording the start time. The time-to-amplitude converter (TCA) starts charging a capacitor. When photons

emitted by the sample upon the excitation reach a detector, the stop signal is activated and the capacitor is discharged. The amplitude of the charged voltage is proportional to the time period between the start and stop signals. Subsequently, this amplitude is recorded into a multi-channel analyser, where every channel corresponds to the specific voltage value, so it contains the time information. After many repetitions, a photoluminescence histogram as a function of time is created.[18]

The samples were photoexcited using a 507 nm laser head (LDH-P-C-510, PicoQuant GmbH) pulsed at 1 MHz, with a pulse duration of 117 ps and fluence of 30 nJ/cm^2/pulse. The samples were exposed to the pulsed light source for ~10 minutes prior to measurement to ensure stable sample emission. The PL was collected using a high resolution monochromator and hybrid photomultiplier detector assembly (PMA Hybrid 40, PicoQuant GmbH).

The quasi steady-state PL measurements presented in Chapter 6 were acquired in the same setup as that used for the time-resolved PL measurements. The detection wavelength of 775 nm was monitored while the sample was excited with 510 nm, 30 nJ/cm^2/pulse, 117 ps pulses at 10 MHz repetition rate. While the steady-state PL measurements were performed by Tomas Leijtens, the time-resolved PL measurements were done by the author, both at the Department of Physics, University of Oxford.

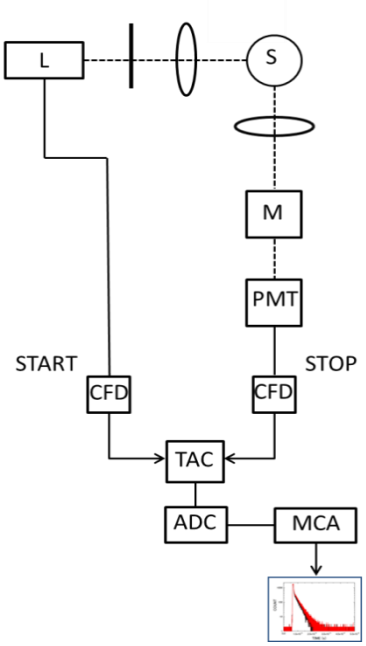


Figure 3.6. Schematic diagram of the TCSPC setup, where L – laser, S – sample, M-monochromator, PMT – photomultiplier, CFD – constant fraction discriminator, TAC – time to amplitude converter, ADC – analog to digital converter, and MCA – multi-channel analyser.

3.4.4 Photoluminescence quantum efficiency

The photoluminescence quantum efficiency (PLQE) of a material is described by the Equation 3.9:

$$PLQE = \frac{N_{em}}{N_{abs}} \tag{3.9}$$

Where N_{em} is the number of emitted photons, and N_{abs} is the number of absorbed photons.

PLQE values were determined using a 532 nm CW laser excitation source (Suwtech LDC-800) to illuminate a sample in an integrating sphere (Oriel Instruments 70682NS), and the laser scatter and PL collected using a fiber-coupled detector (Ocean Optics USB 2000+). The spectral response of the fiber-coupled detector setup was calibrated using a spectral irradiance standard (Oriel Instruments 63358). An excitation intensity of ~200 mW/cm^2 was used for the

measurements. PLQE calculations were carried out in accordance to the reported method.[19] The measurements were taken when the sample was in-plane (laser's intensity attenuated by the material's absorption), and out-of-plane (laser does not hit the sample). PLQE is determined by integrating the emission peak and the absorption peak at the laser's wavelength. PLQE measurements were performed by Sam Stranks at the Department of Physics, University of Oxford.

3.4.5 Electroluminescence

Electroluminescence measurements were carried out directly on the solar cells. Current-voltage characteristics were measured using a Keithley 2600 Source Measure Unit. A constant forward bias of 1.1 V was applied to the solar cells and the current monitored simultaneously. The electroluminescence was detected using a photomultiplier tube (PMT) detector (Fluorolog spectrofluorometer, Horiba Jobin-Yvon). All spectra were corrected for instrumental response using a calibration lamp of known emissivity. EL measurements were performed by Sam Stranks at the Department of Physics, University of Oxford.

3.4.6 Time-resolved microwave conductivity

All the samples were excited at 500 nm through the quartz substrate with 5 ns laser pulses from an optical parametric oscillator (Continuum Panther) pumped by the 355 nm harmonic of a Q-switched Nd:YAG laser (Continuum Powerlite) at a frequency of 10 Hz. The sample was placed inside a resonance cavity at the end of an X-band (ca. 9 GHz) microwave waveguide and the transient change in photoconductance, $\Delta G\,(t)$, was measured via changes in the microwave power in the cavity, $\Delta P(t)$, due to absorption of microwaves by the photogenerated holes and electrons, and is given by Equation 3.10:

$$\Delta G(t) = -\frac{1}{K\left(\frac{\Delta P(t)}{P}\right)} \quad (3.10)$$

where K is a calibration factor determined experimentally from the resonance characteristics of the microwave cavity and the dielectric properties of the sample. [20]

The peak photoconductance, ΔG_{peak}, can be related to the product of the yield of free-carrier generation, φ, and the sum of the 9 GHz-frequency electron and hole mobilities, μ_e and μ_h, respectively (called $\Sigma\mu$), by Equation 3.11:

$$\Delta G_{peak} = \beta q_e I_0 F_A \varphi(\mu_e + \mu_h) = \beta q_e I_0 F_A \varphi \sum \mu \quad (3.11)$$

where β = 2.2 and is the ratio of the interior dimensions of the waveguide, q_e is the electronic charge, I_0 is the incident photon flux of the excitation laser pulse, and F_A is the fraction of absorbed laser pump photons by the sample.

TRMC measurements were performed by Nikos Kopidakis at the National Renewable Energy Laboratory, Colorado, US.

3.4.7 Photothermal deflection spectroscopy

Photothermal deflection spectroscopy (PDS) is an ultra-sensitive, surface averaged technique, which allows probing sub-bandgap optical absorption. The sample was held in a hermetically sealed fused silica cuvette, filled with an inert liquid (Fluorinert FC-72), which refractive index is very sensitive to temperature changes. The material was excited with a light produced by a Light Support MKII 100 W Xenon arc source, passed through a CVI DK240 monochromator. Light absorption in sub-gap states results in a temperature gradient due to a heat released by non-radiative relaxation, which in turn produces a refractive index gradient. The change of refractive index deflects the transverse probe beam (Qioptiq 670 nm fiber-

coupled diode laser was used), which can be correlated with the amount of light absorbed in the sample. The spectrum derived from PDS measurement characterises band-tail states, induced by material's disorder and various defects. The slope of the absorption tail defines the Urbach energy, and provides a measure of the degree of disorder in a given material. Comprehensive details about the principles of this method are given by Kronemeijer *et al*.[21] PDS measurements were performed by Aditya Sadhanala at the Department of Physics, University of Cambridge.

3.4.8 Hard X-ray photoelectron spectroscopy

Hard X-ray photoelectron spectroscopy (HAXPES) measurements were performed at the I09 end station at the Diamond Light Source Ltd. (Didcot, UK) using a EW4000 high energy electron analyser equipped with a wide angle lens (VGScienta, Uppsala, Sweden) . The photon energy was tuned to 8 keV using a Si(004) post monochromator giving a total experimental resolution of 320 meV as calibrated by measuring the Fermi cut-off on a scraped Au foil. For the measurements the incident angle was tuned closed to 1° to maximise electron counts. Since beam damage is known to be an issue, special attention was paid to accumulate undisturbed data. The beam intensity was reduced to a level which allowed at least 20 min of irradiation for a given spot before the first changes in spectra became apparent. The sample was moved under the beam and spectra were measured for ~10 min per spot allowing the acquisition of unperturbed data with high statistics. The intensity ratio of intense core levels of FTO, TiO_2 and the perovskite were monitored to verify that the film thickness was constant. HAXPES measurements were performed by Christoph Schlueter at the Diamond Light Source Ltd.

3.4.9 Fourier transform infrared spectroscopy

Fourier transform infrared (FTIR) spectra were recorded on a Perkin Elmer 100 spectrometer in a transmission mode. The measurements were performed by Olivier Dautel at the AM2N Laboratory, Charles Gerhardt Institute, France.

3.5 Microscopy

3.5.1 Scanning electron microscopy

Scanning electron microscopy (SEM) images were obtained using a Hitachi S-4300 microscope. To avoid charging effects, all samples were coated with a 3 nm thick layer of Pt (deposited by sputter coating) before being imaged.

3.5.2 Atomic force microscopy

Atomic force microscopy (AFM) images were obtained using a ThermoMicroscope M5 in non-contact mode, scanning over a range of 5 μm by 5 μm at a resolution of 256 x 256 data points. The surface roughness was measured as the root mean-squared roughness over the scanning area. The film thickness of the C_{60} layer was determined by scanning over the edge from a scratch made with a razor blade. AFM images presented in Chapter 6 were taken by Maximilian Hörantner at the Department of Physics, University of Oxford.

3.6 References

(1) Wang, J.; Polleux, J.; Lim, J.; Dunn, B. Pseudocapacitive Contributions to Electrochemical Energy Storage in TiO_2 (Anatase) Nanoparticles. *J. Phys. Chem. C* **2007**, *2*, 14925–14931.

(2) Bergin, S. M.; Chen, Y.-H.; Rathmell, A. R.; Charbonneau, P.; Li, Z.-Y.; Wiley, B. J. The Effect of Nanowire Length and Diameter on the Properties of Transparent, Conducting Nanowire Films. *Nanoscale* **2012**, *4*, 1996–2004.

(3) Lee, M. M.; Teuscher, J.; Miyasaka, T.; Murakami, T. N.; Snaith, H. J. Efficient Hybrid Solar Cells Based on Meso-Superstructured Organometal Halide Perovskites. *Science* **2012**, *338*, 643–647.

(4) Ball, J. M.; Lee, M. M.; Hey, A.; Snaith, H. J. Low-Temperature Processed Meso-Superstructured Tp Ton-Film Perovskite Solar Cells. *Energy Environ. Sci.* **2013**, *6*, 1739.

(5) Eperon, G. E.; Burlakov, V. M.; Docampo, P.; Goriely, A.; Snaith, H. J. Morphological Control for High Performance, Solution-Processed Planar Heterojunction Perovskite Solar Cells. *Adv. Funct. Mater.* **2013**, *24*, 151.

(6) Deb, N.; Dasari, R. R.; Moudgil, K.; Hernandez, J. L.; Marder, S. R.; Sun, Y.; Karim, A.; Bucknall, D. G. Thermo-Cross-Linkable Fullerene for Long-Term Stability of Photovoltaic Devices. *J. Mater. Chem. A* **2015**, *3*, 21856–21863.

(7) Abate, A.; Saliba, M.; Hollman, D. J.; Stranks, S. D.; Wojciechowski, K.; Avolio, R.; Grancini, G.; Petrozza, A.; Snaith, H. J. Supramolecular Halogen Bond Passivation of Supramolecular Halogen Bond Passivation of Organic-Inorganic Halide Perovskite Solar Cells. *Nano Lett.* **2014**, *14*, 3247–3254.

(8) Noel, N. K.; Abate, A.; Stranks, S. D.; Parrott, E. S.; Burlakov, V. M.; Goriely, A.; Snaith, H. J. Enhanced Photoluminescence and Solar Cell Performance via Lewis Base Passivation of Organic-Inorganic Lead Halide Perovskites. *ACS Nano* **2014**, *8*, 9815–9821.

(9) Guo, H.; Lin, N.; Chen, Y.; Wang, Z.; Xie, Q.; Zheng, T.; Gao, N.; Li, S.; Kang, J.; Cai, D.; et al. Copper Nanowires as Fully Transparent Conductive Electrodes. *Sci. Rep.* **2013**, *3*, 1–8.

(10) Shrotriya, V.; Li, G.; Yao, Y.; Moriarty, T.; Emery, K.; Yang, Y. Accurate Measurement and Characterization of Organic Solar Cells. *Adv. Funct. Mater.* **2006**, *16*, 2016.

(11) Snaith, H. J. The Perils of Solar Cell Efficiency Measurements. *Nat. Photonics* **2012**, *6*, 337–340.

(12) Pauw, L. J. van der. A Method of Measuring the Resistivity and Hall Coefficient on Lamellae of Arbitrary Sghape. *Philips Tech. Rev.* **1958**, *20*, 220–224.

(13) Kim, H.-S.; Mora-Sero, I.; Gonzalez-Pedro, V.; Fabregat-Santiago, F.; Juarez-Perez, E. J.; Park, N.-G.; Bisquert, J. Mechanism of Carrier Accumulation in Perovskite Thin-Absorber Solar Cells. *Nat. Commun.* **2013**, *4*, 2242.

(14) Johnson, D. H. Origins of the Equivalent Circuit Concept: The Voltage-Source Equivalent. *Proc. IEEE* **2003**, *91*, 636–640.

(15) O'Regan, B. C.; Lenzmann, F. Charge Transport and Recombination in a Nanoscale Interpenetrating Network of N-Type and P-Type Semiconductors : Transient Photocurrent and Photovoltage Studies of TiO_2/Dye/CuSCN Photovoltaic Cells. *J. Phys. Chem. B* **2004**, *108*, 4342–4350.

(16) Barnes, P. R. F.; Miettunen, K.; Li, X.; Anderson, A. Y.; Bessho, T.; Gratzel, M.; O'Regan, B. C. Interpretation of Optoelectronic Transient and Charge Extraction Measurements in Dye-Sensitized Solar Cells. *Adv. Mater.* **2013**, *25*, 1881–1922.

(17) O'Regan, B. C.; Barnes, P. R. F.; Li, X.; Law, C.; Palomares, E.; Marin-Beloqui, J. M. Opto-Electronic Studies of Methylammonium Lead Iodide Perovskite Solar Cells with Mesoporous TiO_2; Separation of Electronic and Chemical Charge Storage, Understanding Two Recombination Lifetimes, and the Evolution of Band Offsets during JV Hysteresis. *J. Am. Chem. Soc.* **2015**, *137*, 5087.

(18) O'Connor, D. V; Phillips, D. *Time-Correlated Single Photon Counting*; Academic

Press, 1984.

(19) Mello, J. C. de; Wittmann, H. F.; Friend, R. H. An Improved Experimental Determination of External Photoluminescence Quantum Efficiency. *Adv. Mater.* **1997**, *9*, 230–232.

(20) Savenije, T. J.; Ferguson, A. J.; Kopidakis, N.; Rumbles, G. Revealing the Dynamics of Charge Carriers in Polymer : Fullerene Blends Using Photoinduced Time-Resolved Microwave Conductivity. *J. Phys. Chem. C* **2013**, *117*, 24085–24103.

(21) Kronemeijer, A. J.; Pecunia, V.; Venkateshvaran, D.; Nikolka, M.; Sadhanala, A.; Moriarty, J.; Szumilo, M.; Sirringhaus, H. Two-Dimensional Carrier Distribution in Top-Gate Polymer Field-Effect Transistors: Correlation between Width of Density of Localized States and Urbach Energy. *Adv. Mater.* **2014**, *26*, 728–733.

Chapter 4

Sub 150 °C Processed Meso-super-structured Perovskite Solar Cells with Enhanced Efficiency

The work presented in this chapter has been published in:

(1) Wojciechowski, K.; Saliba, M.; Leijtens, T.; Abate, A.; Snaith, H. J. Sub-150 °C processed meso-superstructured perovskite solar cells with enhanced efficiency, *Energy Environ. Sci.* **2014**, 7, 1142

4.1 Context

Recent rapid development of organic-inorganic perovskite-based solar cells opens an attractive route for the realization of a cheap alternative to today's commercially available solar technologies. The solution-based and low temperature (<150 °C) processing is commercially very attractive, as it offers low cost and high versatility of manufacturing methods. The low temperature aspect enables a fabrication of monolithic multijunction architectures as well as a broad range of substrates to be used for the solar cells, with potential applications ranging from space to light weight portable power, in addition to high throughput manufacture. Perovskite semiconductors are a perfect candidate to fulfil these needs thanks to their low cost, solution-processability and excellent optoelectronic properties, as discussed in Chapter 2.[1–4] However, most efficient perovskite solar cells, typically employ 500 °C sintered TiO_2 compact layers as charge selective contact.

In this chapter a development of a low temperature processing route for compact TiO_2 films is presented. The resulting layers surpass the properties and subsequent performance in the perovskite solar cells, in comparison with the high temperature processed material. This finally removes all the sintering steps in the highly efficient perovskite solar cells.

4.2 Introduction

Lightweight and mechanically flexible photovoltaic devices are of an increasing interest and demand, mainly due to their ease of integration and versatile functionality. Potential applications range from portable electronic devices, electronic textiles,

synthetic skin, robotics, aerospace technology to large scale industrial roofing.[5–9] Commercially attractive reel-to-reel processing is contingent on low temperature technology in order to fabricate devices on the cheapest deformable flexible substrates, such as polyethylene terephthalate (PET) and polyethylene naphthalate (PFN). Additionally, low temperature fabrication allows for the possibility of new multi-junction device architectures, as has been a successful route to higher efficiencies for organic photovoltaics,[10] and the highest efficiency crystalline photovoltaic technologies.[11] A recently emerged class of solution-processed hybrid solar cells are based on organic-inorganic halide perovskite absorbers, which exhibit exceptional performance[1–4] and are approaching the performances of the best thin film technologies.[12,13] This cell type has been shown to work without high temperature sintering steps for the mesoporous scaffold,[4] closing the gap to achieving fully low-temperature solution-based manufacture. Typically highest efficiency devices employing planar heterojunction architecture (n-i-p configuration, where intrinsic perovskite is processed on top of n-type electron selective material) or meso-superstructured configuration (perovskite coated onto an insulating scaffold of mesoporous aluminium oxide) require sintering of the TiO_2 compact layer, which serves as a selective contact for electron collection at the anode.[14] Typically, this compact layer is prepared by spin-coating or spray pyrolysis of a solution of TiO_2 precursor with subsequent sintering at 500 °C in order to transform the amorphous oxide layer into the crystalline form (anatase), which provides good charge transport properties. The problem of high temperature processing of the TiO_2 compact layer has been addressed previously for dye-sensitized solar cells (DSSCs): atomic layer deposition,[15,16] microwave sintering[17] and inductively coupled plasma (ICP)-assisted

DC magnetron sputtering[18] have been used for deposition. However, the results generally yield lower efficiency in DSSCs than high-temperature processed TiO_2.

This chapter reports a low temperature fabrication (< 150 °C) of a compact layer composed of highly crystalline small nanoparticles of anatase TiO_2. This approach results in a dense TiO_2 layer, which exhibits 100-fold increase in conductivity compared to the TiO_2 produced from the previous high temperature route. The ensuing all-low-temperature processed meso-superstructured solar cell (MSSC) yields in improved photovoltaic performance, delivering a maximum full sun power conversion efficiency of 15.9% as derived from the JV curve (non-stabilised).

4.3 Results and discussion

4.3.1 Low-temperature TiO_2 films

TiO_2 nanoparticles were synthesised by a nonaqueous route from titanium tetrachloride and benzyl alcohol,[19] detailed description of the procedure is given in Chapter 3. In Figure 4.1 X-ray diffractogram of a powdered sample is presented, it can be assigned to anatase TiO_2, with a crystal diameter of approximately 4.5 nm, as determined by Scherrer peak width analysis:[20]

$$d = 0.9\lambda/\omega\cos\theta \qquad (4.1)$$

where *d* is the crystal size, λ is the X-ray wavelength, ω is the full width at the half-maximum (FWHM) of the diffraction peak and θ is the Bragg angle.

In this chapter, the newly developed compact layer processed from the solution of synthesised TiO_2 nanoparticles, termed low temperature TiO_2 (lt-TiO_2) is compared

with the standard recipe used in MSSCs in which a solution of titanium isopropoxide in acidic ethanol is spin-coated onto the substrate.[4] For the conventional route the films were either dried at 150 °C producing amorphous titania (termed TiO_x), or sintered at 500 °C as is typically done in highly efficient perovskite devices. Sintered films were termed high temperature TiO_2 (ht-TiO_2).

It has been shown that adding titanium diisopropoxide bis(acetylacetonate) (TiAcAc) to TiO_2 mesoporous single crystals can greatly enhance the adhesive properties of the film and enhance the operation of dye-sensitized solar cells when processed at low temperature.[21] Here, a small amount of TiAcAc (initially 10 mol% with respect to TiO_2 content) was added to the colloidal TiO_2 dispersion, prior to spin-coating and annealing at 150 °C. The carbonated part of TiAcAc decomposes during film annealing and bridges the gaps between the nanoparticles, in other words it creates the mortar to hold the nanoparticles together.[22] An opaque colloidal dispersion becomes translucent a few hours after TiAcAc addition, which can be attributed to the chelation of acetylacetonate ligands to the TiO_2 nanoparticles.[23] Scanning electron microscopy (SEM) images of the spin-coated lt-TiO_2 films are presented in Figure 4.2a-c, addition of TiAcAc provides "crack-free", uniform and continuous coverage of the substrates.

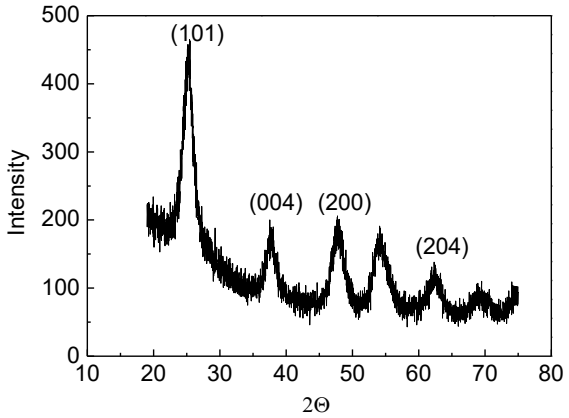


Figure 4.1 X-ray diffractogram of TiO_2 nanoparticles powder sample.

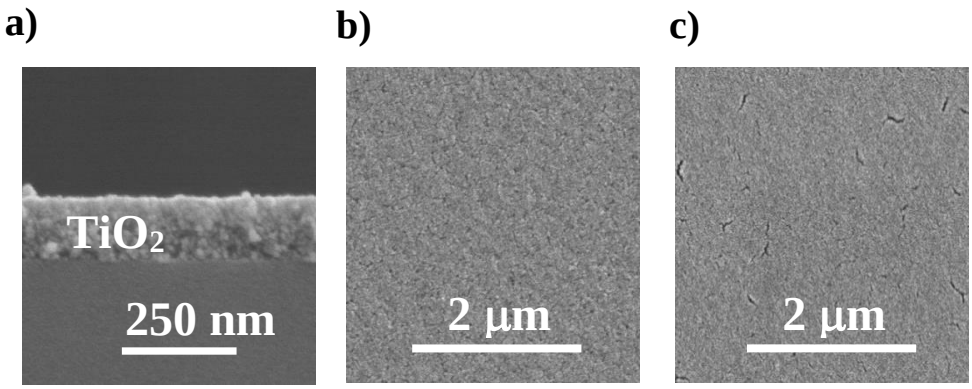


Figure 4.2 (a) Scanning electron microscopy (SEM) cross-section image of TiO_2 film on glass, processed from 3.54 wt% solution of TiO_2 nanoparticles, thickness: 100-120 nm; **(b)** top surface SEM image of the film of TiO_2 nanoparticles processed from the solution with 10 mol% TiAcAc additive and **(c)** without TiAcAc.

Dependence of TiAcAc concentration, from 0 to 80 mol% with respect to TiO_2, on the conductivity of the lt-TiO_2 films was studied, and compared to the TiO_x and ht-TiO_2 films. The results shown in Table 4.1 demonstrate that TiO_x is the least conductive (2×10^{-6} Scm^{-1}), an order of magnitude lower than the conventional ht-TiO_2. Remarkably, films processed from TiO_2 sol show 50-fold increase in conductivity over the ht-TiO_2 and with the addition of a small amount of TiAcAc this increases to a maximum of just below 10^{-3} Scm^{-1}. This demonstrates that at least as far as conductivity and hence series resistance are concerned, the new low temperature TiO_2 compact layer should perform better than high temperature processed TiO_2. However, after calculating the equivalent series resistance for current flowing perpendicularly through a 1 cm^2 slab of 50 nm thick material, as shown in Table 4.1, it appears that only the TiO_x should contribute significantly to the solar cell series resistance.

Table 4.1 Conductivity values of different blocking layers.

Blocking layer	Conductivity ($S \cdot cm^{-1}$)	Calculated Resistance through 50 nm thick film ($\Omega \cdot cm^2$)
TiO_x	$0.02 \cdot 10^{-4}$	2.500
ht-TiO_2	$0.11 \cdot 10^{-4}$	0.455
lt-TiO_2 (0 mol% TiAcAc)	$5.08 \cdot 10^{-4}$	0.010
lt-TiO_2 (10 mol% TiAcAc)	$8.32 \cdot 10^{-4}$	0.006
lt-TiO_2 (20 mol% TiAcAc)	$6.80 \cdot 10^{-4}$	0.007
lt-TiO_2 (40 mol% TiAcAc)	$4.15 \cdot 10^{-4}$	0.012
lt-TiO_2 (80 mol% TiAcAc)	$0.24 \cdot 10^{-4}$	0.208
spiro-OMeTAD (250 nm)	$0.30 \cdot 10^{-4}$	0.833

4.3.2 Solar cell performance

Newly developed TiO_2 compact layers, with varying concentration of TiAcAc additive, were incorporated into complete perovskite MSSCs. The statistics of photovoltaic parameters derived from current-voltage measurements are presented in Figure 4.3a. Devices with the additive show clear improvement in short-circuit current density (J_{sc}), which could be attributed to a better interconnection between particles resulting in an improved charge transport properties. With increased TiAcAc concentration, the amount of non-conductive product in the film increases, resulting in a worse carrier transport and in turn lower device performance. The optimum concentration in terms of solar cell performance was 20 mol% TiAcAc, and that amount was used for the remainder of the study presented in this chapter.

The influence of the TiO_2 layer thickness was also investigated by varying the concentration of TiO_2 nanoparticles, from 3.54 wt% to 0.24 wt%, which corresponds to film thicknesses (on a flat glass substrate) ranging from 110 nm to less than 10 nm, respectively. Devices with thinner

compact layers are mainly affected by a drop of fill factor and J_{sc}. Due to the FTO roughness diluted formulations are less likely to cover the entire surface of the electrode. Uninhibited recombination by electron leakage from FTO to perovskite can cause the drop of the performance in those devices. The more concentrated TiO_2 formulation (> 3 wt%), yielding over 110 nm thick film, is mainly affected by the drop of V_{oc}. In thicker TiO_2 film there might be more unfilled sub-band gap trap states due to lower charge density (charges dissipate over the bigger space), which could result in a higher quasi Fermi-level for electrons (further from vacuum) and drop of V_{oc}.[24] The photovoltaic performance parameters for devices with the range of compact layer thicknesses are presented in Figure 4.3b, the optimum thickness was found to be approximately 45 nm (1.77 wt% lt-TiO_2).

Presented results were obtained from the reverse JV scan (voltage swept from 1.4 V to 0 V at the rate of 150 mV/s). All the cells exhibited lower performance in the forward scan (from 0 V to 1.4 V), especially in FF and V_{oc}. The problem of this hysteretic effect is addressed in more detail in the following chapters. In Figure 4.4a current-voltage curves of the best performing MSSCs fabricated with the optimised lt-TiO_2 formulation, ht-TiO_2 and amorphous TiO_x are compared. Statistics of solar cell performance parameters for a number of devices along with the solar cell series resistance, determined by fitting the slope of the JV curve near open-circuit, are presented in Table 4.2 and Figure 4.4b. Devices with the optimum low temperature processed compact layer surpass the performance of sintered compact layer devices, delivering a maximum power conversion efficiency of 15.3%. The improvement is mainly due to higher fill factor, which rises above 0.7 in the best devices, consistent with reduced overall series resistance in the solar cell.

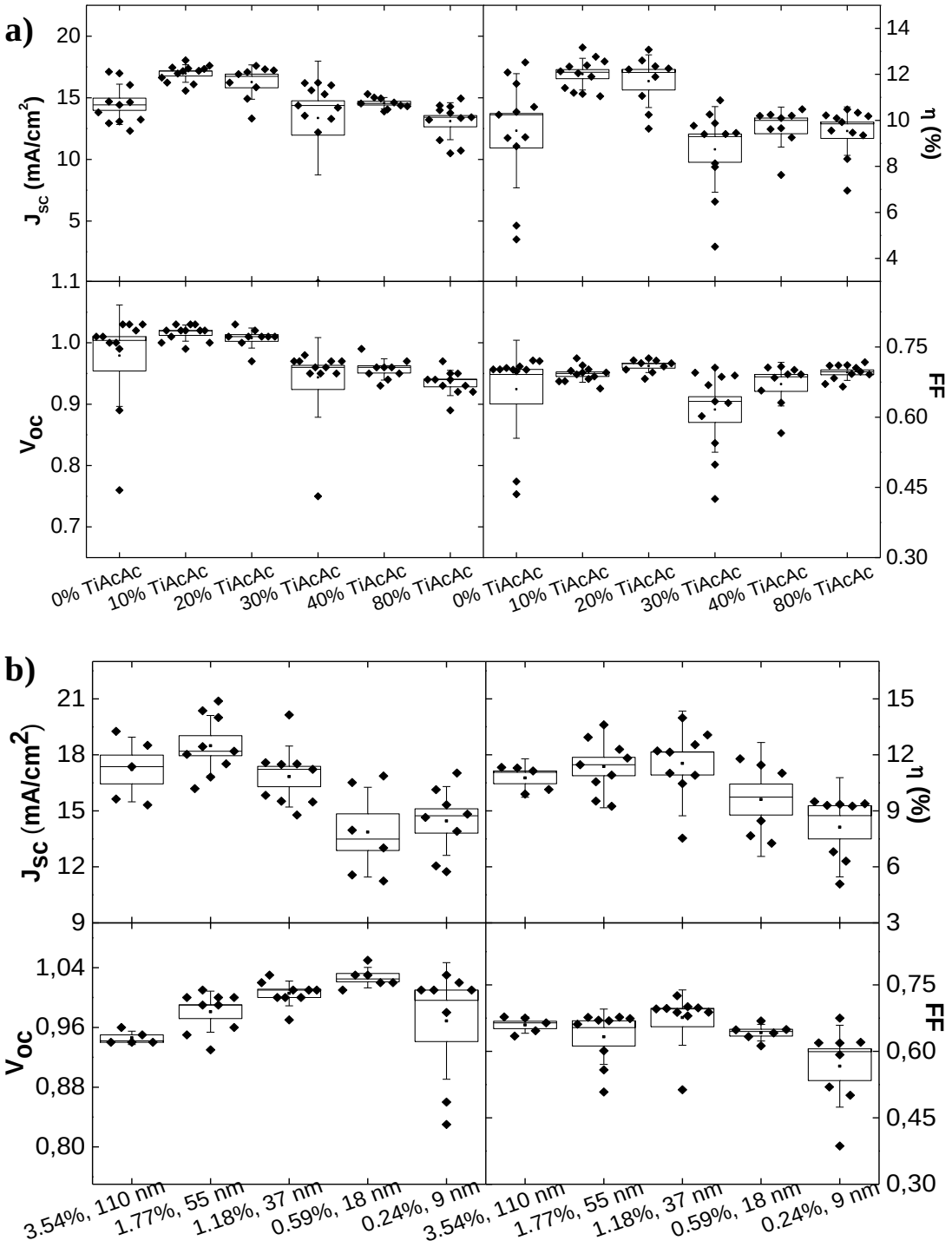


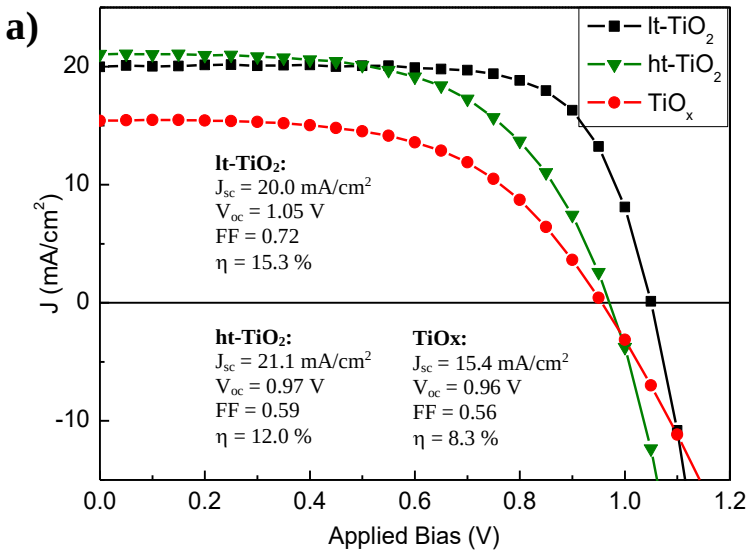
Figure 4.3a. (a) Statistics of photovoltaic parameters (short-circuit current density - J_{SC}, solar cell efficiency – η, open-circuit voltage – V_{OC} and fill factor – FF) extracted from current-voltage measurements (scanned from 1.4 to 0 V) of devices with varying concentration of TiAcAc additive in a compact layer. Each dot represents a single device. **(b)** statistics of photovoltaic parameters extracted from current-voltage measurements of the devices with varying low temperature TiO_2 (lt-TiO_2) compact layer thickness.

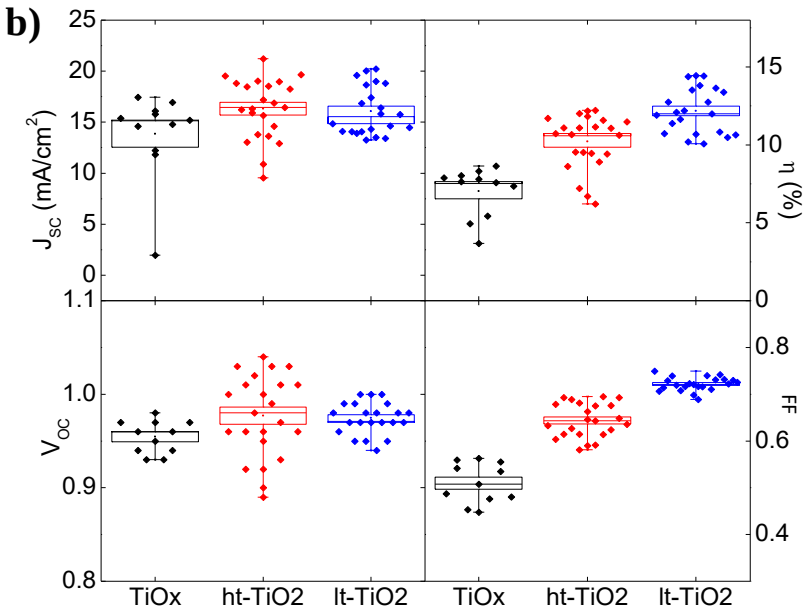
The champion cell with lt-TiO_2 exhibited enhanced V_{oc} compared to the best ht-TiO_2 and TiO_x devices. Higher V_{oc} is especially evident for the cells with thinner lt-TiO_2 layer and lower TiAcAc amount (see Figure 4.3), which as discussed earlier may result from the higher level of filling sub-gap states (electron Fermi level in TiO_2 closer to vacuum). The cells with lt-TiO_2 formulation which resulted in the best average performance (20 mol% TiAcAc, 1.77 wt% lt-TiO_2) exhibited V_{oc} comparable to the ht-TiO_2-based devices (see Figure 4.4b), which suggests similar recombination dynamics.

Following from this work, the perovskite precursor concentration in the spin-coated solution was re-optimised. Higher concentration of solids in the precursor solution allowed fabrication of thicker perovskite films and overall performance of the solar cell was improved, delivering a maximum full sun power conversion efficiency of 15.9 %, with an average of 14.7 %. The current-voltage curve of the champion cell is presented in Figure 4.4c. The increased performance arose from an average increase in the short-circuit photocurrent. The statistical distribution of the photovoltaic parameters of the optimised batch (ht-TiO_2 vs lt-TiO_2) is presented in Figure 4.4d.

Table 4.2. Average values of photovoltaic parameters extracted from current-voltage measurements (scanned from 1.4 to 0 V) of devices with different compact layers (graphical representation in Figure 4.4b).

Compact layer (mean ± s.d.)	J_{sc} (mA·cm^{-2})	η (%)	V_{OC} (V)	FF	R_s (Ω·cm^2)
TiO_x	13.85 ± 4.30	7.03 ± 1.59	0.95 ± 0.02	0.51 ± 0.04	18.93 ± 4.87
ht-TiO_2	16.33 ± 2.98	10.22 ± 1.74	0.98 ± 0.04	0.64 ± 0.04	9.22 ± 1.19
lt-TiO_2 (20 mol% TiAcAc)	16.06 ± 2.37	12.18 ± 1.46	0.97 ± 0.02	0.72 ± 0.01	6.12 ± 0.88


a)
lt-TiO2
ht-TiO2
TiOx
lt-TiO2:
Jsc = 20.0 mA/cm2
Voc = 1.05 V
FF = 0.72
η = 15.3 %
ht-TiO2:
Jsc = 21.1 mA/cm2
Voc = 0.97 V
FF = 0.59
η = 12.0 %
TiOx:
Jsc = 15.4 mA/cm2
Voc = 0.96 V
FF = 0.56
η = 8.3 %
J (mA/cm2)
Applied Bias (V)


b)
JSC (mA/cm2)
η (%)
VOC
FF
TiOx
ht-TiO2
lt-TiO2

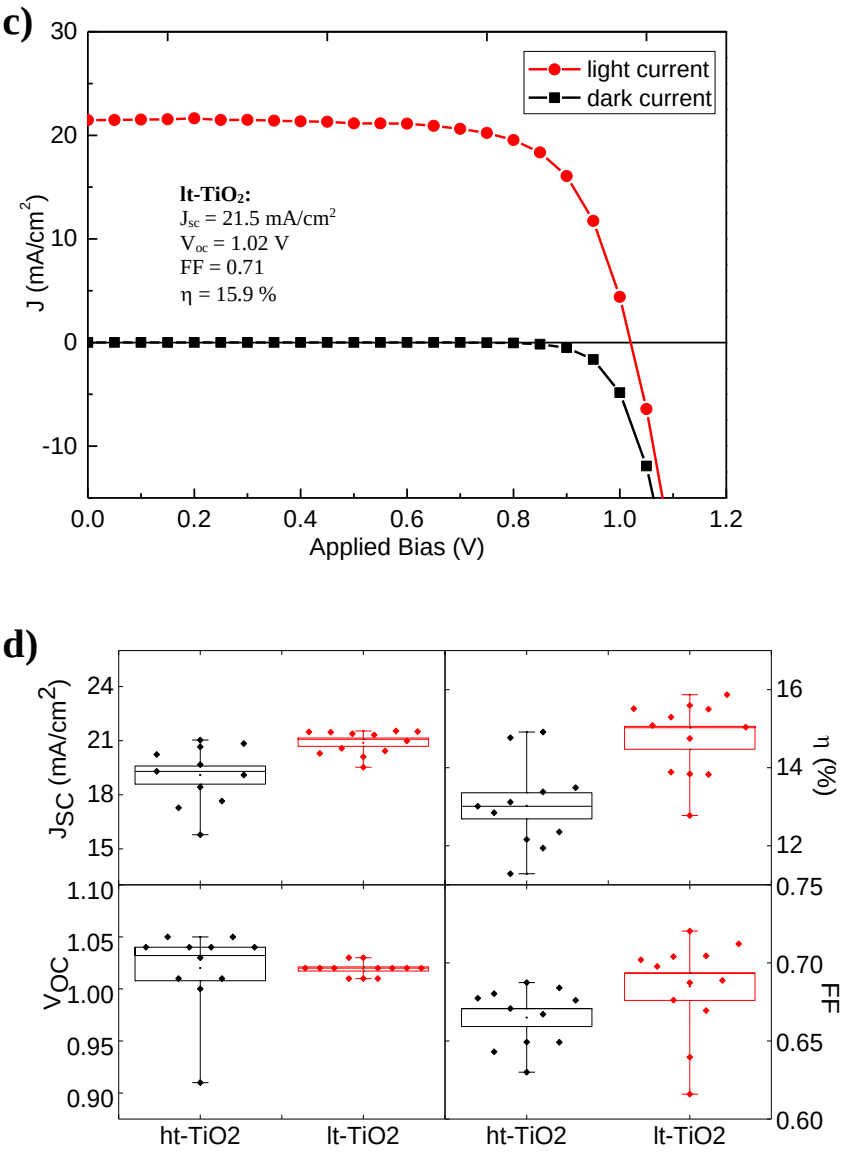


Figure 4.4. (a) Current-voltage characteristics (scanned from 1.4 to 0 V) of the best performing solar cells made with amorphous (TiO_x), high-temperature (ht-TiO_2) and low-temperature (lt-TiO_2) processed compact layer; **(b)** statistics of photovoltaic parameters extracted from current-voltage measurements (scanned from 1.4 to 0 V) of a series of solar cells with the different compact layers, each dot represents a single device; **(c)** record lt-TiO_2 solar cell performance obtained by increasing perovskite film thickness; **(d)** statistics of photovoltaic parameters extracted from current-voltage measurements (scanned from 1.4 to 0 V) of a series of solar cells with optimised perovskite processing conditions and ht-TiO_2 and lt-TiO_2 compact layers.

4.3.3 Electronic characterisation

The new low temperature processed compact TiO_2 is of higher conductivity than the sintered material, and the ensuing solar cells have the characteristics of lower overall series resistance. Measured recombination lifetimes of the devices employing different compact layers, shown in Figure 4.5a, suggest that this offset is not caused by faster recombination. The lifetimes were derived from small perturbation transient photovoltage decay measurements (more explanation about the technique is provided below and in Chapter 3). All the devices display practically invariant recombination kinetics. The cell employing ht-TiO_2 exhibits minimally slower recombination at lower capacitance values (lower light intensities). This could suggest less interfacial defects, but in fact the difference is very small. It is more likely to be caused by sample-to-sample perovskite film variations or accuracy of the transient photovoltage experiment.

At first sight the reduced series resistance in the solar cell is surprising, since the ht-TiO_2 should have only been contributing on the order of 0.5 $\Omega \cdot cm^2$ to the solar cell series resistance. In addition, it has been previously reasoned for solid-state dye-sensitized solar cells that the series resistance at open-circuit is limited by hole-conduction through spiro-OMeTAD.[25] However, here the spiro-OMeTAD is simply a solid capping layer (~250 nm thick as opposed to 2 μm infiltrated into a porous medium in the dye-sensitized solar cells) with a conductivity of close to 3×10^{-5} Scm^{-1}.[25,26] Hence, the overall series resistance expected through a 250 nm thick film of doped spiro-OMeTAD is only 0.8 $\Omega \cdot cm^2$. However, the overall series resistances of the devices are much higher than the sum of the bulk resistances of compact layer and hole transporter (see Table 4.1 and 4.2), and the difference between the devices incorporating lt-TiO_2 and ht-TiO_2 is over 3 $\Omega \cdot cm^2$. Some of the extra resistance could arise from contact resistance, either present at the perovskite/TiO_2 or the TiO_2/FTO contacts. In particular, there is prior evidence for a

potential barrier present at the FTO/TiO_2 interface.[27–29] Via Mott-Schottky analysis, the donor density in conventional high temperature processed compact layers employed in dye-sensitised solar cells has been estimated to be in the order of 10^{19} cm^{-3}.[30] Assuming a dielectric of 50[31] for the TiO_2, a space charge depletion width, *W*, can be calculated using,[30]

$$W = \sqrt{\frac{2\varepsilon\varepsilon_0(E-E_{fb})}{eN}} \tag{4.2}$$

where *N* is the concentration of electron donors, ε is TiO_2 dielectric constant, ε_0 is vacuum permittivity and E_{fb} is the flat-band potential. E-E_{fb} is at approximately the difference between the FTO work function (4.4 eV)[32] and the fermi-level in the TiO_2 (the latter of which should be higher (deeper) than the conduction band edge of TiO_2 at 4.1 eV).[33]

With a charge density of 10^{19} cm^{-3}, a depletion width of approximately 20 nm is estimated. This is on the order of the film thickness employed for the optimum compact layer, which implies that band bending appears to be appropriate. However, it also implies that significant depletion throughout the compact layer could occur for the thinnest films, greatly increasing the bulk series resistance beyond that measured from the isolated films on glass. For the low temperature TiO_2 here, the conductivity is between 10 to 100 times greater than both the high temperature films presented here and those fabricated by spray pyrolysis deposition.[30] If this increase in conductivity is largely due to an increase in the donor density, then with a donor density of 10^{20}, the depletion width would reduce to 6 nm. In this instance, the film would not be completely depleted giving much higher bulk conductivity, and additionally the narrower barrier width should enable a lower contact resistance. Heavy semiconductor doping at semiconductor-metal contacts is a routine procedure to minimise contact resistance.[34] Following this hypothesis, an effective chemical doping of titania nanoparticles could lead to a

further improvement of this contact. Niobium doping for instance has been shown as an effective way to enhance electrical conductivity of the TiO_2.[35,36]

To probe the origin of the reduced series resistance of the lt-TiO_2 devices in more detail, small perturbation transient photovoltage and photocurrent decay measurements were performed, from which the differential capacitance of the solar cell can be determined.[37] This is usually employed to probe the chemical capacitance of mesoporous TiO_2, with the differential capacitance being interpreted to reflect the density of states in the tail of the TiO_2 conduction band. Here, it was used to probe any changes which may have been introduced due to the different TiO_2 compact layers. In Figure 4.5b it is shown that the differential capacitance as a function of open-circuit voltage is considerably different for the devices with the different compact layers. This is quite surprising, since one could assume that the chemical capacitance of such a thin film of TiO_2 to be very low. Devices with ht-TiO_2 show much broader distribution of states than cells with lt-TiO_2, suggesting significant reduction in sub-bandgap states in the low temperature processed films, or that the sub-bandgap states are predominantly filled in the lt-TiO_2, consistent with the enhanced conductivity. Alternatively, the capacitance could be due to the depletion of the compact TiO_2 at the FTO interface, which as discussed above, will lead to a considerably broader depletion region in the ht-TiO_2 than the lt-TiO_2 films. In addition, capacitance which may be present due to accumulation or depletion within the perovskite at the perovskite/TiO_2 interface may also contribute.

It should be noted however, while both these measurements and this rational indicates that that a potential barrier at the FTO-TiO_2 interface could be contributing to the series resistance in the solar cell, further investigation is required to understand in much more detail the nature of the electronic structure across the FTO-TiO_2 and TiO_2-perovskite heterojunctions. Furthermore, it has to be acknowledged that all the perovskite devices presented in this chapter exhibited

anomalous hysteresis in the current-voltage characteristics, meaning that power output derived from the JV curve is dependent on the scanning direction and scanning rate. This phenomenon which is present in many different device architectures has been shown to be particularly pronounced in n-i-p planar heterojunction architectures, and devices employing a TiO_2 blocking layer.[38] The nature of this problem and the means to address it are discussed in the following chapters.

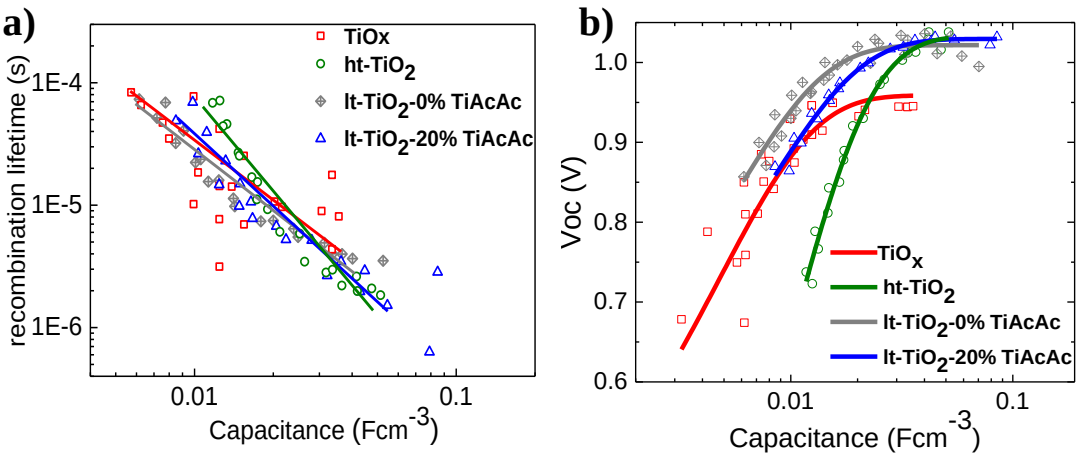


Figure 4.5. Transient photovoltage and photocurrent decay measurements. **(a)** Recombination lifetimes at open-circuit condition plotted against the differential capacitance, measured for solar cells employing different compact layers. Straight lines were fitted to the data points as a guide to the eye; **(b)** Open-circuit voltage against the differential capacitance revealing sub-bandgap density-of-states distribution for solar cells with different compact layers. The measurements were performed by Tomas Leijtens at the Department of Physics, University of Oxford.

4.4 Conclusions

In summary, a route for fabricating a low temperature processed TiO_2 compact layer was successfully developed and in doing so all the high temperature thermal processing steps for the mesosuperstructured and planar heterojunction perovskite solar cells have been removed. Furthermore, through this work it has been discovered that the previously employed high temperature processed compact TiO_2 layer, was contributing significantly to the series

resistance of the solar cells. The new low temperature approach has hence additionally resulted in improved fill factors and efficiency. This work now makes the MSSC compatible with polymer foil flexible substrates, and opens the door for monolithic multi-junction perovskite solar cells.

4.5 References

(1) Kojima, A.; Teshima, K.; Shirai, Y.; Miyasaka, T. Organometal Halide Perovskites as Visible-Light Sensitizers for Photovoltaic Cells. *J. Am. Chem. Soc.* **2009**, *131*, 6050–6051.

(2) Kim, H.-S.; Lee, C.-R.; Im, J.-H.; Lee, K.-B.; Moehl, T.; Marchioro, A.; Moon, S.-J.; Humphry-Baker, R.; Yum, J.-H.; Moser, J. E.; et al. Lead Iodide Perovskite Sensitized All-Solid-State Submicron Thin Film Mesoscopic Solar Cell with Efficiency Exceeding 9%. *Sci. Rep.* **2012**, *2*, 591.

(3) Lee, M. M.; Teuscher, J.; Miyasaka, T.; Murakami, T. N.; Snaith, H. J. Efficient Hybrid Solar Cells Based on Meso-Superstructured Organometal Halide Perovskites. *Science* **2012**, *338*, 643–647.

(4) Ball, J. M.; Lee, M. M.; Hey, A.; Snaith, H. J. Low-Temperature Processed Meso-Superstructured to Thin-Film Perovskite Solar Cells. *Energy Environ. Sci.* **2013**, *6*, 1739.

(5) Lee, C. H.; Kim, D. R.; Cho, I. S.; William, N.; Wang, Q.; Zheng, X. Peel-and-Stick: Fabricating Thin Film Solar Cell on Universal Substrates. *Sci. Rep.* **2012**, *2*, 1000.

(6) Lipomi, D. J.; Bao, Z. Stretchable, Elastic Materials and Devices for Solar Energy Conversion. *Energy Environ. Sci.* **2011**, *4*, 3314.

(7) Schubert, M. B.; Werner, J. H. Flexible Solar Cells for Clothing. *Mater. Today* **2006**, *9*, 42–50.

(8) Baca, A. J.; Yu, K. J.; Xiao, J.; Wang, S.; Yoon, J.; Ryu, J. H.; Stevenson, D.; Nuzzo, R. G.; Rockett, A. a.; Huang, Y.; et al. Compact Monocrystalline Silicon Solar Modules with High Voltage Outputs and Mechanically Flexible Designs. *Energy Environ. Sci.* **2010**, *3*, 208.

(9) Kaltenbrunner, M.; White, M. S.; Głowacki, E. D.; Sekitani, T.; Someya, T.; Sariciftci, N. S.; Bauer, S. Ultrathin and Lightweight Organic Solar Cells with High Flexibility. *Nat. Commun.* **2012**, *3*, 770.

(10) Esiner, S.; van Eersel, H.; Wienk, M. M.; Janssen, R. a J. Triple Junction Polymer Solar Cells for Photoelectrochemical Water Splitting. *Adv. Mater.* **2013**, *25*, 2932–2936.

(11) Green, M. A.; Emery, K.; Hishikawa, Y.; Warta, W.; Dunlop, E. D. Solar Cell Efficiency Tables (version 42). *Prog. Photovoltaics Res. Appl.* **2013**, *21*, 827–837.

(12) Burschka, J.; Pellet, N.; Moon, S.-J.; Humphry-Baker, R.; Gao, P.; Nazeeruddin, M. K.; Grätzel, M. Sequential Deposition as a Route to High-Performance Perovskite-Sensitized Solar Cells. *Nature* **2013**, *499*, 316–319.

(13) Liu, M.; Johnston, M. B.; Snaith, H. J. Efficient Planar Heterojunction Perovskite Solar Cells by Vapour Deposition. *Nature* **2013**, *501*, 395–398.

(14) Peng, B.; Jungmann, G.; Jäger, C.; Haarer, D.; Schmidt, H.-W.; Thelakkat, M. Systematic Investigation of the Role of Compact TiO_2 Layer in Solid State Dye-Sensitized TiO_2 Solar Cells. *Coord. Chem. Rev.* **2004**, *248*, 1479–1489.

(15) Jiang, C. Y.; Koh, W. L.; Leung, M. Y.; Chiam, S. Y.; Wu, J. S.; Zhang, J. Low Temperature Processing Solid-State Dye Sensitized Solar Cells. *Appl. Phys. Lett.* **2012**, *100*, 113901.

(16) Muñoz-rojas, D.; Sun, H.; Iza, D. C.; Weickert, J.; Chen, L.; Wang, H.; Schmidt-mende, L.; Macmanus-driscoll, J. L. High-Speed Atmospheric Atomic Layer Deposition of Ultra Thin Amorphous TiO_2 Blocking Layers at 100 C for Inverted Bulk Heterojunction Solar Cells. *Prog. Photovoltaics Res. Appl.* **2013**, *21*, 393–400.

(17) Hart, J. N.; Menzies, D.; Cheng, Y.-B.; Simon, G. P.; Spiccia, L. Microwave Processing of TiO_2 Blocking Layers for Dye-Sensitized Solar Cells. *J. Sol-Gel Sci. Technol.* **2006**,

40, 45–54.

(18) Kim, H.-J.; Jeon, J.-D.; Kim, D. Y.; Lee, J.-J.; Kwak, S.-Y. Improved Performance of Dye-Sensitized Solar Cells with Compact TiO_2 Blocking Layer Prepared Using Low-Temperature Reactive ICP-Assisted DC Magnetron Sputtering. *J. Ind. Eng. Chem.* **2012**, *18*, 1807–1812.

(19) Wang, J.; Polleux, J.; Lim, J.; Dunn, B. Pseudocapacitive Contributions to Electrochemical Energy Storage in TiO_2 (Anatase) Nanoparticles. *J. Phys. Chem. C* **2007**, *2*, 14925–14931.

(20) Kavan, L.; Procházka, J.; Spitler, T. M.; Kalbáč, M.; Zukalová, M.; Drezen, T.; Grätzel, M. Li Insertion into $Li_4Ti_5O_{12}$ (Spinel). *J. Electrochem. Soc.* **2003**, *150*, A1000.

(21) Crossland, E. J. W.; Noel, N.; Sivaram, V.; Leijtens, T.; Alexander-Webber, J. a.; Snaith, H. J. Mesoporous TiO_2 Single Crystals Delivering Enhanced Mobility and Optoelectronic Device Performance. *Nature* **2013**, *495*, 215–219.

(22) Szeifert, J. M.; Fattakhova-rohlfing, D.; Georgiadou, D.; Kalousek, V.; Rathouský, J.; Kuang, D.; Wenger, S.; Zakeeruddin, S. M.; Gra, M.; Bein, T. "Brick and Mortar" Strategy for the Formation of Highly Crystalline Mesoporous Titania Films from Nanocrystalline Building Blocks. *Chem. Mater.* **2009**, *21*, 1260–1265.

(23) Chen, H.-J.; Wang, L.; Chiu, W.-Y. Chelation and Solvent Effect on the Preparation of Titania Colloids. *Mater. Chem. Phys.* **2007**, *101*, 12–19.

(24) Gouda, L.; Gottesman, R.; Ginsburg, A.; Keller, D. A.; Haltzi, E.; Hu, J.; Tirosh, S.; Anderson, A. Y.; Zaban, A.; Boix, P. P. Open Circuit Potential Build-Up in Perovskite Solar Cells from Dark Conditions to 1 Sun. *J. Phys. Chem. Lett.* **2015**, *6*, 4640–4645.

(25) Abate, A.; Leijtens, T.; Pathak, S.; Teuscher, J.; Avolio, R.; Errico, M. E.; Kirkpatrik, J.; Ball, J. M.; Docampo, P.; McPherson, I.; et al. Lithium Salts as "Redox Active" P-Type Dopants for Organic Semiconductors and Their Impact in Solid-State Dye-Sensitized Solar Cells. *Phys. Chem. Chem. Phys.* **2013**, *15*, 2572–2579.

(26) Leijtens, T.; Lim, J.; Teuscher, J.; Park, T.; Snaith, H. J. Charge Density Dependent Mobility of Organic Hole- Transporters and Mesoporous TiO_2 Determined by Transient

Mobility Spectroscopy : Implications to Dye- Sensitized and Organic Solar Cells. *Adv. Mater.* **2013**, *25*, 3227–3233.

(27) Snaith, H. J.; Grätzel, M. The Role of a "Schottky Barrier" at an Electron-Collection Electrode in Solid-State Dye-Sensitized Solar Cells. *Adv. Mater.* **2006**, *18*, 1910–1914.

(28) Ru, S.; Cahen, D. Electron Tunneling at the TiO_2 / Substrate Interface Can Determine Dye-Sensitized Solar Cell Performance. *J. Phys. Chem. B* **2004**, *108*, 17946–17951.

(29) Rühle, S.; Dittrich, T. Investigation of the Electric Field in TiO_2/FTO Junctions Used in Dye-Sensitized Solar Cells by Photocurrent Transients. *J. Phys. Chem. B* **2005**, *109*, 9522–9526.

(30) Kavan, L.; Graetzel, M. Highly Efficient Semiconducting TiO_2 Photoelectrodes Prepared by Aerosol Pyrolysis. *Electrochim. Acta* **1995**, *40*, 643–652.

(31) Kavan, L.; Tétreault, N.; Moehl, T.; Grätzel, M. Electrochemical Characterization of TiO_2 Blocking Layers for Dye-Sensitized Solar Cells. *J. Phys. Chem. C* **2014**, *118*, 16408–16418.

(32) Andersson, A.; Johansson, N.; Bröms, P.; Yu, N.; Lupo, D.; Salaneck, W. R. Fluorine Tin Oxide as an Alternative to Indium Tin Oxide in Polymer LEDs. *Adv. Mater.* **1998**, *10*, 859–863.

(33) Grätzel, M. Photoelectrochemical Cells. *Nature* **2001**, *414*, 338–344.

(34) Yu, A. Y. C. Electron Tunneling and Contact Resistance of Metal-Silicon Contact Barriers. *Solid. State. Electron.* **1970**, *13*, 239–247.

(35) Liu, C.; Miao, L.; Zhou, J.; Huang, R.; Tanemura, S. Bottom-up Assembly to Ag Nanoparticles Embedded Nb-Doped TiO_2 Nanobulks with Improved N-Type Thermoelectric Properties. *J. Mater. Chem.* **2012**, *22*, 14180.

(36) Tsvetkov, N.; Larina, L.; Shevaleevskiy, O.; Ahn, B. T. Effect of Nb Doping of TiO_2 Electrode on Charge Transport in Dye-Sensitized Solar Cells. *J. Electrochem. Soc.* **2011**, *158*, B1281.

(37) Docampo, P.; Guldin, S.; Stefik, M.; Tiwana, P.; Orilall, M. C.; Hüttner, S.; Sai, H.; Wiesner, U.; Steiner, U.; Snaith, H. J. Control of Solid-State Dye-Sensitized Solar Cell Performance by Block-Copolymer-Directed TiO_2 Synthesis. *Adv. Funct. Mater.* **2010**, *20*, 1787–1796.

(38) Snaith, H. J.; Abate, A.; Ball, J. M.; Eperon, G. E.; Leijtens, T.; Noel, N. K.; Stranks, S. D.; Wang, J. T.; Wojciechowski, K.; Zhang, W. Anomalous Hysteresis in Perovskite Solar Cells. *J. Phys. Chem. Lett.* **2014**, *17*, 1511–1515.

Chapter 5

Heterojunction Modification for Highly Efficient Organic-Inorganic Perovskite Solar Cells

The work presented in this chapter has been published in:

(1) Wojciechowski, K.; Stranks, S. D.; Abate, A.; Sadoughi, G.; Sadhanala, A.; Kopidakis, N.; Rumbles, G.; Li, C.; Friend, R. H.; Jen, A. K.; Snaith, H. J. Heterojunction Modification for Highly Efficient Organic–Inorganic Perovskite Solar Cells, *ACS Nano* **2014**, 8, 12701

(2) Snaith, H. J.; Abate, A.; Ball, J. M.; Eperon, G. E.; Leijtens, T.; Noel, N. K.; Stranks, S. D.; Wang, J. T.; Wojciechowski, K.; Zhang, W. Anomalous Hysteresis in Perovskite Solar Cells, *J. Phys. Chem. Lett.* **2014**, 17, 1511

5.1 Context

Organic-inorganic lead halide perovskites, such as $CH_3NH_3PbX_3$ (X = I, Br, Cl), have emerged as attractive absorber materials for the fabrication of low cost, high efficiency solar cells, as discussed in previous chapters. Over the last 3 years there has been an exceptional rise in power conversion efficiencies (PCEs), demonstrating the outstanding potential of these perovskite materials. However, in most device architectures, including the simplest thin-film planar structure, a current-voltage response displays an "anomalous hysteresis", whereby the power output of the cell varies with measurement time, direction and light exposure or bias history. Recently, the experimental data showing evidences of ion migration in the perovskite films have been reported in a multiple articles.[1–4] It has been suggested that movable ionic species, including halide anions, halide vacancies, and methylammonium cations, respond to the electrostatic potential gradient and screen the built-in voltage in the device, which affects the charge collection efficacy, and in turn may contribute to the hysteretic effects.[5–8] Van Reenen *et al*. have shown that ion migration together with interface trap states are needed to accurately model the hysteresis behavior in the perovskite solar cell.[9] This has been very recently supported by Wu *et al*., who postulated the combination of non-ideal interface behavior and mobile ionic species as the origin of this effect.[10]

In this chapter an insight into the physical processes occurring at the interface between the n-type charge collection layer and the perovskite absorber is provided. Chemical modification of the n-type contact "activates" the electron transfer from the perovskite and in turn significantly reduces the hysteretic behavior, which has persisted as a key challenge in further advancements of this class of solar cells.

5.2 Introduction

Solar to electrical power conversion efficiencies are typically determined from current density-voltage (JV) curves measured under simulated sun light. The JV curves are obtained during light exposure by sweeping an applied bias across the terminals of the cell while measuring the current flowing in the external circuit. This is intended to closely represent the steady state power output of a solar cell at any given bias, and should not be dependent upon bias sweep rate or sweep direction. Perovskite devices often exhibit anomalous hysteresis in their current-voltage curves, with differences in the current measured in the forward and reverse scanning directions.[11,12] Hysteresis in most solar cells is due to the capacitance of the solar cell and should not be significant if the scan rate is slowed to a suitable level. For perovskite solar cells the hysteresis effect is particularly pronounced in planar heterojunction perovskite solar cells, and unlike what would be expected from typical capacitive charging/discharging effects, the hysteresis can persist even at very slow scan rates.[11,13,14] In order to reach stabilized current output, the voltage step in some instances has to be held constant for hundreds of seconds, resulting in impractically slow scan rates required to determine a true "steady state" current voltage curve. This effect is problematic for universal and unambiguous characterization of photovoltaic performance of those devices and comparing efficiencies between changes in materials and device fabrication processes.

In order to report a reliable photovoltaic performance of perovskite solar cells, a new characterisation measurement is introduced – the stabilised power output (SPO) measurement. The current density is measured over a period of time at the constant applied bias, close to the maximum power point (more details are given in Chapter 3). This measurement reflects the steady-state power conversion efficiency of the solar cell. An

example of the hysteresis in JV curves of perovskite device and stabilised measurement is presented in Figure 5.1.

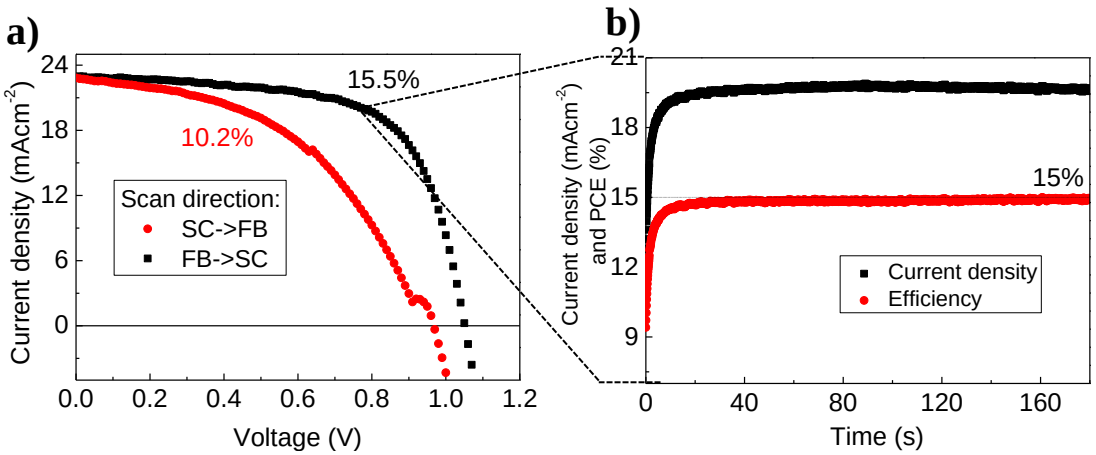


Figure 5.1 (a) JV curves of a meso-superstructured perovskite solar cell (configuration: FTO/compact-TiO_2/meso-Al_2O_3/$CH_3NH_3PbI_{3-x}Cl_x$/spiro-OMeTAD/Ag) measured at the scanning rate of 0.15 V/s at two different scanning directions: from short-circuit to forward bias and from forward bias to short-circuit; **(b)** stabilised power output of the same device measured at fixed voltage of 0.76 V being a maximum power point of the reverse JV curve.

The hysteresis arises due to a change in the effective operation of the solar cell when held under forward bias or short-circuit conditions. The parameters internal to the cell which are different under these two conditions are electric field and charge density. Since the current generated and/or collected after holding the cells under forward bias is larger than under short-circuit, either the efficacy for charge collection at the electrodes is reduced at short-circuit, or the electron lifetime is reduced, or a combination of the two.[11] State-of-the-art perovskite devices typically utilize a thin and uniform compact TiO_2 layer as an electron-selective contact, and a p-type organic hole-conductor as the hole-selective contact.[15] Any bias induced changes to charge collection could either be due to a change to the bulk property of the perovskite, or due to a change to the nature of the contact (either at the surface of the perovskite, nature of interface states or the contact materials themselves).

In this chapter, the contact between the perovskite and the planar n-type TiO_2 charge collection layer is investigated. It has been found that the electron transfer through that interface is not very effective. By modifying this contact with an organic electron accepting fullerene self-assembled monolayer (C_{60}-SAM) significantly enhanced electron injection is achieved. Planar heterojunction perovskite solar cells incorporating the C_{60}-SAM-modified TiO_2 exhibit largely improved photovoltaic performance and a significant decrease in hysteretic behavior. The schematic of the SAM molecules and device architecture is shown in Figure 5.2.

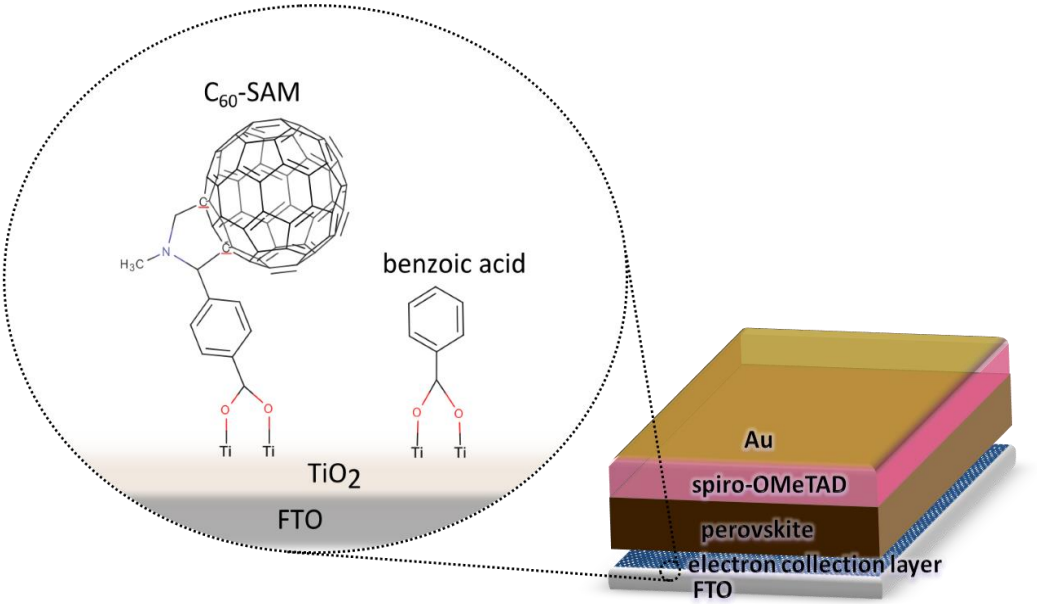


Figure 5.2. Schematic of device structure and in the inset binding of SAMs to TiO_2 surface.

5.3 Results and discussion

5.3.1 Photoinduced charge extraction at perovskite interfaces

In order to investigate the ability of electrons in the perovskite to transfer across to the compact TiO_2, time-resolved photoluminescence decays (Figure 5.3a) and the photoluminescence quantum efficiencies (PLQE; Table 5.1) of the perovskite films deposited upon TiO_2 compact layers and glass slides were measured (experimental details in Chapter 3). The lifetime of the emission from the perovskite is only slightly reduced when coated on the TiO_2 compact layer with the PLQE remaining half that of the perovskite film on glass. This suggests extremely poor or slow electron transfer to the TiO_2. This should be compared to the extremely fast quenching when the perovskite is coated with a fullerene derivative, as has been previously shown,[16,17] where the PL is almost entirely quenched. In order to corroborate the photoluminescence measurements, time-resolved microwave conductivity (TRMC) of the same films was measured (experimental details in Chapter 3). The figure of merit typically extracted from TRMC measurements under optical excitation is the product of the yield of free charge generation per absorbed photon, φ, with the sum of the mobilities of free charges, $\Sigma\mu$.[18] It is found that the peak $\varphi\Sigma\mu$ product (at early time) as a function of absorbed flux does not depend (within experimental error) on the sample architecture (Figure 5.3b). This implies that the generation of mobile conductive charge occurs irrespective of interface, consistent with free carrier generation occurring spontaneously (on shorter than the nanosecond time-scale) following light absorption within the bulk of the perovskite film. In particular, samples with spiro-OMeTAD on top of the perovskite film show very similar initial $\varphi\Sigma\mu_{t=0}$ to the neat perovskite film. Hole injection to spiro-OMeTAD following photoexcitation of the perovskite is expected to be efficient[16,19] and microwave mobility of holes in the spiro-OMeTAD is

expected to be much lower than that in the perovskite.[20] However, the data show no decrease of $\varphi\Sigma\mu_{t=0}$ with the addition of the spiro-OMeTAD, which suggests that the microwave conductivity signal is dominated by electrons in the perovskite. Since $\varphi\Sigma\mu_{t=0}$ is also the same for a perovskite film on glass and on TiO_2, it is concluded that electron injection into the TiO_2 is quite inefficient, at least within the 5 ns excitation pulse used in the TRMC experiment. Efficient ultrafast electron injection to TiO_2 would result in decreased $\varphi\Sigma\mu$ values due to the low, microwave electron mobility in TiO_2.[21] Furthermore, photoconductance transients measured by TRMC are presented in Figure 5.3c, for perovskite films on glass and on compact TiO_2, which are essentially indistinguishable. If substantial electron transfer occurred from the perovskite to the TiO_2 a significant difference in the photoconductance decay profiles for these two samples would be expected, indicative of the removal of electrons from the perovskite films.[22] Since this is not observed it again suggests that after photoexcitation in the perovskite, electron transfer to the compact TiO_2 is poor. Unexpectedly, the perovskite sample with a hole-quenching spiro-OMeTAD layer on top shows an even slower decay of the TRMC transient (Figure 5.3d). As mentioned earlier, an efficient hole transfer to spiro-OMeTAD is expected, which should yield in faster TRMC transient decay if both electrons and holes were detected. However, the results are explicable if the hole mobility is significantly lower than the electron mobility within the perovskite film at the 10 GHz range. Then, following hole extraction[16] the lifetime of the electron conductivity signal would be extended since recombination is inhibited by the fact that the holes have been extracted from the perovskite film. The time-resolved PL and microwave conductivity decays were used for a comparative analysis, i.e. to see how the dynamics are changing with different quenching layers. Considering that the transients are not monoexponential the exact lifetimes and quantitative analysis is not necessary here.

These results suggest that for the current planar heterojunction perovskite solar cells which employ compact TiO_2 as the n-type layer, the electron collection rate is a limiting factor. Under

illumination, the perovskite will transfer holes to the hole-conductor, then accumulate electrons until the quasi-Fermi level for electrons within the perovskite is suitably low (closer to vacuum) to allow a flow of electrons across the TiO_2 interface and enable a steady state current to flow.

Fullerene molecules are known to act as a good electron acceptor for perovskites,[23–25] therefore the impact of modifying the compact TiO_2 with a fullerene self-assembled monolayer was investigated. The C_{60}-SAM, which binds to the TiO_2 surface hydroxyl groups through the carboxylic acid anchoring group,[26–28] was employed. The schematic of the molecule is presented in Figure 5.2. In Figures 5.4a-c scanning electron microscopy (SEM) images of modified and unmodified TiO_2 surfaces are presented. The PL and TRMC data for perovskite films coated on C_{60}-SAM-modified TiO_2 is shown in Figure 5.2. The PL quenching is dramatically enhanced which is consistent with the C_{60}-SAM monolayer enabling better extraction of photoinduced electrons from the perovskite. The TRMC traces also show a significant reduction in decay time upon modification, again consistent with effective electron transfer to the fullerene-modified TiO_2. Notably, it is expected that the C_{60}-SAM-modified TiO_2 should only extract electrons, yet the rate of the TRMC signal decay following photoexcitation is substantially increased for this sample. Again, if the 10 GHz hole-mobility was similar to the electron mobility, this transient would be expected to lengthen as the recombination processes were diminished (after efficient extraction there are fewer electrons to recombine with the remaining holes). These results are once again consistent with the hole-mobility being lower than the electron mobility. In previous investigations,[16,17,22,29] the data suggested that the long-range electron and hole mobilities are balanced, hence this discrepancy with the values predicted at 10 GHz warrants further investigation to determine if it is a property of the material or measurement. In particular, charge confinement effects and scattering associated with grain size.

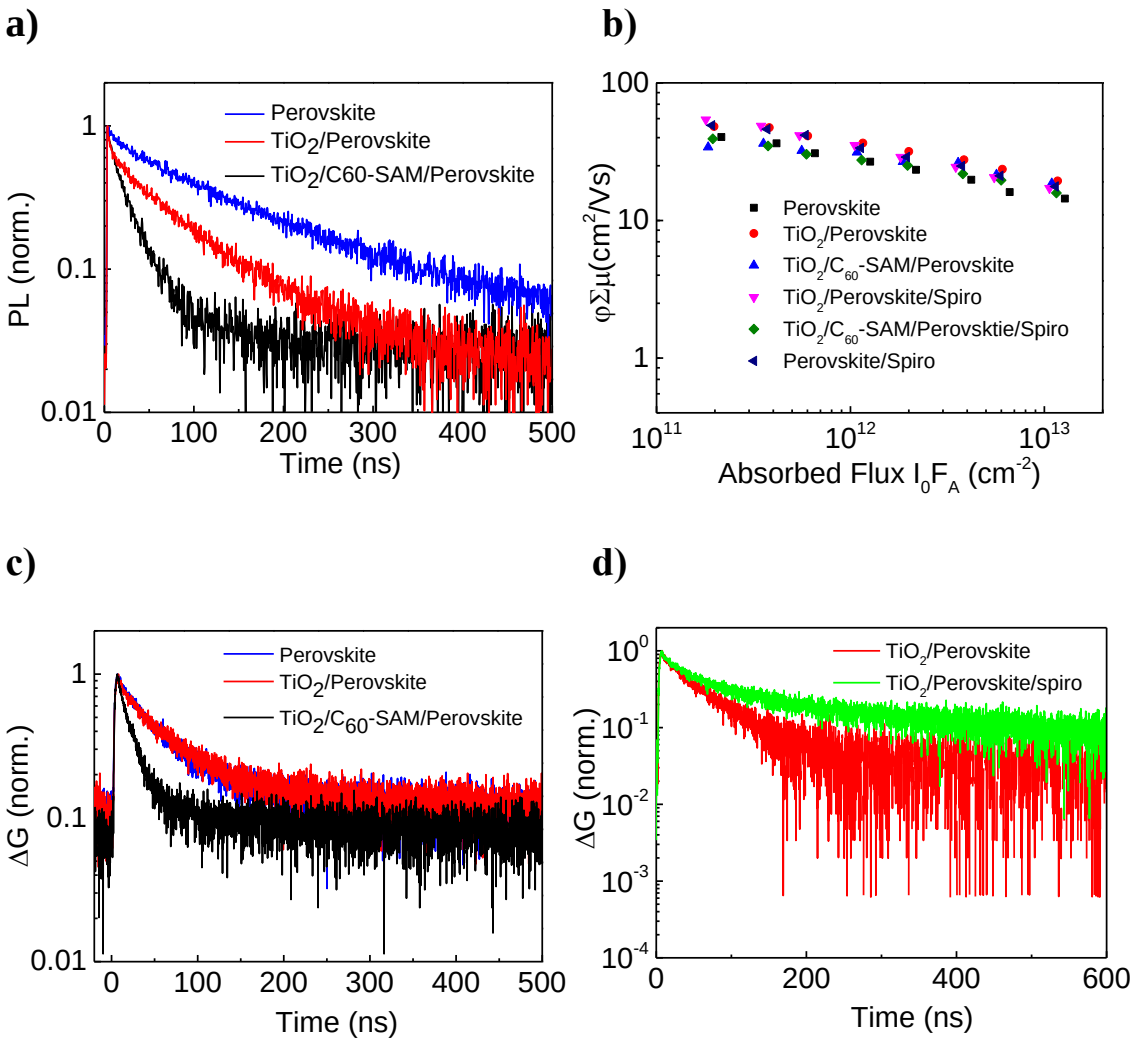


Figure 5.3. (a) Normalized photoluminescence decays following pulsed excitation (507 nm, 1 MHz, 0.03 μJ/cm^2/pulse); (**b)** quantum yield for free carrier generation per absorbed photon times the sum of mobilities as a function of absorbed flux for different perovskite film architectures, taken from the peak of the microwave conductivity signals; (**c)** normalized time-resolved microwave conductivity (TRMC) decays following pulsed excitation (500 nm, 10 Hz, 0.1 μJ/cm^2/pulse) of perovskite both with and without electron quenching layers; **(d)** normalized TRMC decays of TiO_2/Perovskite, both with and without hole transporting layer. TRMC measurements were performed by Nikos Kopidakis at the National Renewable Energy Laboratory, Colorado, US.

Table 5.1. Photoluminescence quantum efficiency (PLQE) values of perovskite films with and without C_{60}-SAM functionalization of the TiO_2. PLQE measurements were performed by Sam Stranks at the Department of Physics, University of Oxford.

Sample	PLQE (%)
No quencher	7.6
TiO_2	3.8
TiO_2/C_{60}-SAM	0.5

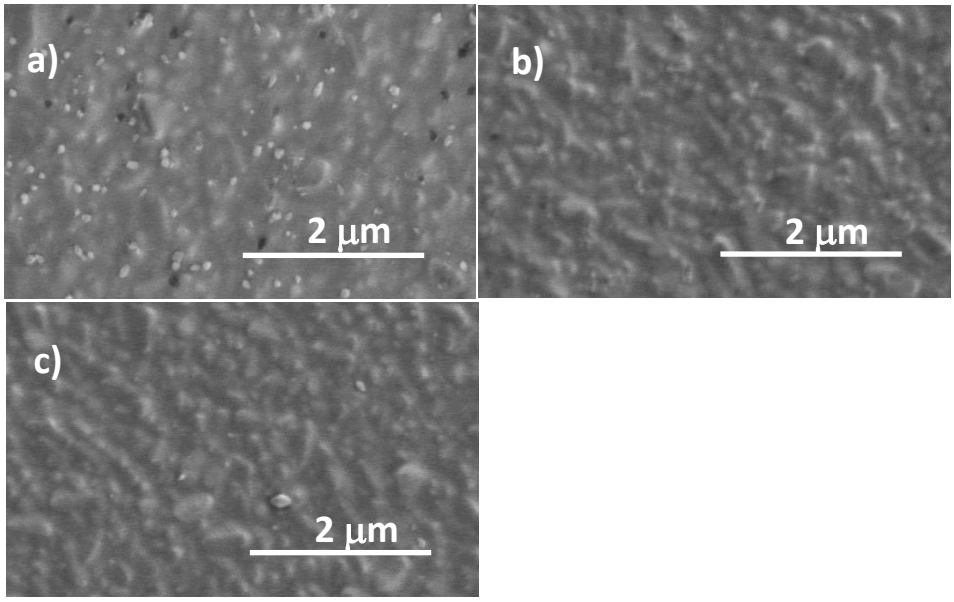


Figure 5.4. Scanning electron microscopy (SEM) top view images of TiO_2 surface **(a)** modified with benzoic acid; **(b)** modified with C_{60}-SAM; **(c)** unmodified.

5.3.2 Density of states in TiO_2

The above data are consistent with the fullerene-modified TiO_2 significantly enhancing the efficacy with which photoinduced electrons can flow out of the perovskite. The modification itself may also have an impact upon the TiO_2. It has been previously shown that crystalline TiO_2 contains inherent localised trap states due to under-coordinated surface Ti(IV)

ions. Those states give an exponentially decreasing tail in the density of states below the conduction band.[30] Adsorption of electron-donating ligands at the surface, such as H_2O molecules, decreases the work function (shifts closer to vacuum) and reduces the number of available states in the sub-bandgap region. However, hydration does not saturate those sites entirely, since water adsorption is not stable and is difficult to control. In order to investigate the influence of C_{60}-SAM treatment on trap states in TiO_2, photothermal deflection spectroscopy (PDS) measurements were performed (experimental details in Chapter 3).[31–33] PDS is a technique which allows to probe with high sensitivity the sub-bandgap optical absorption, and thus the trap states due to under-coordinated surface Ti(IV) ions. The slope of the absorption at the band edge defines the Urbach energy, and provides a measure for the degree of disorder of a material. During the first measurements it was found that the spectrum of TiO_2 films modified with C_{60}-SAM showed a strong contribution from the fullerene (Figure 5.5a), which overlaps with the TiO_2 sub-bandgap absorption, and makes it difficult to probe any change in the TiO_2 density of states (DOS). However, the C_{60}-SAM is anchored to the TiO_2 surface *via* a benzoic acid group (Figure 5.2), which is linked to the fullerene *via* a pyrrolidine derivative group (no π conjugation with the C_{60}), therefore benzoic acid can be used to mimic the effect of the C_{60}-SAM anchoring group on the sub-bandgap absorption of TiO_2. In Figure 5.5b PDS spectra of TiO_2 and TiO_2 modified with benzoic acid on quartz substrates are shown. A significant reduction in the sub-bandgap absorption in TiO_2 upon benzoic acid functionalization can be observed.

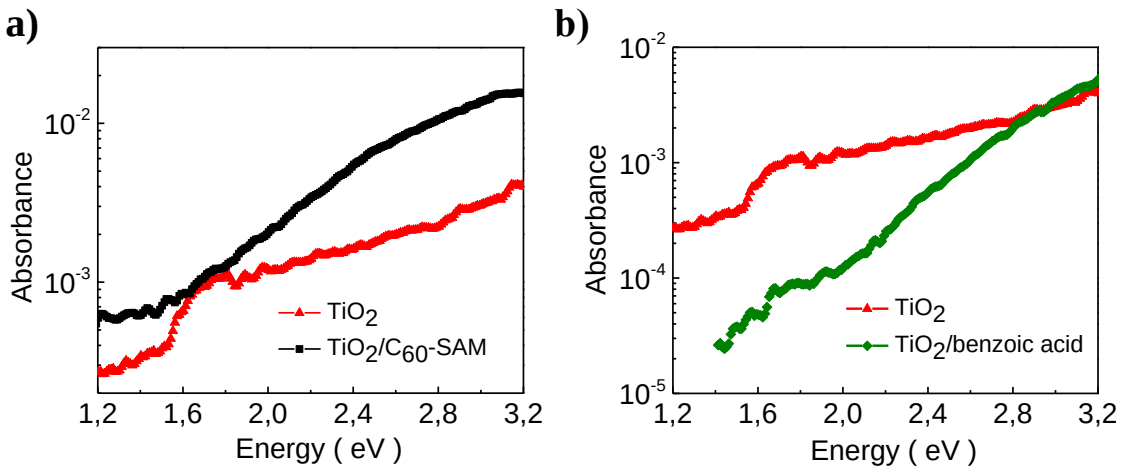


Figure 5.5. (a) Photothermal deflection spectroscopy data of TiO_2 films, unmodified (red curve with triangles) and modified with a monolayer of C_{60}-SAM (black curve with squares); **(b)** PDS spectra of TiO_2 films, unmodified (red curve with triangles) and modified with a monolayer of benzoic acid (green curve with diamonds).
PDS measurements were performed by Aditya Sadhanala at the Department of Physics, University of Cambridge.

In order to show that the effect of the benzoic acid on the TiO_2 trap states is comparable to the C_{60}-SAM, impedance measurements on simple diodes made by a stack of FTO/TiO_2/spiro-OMeTAD/Au layers, where the TiO_2 was modified with benzoic acid and C_{60}-SAM, were performed (experimental details in Chapter 3). Extracted capacitance-voltage characteristics at 1 kHz are shown in Figure 5.6a). At this frequency a high variation of capacitance occurs with increasing bias voltage, which is indicative of charge accumulation at the compact layer and can represent its capacitance.[34,35] To confirm that the capacitance of the TiO_2 is really measured, Mott-Schottky plot of $1/C^2$ vs applied bias of the sample with the unmodified TiO_2 film was plotted (Figure 5.6b). The electron concentration in TiO_2 (N_D) using Mott-Schottky equation was calculated:[36]

$$N_D = \frac{2}{\varepsilon\varepsilon_0 A^2 e \times slope} \quad (5.1)$$

where ε is TiO_2 dielectric constant; ε_0 is vacuum permittivity; A is device area (0.12 cm^2); e is elementary charge; *slope* is taken from the Mott-Schottky plot fit (Figure 5.6b).

With TiO_2 dielectric constant of 50,[37] and Mott-Schottky diagram plotted for impedance values obtained at 1 kHz (Figure 5.6a), the charge concentration of approximately $5x10^{18}$ cm^{-3} was estimated. That value is in good agreement with reported donor densities for TiO_2 blocking layer as calculated from a range of techniques in previous work.[36–38] This is consistent with the primary charge accumulation in the simple diodes occurring in the titania, and in turn the capacitance at that frequency can be used to probe changes in TiO_2 DOS caused by surface modification.

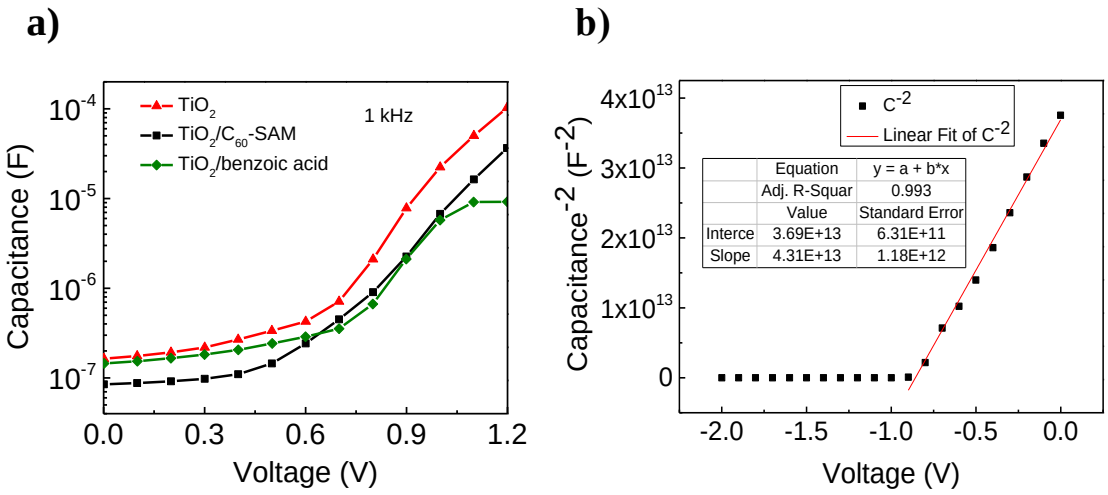


Figure 5.6. (a) Capacitance-voltage characteristics at 1 kHz of TiO_2 films, unmodified (red curve with triangles), modified with a monolayer of C_{60}-SAM (black curve with squares), benzoic acid (green curve with diamonds); **(b)** Mott-Schottky plot for FTO/TiO_2/spiro-OMeTAD/Au sample at 1 kHz.

Upon assembling benzoic acid or C_{60}-SAM, which can be seen in the absorption in the sub-bandgap region (Figure 5.5a), the capacitance of TiO_2 is clearly reduced. This confirms that the DOS in the sub-bandgap region of TiO_2 is altered by the modification with C_{60}-SAM. It should be noted that benzoic acid reduces the capacitance even more effectively than the C_{60}-SAM. This effect could be explained by the contribution of fullerene in the charge accumulation and observed capacitance, but it may also be due to the fact that small molecules like benzoic acid bind with a higher density as compared to the bulkier C_{60}-SAM. A similar decrease in the

overall capacitance of a solar cell upon C_{60}-SAM functionalization of mesoporous TiO_2 has been previously presented.[26–28] However, in the previous instance it was found that the subsequent electron transfer to the mesoporous TiO_2 did not occur readily, and the reduced capacitance was interpreted as being due to blocking of the electron transfer to the TiO_2, and little change was observed with the benzoic acid. This is distinct from the effect presented in this chapter with the compact TiO_2 layers in the planar junction. Presumably the electron density in the C_{60}-SAM is considerably enhanced in this instance enabling forward electron transfer.

5.3.3 Device performance

Complete planar heterojunction perovskite solar cells, both with and without the fullerene modification to the compact TiO_2 were fabricated. At first the electroluminescence (EL) of the photovoltaic devices was measured, the spectra are shown in Figure 5.7a (experimental details in Chapter 3). Non-radiative recombination is indicative of inefficient PV operation.[39] EL is a simple measurement to perform that can quickly give information about any changes to the radiative *versus* the non-radiative recombination. A 5-10-fold increase of the electroluminescence signal for a fullerene-modified sample compared to standard cell can be observed. It is also found that the dark current density is higher for any given applied bias, but by a smaller factor of 2-3 with the C_{60}-SAM treatment (Figure 5.7b). This indicates that the EL efficiency has increased, and as such the non-radiative recombination at the heterojunction reduced with the C_{60}-SAM treatment. This observed increase of EL intensity also suggests that the functionalization has led to a reduction of interface defect sites, either on the TiO_2 or in the perovskite, which would otherwise cause non-radiative recombination of injected carriers. This

is also consistent with recent results suggesting that fullerene can passivate trap states in the perovskite itself.[24,40,41]

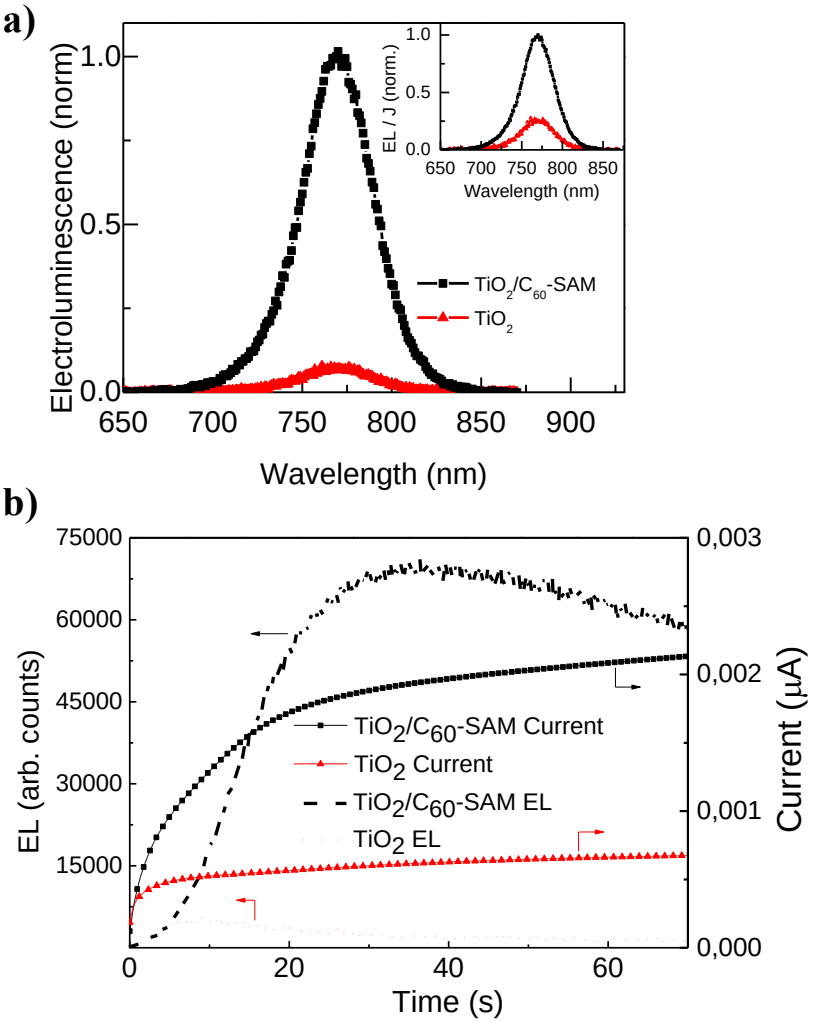


Figure 5.7. (a) Electroluminescence spectra of photovoltaic devices held at forward bias (1.1 V) containing C_{60}-SAM-modified (black curve with squares) and unmodified TiO_2 compact layer (red curve with triangles). Presented spectra are the peak emission following a slow rise. Inset: EL spectra after accounting for differences in injected current density (EL / J); **(b)** Electroluminescence signal (left axis) collected over time for the C_{60}-SAM-modified (black dashed curve) and unmodified (red dotted curve) device. Current flowing through the device was collected at the same time (right axis), black curve with squares corresponds to the C_{60}-SAM device and red curve with triangles to the unmodified cell.

EL measurements were performed by Sam Stranks at the Department of Physics, University of Oxford.

Moving to the solar cell operation, in Figure 5.8a JV curves of the planar heterojunction perovskite solar cells with and without the C_{60}-SAM-modification are presented. All the photovoltaic parameters extracted from the JV curves are shown in Table 5.2. Upon modification there is a significant increase in all parameters. At the scanning rate of 0.15 V/s devices reach PCEs up to 17.3 % on the forward bias to short-circuit scan (FB-SC). The statistics of the results measured for a large batch of devices are shown in Figure 5.8c and Table 5.3.

Two scan directions are presented, from forward bias (FB, 1.4 V) to short circuit (SC, 0V) and reverse – from short circuit (SC, 0 V) to forward bias (FB, 1.4 V). When the scanning rate decreases, the hysteresis for the cells with C_{60}-SAM-modified TiO_2 blocking layer becomes negligible, while it is still very pronounced for the standard unmodified planar heterojunction devices, even at scanning rates 100 times slower (0.0015 V/s, 934 s to scan the entire JV curve). A small decline in fill factor in the fullerene-modified devices when the scanning rate is slower than 0.15 V/s was observed. To corroborate the current-voltage curves, a stabilised power output close to the maximum power point was also measured. Fullerene-modified devices exhibit a faster rise and significantly higher PCE, reaching 15.7 %, as shown in Figure 5.8b.

In order to discriminate between the improved electron extraction and the reduced defect density as a result of incorporating the C_{60}-SAM, solar cells with benzoic acid-modified TiO_2 were also fabricated. No improvement in device performance and persistent large hysteresis in JV curves were observed, even at reduced scanning rates (Figure 5.9). This is consistent with the primary function of the C_{60}-SAM being to enhance electron extraction from the perovskite layer.

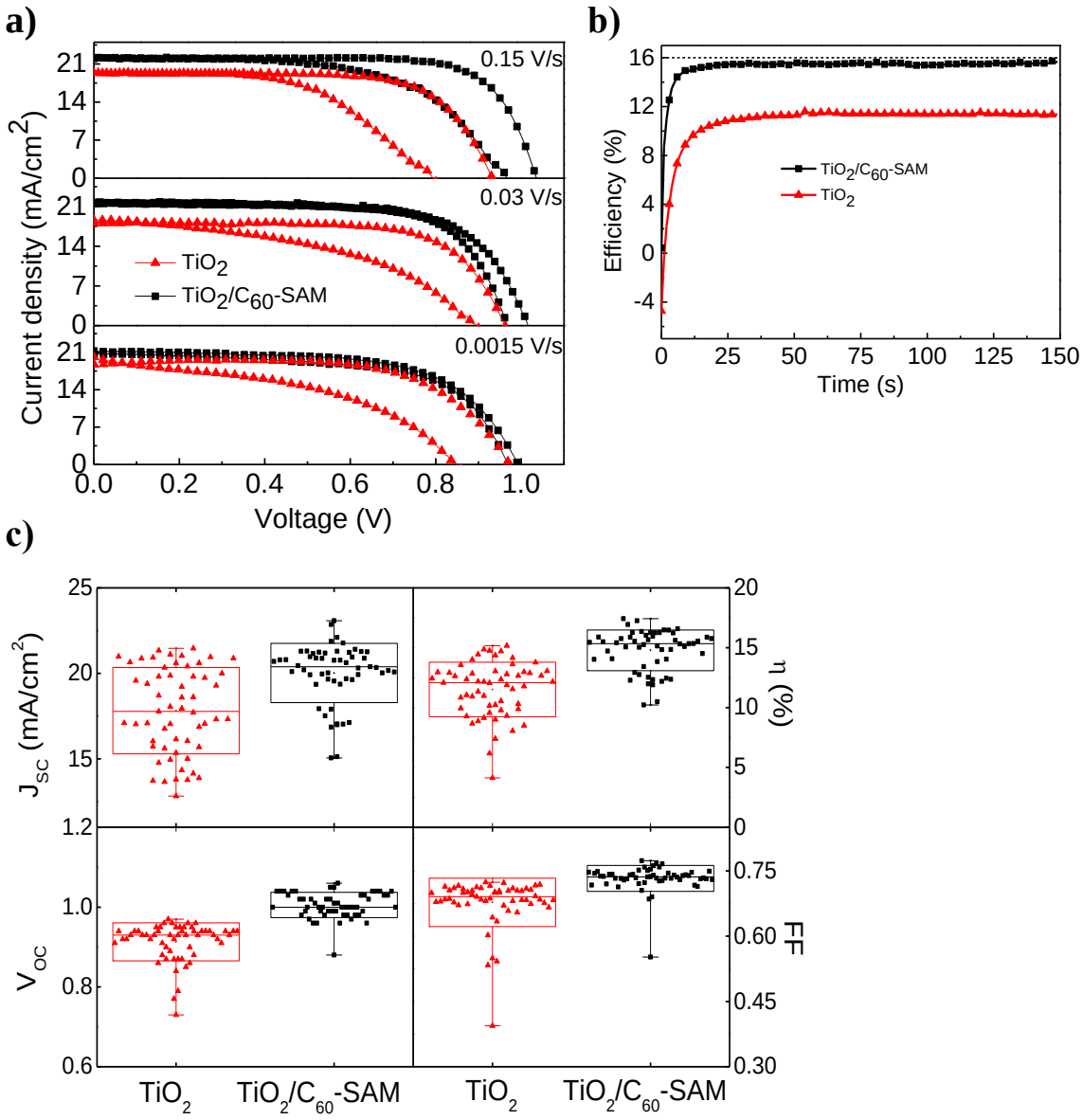


Figure 5.8. (a) JV curves of perovskite solar cells with C_{60}-SAM-modified (black curve with squares) and unmodified TiO_2 (red curve with triangles) compact layer obtained at the scanning rate of 0.15 V/s (top panel), 0.03 V/s (middle panel), and 0.0015 V/s (bottom panel); **(b)** stabilised power output measured close to the maximum power point measured for the devices with C_{60}-SAM-modified (black curve with squares) and unmodified TiO_2 (red curve with triangles) compact layer; **(c)** Statistics of photovoltaic parameters extracted from current voltage measurements (scanning rate: 0.15 V/s, scan direction: FB to SC) of a series of devices with C_{60}-SAM-modified and unmodified TiO_2 compact layer. Each dot represents a single device.

Table 5.2. Photovoltaic parameters extracted from JV curves presented in Figure 5.8a.

scanning rate		0.15 V/s		0.03 V/s		0.0015 V/s	
scanning direction		SC->FB	FB->SC	SC->FB	FB->SC	SC->FB	FB->SC
TiO_2/C_{60}-SAM	J_{sc} (mA/cm^2)	22.0	22.1	21.7	21.6	21.3	20.7
	Eff (%)	12.5	17.3	15.0	14.7	13.4	12.8
	V_{oc} (V)	0.97	1.04	1.02	0.97	0.99	0.97
	FF	0.59	0.75	0.67	0.70	0.63	0.63
TiO_2	J_{sc} (mA/cm^2)	19.3	19.3	18.6	18.0	20.1	18.7
	Eff (%)	8.5	12.7	7.6	12.1	7.5	12.2
	V_{oc} (V)	0.79	0.93	0.90	0.96	0.85	0.97
	FF	0.55	0.70	0.46	0.69	0.44	0.63

Table 5.3. Average values of photovoltaic parameters (with standard deviation) presented in Figure 5.8c.

Device	No of devices	J_{sc} (mAcm^{-2})	V_{oc} (V)	FF	Efficiency (%)
TiO_2	57	17.8 ± 2.5	0.91 ± 0.05	0.68 ± 0.06	11.5 ± 2.3
TiO_2/C_{60}-SAM	55	20.0 ± 1.7	1.01 ± 0.03	0.73 ± 0.03	14.8 ± 1.7

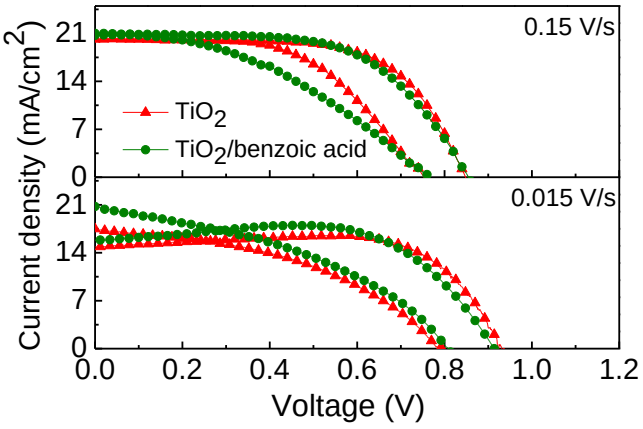


Figure 5.9. JV curves of perovskite solar cells with benzoic acid-modified (green curve with circles) and unmodified TiO_2 (red curve with triangles) compact layer obtained at the scanning rate of 0.15 V/s (top panel) and 0.0015 V/s (bottom panel);

5.4 Conclusions

In conclusion, it has been demonstrated that the interface between the n-type collection layer and the $CH_3NH_3PbI_{3-x}Cl_x$ perovskite absorber has a strong influence on the operation of the solar cells. Photo-induced electron transfer from the perovskite to the compact TiO_2 does not occur efficiently. In the standard devices, good operation relies upon slow electron-hole recombination within the perovskite and at the perovskite-hole transporter interface since a large electron density is likely to reside with the perovskite absorber. By modifying the surface of the TiO_2 compact layer with C_{60}-SAM molecules, a dramatic alteration to the operational mode of the solar cell with largely enhanced electron transfer has been observed. The above findings suggest that there might be an energetic barrier for the electron transfer from perovskite into TiO_2. The nature of this barrier might include unfavourable band bending or the existence of interface dipole. Further investigations shedding more light on the character of this heterojunction are presented in the next chapter.

In addition to altering the operation of the solar cell, the C_{60}-SAM passivates or inhibits the formation of trap states at the interface, on the TiO_2 surface through the anchoring group, and on the perovskite side by the fullerene moiety, reducing the non-radiative recombination channels at this interface. When the scanning rate from forward bias to short-circuit is fast enough, deep trap states can remain filled since the lifetime of an electron in those states can be very long.[42] Passivation of the interface traps or permanent doping of the interfaces could overcome this problem and provide good selective charge collection. However, the time scale over which the photocurrent rises occurs on the order of seconds. This is indicative of the sort of time required for long range ion migration, rather than simply filling of defect sites. Therefore, it is postulated that the hysteresis phenomenon arises due to a combination of trapping and ion migration. These conclusions seem to be in a good agreement with the recent

reports on modelled hysteresis effects and experimental data pointing at ionic migration in the perovskite cells.[3,4,9,10] This matter is discussed in more detail in the next chapter.

The average PCEs increased from 11.5 to 14.8%, with a maximum stabilised power output of 15.7% for the C_{60}-SAM modified devices. The work presented in this chapter significantly improves the understanding of the operation of perovskite solar cells, and it indicates that many further improvements should be possible by focusing upon the nature of the interface between the n-type collection layer and the perovskite absorber.

5.5 References

(1) Yun, J. S.; Seidel, J.; Kim, J.; Soufiani, A. M.; Huang, S.; Lau, J.; Jeon, N. J.; Seok, S. Il; Green, M. A.; Ho-Baillie, A. Critical Role of Grain Boundaries for Ion Migration in Formamidinium and Methylammonium Lead Halide Perovskite Solar Cells. *Adv. Energy Mater.* **2016**, 1–8.

(2) Li, C.; Tscheuschner, S.; Paulus, F.; Hopkinson, P. E.; Kießling, J. Iodine Migration and Its Effect on Hysteresis in Perovskite Solar Cells. *Adv. Mater.* **2016**, *28*, 2446.

(3) Leijtens, T.; Hoke, E. T.; Grancini, G.; Slotcavage, D. J.; Eperon, G. E.; Ball, J. M.; De Bastiani, M.; Bowring, A. R.; Martino, N.; Wojciechowski, K.; et al. Mapping Electric Field-Induced Switchable Poling and Structural Degradation in Hybrid Lead Halide Perovskite Thin Films. *Adv. Energy Mater.* **2015**, *5*, 1500962.

(4) Yuan, Y.; Chae, J.; Shao, Y.; Wang, Q.; Xiao, Z.; Centrone, A.; Huang, J. Photovoltaic Switching Mechanism in Lateral Structure Hybrid Perovskite Solar Cells. *Adv. Energy Mater.* **2015**, *5*, 1500615.

(5) Zhang, Y.; Liu, M.; Eperon, G. E.; Leijtens, T.; McMeekin, D. P.; Saliba, M.; Zhang, W.; De Bastiani, M.; Petrozza, A.; Herz, L.; et al. Charge Selective Contacts, Mobile Ions and Anomalous Hysteresis in Organic-Inorganic Perovskite Solar Cells. *Mater. Horiz.* **2015**, *2*, 315–322.

(6) Tress, W.; Marinova, N.; Moehl, T.; Zakeeruddin, S. M.; Mohammad K., N.; Grätzel, M. Understanding the Rate-Dependent J-V Hysteresis, Slow Time Component, and Aging in $CH_3NH_3PbI_3$ Perovskite Solar Cells: The Role of a Compensated Electric Field. *Energy Environ. Sci.* **2015**, *8*, 995–1004.

(7) Xiao, Z.; Yuan, Y.; Shao, Y.; Wang, Q.; Dong, Q.; Bi, C.; Sharma, P.; Gruverman, A.; Huang, J. Giant Switchable Photovoltaic Effect in Organometal Trihalide Perovskite Devices. *Nat. Mater.* **2014**, *14*, 193–198.

(8) Eames, C.; Frost, J. M.; Barnes, P. R. F.; O'Regan, B. C.; Walsh, A.; Islam, M. S. Ionic Transport in Hybrid Lead Iodide Perovskite Solar Cells. *Nat. Commun.* **2015**, *6*, 7497.

(9) Reenen, S. Van; Kemerink, M.; Snaith, H. J. Modeling Anomalous Hysteresis in Perovskite Solar Cells. *J. Phys. Chem. Lett.* **2015**, *6*, 3808–3814.

(10) Wu, Y.; Shen, H.; Walter, D.; Jacobs, D.; Duong, T.; Peng, J.; Jiang, L.; Cheng, Y.-B.; Weber, K. On the Origin of Hysteresis in Perovskite Solar Cells. *Adv. Funct. Mater.* **2016**, DOI: 10.1002/adfm.201602231.

(11) Snaith, H. J.; Abate, A.; Ball, J. M.; Eperon, G. E.; Leijtens, T.; Noel, N. K.; Stranks, S. D.; Wang, J. T.; Wojciechowski, K.; Zhang, W. Anomalous Hysteresis in Perovskite Solar Cells. *J. Phys. Chem. Lett.* **2014**, *17*, 1511–1515.

(12) Yella, A.; Heiniger, L.-P.; Gao, P.; Nazeeruddin, M. K. Nanocrystalline Rutile Electron Extraction Layer Enables Low- Temperature Solution Processed Perovskite Photovoltaics with 13.7% Efficiency. *Nano Lett.* **2014**, *14*, 2591–2596.

(13) Dualeh, A.; Moehl, T.; Tetreault, N.; Teuscher, J.; Gao, P.; Nazeeruddin, M. K.; Grätzel, M. Impedence Spectroscopic Analysis of Lead Iodide Perovskite-Sensitized Solid-State Sola Cells. *ACS Nano* **2013**, *8*, 362–373.

(14) Jeon, N. J.; Noh, J. H.; Kim, Y. C.; Yang, W. S.; Ryu, S.; Seok, S. Il. Solvent Engineering for High-Performance Inorganic–organic Hybrid Perovskite Solar Cells. *Nat. Mater.* **2014**, *13*, 897–903.

(15) Zhou, H.; Chen, Q.; Li, G.; Luo, S.; Song, T. -b.; Duan, H.-S.; Hong, Z.; You, J.; Liu, Y.; Yang, Y. Interface Engineering of Highly Efficient Perovskite Solar Cells. *Science*

2014, *345*, 542–546.

(16) Stranks, S. D.; Eperon, G. E.; Grancini, G.; Menelaou, C.; Alcocer, M. J. P.; Leijtens, T.; Herz, L. M.; Petrozza, A.; Snaith, H. J. Electron-Hole Diffusion Lengths Exceeding 1 Micrometer in an Organometal Trihalide Perovskite Absorber. *Science* **2013**, *342*, 341–344.

(17) Xing, G.; Mathews, N.; Sun, S.; Lim, S. S.; Lam, Y. M.; Grätzel, M.; Mhaisalkar, S.; Sum, T. C. Long-Range Balanced Electron- and Hole-Transport Lengths in Organic-Inorganic $CH_3NH_3PbI_3$. *Science* **2013**, *342*, 344–347.

(18) Savenije, T. J.; Ferguson, A. J.; Kopidakis, N.; Rumbles, G. Revealing the Dynamics of Charge Carriers in Polymer : Fullerene Blends Using Photoinduced Time-Resolved Microwave Conductivity. *J. Phys. Chem. C* **2013**, *117*, 24085–24103.

(19) Lee, M. M.; Teuscher, J.; Miyasaka, T.; Murakami, T. N.; Snaith, H. J. Efficient Hybrid Solar Cells Based on Meso-Superstructured Organometal Halide Perovskites. *Science* **2012**, *338*, 643–647.

(20) Poplavskyy, D.; Nelson, J. Nondispersive Hole Transport in Amorphous Films of Methoxy-Spirofluorene-Arylamine Organic Compound. *J. Appl. Phys.* **2003**, *93*, 341.

(21) Kroeze, J. E.; Savenije, T. J.; Warman, J. M. Electrodeless Determination of the Trap Density, Decay Kinetics, and Charge Separation Efficiency of Dye-Sensitized Nanocrystalline TiO_2. *J. Am. Chem. Soc.* **2004**, *126*, 7608–7618.

(22) Ponseca, C. S.; Savenije, T. J.; Abdellah, M.; Zheng, K.; Yartsev, A.; Pascher, T.; Harlang, T.; Chabera, P.; Pullerits, T.; Stepanov, A.; et al. Organometal Halide Perovskite Solar Cell Materials Rationalized: Ultrafast Charge Generation, High and Microsecond-Long Balanced Mobilities, and Slow Recombination. *J. Am. Chem. Soc.* **2014**, *136*, 5189–5192.

(23) Docampo, P.; Ball, J. M.; Darwich, M.; Eperon, G. E.; Snaith, H. J. Efficient Organometal Trihalide Perovskite Planar-Heterojunction Solar Cells on Flexible Polymer Substrates. *Nat. Commun.* **2013**, *4*, 2761.

(24) Wang, Q.; Dong, Q.; Xiao, Z.; Yuan, Y.; Huang, J. Large Fill-Factor Bilayer Iodine

Perovskite Solar Cells Fabricated by Low-Temperature Solution-Process. *Energy Environ. Sci.* **2014**, *7*, 2359–2365.

(25) Malinkiewicz, O.; Yella, A.; Lee, Y. H.; Espallargas, G. M.; Graetzel, M.; Nazeeruddin, M. K.; Bolink, H. J. Perovskite Solar Cells Employing Organic Charge-Transport Layers. *Nat. Photonics* **2013**, *8*, 128–132.

(26) Abrusci, A.; Stranks, S. D.; Docampo, P.; Yip, H.-L.; Jen, A. K.-Y.; Snaith, H. J. High Performance Perovskite-Polymer Hybrid Solar Cells via Electronic Coupling with Fullerene Monolayers. *Nano Lett.* **2013**, *13*, 3124–3128.

(27) Hau, S. K.; Yip, H.-L.; Acton, O.; Baek, N. S.; Ma, H.; Jen, A. K.-Y. Interfacial Modification to Improve Inverted Polymer Solar Cells. *J. Mater. Chem.* **2008**, *18*, 5113.

(28) Hau, S. K.; Cheng, Y.-J.; Yip, H.-L.; Zhang, Y.; Ma, H.; Jen, A. K.-Y. Effect of Chemical Modification of Fullerene-Based Self-Assembled Monolayers on the Performance of Inverted Polymer Solar Cells. *ACS Appl. Mater. Interfaces* **2010**, *2*, 1892–1902.

(29) Giorgi, G.; Fujisawa, J.-I.; Segawa, H.; Yamashita, K. Small Photocarrier Effective Masses Featuring Ambipolar Transport in Methylammonium Lead Iodide Perovskite: A Density Functional Analysis. *J. Phys. Chem. Lett.* **2013**, *4*, 4213–4216.

(30) Nunzi, F.; Mosconi, E.; Storchi, L.; Ronca, E.; Selloni, A.; Grätzel, M.; De Angelis, F. Inherent Electronic Trap States in TiO_2 Nanocrystals: Effect of Saturation and Sintering. *Energy Environ. Sci.* **2013**, *6*, 1221.

(31) Jackson, W. B.; Amer, N. M.; Boccara, a C.; Fournier, D. Photothermal Deflection Spectroscopy and Detection. *Appl. Opt.* **1981**, *20*, 1333–1344.

(32) De Wolf, S.; Holovsky, J.; Moon, S.-J.; Löper, P.; Niesen, B.; Ledinsky, M.; Haug, F.-J.; Yum, J.-H.; Ballif, C. Organometallic Halide Perovskites: Sharp Optical Absorption Edge and Its Relation to Photovoltaic Performance. *J. Phys. Chem. Lett.* **2014**, *5*, 1035–1039.

(33) Kronemeijer, A. J.; Pecunia, V.; Venkateshvaran, D.; Nikolka, M.; Sadhanala, A.; Moriarty, J.; Szumilo, M.; Sirringhaus, H. Two-Dimensional Carrier Distribution in

Top-Gate Polymer Field-Effect Transistors: Correlation between Width of Density of Localized States and Urbach Energy. *Adv. Mater.* **2014**, *26*, 728–733.

(34) Kim, H.-S.; Mora-Sero, I.; Gonzalez-Pedro, V.; Fabregat-Santiago, F.; Juarez-Perez, E. J.; Park, N.-G.; Bisquert, J. Mechanism of Carrier Accumulation in Perovskite Thin-Absorber Solar Cells. *Nat. Commun.* **2013**, *4*, 2242.

(35) Bisquert, J.; Bertoluzzi, L.; Mora-Sero, I.; Garcia-Belmonte, G. Theory of Impedance and Capacitance Spectroscopy of Solar Cells with Dielectric Relaxation, Drift-Diffusion Transport and Recombination. *J. Phys. Chem. C* **2014**, *118*, 18983–18991.

(36) Kavan, L.; Graetzel, M. Highly Efficient Semiconducting TiO_2 Photoelectrodes Prepared by Aerosol Pyrolysis. *Electrochim. Acta* **1995**, *40*, 643–652.

(37) Kavan, L.; Tétreault, N.; Moehl, T.; Grätzel, M. Electrochemical Characterization of TiO_2 Blocking Layers for Dye-Sensitized Solar Cells. *J. Phys. Chem. C* **2014**, *118*, 16408–16418.

(38) Wojciechowski, K.; Saliba, M.; Leijtens, T.; Abate, A.; Snaith, H. J. Sub-150 °C Processed Meso-Superstructured Perovskite Solar Cells with Enhanced Efficiency. *Energy Environ. Sci.* **2014**, *7*, 1142.

(39) Miller, O. D.; Yablonovitch, E.; Kurtz, S. R. Strong Internal and External Luminescence as Solar Cells Approach the Shockley–Queisser Limit. *IEEE J. Photovoltaics* **2012**, *2*, 303–311.

(40) Shao, Y.; Xiao, Z.; Bi, C.; Yuan, Y.; Huang, J. Origin and Elimination of Photocurrent Hysteresis by Fullerene Passivation in $CH_3NH_3PbI_3$ Planar Heterojunction Solar Cells. *Nat. Commun.* **2014**, *5*, 5784.

(41) Xu, J.; Buin, A.; Ip, A. H.; Li, W.; Voznyy, O.; Comin, R.; Yuan, M.; Jeon, S.; Ning, Z.; McDowell, J. J.; et al. Perovskite–fullerene Hybrid Materials Suppress Hysteresis in Planar Diodes. *Nat. Commun.* **2015**, *6*, 7081.

(42) Stranks, S. D.; Burlakov, V. M.; Leijtens, T.; Ball, J. M.; Goriely, A.; Snaith, H. J. Recombination Kinetics in Organic-Inorganic Perovskites: Excitons, Free Charge, and Subgap States. *Phys. Rev. Appl.* **2014**, *2*, 034007.

Chapter 6

C_{60} as an Efficient n-Type Compact Layer in Perovskite Solar Cells

The work presented in this chapter has been published in:

(1) Wojciechowski, K.; Leijtens, T.; Siprova, S.; Schlueter, C.; Hörantner, M. T.; Wang, J. T.-W.; Li, C.-Z.; Jen, A. K.-Y.; Lee, T.-L.; Snaith, H. J. C60 as an Efficient N-Type Compact Layer in Perovskite Solar Cells. *J. Phys. Chem. Lett.* **2015**, 6, 2399

6.1 Context

Perovskite solar cells have emerged to the forefront of photovoltaic research in a very short period of time, however, there still remain many unanswered questions and enormous scope for further advancement. One of critical areas for efficient solar cell operation is nature of the interaction between the perovskite absorber material and the charge collection layers. In current device configurations, the electron collection contact has varied from mesoporous to flat TiO_2, and broader still to organic n-type materials. The ideal contact material or configuration has not yet emerged, in part due to the current lack of knowledge of the important aspects of this heterojunction, which influence the device operation.

Another important aspect, crucial for further development of perovskite technology, is stability of the solar cells under stress for a prolonged period of time. Much research is still required to fully understand the processes governing the degradation of these devices. It is very important to perform aging tests at the real operation conditions, i.e. under working bias. Field-induced processes occurring under load are vital for perovskite stability; hence commonly applied light-soaking at open-circuit condition does not provide the full picture of the stability of this system.

The work presented in this chapter highlights a key area in the device, where non-optimum operation occurs, providing not only vital insight into perovskite solar cell operation, but also a promising step towards much more stable and higher efficiency perovskite solar cells.

6.2 Introduction

Recent rapid developments and breakthroughs in enhancing efficiency of the perovskite solar cells were for a large part achieved by enhancing the crystalline nature of the perovskite films, and suitable interface designing and engineering in a n-i-p solar cell architecture.[1–7] The interfaces between the charge selective contacts and the perovskite itself can thus be seen as crucial parameters to explore in attempts to further improve device performance. One pertinent issue for perovskite solar cells is the hysteretic behaviour commonly occurring during current-voltage characterisation. As it has been discussed in the previous chapter, current output measured during sweeping voltage bias across the terminals of the device is dependent on the direction and speed of scanning, which questions the reliability of extracted photovoltaic performance.[5,8–10] The magnitude of that phenomenon varies between different architectures. Numbers of possible origins have been suggested, including ferroelectric properties of perovskite material,[8,10,11] interface trap states[5,8] or ionic displacement.[8,9,12]

It has been shown in Chapter 5 that *via* careful interface engineering the contact between perovskite and charge extraction layers can be largely improved and hysteretic behaviour significantly reduced. By modifying compact TiO_2 with a self-assembled fullerene monolayer the efficacy of photogenerated charge extraction was improved.[5] It has also recently been demonstrated that the hysteretic effect appears to be caused by a long lived polarization, temporarily changing the electric field profile and charge accumulation within the device to favour charge extraction at the contacts.[13]

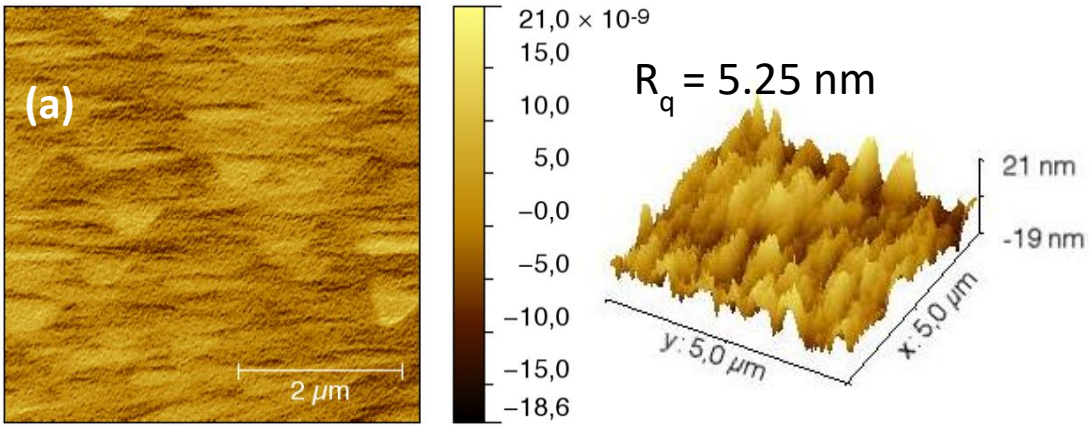
In this chapter efficient perovskite solar cells with an n-type selective contact based on a solution processed fullerene compact layer are presented. This allows removing entirely the compact TiO_2 metal oxide layer as an electroactive component from the

device architecture. The use of organic layers facilitates fabricating the entire solar cell at low temperatures (no need for high temperature sintering step required to get highly crystalline metal oxide layers), suitable for processing involving temperature sensitive substrates, including plastic foil and silicon solar cells. Furthermore, more light is shed on the mechanistic origin of the hysteresis phenomenon, linking it to the electron extraction. Lastly, an initial dataset of stressing encapsulated perovskite solar cells under simulated full sunlight at 60 °C under load for 500 hours is presented.

6.3 Results and discussion

6.3.1 Compact layer-perovskite interface

Solution-processed fullerene (C_{60}) films, spin-coated from 1,2-dichlorobenzene solution, were applied as an electron selective compact layer directly on top of FTO-coated glass substrates (TEC15). In Figure 6.1 scanning electron microscopy (SEM) and atomic force microscopy (AFM) images of C_{60} layers on FTO glass are shown, indicating good coverage and uniformity of the fullerene compact films.



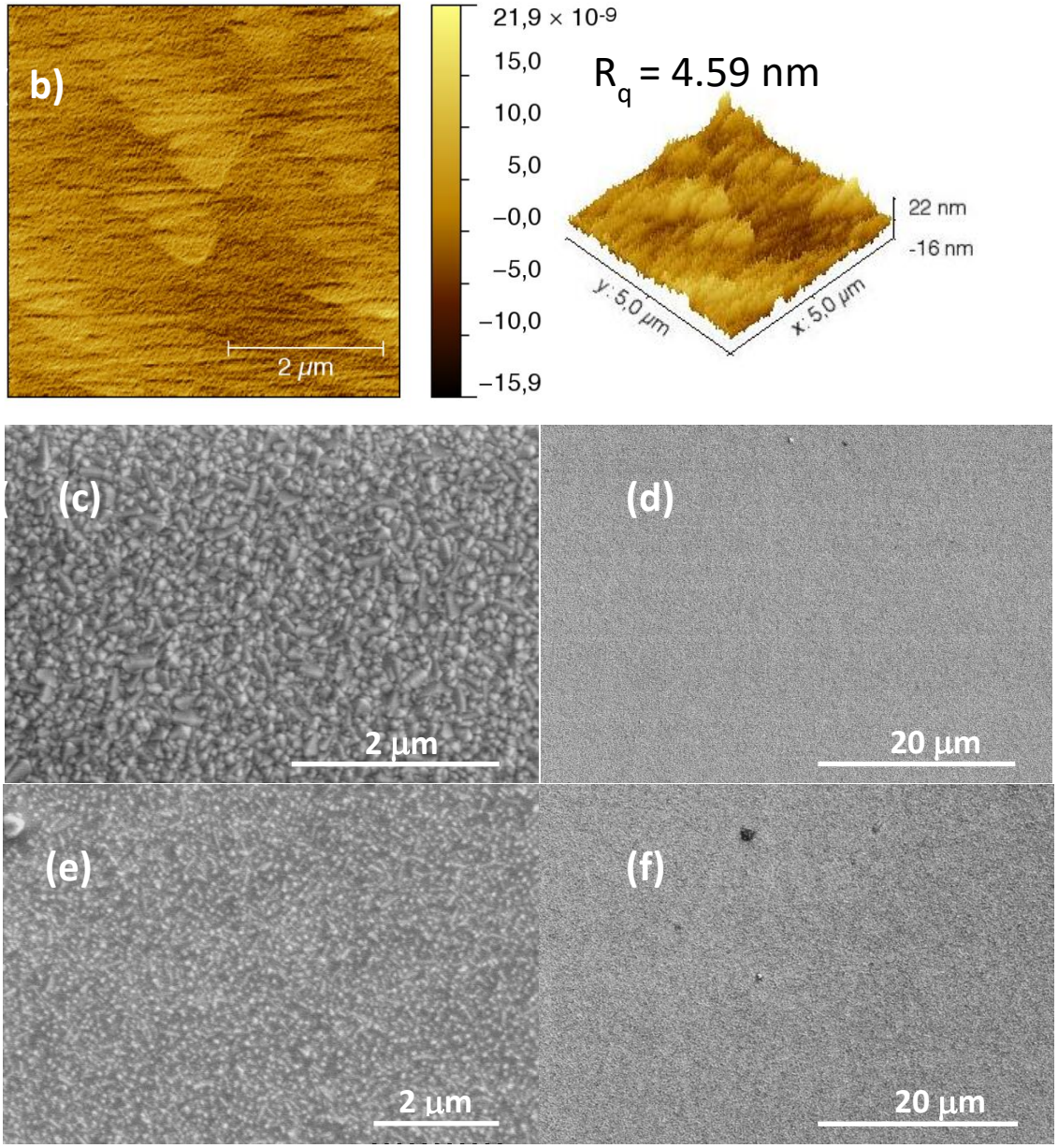


Figure 6.1. Atomic force microscopy (AFM) images and roughness (R_q) of **(a)** FTO glass substrate (TEC15) and **(b)** C_{60} film spin-coated on TEC15, the thickness of C_{60} is 37 nm; Scanning electron microscopy (SEM) top view images of **(c-d)** FTO substrate and **(e-f)** C_{60} film spin-coated on FTO.
AFM images were taken together with Maximilian Hoerantner at the Department of Physics, University of Oxford.

In order to investigate the nature of the C_{60}/perovskite contact and the ability of the organic layer to extract electrons, time-resolved photoluminescence measurements of perovskite films with and without a C_{60} layer were performed. The data presented in Figure 6.2 shows that photoluminescence is quenched more efficiently with C_{60} molecules than TiO_2, which is revealed by significantly faster PL decay. Since electron diffusion within the perovskite is expected to be similar in both cases, the result indicates a difference in the electron transfer efficiency at the perovskite/quencher interface, suggesting a greatly improved electronic coupling between the perovskite and fullerene as compared to the perovskite and TiO_2.

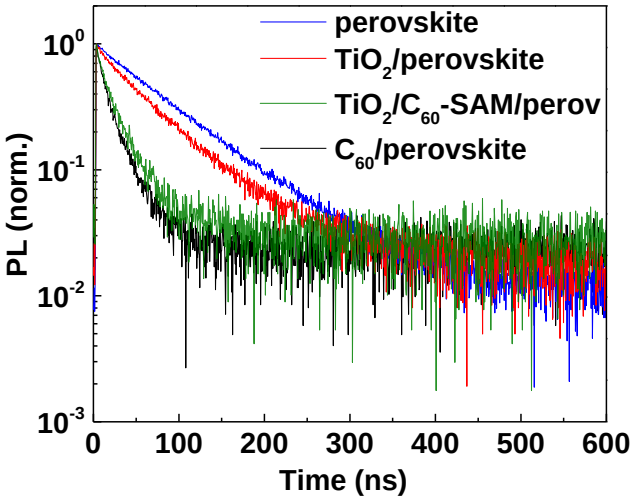


Figure 6.2. Normalized photoluminescence decays following pulsed excitation (507 nm, 1 MHz, 0.03 μJ/cm^2/pulse) of perovskite both with and without electron quenching layers.

To gain insight into the band alignment and nature of the contact between the n-type collection layer and the perovskite, hard X-ray photoelectron spectroscopy (HAXPES) measurements were performed. Experimental details of the measurements are provided in Chapter 3. Valence band spectra for TiO_2, TiO_2 modified with C_{60}-SAM (as presented in the previous chapter and other reports[5,14]), and both layers with a very thin film of $CH_3NH_3PbI_3$ (sub 20 nm) are presented in Figure 6.3a. The binding energies of intense core levels for all structural units of

the sample were measured, as well as respective references to determine the valence band offset following the procedure described by Kraut et al.[15] The XPS spectra of Ti 2p core level and the relative binding energy shifts for the different samples are shown in Figure 6.3b. Using the valence band (VB) offset and band gap values presented in Table 6.1, the band alignment shown in Figure 6.3c is derived. The Fermi level of the perovskite in contact with TiO_2 is very close to the conduction band minimum, a highly n-type characteristic that has been observed previously.[16,17] A number of studies, *via* both photoelectron spectroscopy and conductivity measurements, have shown that metal oxides, such as TiO_2 or Al_2O_3, tend to cause electron accumulation in the perovskite material at the interface with an oxide.[16,18–20] Miller et al. have also observed that lead halide perovskites coated upon some p-type materials, such as PEDOT:PSS, exhibit a more intrinsic character.[20] Inserting a C_{60} self-assembled monolayer (SAM) between the perovskite and the TiO_2 contact shifts the perovskite valence band to lower binding energies, leading to a Fermi level more centred within the band gap and thus a more intrinsic surface. Having a different interface in the form of the C_{60}-SAM molecules, with a non-polar surface and high electron affinity, could potentially cause this effect, although its exact origin is far from understood. When the perovskite film directly contacts the TiO_2, the conduction band edge of the perovskite appears to be below that of TiO_2, indicating the possibility of a barrier to electron extraction across this interface. In the sample with the C_{60}-SAM-modified TiO_2 and the perovskite, the relative shift between the vacuum levels raises the conduction band of the perovskite and removes this electronic barrier. This finding is consistent with the low efficiency of PL quenching for the perovskite coated upon compact TiO_2, which is enhanced considerably with the C_{60}-SAM modification, or by replacing the TiO_2 with a C_{60} film, as is shown in Figure 6.2.

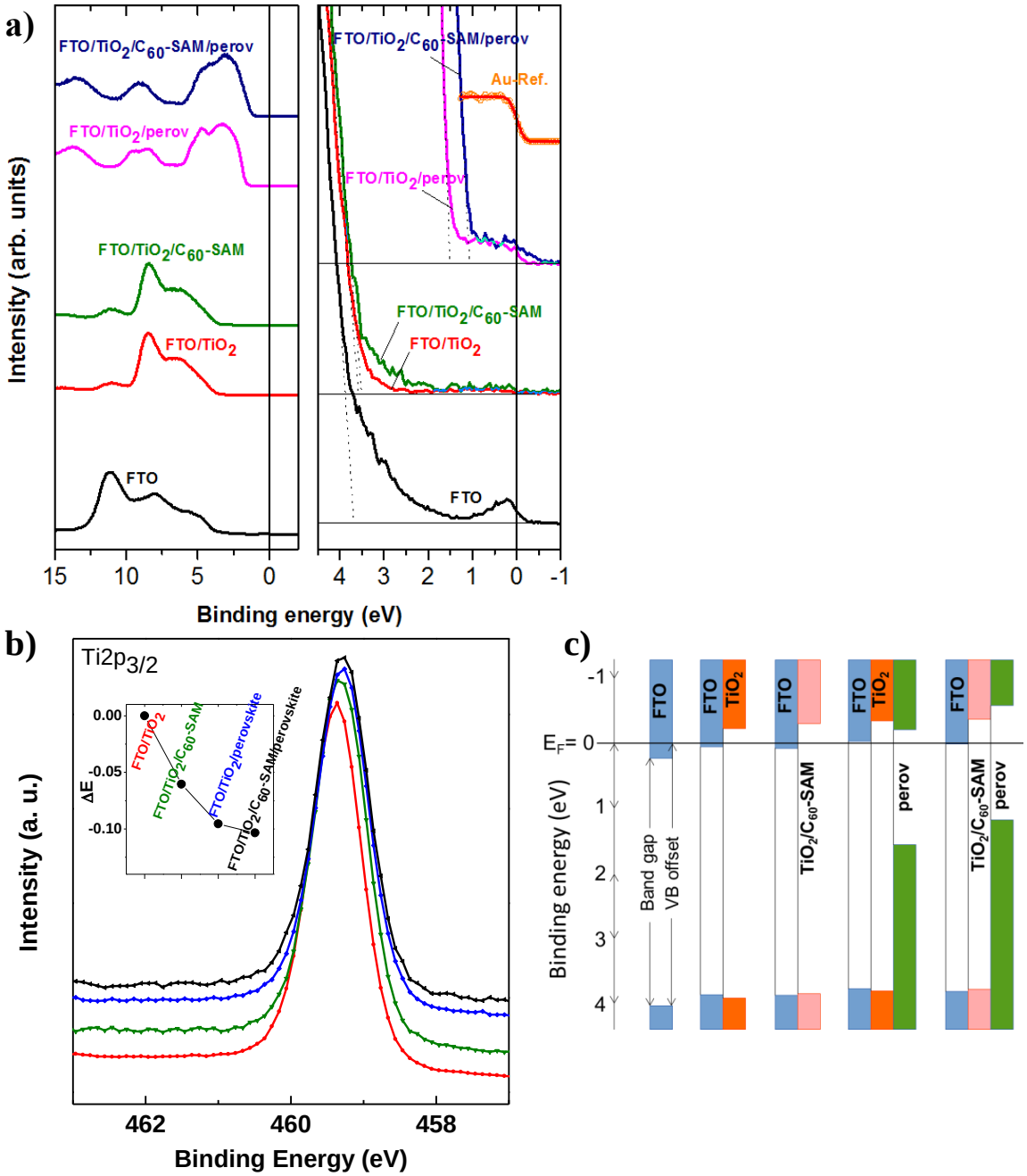


Figure 6.3. (a) HAXPES spectra measured with a photon energy of 8 keV for FTO (black curve), FTO/compact TiO_2 (red curve), FTO/compact TiO_2 modified with a monolayer of C_{60}-SAM (green curve), FTO/compact TiO_2/flat perovskite film (pink curve), FTO/ compact TiO_2 modified with a monolayer of C_{60}-SAM/flat perovskite film (blue curve). Left panel displays the whole spectrum, right panel is a close-up on the band gap region; **(b)** Binding energies of Ti 2p core level for all different samples, inset: relative shifts of Ti 2p core level binding energy for all given samples in respect to FTO/TiO_2 sample; **(c)** Diagram displaying conduction and valence bands respective to the Fermi level for all measured samples. HAXPES measurements were performed and analyzed by Christoph Schlueter at the Diamond Light Source Ltd.

Table 6.1. Valence band offsets measured by HAXPES and band gaps of the materials in the samples.

Sample	Band gap (eV)	VB offset (eV)
FTO	3.35	3.68
TiO_2	3.65	-
$CH_3NH_3PbI_3$	1.55	-
FTO/TiO_2	-	3.58
FTO/TiO_2/C_{60}-SAM	-	3.48
FTO/TiO_2/$CH_3NH_3PbI_3$	-	1.50
FTO/TiO_2/C_{60}-SAM/$CH_3NH_3PbI_3$	-	1.07

It should be noted that although these measurements appear to indicate a favourable shift in the conduction band offsets across this heterojunction, there could also be significant changes to the surface and interface states at this junction, which were not probed in this measurement. Any changes to the interface (or surface) state density at the heterojunction are likely to have a strong influence upon the electronic properties of the subsequent device.

6.3.2 Device performance

To characterise the performance, photovoltaic devices applying the meso-superstructured architecture (porous alumina infiltrated and capped with $CH_3NH_3PbI_{3-x}Cl_x$ perovskite, as reported in previous chapters and other reports[1,21,22]) were constructed at first. The best PCE achieved for cells with fullerene n-type compact layers was 13.5%, as calculated from the current-voltage scan (scan rate: 450 mV/s, scan direction: forward bias to short-circuit), and 12.7% for the steady-state measurement at the maximum power point (see Figure 6.4a-b). This is comparable to the highest JV-determined efficiency of the TiO_2-based cell prepared here (13.9%), when scanned from forward-bias to short-circuit. The use of fullerene though noticeably reduces the hysteretic behaviour in the JV curves, improves the stabilised PCE (10.9% for TiO_2-based cell), and the ratio of the PCE measured at the maximum power point to JV-scan-derived PCE. Photovoltaic parameters for the forward and backward scan directions as well as the stabilised efficiencies for TiO_2 and C_{60}-based cells are presented in Table 6.2.

C_{60} is poorly soluble in dimethylformamide (DMF), the solvent used in the perovskite precursor solution, but the exposure to the solvent during spin-coating might be enough to cause partial dissolution of the fullerene film and in turn deterioration of the hole-blocking properties of the n-type contact. UV-Vis spectra of the C_{60} films treated with different solvents were measured in order to investigate the robustness to solution processing (see Figure 6.5). There is a significant drop in the absorption band at 440 nm, which is characteristic of the fullerene absorption, upon spin-coating DMF directly on a C_{60} film. It should be noted that the C_{60} dissolution caused by pure DMF, as shown in Figure 6.5, is likely to be more pronounced than for the saturated DMF-based perovskite solution which is used during solar cell fabrication. Nevertheless, even small pinholes and loss of continuity of the compact layer may influence the performance and reproducibility of the manufactured devices, and will increase the hysteretic behaviour in the current-voltage curves since it is known that hysteresis is extremely pronounced in devices devoid of a compact layer, where the perovskite makes direct contact to the transparent conducting FTO layer.[13]

In order to avoid this problem, devices in planar heterojunction architecture were constructed by depositing perovskite films with a 2-step vapour deposition method. A PbI_2 layer was thermally evaporated directly onto the n-type compact layer (C_{60} or TiO_2) and then converted into the perovskite structure *via* spin-coating methylammonium iodide (MAI) in an isopropanol solution,[23] which is a very poor solvent for the C_{60} layer. The details of the procedure are reported in Chapter 3. Photovoltaic performance (JV curves and steady-state measurements) of the champion devices are presented in Figure 6.4c-d and Table 6.2. By following the DMF-free route the solar cell performance was enhanced and the hysteresis in the JV curves yet further reduced, in conjunction with employing the fullerene compact layer. Notably, these cells are planar heterojunction devices in the n-i-p configuration, which usually exhibits much more enhanced hysteresis as compared to cells incorporating mesoporous scaffolds.[8,10,13] In strong

contrast, some C_{60}-based devices show negligible hysteretic behaviour over a broad range of voltage scanning rates (see Figure 6.6 and Table 6.3). Statistics of photocurrents and efficiencies extracted for a number of devices from maximum power point measurements are presented in Figure 6.7 and Table 6.4. Both architectures are shown, solution-processed meso-superstructured cells (a), and evaporated planar heterojunction devices (b).

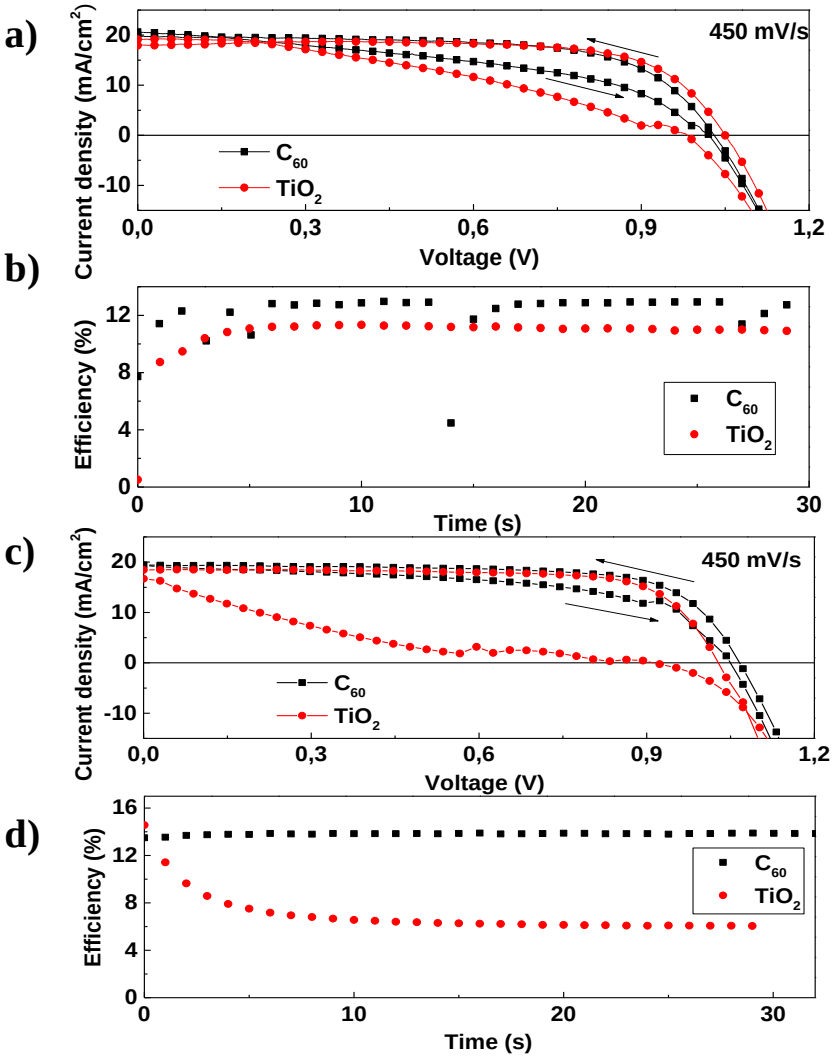


Figure 6.4. (a) JV curves of meso-superstructured perovskite solar cells (incorporating solution-processed $CH_3NH_3PbI_{3-x}Cl_x$) with a C_{60} (black curve with squares) and a TiO_2 (red curve with circles) compact layer, respectively, obtained at the scanning rate of 450 mV/s and **(b)** stabilized power output measured close to the maximum power point of the same cells. **(c)** JV curves of planar heterojunction perovskite solar cells (incorporating vapour-deposited PbI_2 with solution conversion to $MAPbI_3$) with C_{60} and TiO_2 layers, and **(d)** stabilized power output of the cells. Planar cells with perovskite deposited by sequential method were fabricated together with Svetlana Siprova at the Department of Physics, University of Oxford.

Table 6.2. Photovoltaic Parameters Extracted from JV Curves presented in Figure 6.4. Planar cells with perovskite deposited by sequential method were fabricated together with Svetlana Siprova at the Department of Physics, University of Oxford.

Compact layer		Meso-superstructured (450 mV/s)		Planar (450 mV/s)	
		SC->FB	FB->SC	SC->FB	FB->SC
C_{60}	J_{SC}	20.6	19.8	19.4	19.6
	V_{OC}	1.02	1.03	1.04	1.07
	FF	0.45	0.65	0.56	0.69
	PCE	9.5	13.5	11.4	14.5
	Stab. PCE	12.7		13.9	
TiO_2	J_{SC}	19.1	17.9	16.7	18.4
	V_{OC}	0.98	1.05	0.92	1.04
	FF	0.37	0.70	0.14	0.72
	PCE	7.1	13.9	2.1	13.6
	Stab. PCE	10.9		6.1	

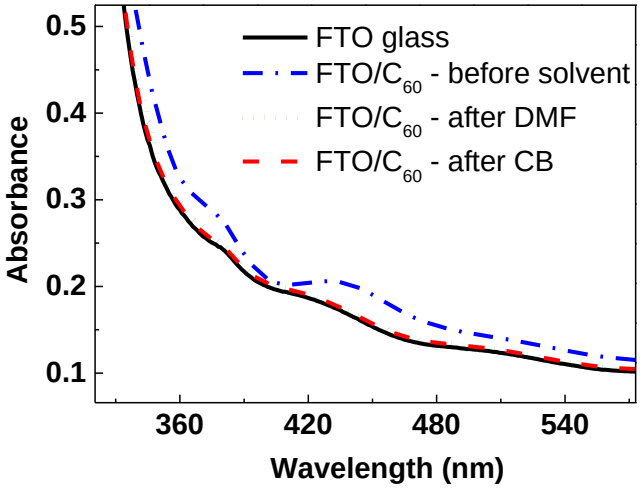


Figure 6.5. UV-Vis absorption spectra of FTO glass (black line), C_{60} film spin-coated on FTO glass (blue solid dash line), and C_{60} film after spin-coating dimethylformamide (green dotted line) and chlorobenzene (red dashed line) on top.

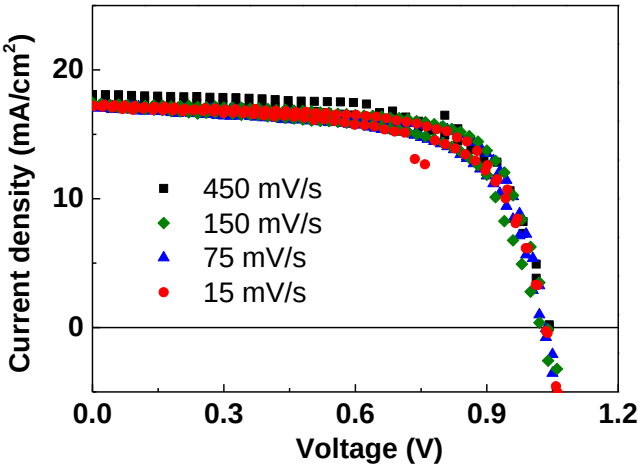
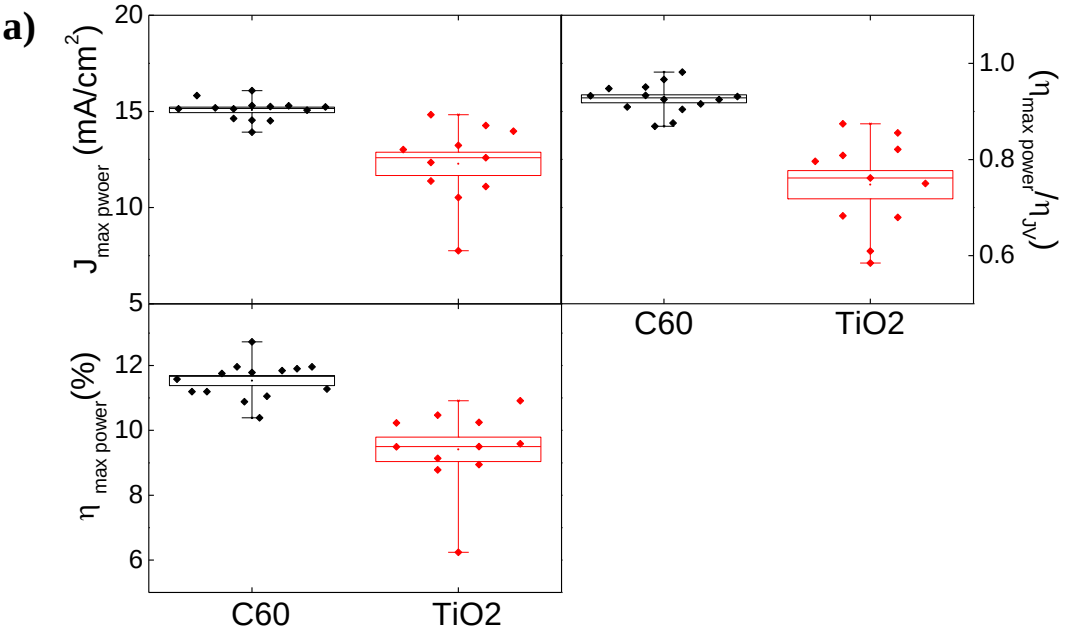


Figure 6.6. JV curves of planar heterojunction perovskite solar cell employing C_{60} compact layer, measured at different scanning rates and scanning directions. The cell was fabricated together with Svetlana Siprova at the Department of Physics, University of Oxford.

Table 6.3. Photovoltaic Parameters Extracted from JV Curves presented in Figure 6.6. The cell was fabricated together with Svetlana Siprova at the Department of Physics, University of Oxford.

Scanning rate	**450 mV/s**		**150 mV/s**		**75 mV/s**		**15 mV/s**	
Scanning direction	SC->FB	FB->SC	SC->FB	FB->SC	SC->FB	FB->SC	SC->FB	FB->SC
J_{SC}	17.9	18.1	17.3	17.5	17.1	17.1	17.2	17.3
V_{OC}	1.04	1.04	1.02	1.04	1.04	1.04	1.03	1.04
FF	0.65	0.70	0.65	0.70	0.64	0.71	0.65	0.70
PCE	12.2	13.4	11.6	12.9	11.5	12.7	11.7	12.6



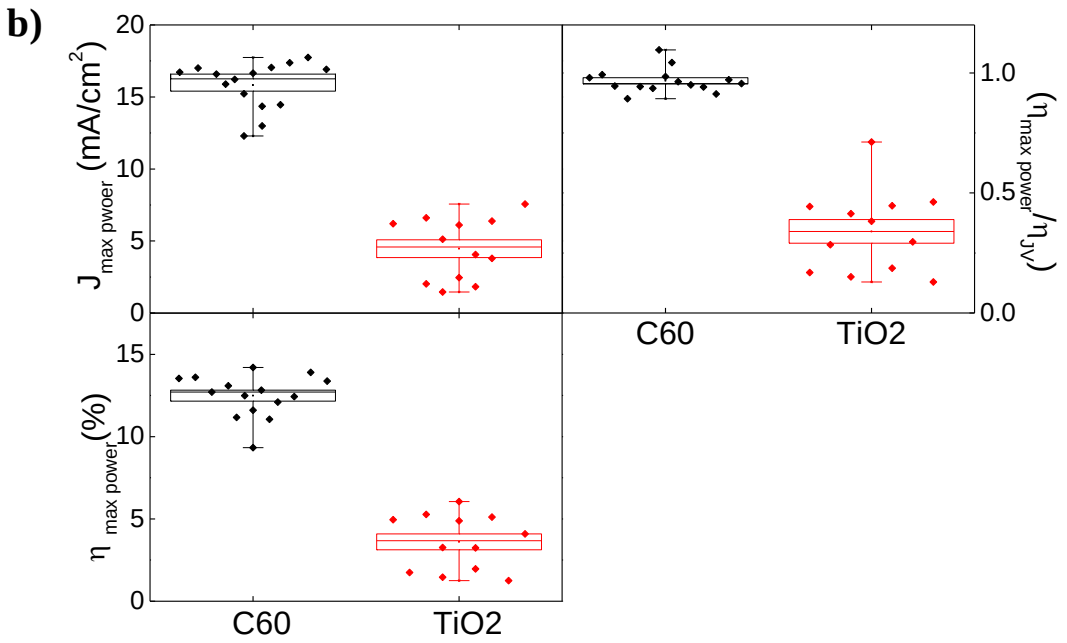


Figure 6.7. Statistics of photovoltaic parameters extracted from steady-state photocurrent measurements at maximum power point of **(a)** meso-superstructured perovskite solar cells (incorporating solution-processed $CH_3NH_3PbI_{3-x}Cl_x$) and **(b)** planar heterojunction perovskite solar cells (incorporating vapour-deposited PbI_2 with solution conversion to $MAPbI_3$): (i) left top panel: current density at maximum power point, (ii) left bottom panel: efficiency at maximum power point and (iii) right top panel: the ratio of efficiency at maximum power point to the efficiency from JV scan (scan direction: forward bias->short-circuit, scan rate: 0.45 V/s) for a series of devices with C_{60} and TiO_2 compact layer. Each point represents a single device. Planar cells with perovskite deposited by sequential method were fabricated together with Svetlana Siprova at the Department of Physics, University of Oxford.

Table 6.4. Statistics of photovoltaic parameters (with standard deviation) presented in Figure 6.7. Planar cells with perovskite deposited by sequential method were fabricated together with Svetlana Siprova at the Department of Physics, University of Oxford.

Compact layer		**Meso-superstructured**	**Planar**
C_{60}	No of devices	14	15
	$J_{MAX\ POWER}$	15.1 ± 0.5	15.8 ± 1.6
	$PCE_{MAX\ POWER}$	11.5 ± 0.6	12.5 ± 1.3
	$PCE_{MAX\ POWER}/PCE_{JV}$	0.93 ± 0.03	0.97 ± 0.05
TiO_2	No of devices	11	12
	$J_{MAX\ POWER}$	12.3 ± 2.0	4.5 ± 2.1
	$PCE_{MAX\ POWER}$	9.4 ± 1.2	3.6 ± 1.7
	$PCE_{MAX\ POWER}/PCE_{JV}$	0.75 ± 0.10	0.34 ± 0.17

6.3.3 Charge extraction study

Since the hysteresis in the J-V curves appears to be related to the electron extraction contact, the photoluminescence of the full devices at different conditions (short-circuit, forward bias, and reverse bias) was monitored in order to directly probe changes to the electron transfer efficiency. In Figure 6.7a-b the steady state photoluminescence measured in time (at the peak emission of 775 nm) of the full solar cells employing TiO_2 and C_{60} compact layers is presented. Here, the steady-state photoluminescence, generated by recombination of free carriers within the perovskite film, is representative of the density of carriers that have not recombined non-radiatively or have not been extracted from the device. Assuming the non-radiative pathways are not significantly varying for a given sample, higher photoluminescence indicates poorer charge extraction at particular conditions. Applying a forward bias to the cells resulted in an increase in the background emission, which was assigned to electroluminescence. Notably, the electroluminescence for the devices with the C_{60} compact layers was far higher than that with the TiO_2 compact layers at the same applied bias (see Figure 6.8c-d). Some early EL onset may be already observed at 0.9 V as increased and noisier signal level (Figure 6.8b). This suggests improved electronic coupling between the C_{60} and perovskite conduction band, and reduced non-radiative decay at this contact under forward bias conditions. This is consistent with reports from Bolink and co-workers of efficient electroluminescence of perovskite collar cells employing C_{60} based n-type layers.[24]

Most interestingly, it is found that when the applied bias is rapidly switched from forward bias back to short-circuit, the photoluminescence is temporarily strongly quenched as compared to the situation before any biasing. This effect occurs on timescales (seconds) similar to those characteristic of the hysteresis in the JV curves.[8] It also has a clear dependence on the magnitude of the applied bias, unlike what is expected from a ferroelectric type of

response.[25,26] To further probe this effect, time-resolved PL measurements on complete cells, before and immediately (within 3 seconds) after the application of 1 V forward bias (for 20 seconds), were carried out. The results are plotted in Figure 6.9, where much faster PL quenching directly after forward biasing can be observed. This is consistent with the postulation that electron transfer temporarily occurs much more effectively after the application of a forward bias. However, the behaviour for the TiO_2 and C_{60} based solar cells is qualitatively different, in that the extraction in the TiO_2 based solar cell before bias is much slower than that in the C_{60} based solar cell. As a result, the PL decay rate is only slightly increased for the C_{60} based device, but greatly increased for the TiO_2 one. It should be noted that the observed decay is a convolution of hole and electron extraction, so that the extraction of electrons at the TiO_2 interface, as represented by the PL decay in Figure 6.2, is actually much slower than that showed in Figure 6.9. After application of the electric field, the extraction rates for both samples appear to be very similar. Hence, it can be concluded that solar cells employing a TiO_2 compact layer suffer from poor electron extraction, which can be temporarily improved by the application of a forward bias. Applying a reverse bias before switching back to short-circuit was also investigated. The opposite effect was observed: reverse biasing temporarily slows the PL decay at short-circuit, which can be interpreted as worsening the charge extraction after reverse biasing (see Figures 6.8e-f). The timescale of PL recovery after biasing and short-circuiting the cell is very similar to the time of current rise in steady-state measurement or the rise of electroluminescence,[5] which suggests that it is governed by the same processes.

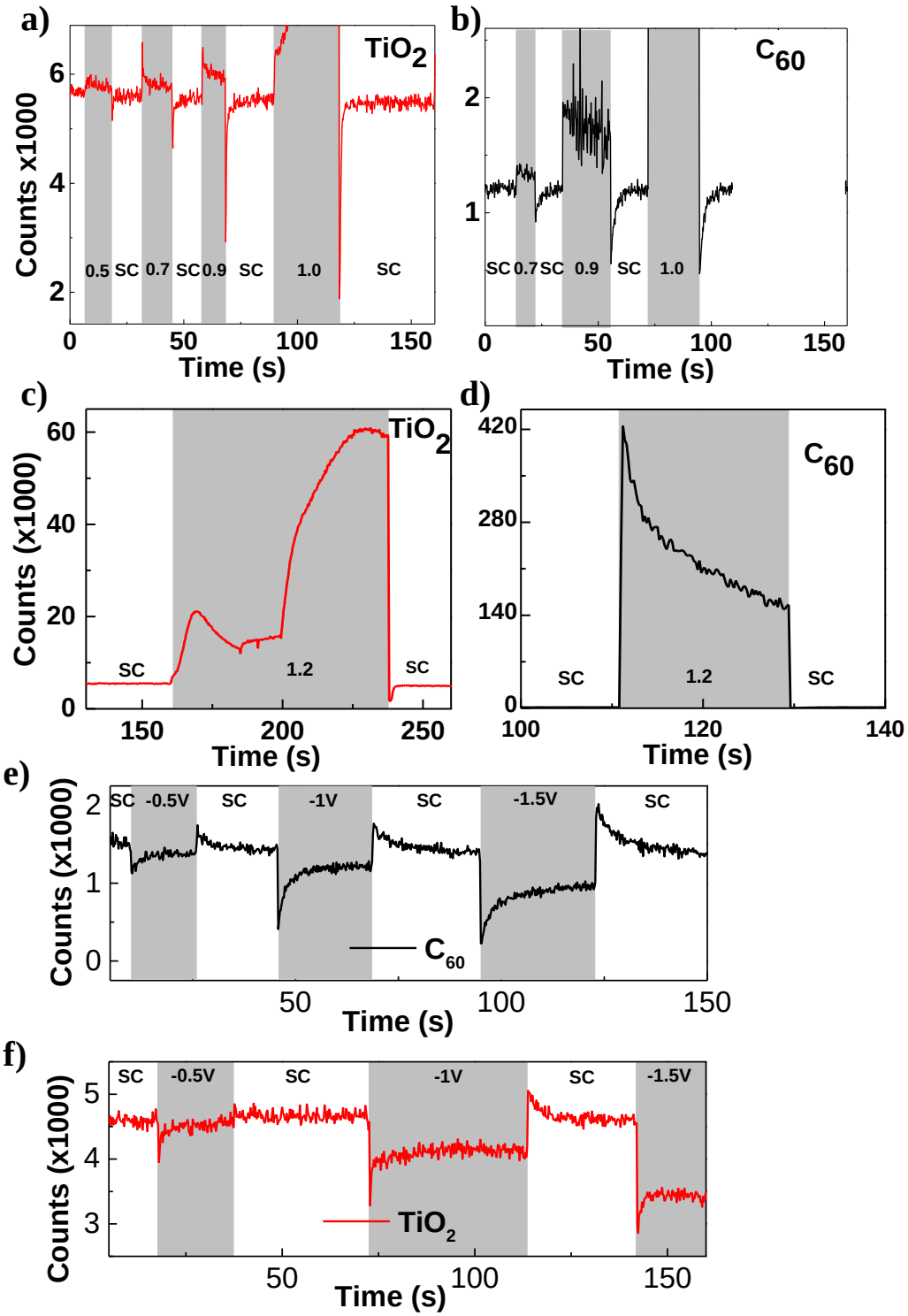


Figure 6.8. Steady state PL and EL monitored over time at the PL peak of 775 nm in working devices at short-circuit and various applied forward biases with **(a, c)** compact TiO_2 or **(b, d)** C_{60} acceptor layers; PL monitored at short-circuit and various reverse biases of the same devices, with **(e)** C_{60} and **(f)** TiO_2 compact layers. The measurements were performed by Tomas Leijtens at the Department of Physics, University of Oxford.

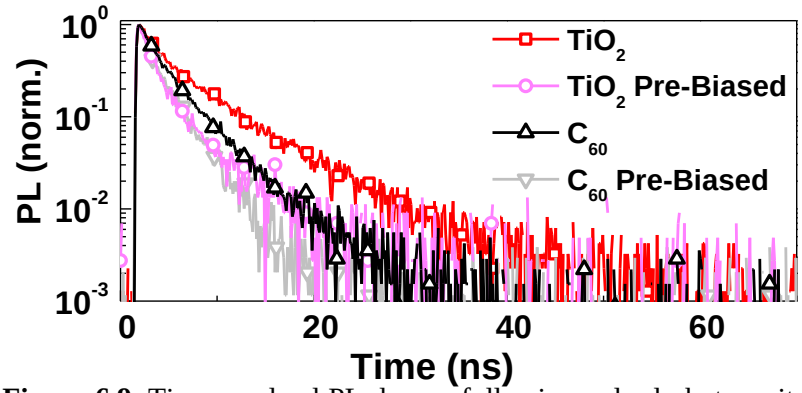


Figure 6.9. Time-resolved PL decays following pulsed photoexcitation (507 nm, 1 MHz, 0.03 μJ/cm^2/pulse) for the devices before and immediately (within 3 seconds) after the application of 1 V forward bias. The measurement was performed by Tomas Leijtens at the Department of Physics, University of Oxford.

6.3.3.1 Hysteresis mechanism

Recently Tress et al,[9] Xiao et al,[12] and Zhao at al[25] independently presented data consistent with ion migration in the perovskite material being the origin of hysteretic behaviour in current-voltage characterisation. Under forward bias, negatively charged mobile ions (ionic species) will migrate towards the p-type charge extraction layer, and mobile positive ions will migrate towards the n-type charge collection layer. Once the external field is removed (under working conditions) the displaced ions should be able to stabilise negative electronic space charge near the n-type collection layer and positive electronic space charge near the p-type collection layer, i.e. create n- and p-type doping in the perovskite layer in the regions adjacent to the appropriate charge collection layers. In reverse bias conditions, the external field will cause the ions to migrate in the opposite direction, resulting in unfavourable space charge distribution once the field is removed under working conditions (i.e. hole accumulation on the n-type collection side and electron accumulation on the p-type collection side). This is consistent with enhancing or inhibiting charge extraction dependent upon the pre-biasing history. Schematic representations of band bending induced in the perovskite layer by the displaced ions and external electric field have been recently proposed.[9,13,25] The concept of a

polarisable p-n or p-i-n junction solar cell was first proposed by Riess in 1987, for a semiconductor with both mobile charge and ionic species,[27] and this concept has since been applied to understand the operation of light emitting electrochemical cells.[28–31] It is likely that some adaptations of these theories are still required to properly explain the origin of hysteresis in perovskite solar cells.

Assuming this picture to be largely correct, the ion migration could in effect compensate for an imperfect electronic contact between the charge collection layers and the perovskite absorber. However, for low hysteresis and high stabilised power conversion efficiency, it is clearly of vital importance for there to be a good electronic contact between perovskite and charge extraction layers and to not rely on a temporarily improved contact enabled by ion migration. The data presented in Figures 6.2 and 6.9 suggests that charge transfer from perovskite into TiO_2 in planar heterojunction architecture does not occur efficiently, and hence the large hysteresis observed in JV curves in that system. In this work a direct observation of the "switching" on and off of charge extraction *via* the pre-biasing direction has been shown. Electron transfer to C_{60} occurs much more efficiently, so that the enhancements due to ion migration are only marginal, and notably under maximum power point conditions where electric field throughout the film should be low (close to flat band) the stabilised power output is high. Furthermore, the amount of interface recombination and defect density in the perovskite layer may be reduced when TiO_2 is replaced with C_{60}, as indicated by the differences in electroluminescence (Figure 6.8c-d), but further experiments are needed to draw final conclusions.

6.3.4 Stability measurements

It is still unknown which ionic species could undergo a displacement under the applied external electric field. They could include interstitial ions and halide vacancies, whose displacement could be on the order of tens of seconds.[25] Ionic motion in the material could have implications on the long-term stability of such devices, especially if the electric fields existing in the device during its operation could cause displacement of ions in the crystal lattice, which in time could result in material degradation due to regions of the film becoming increasingly non-stoichiometric.

In order to assess this possibility and compare the relative impact of TiO_2 versus C_{60} charge collection layers on device stability, aging tests were performed. Larger than normal devices were used (1 cm^2 active area, meso-superstructured architecture). Tests were carried out under simulated full spectrum AM1.5 illumination (generated from a Suntest CPS plus xenon lamp light soaking test chamber with no UV filter) at maximum power point, and 60 °C. It has been previously demonstrated that encapsulated solar cells based on mesoporous TiO_2 suffer from rapid degradation when aged under full solar irradiation, while meso-superstructured perovskite solar cells employing compact TiO_2 and mesoporous Al_2O_3 displayed greatly enhanced stability.[32] It should be noted that those results were obtained when aging the solar cells at open-circuit rather than under load near maximum power point, as would be the case in real operation conditions, and at a temperature lower than 40 °C. Aging the cells under a constant load gives an indication of the real stability of the solar cell's performance.

Photovoltaic parameters at maximum power point of 1 cm^2 encapsulated cells before aging, with TiO_2 and C_{60} n-type collection layers, are presented in Table 6.5. In Figure 6.10 the initial results of the stability study are presented. The changes of the photovoltaic parameters measured over the period of 500 hours of device operation at maximum power and elevated

temperature are plotted. JV curves were recorded every 65 minutes with the maximum power point voltage at which the cell is aged being reset to that determined from the latest scan. Following an initial rise, the devices based on TiO_2 compact layers exhibit a steady drop in the short-circuit photocurrent within the first 300 hours (ca. 50% of the initial value), whereas the fullerene-based cells preserved over 90% of the short-circuit photocurrent in the entire time window. For these stability experiments 4 or 5 devices of each configuration were tested and aging was carried out on the best cells. Although much more extensive stability testing is required to fully corroborate these results, this is an important demonstration suggesting that the fullerene-based stack can be fundamentally more stable than that incorporating compact TiO_2, and that the perovskite film does not lose the ability to generate photocurrent over this stressing period.

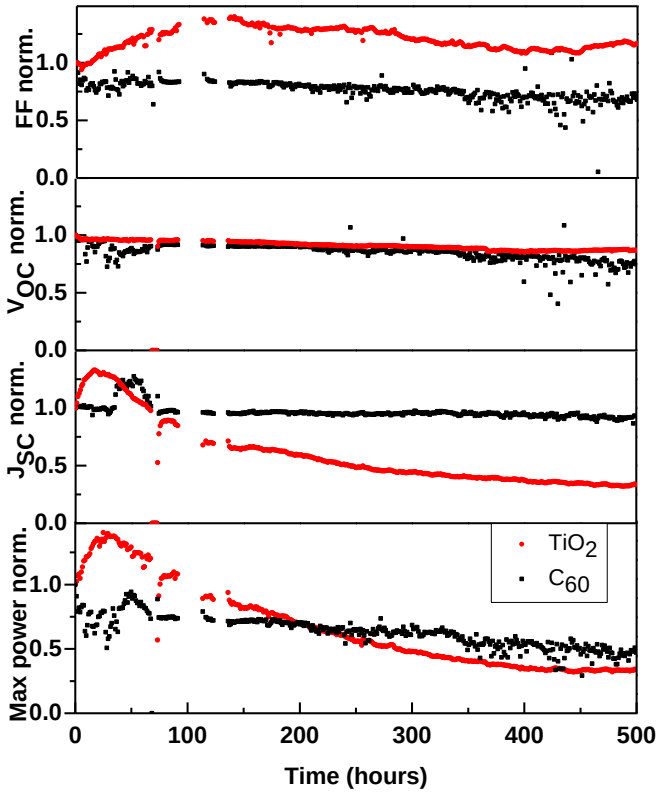


Figure 6.10. Evolution of normalized photovoltaic parameters extracted from JV curves measured every 65 minutes (from the top: fill factor, open circuit-voltage, short-circuit current), and efficiency at maximum power point (bottom panel) of the cells with C_{60} and TiO_2 compact layer kept under load for the period of 500 hours at 60 °C. Aging tests were performed at Oxford Photovoltaics Ltd.

Table 6.5. Stabilised photovoltaic parameters at maximum power point of the cells with 1cm^2 active area tested at 0.811 sun illumination, before 500 hours of stability testing, with C_{60} and TiO_2 compact layers. The measurements were performed at Oxford Photovoltaics Ltd.

Sample		Vmpp (V)	J stab. (mA/cm^2)	PCE stab. (%)
C_{60}	Before aging	0.73	11.5	10.4
TiO_2	Before aging	0.58	11.5	8.2

The mechanism of TiO_2 instability under UV light illumination, which is responsible for photocurrent degradation in the solar cells based on mesoporous TiO_2, has recently been discussed.[32,33] It has been postulated that upon TiO_2 excitation, the holes in valence band recombine with adsorbed molecular oxygen causing its desorption and leaving positively charged deep trap sites in the TiO_2 surface. High oxygen partial pressure reduces the rate of oxygen release, but in the case of encapsulated cells, which seems to be essential for long term protection of the perovskite from moisture, the activation of those trap sites can increase. These deep traps sites then act as sinks for electrons, with recombination of the trapped electrons occurring directly with the holes in the perovskite or hole transporter. Photocurrent degradation in TiO_2-based cells could be inhibited by application of UV-filters, but that would increase the cost of solar cell production, reduce photocurrent of the solar cell, and likely not be able to completely filter all of the absorption in the tail of the TiO_2 absorption band. The trends presented in Figure 6.10 for TiO_2-based cells are very similar to the ones reported previously for meso-TiO_2-based devices, when aged at open-circuit condition.[32] That might suggest that in both cases same processes govern the drop of performance in those devices. C_{60} seems to help overcoming the issue of UV instability, which is indicated by the preserved photocurrent density in the stressing period.

It should be noted that although the C_{60}-based device preserves the photocurrent very well, a decline in voltage and fill factor can be observed, which is responsible for the drop of overall

performance to ca. 55% of the initial value of max power. More investigations are required to explain with confidence the persistent drop in voltage and fill factor, but it is possible that imperfect layer formations and pin-holes are largely responsible. Furthermore, in these devices spiro-OMeTAD was employed as the hole conductor, which has been previously shown to be non-advantageous for enhancing the thermal stability of the perovskite.[34] Further improvements in stability can be expected by replacing this with more stable hole-conductors, such as carbon nanotubes embedded in an insulating polymer matrix.[34]

6.4 Conclusions

In summary, it has been shown that both solution and vapour deposited perovskite solar cells can be fabricated employing a fullerene compact layer as the bottom n-type charge extraction layer. Through spectroscopic characterisation a significant speeding up of the photoluminescence decay has been observed, which can be interpreted as an improvement in the electron extraction from the photoexcited perovskite to the C_{60}, as compared to the commonly employed TiO_2 compact layer. Notably, the luminescent measurements on complete devices showed for the first time direct observation of switching on and off of charge extraction depending upon the pre-biasing history. In addition to the devices displaying negligible hysteresis and high stabilised power conversion efficiency, stability data of the cells under operation and under full sunlight at 60 ^{0}C for 500 hours was demonstrated. Before the final conclusion of C_{60}-based cells being stable can be drawn, more tests need to be performed and the existing engineering issues get resolved, but the demonstrated stable photocurrent in presented initial aging tests, is a very encouraging observation, which points at differences in intrinsic characteristics between the employed organic and metal oxide materials. This work

reveals that organic semiconductors potentially may be ideal materials as both p- and n-type charge collection layers to achieve high stabilised power output and long term operational stability of perovskite solar cells.

In future work, an important aspect that still requires investigation is how the properties of the perovskite are influenced by the surface on which it crystallises. The morphology of the perovskite layer does not seem to change significantly when the TiO_2 substrate is replaced with the C_{60} layer, as judged from SEM images. Nevertheless, the density of defects in the perovskite layer might vary depending on the surface energy, chemical character or electronic nature of the material on which it is grown. A photoluminescence study cannot probe these effects when a charge extraction layer is in contact with the perovskite material, as the signal is typically quenched due to effective charge transfer. Determination of the electroluminescence quantum efficiency together with electroluminescence spatial mapping could deliver a quantitative investigation of the amount of interfacial non-radiative recombination in these devices, which in turn, could shed light on the density of electronic defects in the perovskite layer as a function of the material on which it is grown.

6.5 References

(1) Wojciechowski, K.; Saliba, M.; Leijtens, T.; Abate, A.; Snaith, H. J. Sub-150 °C Processed Meso-Superstructured Perovskite Solar Cells with Enhanced Efficiency. *Energy Environ. Sci.* **2014**, *7*, 1142.

(2) Liu, D.; Kelly, T. L. Perovskite Solar Cells with a Planar Heterojunction Structure Prepared Using Room-Temperature Solution Processing Techniques. *Nat. Photonics* **2014**, *8*, 133–138.

(3) Zhou, H.; Chen, Q.; Li, G.; Luo, S.; Song, T. -b.; Duan, H.-S.; Hong, Z.; You, J.; Liu, Y.; Yang, Y. Interface Engineering of Highly Efficient Perovskite Solar Cells. *Science* **2014**, *345*, 542–546.

(4) Noel, N. K.; Abate, A.; Stranks, S. D.; Parrott, E. S.; Burlakov, V. M.; Goriely, A.; Snaith, H. J. Enhanced Photoluminescence and Solar Cell Performance via Lewis Base Passivation of Organic-Inorganic Lead Halide Perovskites. *ACS Nano* **2014**, *8*, 9815–9821.

(5) Wojciechowski, K.; Stranks, S. D.; Abate, A.; Sadoughi, G.; Sadhanala, A.; Kopidakis, N.; Rumbles, G.; Li, C.; Friend, R. H.; Jen, A. K.; et al. Heterojunction Modification for Highly Efficient Organic-Inorganic Perovskite Solar Cells. *ACS Nano* **2014**, *8*, 12701–12709.

(6) Zhang, Q.; Park, K.; Xi, J.; Myers, D.; Cao, G. Recent Progress in Dye-Sensitized Solar Cells Using Nanocrystallite Aggregates. *Adv. Energy Mater.* **2011**, *1*, 988–1001.

(7) Shi, J.; Xu, X.; Li, D.; Meng, Q. Interfaces in Perovskite Solar Cells. *Small* **2015**, *11*, 2472–2486.

(8) Snaith, H. J.; Abate, A.; Ball, J. M.; Eperon, G. E.; Leijtens, T.; Noel, N. K.; Stranks, S. D.; Wang, J. T.; Wojciechowski, K.; Zhang, W. Anomalous Hysteresis in Perovskite Solar Cells. *J. Phys. Chem. Lett.* **2014**, *17*, 1511–1515.

(9) Tress, W.; Marinova, N.; Moehl, T.; Zakeeruddin, S. M.; Mohammad K., N.; Grätzel, M. Understanding the Rate-Dependent J-V Hysteresis, Slow Time Component, and Aging in $CH_3NH_3PbI_3$ Perovskite Solar Cells: The Role of a Compensated Electric Field. *Energy Environ. Sci.* **2015**, *8*, 995–1004.

(10) Unger, E. L.; Hoke, E. T.; Bailie, C. D.; Nguyen, W. H.; Bowring, A. R.; Heumuller, T.; Christoforo, M. G.; McGehee, M. D. Hysteresis and Transient Behavior in Current-Voltage Measurements of Hybrid-Perovskite Absorber Solar Cells. *Energy Environ. Sci.* **2014**, *7*, 3690–3698.

(11) Liu, S.; Zheng, F.; Koocher, N. Z.; Takenaka, H.; Wang, F.; Rappe, A. M. Ferroelectric Domain Wall Induced Band-Gap Reduction and Charge Separation in Organometal Halide Perovskites. *J. Phys. Chem. Lett.* **2015**, *6*, 693–699.

(12) Xiao, Z.; Yuan, Y.; Shao, Y.; Wang, Q.; Dong, Q.; Bi, C.; Sharma, P.; Gruverman, A.; Huang, J. Giant Switchable Photovoltaic Effect in Organometal Trihalide Perovskite Devices. *Nat. Mater.* **2014**, *14*, 193–198.

(13) Zhang, Y.; Liu, M.; Eperon, G. E.; Leijtens, T.; McMeekin, D. P.; Saliba, M.; Zhang, W.; De Bastiani, M.; Petrozza, A.; Herz, L.; et al. Charge Selective Contacts, Mobile Ions and Anomalous Hysteresis in Organic-Inorganic Perovskite Solar Cells. *Mater. Horiz.* **2015**, *2*, 315–322.

(14) Abrusci, A.; Stranks, S. D.; Docampo, P.; Yip, H.-L.; Jen, A. K.-Y.; Snaith, H. J. High Performance Perovskite-Polymer Hybrid Solar Cells via Electronic Coupling with Fullerene Monolayers. *Nano Lett.* **2013**, *13*, 3124–3128.

(15) Kraut, E.; Grant, R.; Waldrop, J.; Kowalczyk, S. Precise Determination of the Valence-Band Edge in X-Ray Photoemission Spectra: Application to Measurement of Semiconductor Interface Potentials. *Phys. Rev. Lett.* **1980**, *44*, 1620–1623.

(16) Leijtens, T.; Stranks, S. D.; Eperon, G. E.; Lindblad, R.; Johansson, E. M. J.; McPherson, I. J.; Rensmo, H.; Ball, J. M.; Lee, M. M.; Snaith, H. J. Electronic Properties of Meso-Superstructured and Planar Organometal Halide Perovskite Films: Charge Trapping, Photodoping, and Carrier Mobility. *ACS Nano* **2014**, *8*, 7147–7155.

(17) Edri, E.; Kirmayer, S.; Mukhopadhyay, S.; Gartsman, K.; Hodes, G.; Cahen, D. Elucidating the Charge Carrier Separation and Working Mechanism of $CH_3NH_3PbI_{3-x}Cl_x$ Perovskite Solar Cells. *Nat. Commun.* **2014**, *5*, 1–8.

(18) Lindblad, R.; Bi, D.; Park, B.; Oscarsson, J.; Gorgoi, M.; Siegbahn, H.; Odelius, M.; Johansson, E. M. J.; Rensmo, H. Electronic Structure of TiO_2 /$CH_3NH_3PbI_3$ Perovskite Solar Cell Interfaces. *J. Phys. Chem. Lett.* **2014**, *5*, 648–653.

(19) Schulz, P.; Edri, E.; Kirmayer, S.; Hodes, G.; Cahen, D.; Kahn, A. Interface Energetics in Organo-Metal Halide Perovskite-Based Photovoltaic Cells. *Energy Environ. Sci.* **2014**, *7*, 1377–1384.

(20) Miller, E. M.; Zhao, Y.; Mercado, C.; Saha, S.; Luther, J. M.; Zhu, K.; Stevanovic, V.; Perkins, C. L.; van de Lagemaat, J. Substrate-Controlled Band Positions in $CH_3NH_3PbI_3$ Perovskite Films. *Phys. Chem. Chem. Phys.* **2014**, *16*, 22122–22130.

(21) Lee, M. M.; Teuscher, J.; Miyasaka, T.; Murakami, T. N.; Henry, J. Efficient Hybrid Solar Cells Based on Meso-Superstructured Organometal Halide Perovskites. *Science* **2012**, *338*, 643–647.

(22) Ball, J. M.; Lee, M. M.; Hey, A.; Snaith, H. J. Low-Temperature Processed Meso-Superstructured To Thin-Film Perovskite Solar Cells. *Energy Environ. Sci.* **2013**, *6*, 1739.

(23) Xiao, Z.; Bi, C.; Shao, Y.; Dong, Q.; Wang, Q.; Yuan, Y.; Wang, C.; Gao, Y.; Huang, J. Efficient, High Yield Perovskite Photovoltaic Devices Grown by Interdiffusion of Solution-Processed Precursor Stacking Layers. *Energy Environ. Sci.* **2014**, *7*, 2619–2623.

(24) Schmidt, L. C.; Pertegás, A.; Gonzalez-carrero, S.; Malinkiewicz, O.; Agouram, S.; Espallargas, G. M.; Bolink, H. J.; Galian, R. E.; Pérez-prieto, J.; González-carrero, S. Non-Template Synthesis of $CH_3NH_3PbBr_3$ Perovskite Nanoparticles. *J. Am. Chem. Soc.* **2014**, *136*, 850−853.

(25) Zhao, Y.; Liang, C.; Zhang, H. M.; Li, D.; Tian, D.; Li, G.; Jing, X.; Zhang, W.; Xiao, W.; Liu, Q.; et al. Anomalously Large Interface Charge in Polarity-Switchable Photovoltaic Devices: An Indication of Mobile Ions in Organic-Inorganic Halide Perovskites. *Energy Environ. Sci.* **2015**, *8*, 1256–1260.

(26) Merz, W. J. Switching Time in Ferroelectric $BaTiO_3$ and Its Dependence on Crystal Thickness. *J. Appl. Phys.* **1956**, *27*, 938.

(27) Riess, I. Voltage-Controlled Structure of Certain P-N and P-I-N Junctions. *Phys. Rev. B* **1987**, *35*, 5740.

(28) Riess, I.; Cahen, D.; Introduction, I. Analysis of Light Emitting Polymer Electrochemical Cells. *J. Appl. Phys.* **1997**, *82*, 3147–3151.

(29) Pei, Q.; Yu, G.; Zhang, C.; Yang, Y.; Heeger, A. J. Polymer Light-Emitting Electrochemical Cells. *Science* **1995**, *269*, 1086–1088.

(30) Pei, Q.; Yang, Y.; Yu, G.; Zhang, C.; Heeger, A. J. Polymer Light-Emitting Electrochemical Cells : In Situ Formation of a Light-Emitting P - N Junction. *J. Am. Chem. Soc.* **1996**, *118*, 3922–3929.

(31) Edman, L. Bringing Light to Solid-State Electrolytes: The Polymer Light-Emitting Electrochemical Cell. *Electrochim. Acta* **2005**, *50*, 3878–3885.

(32) Leijtens, T.; Eperon, G. E.; Pathak, S.; Abate, A.; Lee, M. M.; Snaith, H. J. Overcoming Ultraviolet Light Instability of Sensitized TiO_2 with Meso-Superstructured Organometal Tri-Halide Perovskite Solar Cells. *Nat. Commun.* **2013**, *4*, 2885.

(33) Pathak, S. K.; Abate, A.; Ruckdeschel, P.; Roose, B.; Gödel, K. C.; Vaynzof, Y.; Santhala, A.; Watanabe, S.-I.; Hollman, D. J.; Noel, N.; et al. Performance and Stability Enhancement of Dye-Sensitized and Perovskite Solar Cells by Al Doping of TiO_2. *Adv. Funct. Mater.* **2014**, *24*, 6046–6055.

(34) Habisreutinger, S. N.; Leijtens, T.; Eperon, G. E.; Stranks, S. D.; Nicholas, R. J.; Snaith, H. J. Carbon Nanotube/Polymer Composites as a Highly Stable Hole Collection Layer in Perovskite Solar Cells. *Nano Lett.* **2014**, *14*, 5561–5568.

Chapter 7

Cross-linkable Fullerene Derivatives for Solution-processed n–i-p Perovskite Solar Cells

7.1 Context

Hybrid halide perovskites constitute a very attractive class of materials for many optoelectronic applications, including solar cells, light emitting diodes, lasers and photodetectors.[1–8] Photovoltaic devices based on these materials recorded unprecedented rise of power conversion efficiencies (PCEs), reaching 21 % of certified value.[9]

One of the keys in pushing the photovoltaic performance of perovskite cells closer to the radiative limit is 'switching off' the non-radiative recombination.[10,11] Large part of these losses originate at the interfaces with charge selective materials, due to interface trap states or non-ideal electronic contacts, which can affect charge collection efficiency and increase the recombination.[12,13]

Furthermore, hybrid perovskites display mixed ionic-electronic conductive properties.[14] This has several implications on the device operation and can be linked with a hysteresis phenomenon, which has been discussed in Chapter 6.

7.2 Introduction

The quality of the electronic contact between the perovskite layer and charge selective material has a major influence on the magnitude of the hysteretic behaviour. In the previous chapters it has been shown that TiO_2, commonly used for electron collection in n-i-p planar heterojunction architectures, does not provide good charge extraction properties.[15] In Chapter 5 it has been demonstrated that appropriate interface engineering of the n-type contact can dramatically improve the device operation and reduce the hysteresis effect. Fullerene-based molecules significantly facilitate the electron transfer from the perovskite material.[12,15–17]

Furthermore, in Chapter 6 it has been shown that solution-processed fullerene can also provide good hole blocking properties, and act as an effective electron selective layer in n-i-p architecture, eliminating the need of using metal oxides.[18,19] Nevertheless, the solubility of fullerene material in organic solvents, such as DMF and chlorobenzene, which are commonly used for processing the device stack, limits the versatility of processing routes and possible architectures. Dissolution of the blocking layer creates shunting paths and gives raise to the hysteresis.[19]

Chemical modification, which can trigger bonding of the individual molecules or polymer units, is often applied to increase material's mechanical and thermal stability, as well as its solvent resistance. The process is termed chemical crosslinking.

In this chapter, two cross-linkable fullerene derivatives are reported as robust n-type contacts for use with solution-processed perovskite films. Both molecules are practically insoluble in the relevant solvents after crosslinking reaction, which results in a significantly reduced shunting paths and improved hole-blocking properties. This, combined with the efficient electron extraction from the perovskite material, leads to enhanced steady-state power conversion efficiency. Furthermore, the fullerene-FTO contact has been investigated, and non-ideal operation at this interface is identified, which contributes to the hysteretic behaviour of the cells. Finally, stability data of perovskite solar cells, employing fullerene-based compact layers and aged under operational conditions, has been collected. Initial dataset of 200 hours of aging shows promising stability for the cells with crosslinked organic contact. Some cells preserve around 80% of the initial performance in the measured time window.

7.3 Results and discussion

7.3.1 Properties of cross-linkable fullerene derivatives

The first crosslinking approach involves a fulleropyrrolidine derivative containing triethoxysilane moiety (N-[3-(Triethoxysilyl)propyl]-2-carbomethoxy-3,4-fulleropyrrolidine), termed sol-gel C_{60} (chemical structure is shown in Figure 7.1a). The molecule was developed by Bianco *et al*. for molecular recognition application.[20] Sol-gel C_{60} films were deposited by spin-coating from the solution in 1,2-dichlorobenzene. The experimental details are given in Chapter 3. Material's crosslinking is realized by its exposure to trifluoroacetic acid (TFA) vapour. The hydrolysis-condensation reactions occur, the ethoxy groups of the sol-gel C_{60} are eliminated while Si-O-Si bonds appear. The transformation can be monitored in the sol-gel C_{60} FTIR spectrum (Figure 7.2), from the band intensity of the asymmetric ($\nu_{as}CH_3$) and symmetric (ν_sCH_3) stretching vibrations of the CH_3, at 2973 and 2882 cm^{-1}, respectively. In the sol-gel C_{60}/TFA spectrum these bands completely disappear which is significant of the hydrolysis of the Si-OEt bonds. Similarly, formation of the Si-O-Si network can be followed by the decrease of the band intensity of the asymmetric (ν_{as}Si-O-Et, 1103 cm^{-1}) and symmetric (ν_sSi-O-Et, 1078 cm^{-1}) stretching vibrations of the Si-OEt bond, the decrease of the band intensity of the asymmetric (ν_{as}C-OSi, 1170 cm^{-1}) and symmetric (ν_aC-OSi, 955 cm^{-1}) stretching vibrations of the CH_3CH_2C-OSi bond, and the appearance of the broad band from 980 to 1255 cm^{-1} corresponding to the asymmetric and symmetric stretching vibrations of various Si-O-Si bonds of the silicate network. After TFA vapour exposure, absorption bands corresponding to the acid can be observed in the sol-gel C_{60}/TFA spectrum, with the vibration of the carbonyl (νC=O, 1784 cm^{-1}), C-O (1210 cm^{-1}), and C-F (1175 cm^{-1}) functions. Accordingly, residual Si-OH functions (νSiO-H, around 3400 cm^{-1}, Figure 7.1b) can be monitored, indicating the level of

completion of the condensation process. The removal of the TFA traces and complete condensation is achieved after 30 minutes of thermal annealing at 130 °C in a nitrogen-filled glovebox. This is confirmed by the disappearance of the vibrations corresponding to the TFA (νC=O, νC-O, νC-F), and the one corresponding to the silanol (νSiO-H) in the sol-gel C_{60}/TFA/130°C spectrum.

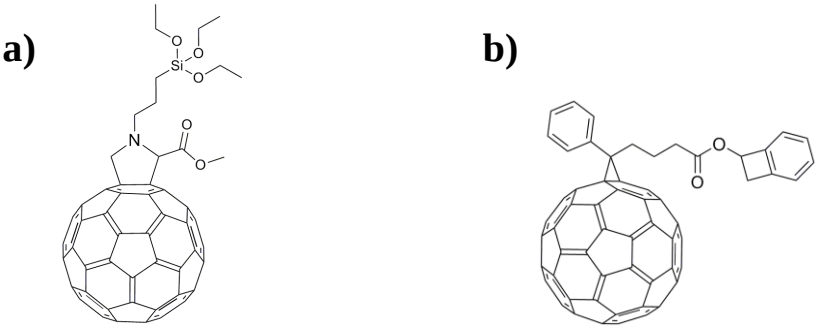


Figure 7.1. Chemical structure of **(a)** the sol-gel C_{60} molecule, and **(b)** PCBCB.

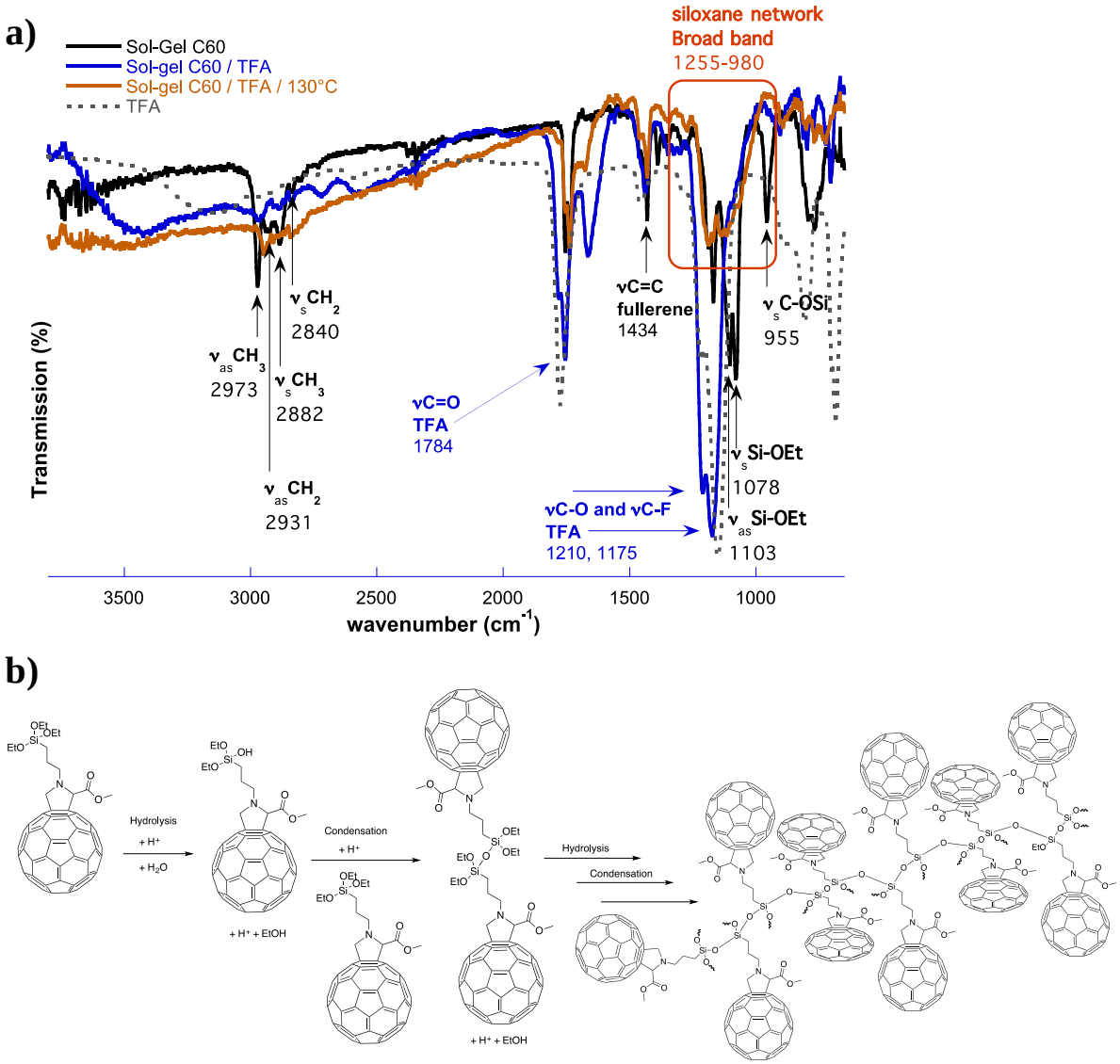


Figure 7.2. (a) FT-IR spectrum of a spin-coated thin film of sol-gel C_{60} on a silicon wafer from a chlorobenzene solution, before exposure to TFA vapour (black curve), after exposure to TFA vapour (blue curve), and after exposure to TFA vapour followed by a thermal annealing at 130°C (red curve). The grey dashed curve is corresponding to the FT-IR spectrum of pure TFA; **(b)** schematic of a hybrid network generated by the acid-catalysed hydrolysis and polycondensation of the sol-gel C_{60}. The measurements were taken and analysed by Olivier Dautel at the AM2N Laboratory, Charles Gerhardt Institute, France.

The second crosslinking approach investigated in this chapter employs a PCBM derivative with a benzocyclobutene group (PCBCB). Chemical structure of the molecule is shown in Figure 7.1b. The crosslinking undergoes via thermally activated benzocyclobutene moiety, and

involves annealing at 200 °C for 10 minutes. The detailed mechanism has been recently described by Deb *et al.*[21]

Fullerene derivatives tend to aggregate over time in a solution, but at the concentration range used in this chapter (2-6 mg/ml) the solutions are stable at least for a period of few weeks. Substrate cleaning plays a crucial role in achieving uniform and smooth films. Piranha etching was used to oxidize organic residues present on the FTO surface. Clean surface improves the wetting properties, which results in a compact film with a very few aggregates. Uniform layers of the sol-gel C_{60} were produced from the solutions of the concentration as low as 2 mg/ml, which yields the film thickness below 10 nm. Scanning electron microscopy (SEM) images of the spin-coated and crosslinked films are presented in Figure 7.3.

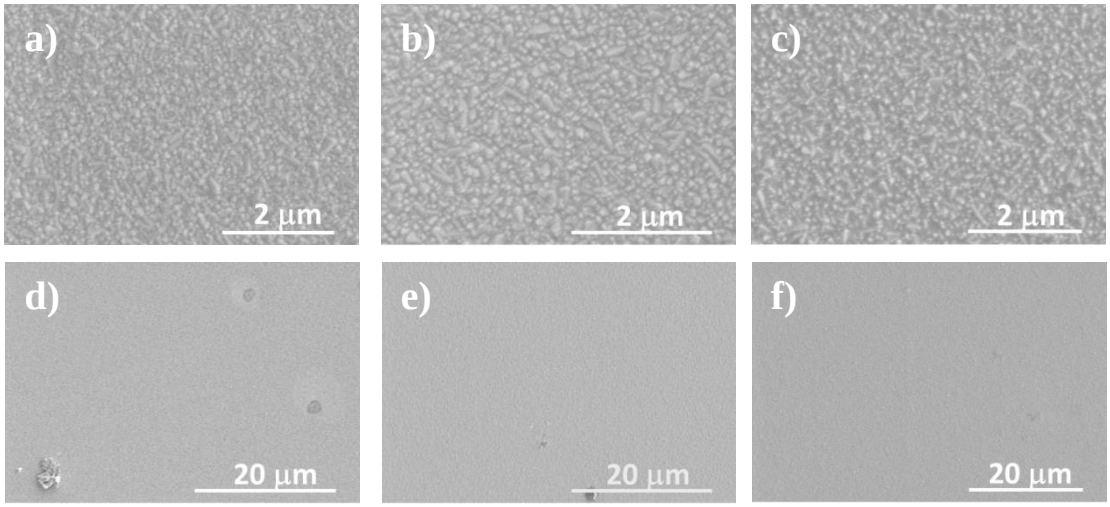


Figure 7.3. SEM images of **(a,d)** sol-gel C_{60}, **(b,e)** PCBCB, and **(c,f)** C_{60} films, processed on FTO glass.

In order to investigate the effectiveness of the crosslinking reaction and how resistant the films are to the organic solvents, UV-Vis absorption spectra of the crosslinked layers, before and after solvent treatment, were measured. The spectra shown in Figure 7.4 indicate that both crosslinked fullerenes are very resistant to DMF. Chlorobenzene washing caused very minor drop in absorption for the PCBCB sample.

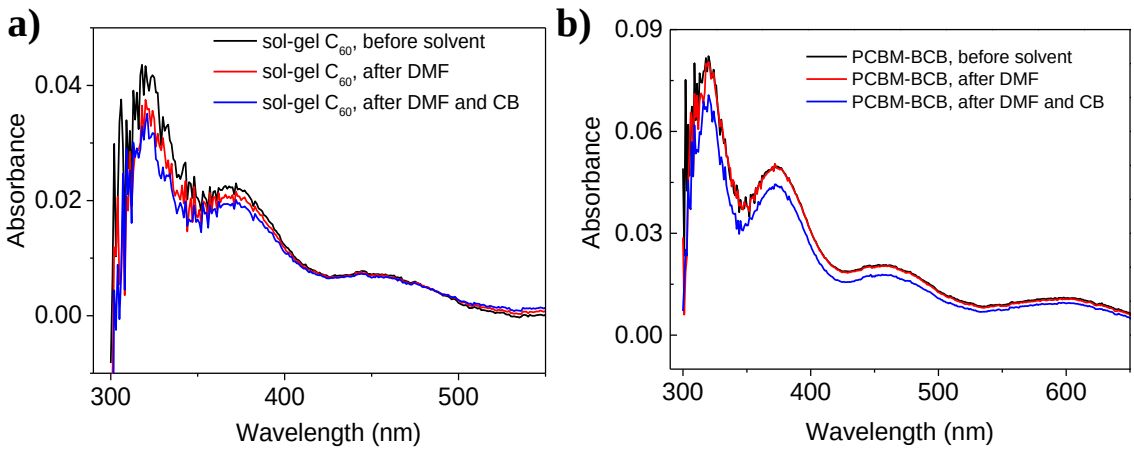


Figure 7.4. UV-Vis absorption spectra of **(a)** crosslinked sol-gel C_{60} spin-coated on FTO glass, before solvent treatment (black line), after spin-coating DMF (red line), and after subsequent spin-coating chlorobenzene (blue line); **(b)** crosslinked PCBCB processed on FTO glass, before solvent treatment (black line), after DMF (red line), and after chlorobenzene (blue line). Absorption spectrum of a reference FTO glass was subtracted from all the above spectra.

The electron mobility values of the PCBCB, determined from the space-charge limited current (SCLC) measurements, before and after crosslinking, were reported by Deb et al.[21] After PCBCB polymerisation, the mobility substantially increases, exceeding the value of the reference PCBM (see Table 7.1). Electrical properties of the sol-gel C_{60} films were characterised by fabricating organic field-effect transistors (OFETs), and compared with the reference employing PCBM layer (experimental details of OFET fabrication are given in Chapter 3). Extracted mobility values are shown in Table 7.1. Sol-gel C_{60} film displays an order of magnitude lower electron mobility than PCBM, and it further drops after crosslinking reaction.

Table 7.1. Electron mobilities of the fullerene derivatives, determined from SCLC measurements (PCBCB, literature values), and OFETs (sol-gel C_{60}). The transistors were fabricated and measured by Therese Gorisse at the Bordeaux Institute of Technology (IMS), France.

Molecule		Mobility, μ_e ($cm^2V^{-1}s^{-1}$), OFET	Mobility, μ_e ($cm^2V^{-1}s^{-1}$), SCLC[21]
PCBM-BCB	before crosslinking	-	$1.3\pm0.3 \times 10^{-4}$
	after crosslinking	-	$5.9\pm1.8 \times 10^{-3}$
sol-gel C_{60}	before crosslinking	$1.0\pm0.1 \times 10^{-3}$	-
	after crosslinking	$7.8\pm0.1 \times 10^{-5}$	-
PCBM		$1.1\pm0.1 \times 10^{-2}$	$9.1\pm1.0 \times 10^{-4}$

7.3.2 Electron extraction with crosslinked fullerenes

In order to assess the efficacy of electron transfer from perovskite into different fullerenes, time-resolved photoluminescence measurements were performed. PL transients of $MAPbI_{3-x}Cl_x$ films processed on glass, and glass coated with different electron accepting layers (TiO_2, C_{60}, and both crosslinked fullerenes) were measured. The PL decays of all the samples are presented in Figure 7.5. Similarly to the quenching data reported in the previous chapters and other reports,[22,23] perovskite PL lifetimes are significantly shorter for the samples with fullerene-based contact than the one with TiO_2 layer. Fast PL decay indicates good electronic contact with the perovskite material, and efficient charge transfer across the interface. It should be noted that cross-linked PCBCB is not as fast as cross-linked sol-gel C_{60}, or plain C_{60}. It may suggest worse electronic coupling and slower charge extraction rate for this sample.

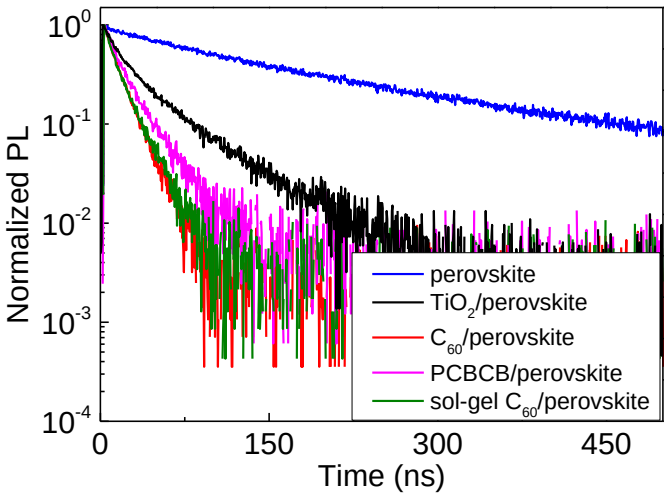


Figure 7.5. Normalized photoluminescence decays following pulsed excitation (507 nm, 1 MHz, 0.03 μJ/cm2/pulse) of perovskite both, with and without electron quenching layers.

7.3.3 Photovoltaic performance

Perovskite photovoltaic devices have been fabricated in a planar heterojunction architecture, applying crosslinked fullerenes as an electron selective contact. As a reference, the cells with solution-processed C_{60} have also been made. SEM images of perovskite films grown on different n-type materials are shown in Figure 7.6.

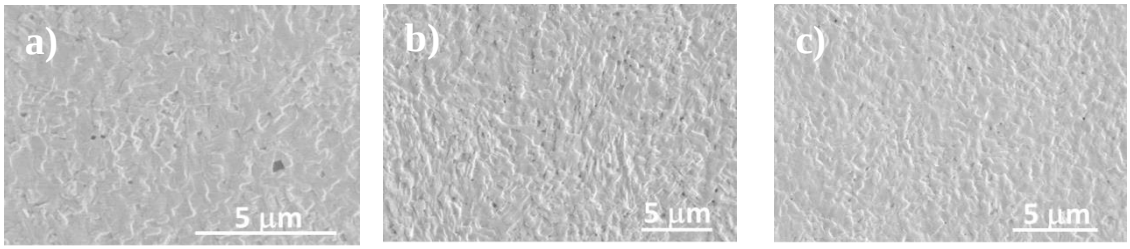


Figure 7.6. SEM images of perovskite films grown on **(a)** sol-gel C_{60}, **(b)** PCBCB, and **(c)** C_{60} layer.

Current density-voltage curves and stabilised power output (SPO) of the champion devices for each n-type contact are shown in Figure 7.7a-b. In this graph only one scan direction is shown. Photovoltaic parameters extracted from these JV curves are presented in Table 7.2. Both fullerene derivatives delivered nearly 18% of power conversion efficiency (PCE) for the best cells, when scanned from forward bias to short-circuit (scanning rate: 0.15 V/s). Steady-state power conversion efficiency measured at close to maximum power point yielded 16.6% and 15.2% for sol-gel C_{60} and PCBCB, respectively. The best reference device, employing solution-processed C_{60} compact layer, delivered PCE of 14.7% at the JV scan, and 13.9% at the stabilised measurement. The statistics of photovoltaic parameters derived from JV curves and SPO measurements for a large number of cells employing each compact layer are presented in Figure 7.7c-d and Table 7.3. Crosslinked fullerenes exhibit a significant improvement in all photovoltaic parameters compared to the plain C_{60}. The most noticeable difference is enhancement in V_{OC} and J_{SC}, which can be related to the reduced shunting paths and improved

hole blocking properties (no dissolution of the fullerene layer, as it has been discussed in Chapter 6). Due to low electron mobility in the crosslinked sol-gel C_{60} (significantly lower than in PCBM, see Table 7.1), the layers should be very thin to not introduce resistive losses. The films for the optimal PV performance were processed from the solution of 2 mg/ml (spinning rate: 2000 rpm), which yielded a thickness of sub 10 nm. Crosslinked PCBCB exhibits significantly higher electron mobility,[21] the optimal solution concentration was 5 mg/ml (spinning rate: 2000 rpm), resulting in a film thickness of ca. 15 nm. It should be noted that sol-gel C_{60} delivers higher SPO values and better PCE_{stab}/PCE_{JV} ratio than PCBCB, which indicates more pronounced hysteresis for the second n-type material.

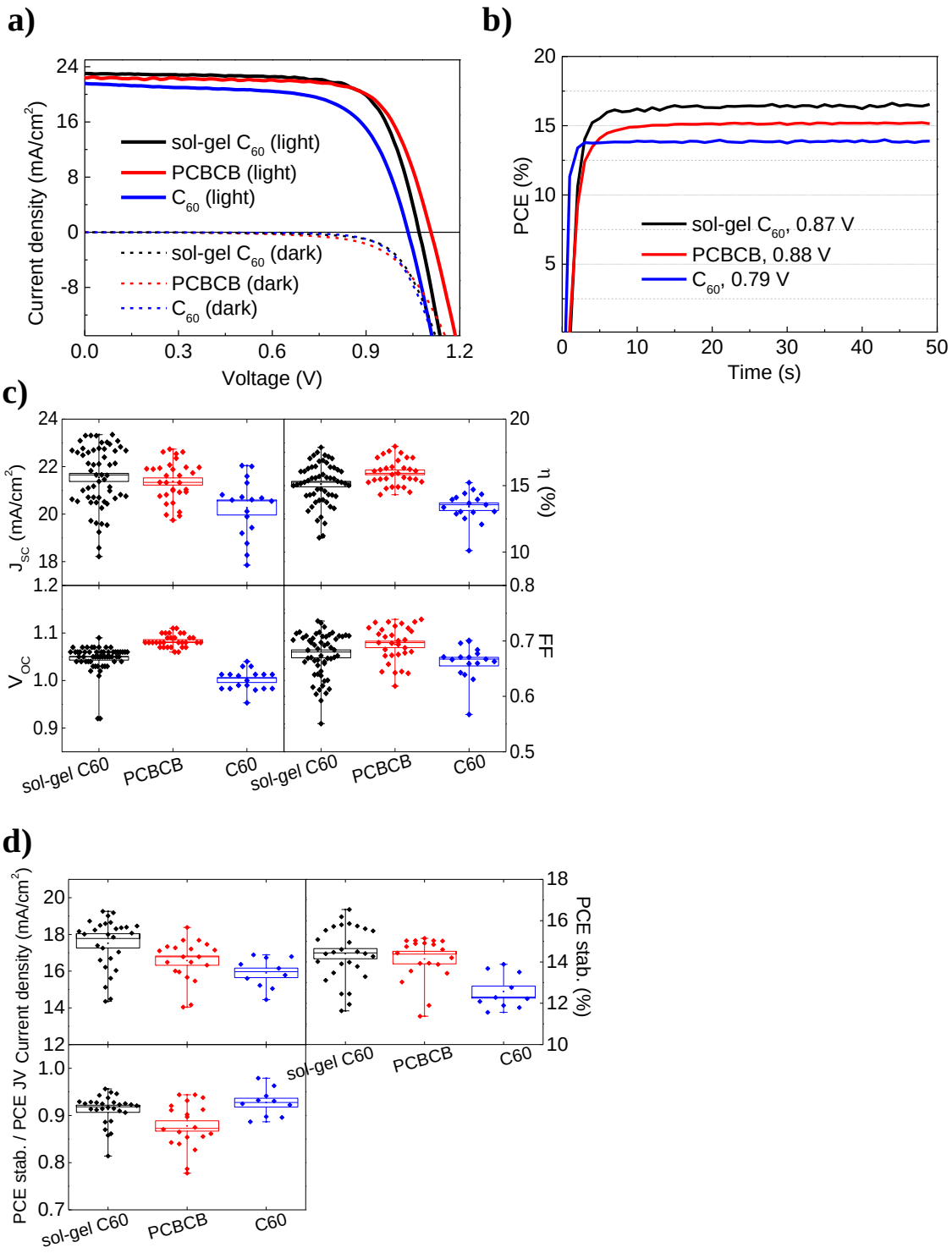


Figure 7.7. (a) Current density – voltage curves (FB-SC scan direction, 0.15 V/s) of the best devices employing different compact layers; **(b)** Stabilised power output of the same devices; statistics of **(c)** the JV curves (FB-SC scan direction, 0.15 V/s) and **(d)** SPO measurements for a larger set of devices. Each dot represents a single device.

Table 7.2. Photovoltaic Parameters Extracted from JV Curves presented in Figure 7.6a-b.

Compact layer	FB-SC scan, 0.15 V/s				Stabilised		
	J_{SC} (mA/cm^2)	V_{OC} (V)	FF	PCE (%)	J_{stab} (mA/cm^2)	PCE_{stab} (%)	PCE_{stab}/PCE_{JV}
sol-gel C_{60}	23.0	1.07	0.73	17.9	19.0	16.6	0.93
PCBCB	22.4	1.11	0.73	17.9	17.2	15.2	0.85
C_{60}	21.6	1.03	0.67	14.7	16.7	13.9	0.95

Table 7.3. Statistics of photovoltaic parameters (with standard deviation) presented in Figure 7.6c-d.

n-type layer	FB-SC scan, 0.15 V/s					Stabilised			
	No.	J_{SC} (mA/cm^2)	V_{OC} (V)	FF	PCE (%)	No.	J_{stab} (mA/cm^2)	PCE_{stab} (%)	PCE_{stab}/PCE_{JV}
sol-gel C_{60}	57	21.5±1.3	1.05± 0.03	0.67± 0.04	15.1±1.6	28	17.5±1.4	14.4±1.3	0.91±0.03
PCBCB	31	21.4±0.8	1.08± 0.01	0.69± 0.03	16.0±1.0	20	16.6±1.1	14.2±1.1	0.88±0.05
C_{60}	17	20.3±1.2	1.00± 0.02	0.67± 0.04	13.4±1.2	10	15.9±0.8	12.6±0.8	0.91±0.06

7.3.4 Hysteresis consideration

Fabricated perovskite devices employing crosslinked fullerenes still exhibit differences between steady-state and JV-derived PCE, and hysteresis in current-voltage curves. The magnitude of the hysteresis varies between different cells. Examples of the current-voltage characteristics changing with the scanning rate and scanning direction, and corresponding SPO of the three separate devices (two employing crosslinked sol-gel C_{60}, one crosslinked PCBCB) are shown in Figure 7.8a-c, extracted photovoltaic parameters are presented in Table 7.4. At the faster scanning rate (0.15 V/s), when applied voltage is swept from short-circuit to forward bias, most of the JV curves display a characteristic ‘kink’ at the high voltage region, before the open-circuit, which may suggests contact resistance problems.

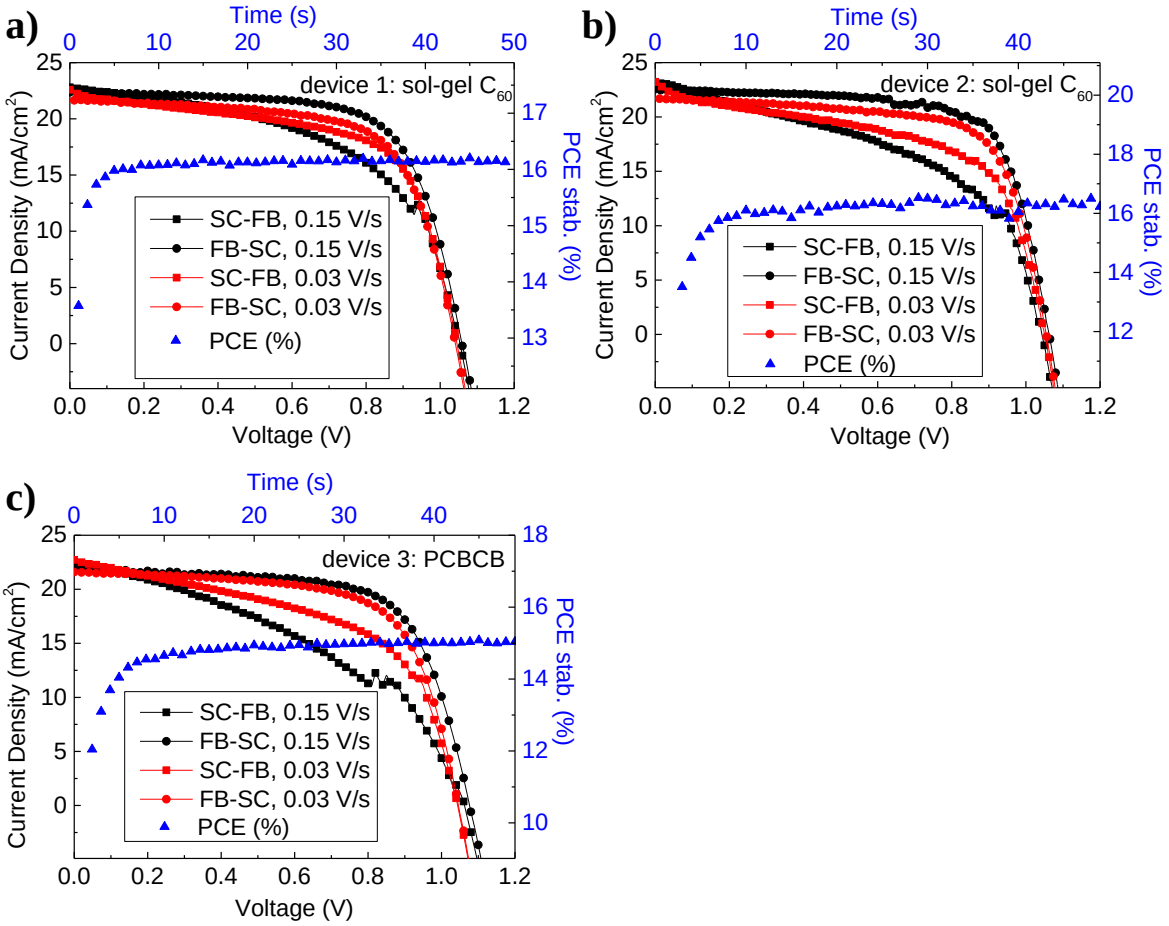


Figure 7.8. Current density-voltage curves of three separate devices, employing **(a-b)** crosslinked sol-gel C_{60}, and **(c)** crosslinked PCBCB, scanned at both directions with the rate of 0.15 V/s and 0.03 V/s.

Table 7.4. Photovoltaic Parameters Extracted from JV Curves presented in Figure 7.8.

Device	SC-FB scan, 0.15 V/s				Stabilised		
	J_{SC} (mA/cm^2)	V_{OC} (V)	FF	PCE (%)	J_{stab} (mA/cm^2)	PCE_{stab} (%)	$PCE_{stab}/PCE_{bes\ t\ JV}$
sol-gel C_{60} – 1	22.8	1.05	0.54	12.8	19.4	16.1	1.00
sol-gel C_{60} – 2	23.2	1.05	0.48	11.6	18.4	16.2	0.95
PCBCB	22.2	1.06	0.44	10.2	17.7	15.0	0.94
	FB-SC scan, 0.15 V/s						
sol-gel C_{60} – 1	22.4	1.06	0.69	16.1			
sol-gel C_{60} – 2	22.6	1.07	0.72	17.1			
PCBCB	21.9	1.08	0.68	15.9			
	SC-FB scan, 0.03 V/s						
sol-gel C_{60} – 1	22.6	1.05	0.62	14.5			
sol-gel C_{60} – 2	23.2	1.05	0.57	13.7			
PCBCB	22.7	1.04	0.54	12.5			
	FB-SC scan, 0.03 V/s						
sol-gel C_{60} – 1	21.7	1.04	0.67	15.1			
sol-gel C_{60} – 2	21.7	1.05	0.70	15.8			
PCBCB	21.6	1.05	0.67	14.9			

The contact between an inorganic bottom electrode and organic n-type semiconductor has been shown that in some cases can be a limiting factor for the photovoltaic performance of the organic solar cells.[24,25] Polyethylenimine, ethoxylated (PEIE) has been reported as an effective interface modifier.[18,26] It lowers the work function (WF) of the transparent electrode (FTO or ITO), which improves the electronic contact, making it more suitable for the electron collection. The change of the work function upon the treatment has been assigned to a creation of the interface dipole.[26]

PEIE treatment (aqueous solution of 0.4 wt% processed by spin-coating) was applied to reduce the contact losses originating at the FTO/fullerene interface. JV curves (both scan directions) of perovskite solar cells employing crosslinked sol-gel C_{60} compact layer (processed from the solution of 6 mg/ml), spin-coated on modified and unmodified FTO, are shown in Figure 7.9a (photovoltaic parameters are listed in Table 7.5). Significant reduction in the hysteretic behaviour can be observed, as well as enhanced steady-state power output. Statistics of the photovoltaic parameters of the devices with and without the treatment are shown in Figure 7.9b-c and Table 7.6. A clear improvement in fill factor (for the SC-FB scans) and open-circuit voltage is shown. This is an important finding suggesting that part of the hysteresis and some PV performance losses can also come from the contribution of non-perovskite interfaces.

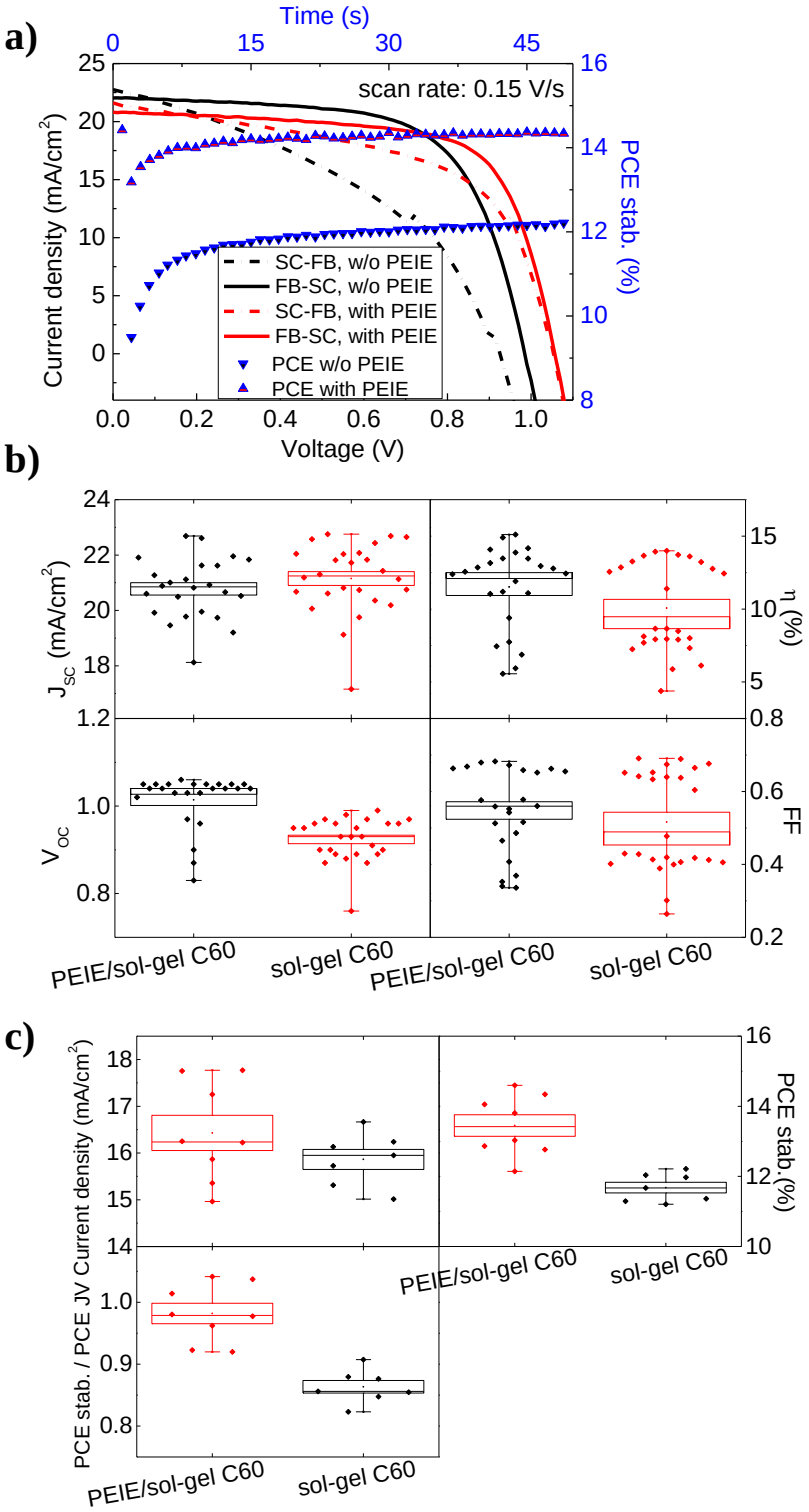


Figure 7.9. (a) JV curves (both scan directions, 0.15 V/s) and SPO measurements of the perovskite devices employing crosslinked sol-gel C_{60}, with PEIE-modified and unmodified FTO; statistics of **(b)** the JV curves (both scan directions, 0.15 V/s), and **(c)** SPO measurements for a series of devices, with and without PEIE modification. Each dot represents a single device.

Table 7.5. Photovoltaic Parameters Extracted from JV Curves and SPO measurements presented in Figure 7.9a.

Device	SC-FB scan, 0.15 V/s				Stabilised		
	J_{SC} (mA/cm^2)	V_{OC} (V)	FF	PCE (%)	J_{stab} (mA/cm^2)	PCE_{stab} (%)	$PCE_{stab}/PCE_{best\ JV}$
w/o PEIE	22.8	0.93	0.41	8.7	16.2	12.2	0.88
with PEIE	21.6	1.05	0.56	12.6	17.3	14.3	0.96
	FB-SC scan, 0.15 V/s						
w/o PEIE	22.0	0.98	0.65	13.9			
with PEIE	20.8	1.06	0.68	14.9			

Table 7.6. Statistics of photovoltaic parameters (with standard deviation) presented in Figure 7.9b-c.

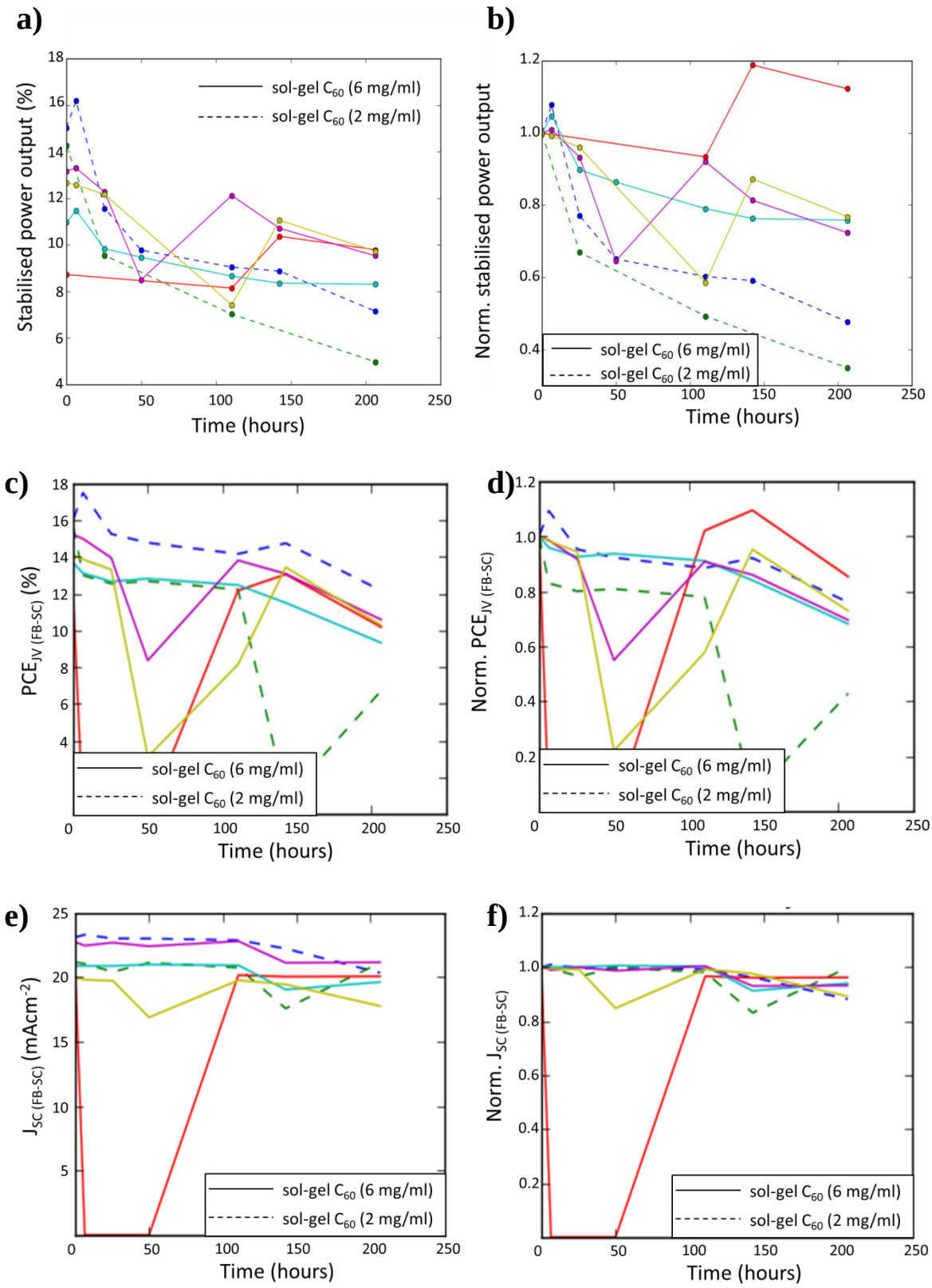
n-type layer	SC-FB and FB-SC scan, 0.15 V/s					Stabilised			
	No.	J_{SC} (mA/cm^2)	V_{OC} (V)	FF	PCE (%)	No.	J_{stab} (mA/cm^2)	PCE_{stab} (%)	PCE_{stab}/PCE_{JV}
w/o PEIE	26	21.2±1.3	0.92± 0.05	0.52± 0.14	10.1±3.1	7	15.9±0.6	11.7±0.4	0.86±0.03
with PEIE	24	20.8±1.1	1.01± 0.06	0.55± 0.12	11.5±2.8	8	16.4±1.1	13.5±0.9	0.98±0.05

7.3.5 Stability measurements

Stability of the perovskite solar cells remains a significant hurdle and one of the main challenges to overcome for the commercial viability of the technology. Many hybrid organic-inorganic perovskites suffer from the structural and thermal instability and have poor resilience to the atmospheric stress, especially moisture.[27] The stability data presented in Chapter 6 indicates that the quality of the electronic contact at the interfaces with the perovskite material significantly affects long-term performance of a device. It also highlights the importance of performing ageing tests under operational conditions. Leijtens *et al*. recently reported that at an ambient atmosphere, with a presence of moisture, perovskite material undergoes irreversible degradation when an electric field exists in the film (operational conditions).[28] The degradation process occurs within few hours and it has been linked to the field-induced drift of the organic cation, which is weakly bound to the PbI_6^{4-} octahedra in the case of hydrated perovskite phase (presence of moisture). Therefore, inert atmosphere is essential for providing structural stability of the perovskite material under operational conditions.

Improved morphology and solvent resistance of the cross-linkable fullerenes (over solution-processed plain C_{60}) can potentially lead to enhanced long-term stability. In this chapter, initial dataset of 200 hours of aging of the cells with crosslinked sol-gel C_{60} (two different thicknesses) is presented. The measurements were carried out under inert atmosphere (nitrogen flowing through the sealed box), and at controlled temperatures (below 60 °C). Constant AMG1.5 illumination and fixed voltage (0.7 V, close to maximum power point) was applied during the entire stressing period. The aging was interrupted to test the photovoltaic performance (measured in air) after every 20-40 hours. The evolution of photovoltaic parameters for a series of devices is shown in Figure 7.10i-j.

The electronic contact between the perovskite and n-type layer 'wears off' under prolonged device operation, which is evidenced by the faster drop of SPO than JV-derived efficiency (hysteresis increases). The thinner sol-gel C_{60} layer (processed from the solution of 2 mg/ml), which delivers the highest photovoltaic performance (see Figure 7.7), exhibits considerably lower stability than thicker films (processed from the solution of 6 mg/ml). One of the possible explanations could be a loss of uniformity and worsening of hole-blocking properties for the thinner films due to long-term operation, which results in an increase of shunting paths. Some devices fabricated with thicker crosslinked sol-gel C_{60} exhibit very promising stability, preserving even 80% of the initial performance after 200 hours of aging. Nevertheless, the data suggests that more focus needs to be put on the interfaces and the quality of the electronic contacts under prolonged stress conditions in order to realise fully stable perovskite devices. Presented aging data should be complemented with stressing at the open-circuit conditions, which would give better understanding of different influences on the degradation processes.


a)
Stabilised power output (%)
Time (hours)
sol-gel C60 (6 mg/ml)
sol-gel C60 (2 mg/ml)
b)
Norm. stabilised power output
Time (hours)
sol-gel C60 (6 mg/ml)
sol-gel C60 (2 mg/ml)
c)
PCEJV (FB-SC) (%)
Time (hours)
sol-gel C60 (6 mg/ml)
sol-gel C60 (2 mg/ml)
d)
Norm. PCEJV (FB-SC)
Time (hours)
sol-gel C60 (6 mg/ml)
sol-gel C60 (2 mg/ml)
e)
JSC (FB-SC) (mAcm-2)
Time (hours)
sol-gel C60 (6 mg/ml)
sol-gel C60 (2 mg/ml)
f)
Norm. JSC (FB-SC)
Time (hours)
sol-gel C60 (6 mg/ml)
sol-gel C60 (2 mg/ml)

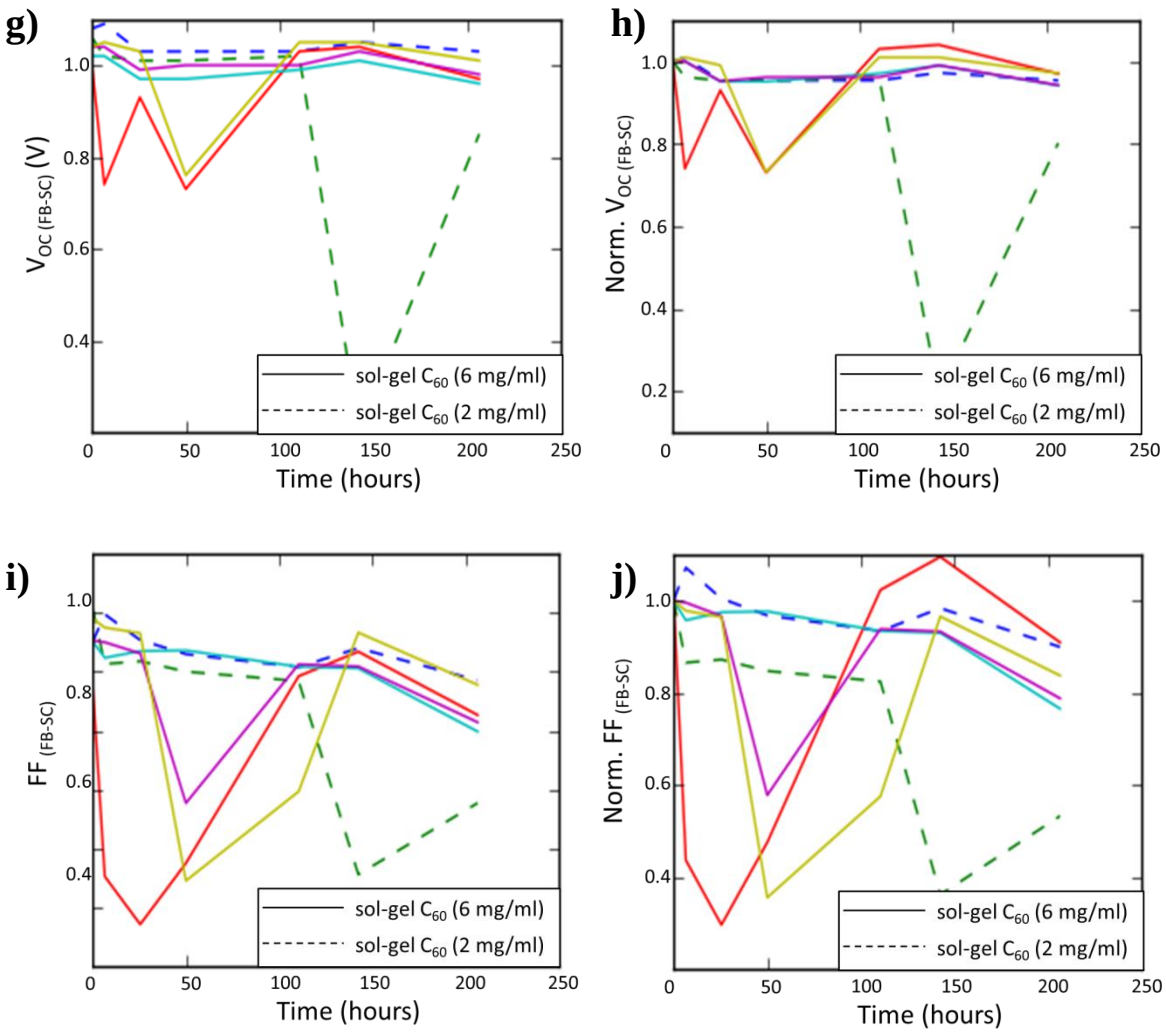


Figure 7.10. Evolution of photovoltaic parameters with aging time: **(a)** SPO, **(b)** normalised SPO, **(c)** PCE_{JV} (FB-SC scan), **(d)** normalised PCE_{JV}, **(e)** J_{SC} (FB-SC scan), **(f)** normalised J_{SC}, **(g)** V_{OC} (FB-SC scan), **(h)** normalised V_{OC}, **(i)** fill factor (FB-SC scan) and **(j)** normalised fill factor. Dashed line represents solar cells with thinner sol-gel C_{60} film (processed from the solution of 2 mg/ml), devices with thicker fullerene film (processed from the solution of 6 mg/ml) are marked with continuous line. The abrupt drop of photovoltaic performance at some points was caused by worn out contact between the pins of the solar simulator setup and evaporated gold. The metal was re-evaporated to fix this problem. Stability measurements were done together with Ivan Ramirez at the Department of Physics, University of Oxford.

7.4 Conclusions

In conclusion, highly efficient planar heterojunction perovskite solar cells with cross-linked fullerene derivatives as an electron selective contact have been fabricated. The crosslinking reaction has been monitored with spectroscopic tools. Polymerised films are resistant to organic solvents used in processing perovskite and HTM layers (DMF and chlorobenzene), which allows fabrication of solution-processed devices with largely reduced shunting paths. Compared to the cells employing plain C_{60} compact layer, all photovoltaic parameters were improved, most notably an open-circuit voltage and stabilised power output.

Furthermore, limitations to the device operation originating at the FTO/fullerene contact have been identified. Modification of the FTO work function with PEIE provides better electronic contact with an n-type material, which results in a significant enhancement of the SPO and further reduction of the hysteretic effects in fabricated cells.

Initial stability data of the devices employing crosslinked fullerene and aged under operating conditions was collected. The evolution of photovoltaic parameters upon prolonged device operation suggests detrimental changes occurring at the charge selective interfaces. The degradation process happened significantly faster for the devices with thinner crosslinked fullerene layer, where even small morphological changes are likely to affect the coverage and hole-blocking properties at that contact. The cells with thicker compact layer display very promising stability within the first 200 hours. These measurements indicate the importance of performing stressing tests under real working conditions.

7.5 References

(1) Lee, M. M.; Teuscher, J.; Miyasaka, T.; Murakami, T. N.; Henry, J. Efficient Hybrid Solar Cells Based on Meso-Superstructured Organometal Halide Perovskites. *Science* **2012**, *338*, 643–647.

(2) Tan, Z.-K.; Moghaddam, R. S.; Lai, M. L.; Docampo, P.; Higler, R.; Deschler, F.; Price, M.; Sadhanala, A.; Pazos, L. M.; Credgington, D.; et al. Bright Light-Emitting Diodes Based on Organometal Halide Perovskite. *Nat. Nanotechnol.* **2014**, *9*, 687–692.

(3) Cho, H.; Jeong, S.; Park, M.; Kim, Y.; Wolf, C.; Lee, C.; Heo, J. H.; Sadhanala, A.; Myoung, N.; Yoo, S.; et al. Overcoming the Electroluminescence Efficiency Limitations of Perovskite Light-Emitting Diodes. *Science* **2015**, *350* (6265), 1222–1226.

(4) Zhu, H.; Fu, Y.; Meng, F.; Wu, X.; Gong, Z.; Ding, Q.; Gustafsson, M. V; Trinh, M. T.; Jin, S.; Zhu, X.-Y. Lead Halide Perovskite Nanowire Lasers with Low Lasing Thresholds and High Quality Factors. *Nat. Mater.* **2015**, *14*, 636–642.

(5) Deschler, F.; Price, M.; Pathak, S.; Klintberg, L. E.; Jarausch, D.; Higler, R.; Hu, S.; Leijtens, T.; Stranks, S. D.; Snaith, H. J.; et al. High Photoluminescence Efficiency and Optically Pumped Lasing in Solution-Processed Mixed Halide Perovskite Semiconductors. *J. Phys. Chem. Lett.* **2014**, *5*, 1421–1426.

(6) Fu, Y.; Zhu, H.; Schrader, A.; Liang, D.; Ding, Q.; Joshi, P.; Hwang, L.; Zhu, X.-Y.; Jin, S. Nanowire Lasers of Formamidinium Lead Halide Perovskites and Their Stabilized Alloys with Improved Stability. *Nano Lett.* **2016**, *16*, 1000–1008.

(7) Lin, Q.; Armin, A.; Burn, P. L.; Meredith, P. Filterless Narrowband Visible Photodetectors. *Nat. Photonics* **2015**, *9*, 687.

(8) Fang, Y.; Dong, Q.; Shao, Y.; Yuan, Y.; Huang, J. Highly Narrowband Perovskite Single-Crystal Photodetectors Enabled by Surface-Charge Recombination. *Nat. Photonics* **2015**, *9*, 679.

(9) NREL. http://www.nrel.gov/ncpv/images/efficiency_chart.jpg.

(10) Yao, J.; Kirchartz, T.; Vezie, M. S.; Faist, M. a.; Gong, W.; He, Z.; Wu, H.; Troughton, J.; Watson, T.; Bryant, D.; et al. Quantifying Losses in Open-Circuit Voltage in Solution-Processable Solar Cells. *Phys. Rev. Appl.* **2015**, *4*, 014020.

(11) Miller, O. D.; Yablonovitch, E.; Kurtz, S. R. Strong Internal and External Luminescence as Solar Cells Approach the Shockley–Queisser Limit. *IEEE J. Photovoltaics* **2012**, *2*, 303–311.

(12) Shi, J.; Xu, X.; Li, D.; Meng, Q. Interfaces in Perovskite Solar Cells. *Small* **2015**, *11*, 2472–2486.

(13) Wojciechowski, K.; Stranks, S. D.; Abate, A.; Sadoughi, G.; Sadhanala, A.; Kopidakis, N.; Rumbles, G.; Li, C.; Friend, R. H.; Jen, A. K.; et al. Heterojunction Modification for Highly Efficient Organic-Inorganic Perovskite Solar Cells. *ACS Nano* **2014**, *8*, 12701–12709.

(14) Eames, C.; Frost, J. M.; Barnes, P. R. F.; O'Regan, B. C.; Walsh, A.; Islam, M. S. Ionic Transport in Hybrid Lead Iodide Perovskite Solar Cells. *Nat. Commun.* **2015**, *6*, 7497.

(15) Wojciechowski, K.; Stranks, S. D.; Abate, A.; Sadoughi, G.; Sadhanala, A.; Kopidakis, N.; Rumbles, G.; Li, C.; Friend, R. H.; Jen, A. K.; et al. Heterojunction Modification for Highly Efficient Organic-Inorganic Perovskite Solar Cells. *ACS Nano* **2014**, *8*, 12701–12709.

(16) Tao, C.; Neutzner, S.; Colella, L.; Marras, S.; Ram, A.; Kandada, S.; Gandini, M.; Bastiani, M. De. 17.6% Stabilized Efficiency in Low-Temperature Processed Planar Perovskite Solar Cells. *Energy Environ. Sci.* **2015**, *8*, 2365–2370.

(17) Chueh, C.-C.; Li, C.-Z.; Jen, A. K.-Y. Recent Progress and Perspective in Solution-Processed Interfacial Materials for Efficient and Stable Polymer and Organometal Perovskite Solar Cells. *Energy Environ. Sci.* **2015**, *8*, 1160–1189.

(18) Ryu, S.; Seo, J. W.; Shin, S. S.; Kim, Y. C.; Jeon, N. J.; Noh, J. H.; Seok, S. Il. Fabrication of Metal-Oxide-Free $CH_3NH_3PbI_3$ Perovskite Solar Cells Processed at Low Temperature. *J. Mater. Chem. A* **2015**, *3*, 3271–3275.

(19) Wojciechowski, K.; Leijtens, T.; Siprova, S.; Schlueter, C.; Hörantner, M. T.; Wang, J. T.-W.; Li, C.-Z.; Jen, A. K.-Y.; Lee, T.-L.; Snaith, H. J. C_{60} as an Efficient N-Type Compact Layer in Perovskite Solar Cells. *J. Phys. Chem. Lett.* **2015**, *6*, 2399−2405.

(20) Bianco, A.; Gasparrini, F.; Maggini, M.; Misiti, D.; Polese, A.; Prato, M.; Scorrano, G.; Toniolo, C.; Villani, C. Molecular Recognition by a Silica-Bound Fullerene Derivative. *J. Am. Chem. Soc.* **1997**, *119*, 7550–7554.

(21) Deb, N.; Dasari, R. R.; Moudgil, K.; Hernandez, J. L.; Marder, S. R.; Sun, Y.; Karim, A.; Bucknall, D. G. Thermo-Cross-Linkable Fullerene for Long-Term Stability of Photovoltaic Devices. *J. Mater. Chem. A* **2015**, *3*, 21856–21863.

(22) Stranks, S. D.; Eperon, G. E.; Grancini, G.; Menelaou, C.; Alcocer, M. J. P.; Leijtens, T.; Herz, L. M.; Petrozza, A.; Snaith, H. J. Electron-Hole Diffusion Lengths Exceeding 1 Micrometer in an Organometal Trihalide Perovskite Absorber. *Science* **2013**, *342*, 341–344.

(23) Xing, G.; Mathews, N.; Sun, S.; Lim, S. S.; Lam, Y. M.; Grätzel, M.; Mhaisalkar, S.; Sum, T. C. Long-Range Balanced Electron- and Hole-Transport Lengths in Organic-Inorganic $CH_3NH_3PbI_3$. *Science* **2013**, *342*, 344–347.

(24) He, Z.; Zhong, C.; Su, S.; Xu, M.; Wu, H.; Cao, Y. Enhanced Power-Conversion Efficiency in Polymer Solar Cells Using an Inverted Device Structure. *Nat. Photonics* **2012**, *6*, 593–597.

(25) Seo, J. H.; Gutacker, A.; Walker, B.; Cho, S.; Garcia, A.; Yang, R.; Nguyen, T. Q.; Heeger, A. J.; Bazan, G. C. Improved Injection in N-Type Organic Transistors with Conjugated Polyelectrolytes. *J. Am. Chem. Soc.* **2009**, *131*, 18220–18221.

(26) Zhou, Y.; Fuentes-Hernandez, C.; Shim, J.; Meyer, J.; Giordano, A. J.; Li, H.; Winget, P.; Papadopoulos, T.; Cheun, H.; Kim, J.; et al. A Universal Method to Produce Low-Work Function Electrodes for Organic Electronics. *Science* **2012**, *336*, 327–332.

(27) Leijtens, T.; Eperon, G. E.; Noel, N. K.; Habisreutinger, S. N.; Petrozza, A.; Snaith, H. J. Stability of Metal Halide Perovskite Solar Cells. *Adv. Energy Mater.* **2015**, *5*, 1500963.

(28) Leijtens, T.; Hoke, E. T.; Grancini, G.; Slotcavage, D. J.; Eperon, G. E.; Ball, J. M.; De Bastiani, M.; Bowring, A. R.; Martino, N.; Wojciechowski, K.; et al. Mapping Electric Field-Induced Switchable Poling and Structural Degradation in Hybrid Lead Halide Perovskite Thin Films. *Adv. Energy Mater.* **2015**, *5*, 1500962.

Chapter 8

Transparent Electrodes Based on Silver Nanowires for Perovskite Solar Cells

The work included in this chapter has been presented in a poster:

(1) Wojciechowski, K.; Snaith, H. J. Transparent electrodes based on silver nanowires for solar cell applications, European Materials Research Society - Spring Meeting 2013, Strasbourg

8.1 Context

In the previous chapters, the development of a low temperature processed electron selective contact for perovskite solar cells has been demonstrated. However, while fabrication of a PV stack on a flexible, polymeric substrate is now possible, in order for truly flexible, light weight solar cells to be realised, there also needs to be substantial advancement in the area of transparent bottom electrodes. Indium tin oxide (ITO) and fluorine-doped tin oxide (FTO) are the most commonly used transparent conductors in photovoltaic applications. However, neither of these materials is well suited for flexible devices, which are generating tremendous interest. FTO is typically grown via chemical vapour deposition,[1] sputtering,[2] or spray pyrolysis[3] at high temperatures (>300 °C), which makes it unsuitable for flexible, plastic substrates, such as polyethylene terephthalate (PET). ITO, on the other hand, can be deposited on PET via a low temperature sputtering process (<150 °C),[4,5] but is fragile and brittle[6–8] resulting in cracking and a loss of conductivity after a few tens of bending cycles.[9] Furthermore, due to the low temperature deposition, at a given transmittance these electrodes exhibit a lower conductivity as compared to those processed on glass at higher temperatures. Additionally, the scarcity of indium makes ITO a relatively costly material.[7] In the last few years, multiple alternatives have been investigated. The prospective new material has to satisfy all the requirements for electrodes in solar cells, typically average visible transmission beyond 85%, and sheet resistance below 15 Ω/sq.[8] Carbon nanotubes,[10,11] graphene[12] and conductive polymers[13,14] have all been employed as flexible, transparent electrodes but while promising performances have been reported, in most cases the figures of merit of the alternatives have still fallen short of ITO.

In this chapter, the fabrication of transparent electrodes made with solution-processed silver nanowires is reported, and their potential application in perovskite solar cells is discussed.

8.2 Introduction

Transparent conducting materials are in high demand in optoelectronic industry. Applications span a broad range of systems, including liquid crystal displays, touch panels, UV detectors, organic/inorganic light emitting diodes, and solar cells. The role of a transparent conducting film in an optoelectronic device is to transmit as much light as possible, typically in the visible/near infrared range, and provide an ohmic contact, transporting and collecting charges with minimal resistance losses. Therefore, the most important figures of merit to consider in classifying these types of materials are; transmission in the visible range, and electrical conductivity across the surface of the thin film, typically given in sheet resistance (2-dimensional resistance of the thin film). Furthermore, it is highly desirable for these transparent conductors to be inexpensive, flexible, and compatible with industrial processing on light-weight, flexible polymeric substrates, on which low temperature processing is required.

Indium tin oxide (ITO), the material most commonly used as a transparent conductor in flexible photovoltaic applications has certain limitations, as discussed in the above paragraph. One of the most promising approaches for the replacement of ITO is the use of a metal nanowire mesh. Particularly successful in this class of materials are solution-processed silver nanowires (AgNWs). Metallic nanostructures are commonly synthesised in a polyol process, where ethylene glycol is used both as a solvent and a reducing agent.[15] The important breakthrough in the development of AgNWs came with an advancement in a synthetic approach. The addition of the surfactant, polyvinylpyrrolidone (PVP), allowed to stimulate much more effectively one-dimensional growth of the metallic structures, and nanowires with very high aspect ratios, exceeding 1000, in a soft, scalable process were demonstrated.[16] In the last several years, a number of research groups have demonstrated the remarkable performance

of electrodes based on AgNWs,[17–20] some matching or even exceeding that of ITO on glass (transmittance at 550 nm around 90%, sheet resistance below 10 Ω/square).[21,22] Additionally, as a further advantage, AgNWs have been shown to exhibit excellent mechanical flexibility.[17,23,24]

The as-synthesized nanowires are typically wrapped in a thin, insulating shell of PVP, and as such require a post-deposition treatment in order to lower the wire-to-wire resistance and increase the lateral conductivity of the processed film.[25] Thermal annealing,[25,26] mechanical pressing,[23,26] galvanic displacement,[23] plasmonic welding[27] and plasma etching[28] have all been explored as possible treatments. Some of these methods have yielded very good results, but they all limit the application of AgNWs in a broader range of configurations, such as a top electrode for semi-transparent solar cells, or an interlayer in multi-junction architectures. The above treatments could be too severe for some of the materials in the underlying PV stack. Furthermore, thermal annealing (typically done at temperatures above 200 °C), the most commonly applied post-treatment, also limits the choice of a substrate.

In this chapter the synthesis of long nanowires and the low temperature fabrication of transparent, conductive electrodes based on AgNWs is reported. Different deposition methods and different ways of removing the PVP shell were investigated. Stability problems in the application of these electrodes in perovskite solar cells are discussed and potential solutions are presented.

8.3 Results and discussion

8.3.1 Synthesis of silver nanowires and film fabrication

Silver nanowires were synthesized by a polyol method. In this process silver nitrate ($AgNO_3$) is used as a source of silver, and ethylene glycol (EG) has the double role of both solvent and reducing agent.[29] EG undergoes oxidation upon heating and glycolaldehyde is formed. This compound then works as a reducing agent for silver ions (Equations 8.1-8.2).

$$2HOCH_2CH_2OH + O_2 \xrightarrow{130-160\,℃} 2HOCH_2CHO + 2H_2O \quad (8.1)$$

$$HOCH_2COH + 2Ag^+ + H_2O \rightarrow HOCH_2COOH + 2Ag^0 + 2H^+ \quad (8.2)$$

The reducing power of ethylene glycol increases with temperature.[30]

In order to achieve both high transmission and high conductivity in the nanowire network, the dimensions of the synthesised structures are of vital consideration. Intuitively, longer and thinner wires should fare better in these categories, and so the general effort in the research community was aimed at producing wires of the highest aspect ratios. However, it turns out that this is only partially true. Wiley *et al*. with the use of finite-difference time-domain calculations, to back up with experimental data, argued that there are two competing effects when considering the diameter of the nanowires. For nanowires of a given length covering a specific area, thinner structures exhibit better optoelectronic properties only in low density regimes (highly transmissive networks), where the number of connections (less for thicker wires) limits the conductivity. In high density networks however, there are many connection points and the wires with lower aspect ratios yield higher conductivities due to their higher conductance to extinction ratio.[30]

Numerous additives have been reported to influence the growth, and resulting dimensions, of silver nanostructures in a polyol process. The AgNWs reported in this chapter were synthesised with the addition of sodium chloride (NaCl), iron(III) nitrate ($Fe(NO_3)_3$) and polyvinylpyrrolidone (PVP).[30] The details of experimental procedures are provided in Chapter 3. PVP adsorbs selectively to {100} facets, in turn promoting uniaxial elongation in {111} direction.[31] The iron nitrate works as an oxidant and accelerates the production of the reducing agent, glycolaldehyde.[29] Finally, NaCl provides electrostatic stabilisation for the initial silver seeds, and allows for the growth of longer and thinner wires by reducing the concentration of free Ag^+ ions, and controlling the rate of reduction through the formation of silver chloride (AgCl), which is slowly reduced.[32]

Further control over the dimension of AgNWs was achieved by lowering the temperature at the early stage of the reaction and by controlling the rate of $AgNO_3$ addition, which allowed tuning of the nucleation rate. At the slowed rate there are fewer silver nuclei and one-dimensional growth is facilitated, hence the longer and bigger nanowires can be grown. When the initial temperature is too low, there might be too few nuclei, which would affect the conversion yield and wire-to-particle ratio. Scanning electron microscopy (SEM) images of AgNWs synthesised at a few different reaction conditions are shown in Figure 8.1. As previously mentioned, by lowering the temperature of the first stage of the reaction and slowing down the rate of $AgNO_3$ addition much longer wires were grown, however, at a certain point the yield of conversion started dropping, which can be observed in Figure 8.1d. The summary of nanowire dimensions and reaction conditions are listed in Table 8.1. The optimised conditions (batch A8), used for the remainder of the study are described in detail in Chapter 3. The stock solution was kept at the concentration of ca. 5 mg/ml. AgNWs produced in this batch had lengths up to 60 μm and the diameter of 130 ± 30 nm.

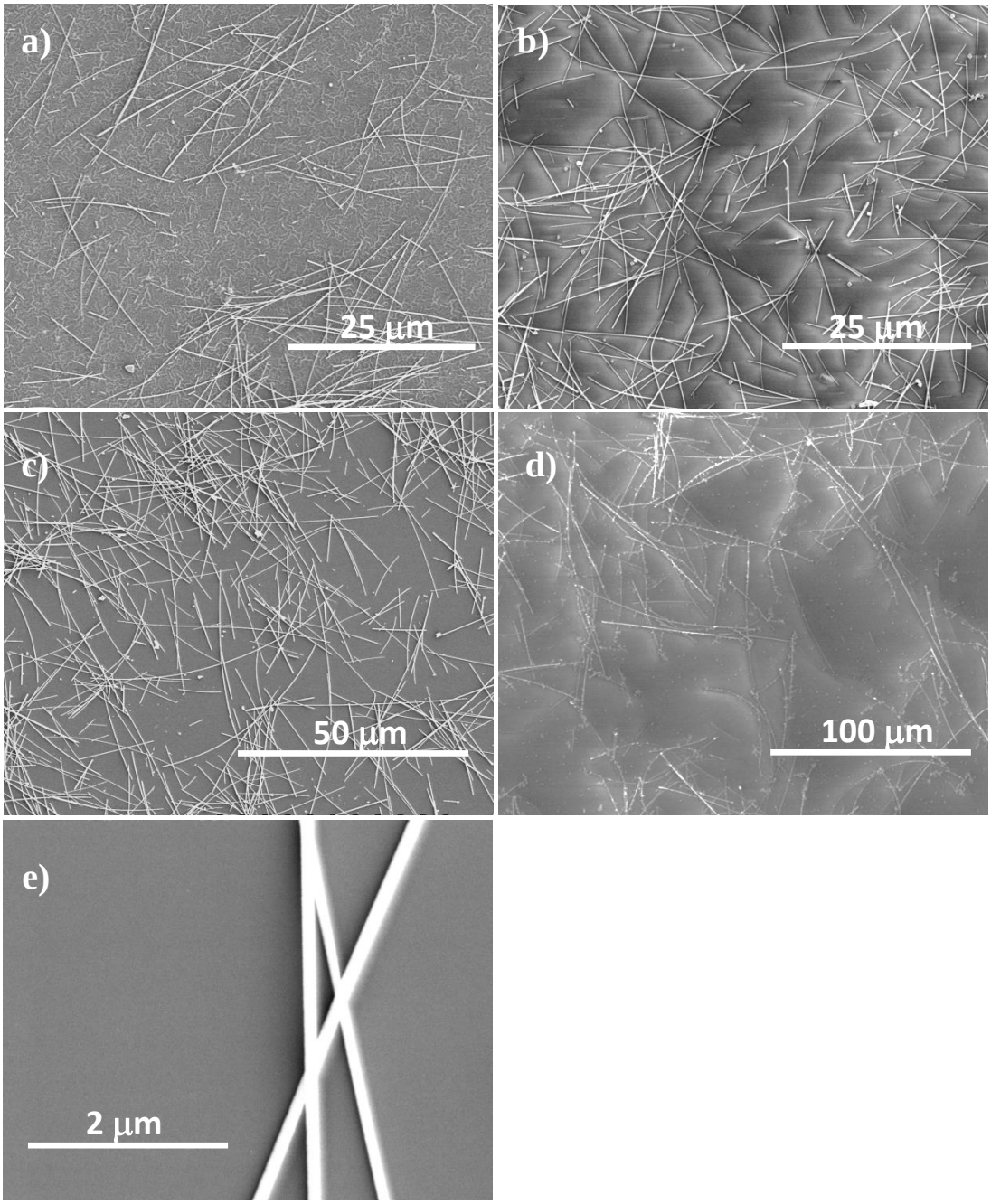


Figure 8.1. Scanning electron microscopy (SEM) images of as-sythesised silver nanowires grown in different reaction conditions and having different dimensions: **(a)** A7 – lengths up to 40 μm; **(b)** A8 – lengths up to 60 μm; **(c)** A9 – lengths up to 70 μm; **(d)** A10 – lengths over 100 μm; **(e)** close up of A8 reaction batch, which was chosen for the remainder of the study. The details of reaction conditions are listed in Table 8.1.

Table 8.1. Details of different reaction conditions of silver nanowire synthesis.

Batch label	First reaction stage	$AgNO_3$ dosing rate	Total reaction time and temperature	AgNWs length
A7	130.5 °C	1 ml/min	130.5 °C, 4 hours	Up to 40 μm
A8	120.5 °C, 10 min	0.5 ml/min	130.5 °C, 5 hours	Up to 60 μm
A9	110.5 °C, 10 min	0.5 ml/min	130.5 °C, 5.5 hours	Up to 70 μm
A10	100.5 °C, 20 min	0.5 ml/min	130.5 °C, 6 hours	Over 100 μm

In order to investigate the optoelectronic properties of nanowires synthesised under different conditions, thin films were fabricated by spin-coating nanowire dispersions on pre-cleaned glass slides. The dispersions were adjusted to have the same solids content. Dynamic spin-coating with dropwise deposition of the solution was used. By varying the time between the doses and spin speed, the rate of solvent evaporation and hence the density of nanowires can be controlled. The latter can be further tuned by varying the volume of deposited solution. The parameters for each deposition were optimised to achieve the highest uniformity and desired density of nanowires, which corresponds to a specific transmittance. SEM images of a AgNW film deposited via dynamic dropwise spin-coating are shown Figure 8.2. The method of solution dosage (AgNW suspension being pipetted onto the centre of the spinning substrate) imposes a certain level of nanowire orientation across the sample. Close to the central part of the sample centrifugal forces act in more directions, which results in the wires having more random orientations with many intersection points (see Figure 8.2a). The further to the edge of the sample the more aligned the wires are due to dominant directionality of the centrifugal forces (see Figure 8.2c). High directionality can limit the number of connection points, which in turn might affect the conductivity of a coating. Nevertheless, the dynamic dropwise spin-coating method gave the most uniform coatings of the AgNW networks. After deposition, the films were annealed for 10 minutes at 150 °C, followed by 10 minutes at 220 °C in order to melt the PVP shell and provide good lateral conductivity. Transmission spectra and sheet resistance values of transparent electrodes fabricated with nanowires of different sizes are

presented in Figure 8.3. The nanowires synthesised in the batches denoted A8 and A9 showed the best optoelectronic properties.

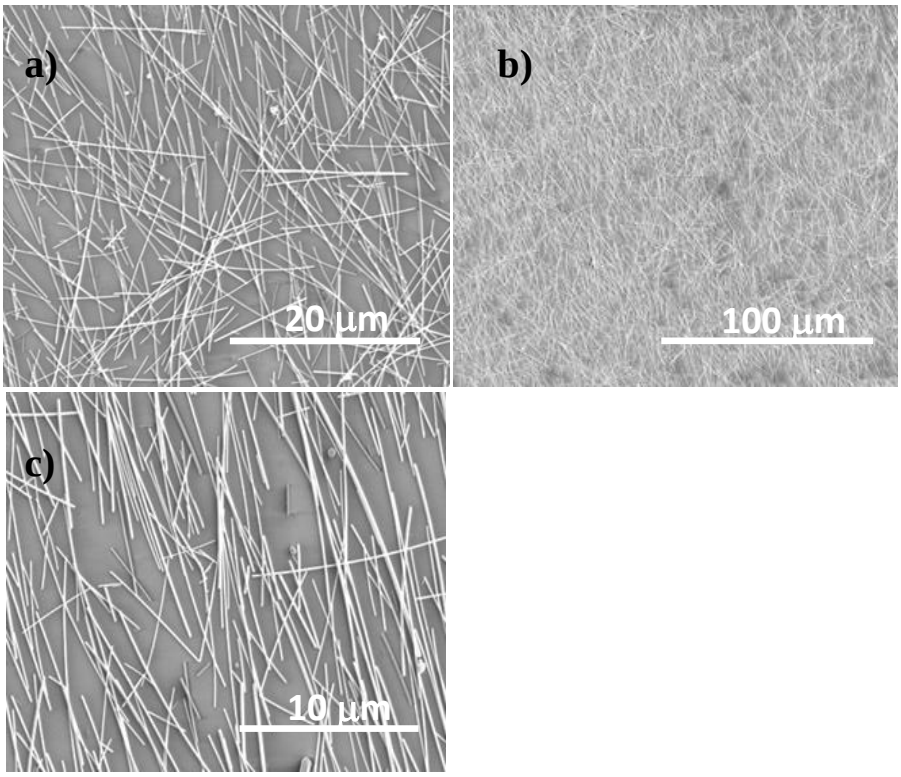


Figure 8.2. SEM images of spin-coated silver nanowires, batch A8: **(a)** higher magnification image of the centre of the sample; **(b)** smaller magnification image, area close to the centre of the sample, high uniformity of nanowires, very few aggregation spots; **(c)** distribution of nanowires closer to the edge of the sample, high directionality of nanowires in this area.

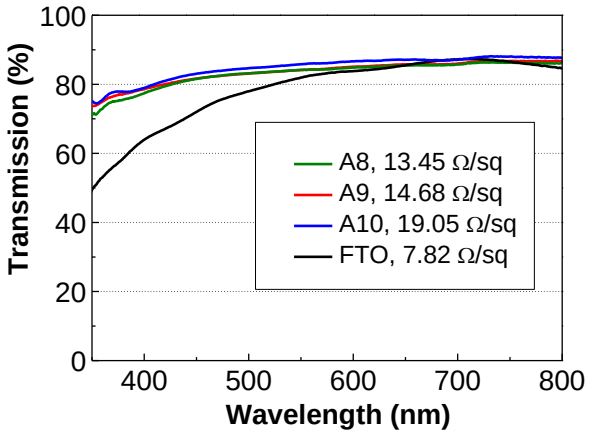


Figure 8.2. Specular transmission spectra of FTO glass (TEC 7) and silver nanowires synthesised in different reaction conditions (details for each batch are given in Table 8.1). The spectra were corrected against the transmission of a reference glass slide. Sheet resistance was measured for each electrode.

8.3.2 Removal of PVP shell

Polyvinylpyrrolidone is used as a surfactant in the silver nanowire reaction stimulating one-dimensional growth of the nanowires.[31] In order to achieve good wire-to-wire contact and the overall conductivity of the film, the insulating shell of the polymer has to be removed from the surface of the nanowires.

The electrodes presented in the previous section were thermally annealed at temperatures above 200 ºC, which resulted in the melting of the PVP layer and a corresponding increase in conductivity of the nanowire network. Despite promising results, this approach is not very effective. At that temperature range, not only can the silver nanowires undergo morphological changes, but substrate choices and possible architectures become quite limited.

8.3.2.1 Methanol washing

PVP is soluble in many polar solvents, such as water or methanol, but it is very difficult to remove it from the surface of silver by simple washing. Prolonged sonication in the appropriate solvent could be very effective, but the nanowires break after longer exposure to ultrasound waves, as shown in Figure 8.3a.

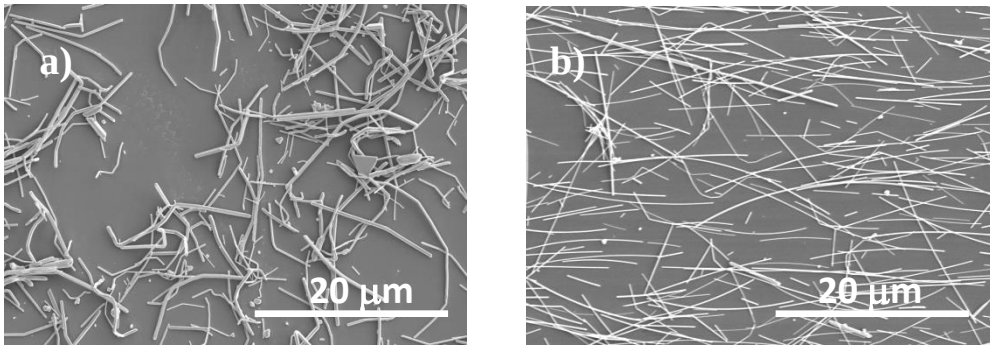


Figure 8.3. SEM images of spin-coated silver nanowire films, processed from the dispersion sonicated in an ultrasound bath for **(a)** 20 minutes and **(b)** 2 minutes.

In this sub-section, a vacuum filtration method was employed, utilising a polypropylene filter of mesh size of 5 μm. This size was chosen to further improve the separation of nanowires with high aspect ratios. In this process, long AgNWs stay on the filter, are generously washed with solvent, and then are redispersed in fresh solvent. Due to hydrophobicity of the polypropylene, the nanowires can be easily removed from the filter, and redispersion is further facilitated by a short sonication in an ultrasound bath. Moderate sonication for short periods of time (less than 1 minute) does not break even the longest and thinnest wires (see Figure 8.3b). A schematic diagram of the filtration procedure is shown in Figure 8.4. As methanol is a very effective solvent for PVP, several repetitions of the filtration-redispersion cycle can significantly erode the PVP layer on the surface of nanowires. A similar approach was reported by Lee *et al.*[24]

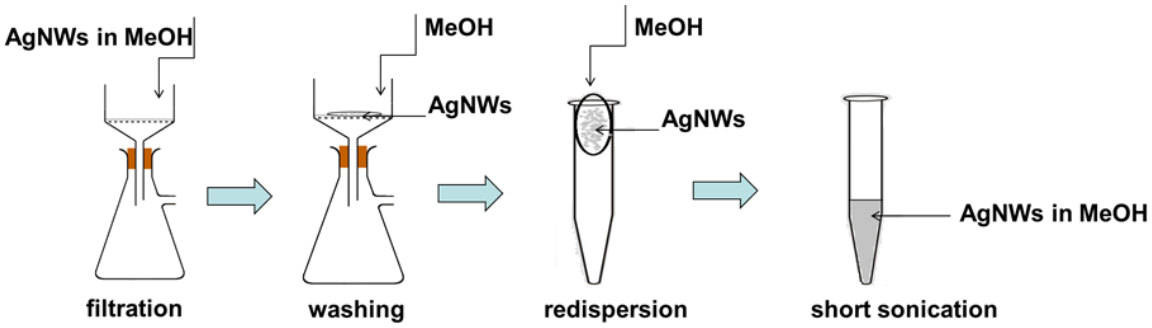


Figure 8.4. Schematic diagram of the vacuum filtration method.

In order to investigate the effect of the filtration method on the optoelectronic properties of silver nanowires, conductivities and transmittances of the AgNW electrodes were measured. Figure 8.5a-b compares the total transmittance at 550 nm (corrected against glass reference) and the sheet resistances for different post-treatments (varying annealing time and temperature) of the AgNW electrodes. These were prepared by spincoating an unfiltered dispersion of nanowires in IPA, as well as the nanowire dispersion which had been subjected to 5 filtration cycles, and then finally redispersed in IPA after the last cycle. The filtered sample (with a thinner PVP shell) had relatively high conductivity without undergoing any heat treatment, yielding a sheet resistance of ca. 160 Ω/square, with a transmission of 90% at 550 nm.

Moderate annealing helped the neighbouring wires fuse with each other, which further lowered the wire-to-wire contact resistance, bringing the sheet resistance below 20 Ω/square after 20 minutes at 150 °C. The sample prepared from the unfiltered AgNW dispersion, with a thick polymer layer, required severe annealing in order to melt the PVP shell and expose the silver, thus increasing the lateral conductivity.

In Figure 8.5c the characteristics of the electrode prepared from filtered AgNW dispersion in methanol is shown. The change of solvent yielded higher conductivities, reaching 10 Ω/square after 20 minutes annealing at 150 °C, as well as a transmission of 88% at 550 nm. The difference might come from better film formation and a higher uniformity of the nanowire network when processed from methanol. On the other hand, the methanol dispersion was significantly less stable, with irreversible aggregation of nanowires in the solution observed within 2-3 weeks after PVP removal, which was not the case in IPA dispersion.

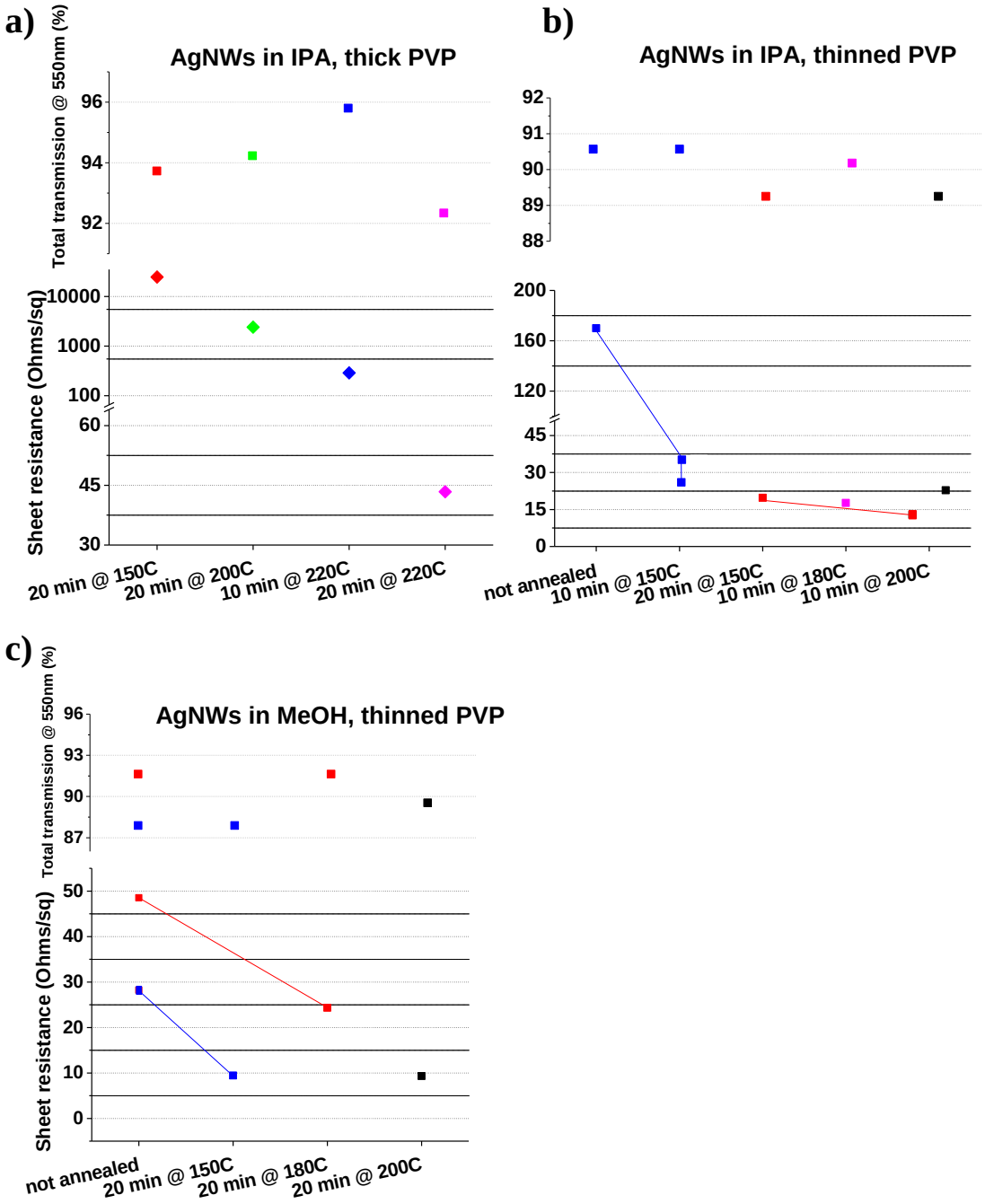


Figure 8.5. Sheet resistance and transmittance data of the AgNW-based electrodes processed from: **(a)** unfiltered dispersion in IPA; **(b)** dispersion in IPA, after vacuum filtration PVP removal treatment; **(c)** dispersion in methanol, after vacuum filtration PVP removal treatment. The electrodes were subjected to post-deposition annealing. Connected dots represent one sample, which underwent subsequent annealing steps.

8.3.2.2 Nitrogen plasma etching

Plasma irradiation of AgNW films has been recently reported as an effective way of PVP removal.[28] In this sub-section, the use of nitrogen plasma etching on silver nanowire networks which were deposited on nitrocellulose filters, as a mean to fabricate high conductivity AgNW electrodes is discussed.

Nitrocellulose is a very good material to use as a platform for transferring a nanowire mesh onto a number of substrates, because the adhesive forces between the nanowires and nitrocellulose are rather weak.[33] The dispersion of AgNWs in IPA was diluted, and the resulting solution was vacuum filtered through a nitrocellulose membrane of pore size 0.2 μm. This resulted in the formation of a very uniform film of nanowires on the membrane. The density of the nanowire network can easily be tuned by changing the concentration of the dispersion and the volume of the filtered solution. The mesh can be transferred from the membrane onto many types of substrates by mechanical pressing and peeling off of the filter. Polyvinyl alcohol (PVA) was found to have a relatively strong adhesion to silver nanowires, so PVA-coated glass was used as a target substrate for fabricating AgNW electrodes with this method. The scheme of the process is shown in Figure 8.6.



Figure 8.6. Schematic diagram of the vacuum filtration and transferring process.

Nitrocellulose membranes containing the mesh of silver nanowires were treated with the nitrogen plasma irradiation before being transferred onto the target substrate. Relatively long plasma etching times are required to entirely remove the PVP layer however, prolonged plasma treatment can induce nitrocellulose degradation, which in turn, may affect the AgNW network. In order to shorten the etching times, the nanaowire dispersion was subjected to a few cycles of filtration and redispersion, as described in the previous sub-section. The sheet resistances of electrodes prepared from filtered (thinned PVP) and unfiltered (thick PVP) dispersions as a function of plasma etching time are plotted in Figure 8.7a. Both solutions had the same concentration of nanowires, such that the resulting electrodes yielded approximately the same density of nanowire network. Plasma etching removes the residual PVP and helps to weld the wires. For the electrode, applying 20 minutes of irradiation to films spun from the filtered dispersion seemed to be enough to obtain a well interconnected network with high conductivity.

In Figure 8.7b transmission spectra and sheet resistance values of the electrodes prepared by spincoating are compared with the electrodes made by the transferring method. The spincoated samples (from filtered dispersion) were annealed at 150 °C for 20 minutes. Nitrocellulose membranes used for the transferred samples were treated with 20 minutes of nitrogen plasma etching, and the mesh was fabricated from the filtered dispersion. The electrodes prepared by the transferring method were free of any post-deposition heat treatment.

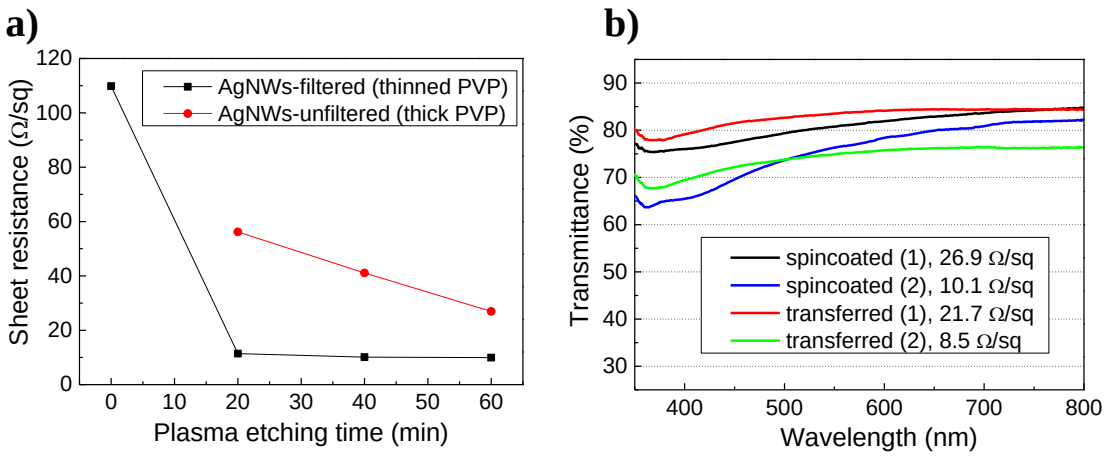


Figure 8.7. (a) Sheet resistance as a function of nitrocellulose membrane plasma etching time for the nanowire mesh processed from filtered and unfiltered dispersion; **(b)** specular transmission spectra (corrected against glass reference spectrum) and sheet resistance values for AgNW electrodes prepared by spincoating (with post-deposition annealing), or transferring method (with nitrogen plasma etching of the membrane).

8.3.3 Silver nanowires embedded in a matrix

Silver nanowire films normally have quite a rough morphology and very poor adhesion to the substrate, regardless of whether it is glass or polymer foil. In this chapter AgNW electrodes were planarised by coating the nanowire network with a layer of semiconducting material, as is schematically shown in Figure 8.7. Materials of different resistivities were applied as a matrix: TiO_2, ZnO, Al-doped ZnO (AZO), and PEDOT:PSS. Conductivity and transmittance data of the composite electrodes are shown in Figure 8.9a.

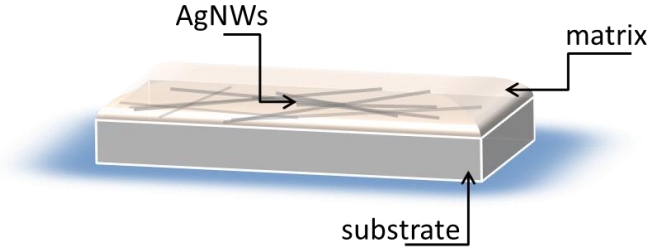


Figure 8.8. Schematic diagram of the silver nanowire composite electrode.

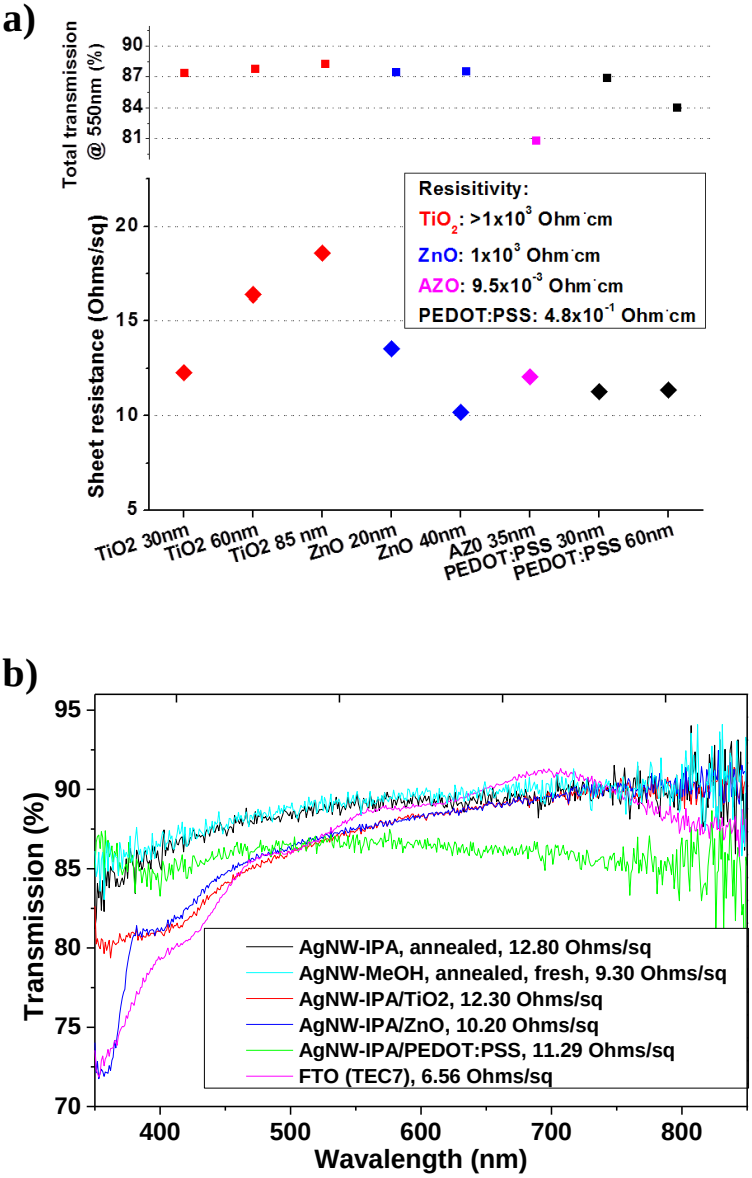


Figure 8.9. (a) Sheet resistance and total transmission values at 550 nm (corrected against glass reference) of silver nanowire composite electrodes, with varying semiconducting material and its thickness; **(b)** Total transmission spectra (corrected against glass reference) of FTO-coated glass electrode (pink curve) compared with the AgNW-based electrodes: black curve – IPA-dispersed nanowires with thinned PVP, light blue curve - methanol-dispersed nanowires with thinned PVP, red curve – AgNW/TiO_2 composite, dark blue curve – AgNW/ZnO composite, green curve – AgNW-PEDOT:PSS composite.

The data presented above suggests that resistivity of a semiconducting matrix does not influence the overall sheet resistance of the electrode. TiO_2, processed from the dispersion of

TiO_2 nanoparticles, has orders of magnitude lower conductivity than spincoated PEDOT:PSS, or AZO processed by atomic layer deposition. The long-range conductivity of silver nanowires is paired with the short-range charge transport of a matrix, resulting in the composite having a low sheet resistance without the need of post-deposition treatment. AgNW composite electrodes prepared here were approaching 10 Ω/square for all semiconducting materials. The sheet resistance starts rising when the thickness of the matrix is increased to the level where the bulk semiconductor's resistivity limits charge transport in the composite. This is seen in the series of AgNW-TiO_2 samples shown in Figure 8.9a. Furthermore, the semiconductor coating dramatically improves the adhesion of nanowires to the substrate.

The total transmission spectra (corrected against glass reference) and sheet resistance values of the silver nanowire-based electrodes which exhibited the best optoelectronic properties are shown in Figure 8.9b. The electrodes spincoated from alcoholic dispersions (IPA or methanol) of filtered nanowires subjected to post-deposition annealing, are compared with AgNW-semiconductor composite networks. An FTO electrode (TEC7) is included as a reference.

8.3.4 Silver nanowires in perovskite solar cells

In this section, silver nanowire electrodes were applied as transparent electrodes in perovskite solar cells in two different configurations: as a bottom electrode replacing FTO, and as a top electrode replacing opaque evaporated metal. Methylammonium lead triiodide processed from the mixed halide precursor solution, $CH_3NH_3PbI_{3-x}Cl_x$, was used as a perovskite material, according to the procedures described in previous chapters. The devices employed the meso-superstructured architecture, where mesoporous alumina is used as a scaffold. Diagrams of the two architectures are shown in Figure 8.10.

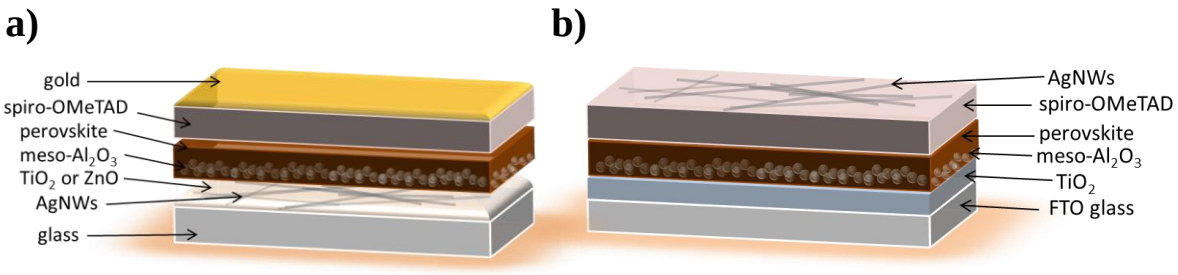


Figure 8.10. Schematic diagram of perovskite solar cell employing silver nanowires as a **(a)** bottom and **(b)** top electrode.

The devices fabricated in this work did not yield respectable power conversion efficiencies. The biggest problem with the utilisation of AgNW electrodes in these cells was the stability of the perovskite layer in contact with silver. In Figure 8.11a images of perovskite devices containing AgNWs as the bottom electrode are shown. A thin layer of TiO_2, or ZnO was coated on top of the nanowire network, serving as both a matrix for the AgNW composite and an electron selective contact. Yellow patches, indicating perovskite degradation, could already be clearly observed on the very day of sample preparation. Figures 8.11b and c show images of perovskite samples with nanowires processed on top of the device, on the day of preparation and after 7 days of being stored in air. Here, the AgNWs were spincoated on top of the hole-transporting material, spiro-OMeTAD. Two sets of samples are shown, one with the Li-TFSI additive in the spiro film, the other without. Li-TFSI is a very hygroscopic dopant used to oxidise the hole-transporting material in order to increase its conductivity and provide good hole transport characteristics.[34] Samples devoid of the dopant showed only minor degradation after seven days of being stored in air, whereas the ones containing Li-TFSI started degrading on the very day of sample preparation.

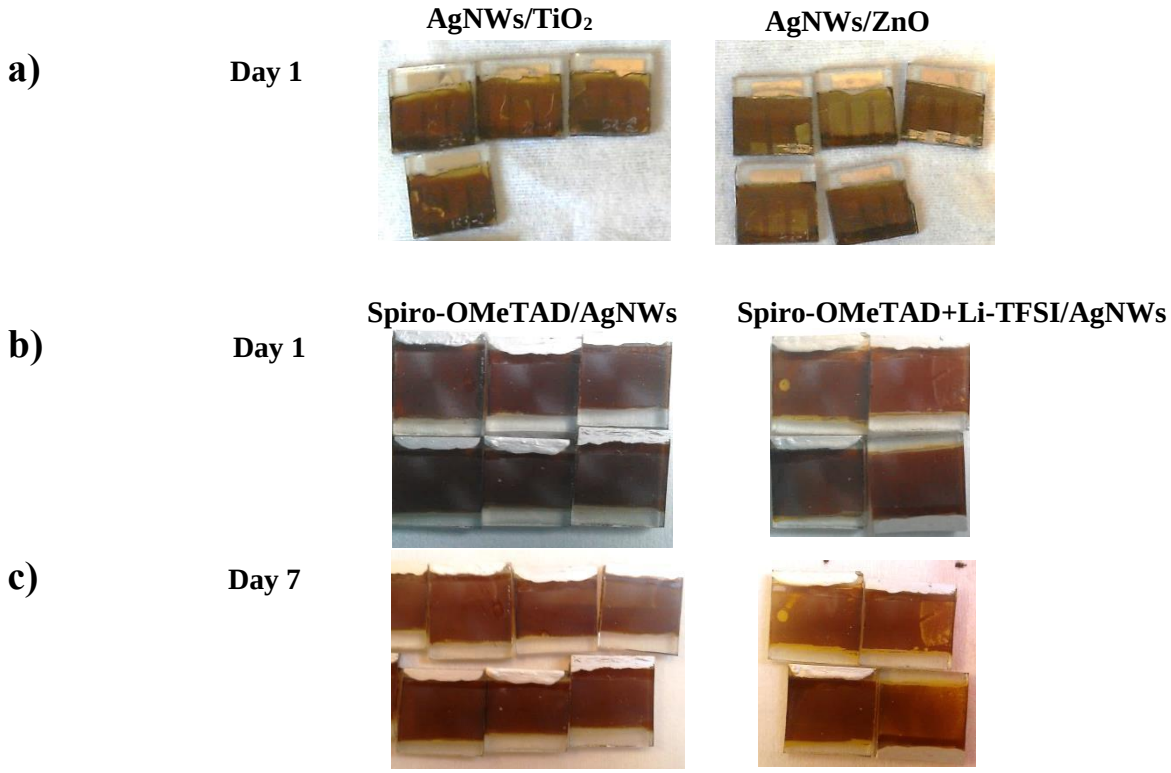


Figure 8.11. Photographs of perovskite samples with silver nanowires **(a)** as a bottom electrode at the day of preparation, **(b)** top electrode at the day of preparation, **(c)** and top electrode after 7 days of storage in ambient conditions.

It has recently been proposed that water molecules present in air diffuse into the perovskite layer causing its partial degradation and significantly increasing the release of volatile iodine-containing species, which in turn diffuse into the top surface of the device, where they react with silver electrode forming silver iodide (AgI).[35] The suggested mechanism corroborates the observation of rapidly accelerated silver corrosion in a humid environment.

In order to successfully utilise silver nanowires in perovskite solar cells, the iodine-rich perovskite layer has to be effectively separated from the silver electrode. A dense and uniform anti-corrosion interlayer inserted between the electrode and perovskite film could potentially prevent the diffusion of the halide species. Furthermore, good encapsulation of the entire device stack is required in order to stop water ingress. A thin layer of chromium (Cr) is commonly deposited on many metals as an anti-tarnish buffer coating.[36] In contact with air Cr forms a thin

layer of chromium(III) oxide (Cr_2O_3), which is a relatively inert and very dense material. Kaltenbrunner *et al.* recently reported very promising results with a Cr/Cr_2O_3 interlayer applied on top of the perovskite cell, before the top electrode.[37] They reported an efficient screening of the perovskite film by chromium oxide, which resulted in a largely improved stability of the solar cells in air.[37] Atomic layer deposition (ALD) is a technique which allows the deposition of a very dense and compact layers of a broad range of materials, including various metal oxides.[38–41] ALD potentially could be used as a tool to deposit materials functioning as an effective protection barrier.

Another approach to increasing stability of the AgNWs-perovskite stack could be the formation of nanowire alloys, where the surface of the silver is covered with a uniform shell of a more stable metal. Wiley *et al.* reported the synthesis of copper nanowires with a nickel shell which dramatically increased the resistance of the nanowires to oxidation.[42] Silver nanowires can be galvanically replaced with gold, which is significantly more stable in contact with halide perovskites. The creation of uniform gold coatings on silver nanowires by galvanic displacement has been previously reported.[23,43] Alloys such as these have the potential to exhibit improved stability in perovskite solar cells without compromising the optoelectronic properties of the transparent electrode.

8.4 Conclusions

In summary, silver nanowires of optimised dimensions have been synthesised via a polyol process. It has been shown that the nucleation rate at the early stages of the reaction, which can be easily controlled by the temperature and the rate of addition of silver ions, has a significant impact on the length of the nanowires.

Various methods of AgNW network fabrication have been presented, including dynamic dropwise spincoating, and the transferring method utilising nitrocellulose filters as stamps. The as-synthesised nanowires have an insulating coating of PVP on their surface, which needs to be removed in order to fabricate a conductive mesh. One of the most commonly used approaches includes annealing at temperatures above 200 °C. Alternative methods have been presented in this chapter. The optimised process allows the fabrication of AgNW electrodes of low sheet resistance and high transmission in the visible region, without the application of any heat treatment. Combining the methods of filtration and redispersion with the nitrogen plasma etching of nanowires deposited on nitrocellulose filters, delivered conductive meshes with good interconnectivity. Such networks are readily transferable onto a number of substrates without the need of additional treatment.

Composites of the silver nanowires embedded in a semiconducting matrix have also been fabricated. Notably, the composites yield higher conductivities than bare nanowires, and no welding of the metal interconnections is necessary. Furthermore, the sheet resistance of these electrodes does not depend on the resistivity of the coating if the layer covering the nanowires is thin enough.

The fabrication of transparent electrodes which do not require any post-deposition treatment will allow for a large degree of flexibility with respect to the choice of target substrate. This will prove to be an important development for many optoelectronic applications, including photovoltaics. The application of AgNW electrodes in perovskite solar cells has been found challenging due to instability issues and the rapid silver corrosion at the presence of halides. Since the time of the research work presented in this chapter number of AgNW-based transparent electrodes utilised in perovskite solar cells have been reported.[44–48] Even though efficiencies approaching the values for devices with opaque, evaporated metal contacts have

been obtained, the long term performance or stability issues have been rarely discussed. The viability of AgNWs application with the perovskite materials remains an open question. Possible solutions and avenues for further development include the application of anti-corrosive buffer layers, such as chromium (III) oxide, or the fabrication of gold shell-silver core nanowire alloys by galvanic displacement.

8.5 References

(1) Suh, S.; Zhang, Z.; Chu, W.; Hoffman, D. M. Atmospheric Pressure Chemical Vapor Deposition of Fluorine-Doped Tin Oxide Thin Films. *Thin Solid Films* **1999**, *345*, 240–243.

(2) Liao, B.-H.; Kuo, C.-C.; Chen, P.-J.; Lee, C.-C. Fluorine-Doped Tin Oxide Films Grown by Pulsed Direct Current Magnetron Sputtering with an Sn Target. *Appl. Opt.* **2011**, *50*, C106–C110.

(3) Rakhshani, a. E.; Makdisi, Y.; Ramazaniyan, H. a. Electronic and Optical Properties of Fluorine-Doped Tin Oxide Films. *J. Appl. Phys.* **1998**, *83*, 1049.

(4) Wang, Y. Y.; Wei, Q. F.; Shao, D. F.; Cai, Y. B.; Yu, L. Y. Optoelectrical Properties of PET Spunbonded Nonwovens Deposited with ITO Thin Films by RF Sputter Coating. *Surf. Eng.* **2009**, *25*, 531–534.

(5) Eisa, M. H.; Faraj, M. G.; Azhari, F. Deposited Indium Tin Oxide (ITO) Thin Films by Dc- Magnetron Sputtering on Polyethylene Terephthalate Substrate (PET). *Film* **2011**, *56*, 730–741.

(6) Krebs, F. C. Roll-to-Roll Fabrication of Monolithic Large-Area Polymer Solar Cells Free from Indium-Tin-Oxide. *Sol. Energy Mater. Sol. Cells* **2009**, *93*, 1636–1641.

(7) Olle Inganäs. Organic Photovoltaics: Avoiding Indium. *Nat. Photonics* **2011**, *5*, 201–203.

(8) Yuan, Y.; Bi, Y.; Huang, J. Achieving High Efficiency Laminated Polymer Solar Cell with Interfacial Modified Metallic Electrode and Pressure Induced Crystallization. *Appl. Phys. Lett.* **2011**, *98*, 063306.

(9) Alzoubi, K.; Hamasha, M. M.; Lu, S.; Sammakia, B. Bending Fatigue Study of Sputtered ITO on Flexible Substrate. *IEEE/OSA J. Disp. Technol.* **2011**, *7*, 593–600.

(10) Wu, Z.; Chen, Z.; Du, X.; Logan, J. M.; Sippel, J.; Nikolou, M.; Kamaras, K.; Reynolds, J. R.; Tanner, D. B.; Hebard, A. F.; et al. Transparent, Conductive Carbon Nanotube Films. *Science* **2004**, *305*, 1273–1276.

(11) Kim, S.; Yim, J.; Wang, X.; Bradley, D. D. C.; Lee, S.; DeMello, J. C. Spin- and Spray-Deposited Single-Walled Carbon-Nanotube Electrodes for Organic Solar Cells. *Adv. Funct. Mater.* **2010**, *20*, 2310–2316.

(12) Kim, K. S.; Zhao, Y.; Jang, H.; Lee, S. Y.; Kim, J. M.; Kim, K. S.; Ahn, J.-H.; Kim, P.; Choi, J.-Y.; Hong, B. H. Large-Scale Pattern Growth of Graphene Films for Stretchable Transparent Electrodes. *Nature* **2009**, *457*, 706–710.

(13) Kim, Y. H.; Sachse, C.; Machala, M. L.; May, C.; Müller-Meskamp, L.; Leo, K. Highly Conductive PEDOT:PSS Electrode with Optimized Solvent and Thermal Post-Treatment for ITO-Free Organic Solar Cells. *Adv. Funct. Mater.* **2011**, *21*, 1076–1081.

(14) Bryant, D.; Greenwood, P.; Troughton, J.; Wijdekop, M.; Carnie, M.; Davies, M.; Wojciechowski, K.; Snaith, H. J.; Watson, T.; Worsley, D. A Transparent Conductive Adhesive Laminate Electrode for High-Efficiency Organic-Inorganic Lead Halide Perovskite Solar Cells. *Adv. Mater.* **2014**, *26*, 7499–7504.

(15) Ayyappan, S.; Subbanna, G. N.; Gopalan, R. S.; Rao, C. N. R. Nanoparticles of Nickel and Silver Produced by the Polyol Reduction of the Metal Salts Intercalated in Montmorillonite. *Solid State Ionics* **1996**, *84*, 271–281.

(16) Sun, Y.; Gates, B.; Mayers, B.; Xia, Y. Crystalline Silver Nanowires by Soft Solution Processing. *Nano Lett.* **2002**, *2*, 165–168.

(17) De, S.; Higgins, T. M.; Lyons, P. E.; Doherty, E. M.; Nirmalraj, P. N.; Blau, W. J.; Boland, J. J.; Coleman, J. N. Silver Nanowire Networks as Flexible, Transparent,

Conducting Films: Extremely High DC to Optical Conductivity Ratios. *ACS Nano* **2009**, *3*, 1767–1774.

(18) Leem, D.-S.; Edwards, A.; Faist, M.; Nelson, J.; Bradley, D. D. C.; de Mello, J. C. Efficient Organic Solar Cells with Solution-Processed Silver Nanowire Electrodes. *Adv. Mater.* **2011**, *23*, 4371–4375.

(19) Scardaci, V.; Coull, R.; Lyons, P. E.; Rickard, D.; Coleman, J. N. Spray Deposition of Highly Transparent, Low-Resistance Networks of Silver Nanowires over Large Areas. *Small* **2011**, *7*, 2621–2628.

(20) Zhu, R.; Chung, C.-H.; Cha, K. C.; Yang, W.; Zheng, Y. B.; Zhou, H.; Song, T.-B.; Chen, C.-C.; Weiss, P. S.; Li, G.; et al. Fused Silver Nanowires with Metal Oxide Nanoparticles and Organic Polymers for Highly Transparent Conductors. *ACS Nano* **2011**, *5*, 9877–9882.

(21) Krantz, J.; Richter, M.; Spallek, S.; Spiecker, E.; Brabec, C. J. Solution-Processed Metallic Nanowire Electrodes as Indium Tin Oxide Replacement for Thin-Film Solar Cells. *Adv. Funct. Mater.* **2011**, *21*, 4784–4787.

(22) Kim, A.; Won, Y.; Woo, K.; Kim, C.-H.; Moon, J. Highly Transparent Low Resistance ZnO/Ag nanowire/ZnO Composite Electrode for Thin Film Solar Cells. *ACS Nano* **2013**, *7*, 1081–1091.

(23) Hu, L.; Kim, H. S.; Lee, J.; Peumans, P.; Cui, Y. Scalable Coating and Properties of Transparent, Flexible, Silver Nanowires Electrodes. *ACS Nano* **2010**, *4*, 2955–2963.

(24) Lee, J.; Lee, I.; Kim, T.-S.; Lee, J.-Y. Efficient Welding of Silver Nanowire Networks without Post-Processing. *Small* **2013**, *9*, 2887.

(25) Lee, J.-Y.; Connor, S. T.; Cui, Y.; Peumans, P. Solution-Processed Metal Nanowire Mesh Transparent Electrodes. *Nano Lett.* **2008**, *8*, 689–692.

(26) Tokuno, T.; Nogi, M.; Karakawa, M.; Jiu, J.; Nge, T. T.; Aso, Y.; Suganuma, K. Fabrication of Silver Nanowire Transparent Electrodes at Room Temperature. *Nano Res.* **2011**, *4*, 1215–1222.

(27) Garnett, E. C.; Cai, W.; Cha, J. J.; Mahmood, F.; Connor, S. T.; Greyson Christoforo, M.; Cui, Y.; McGehee, M. D.; Brongersma, M. L. Self-Limited Plasmonic Welding of Silver Nanowire Junctions. *Nat. Mater.* **2012**, *11*, 241–249.

(28) Zhu, S.; Gao, Y.; Hu, B.; Li, J.; Su, J.; Fan, Z.; Zhou, J. Transferable Self-Welding Silver Nanowire Network as High Performance Transparent Flexible Electrode. *Nanotechnology* **2013**, *24*, 335202.

(29) Skrabalak, S. E.; Wiley, B. J.; Kim, M.; Formo, E. V.; Xia, Y. On the Polyol Synthesis of Silver Nanostructures: Glycolaldehyde as a Reducing Agent. *Nano Lett.* **2008**, *8*, 2077–2081.

(30) Bergin, S. M.; Chen, Y.-H.; Rathmell, A. R.; Charbonneau, P.; Li, Z.-Y.; Wiley, B. J. The Effect of Nanowire Length and Diameter on the Properties of Transparent, Conducting Nanowire Films. *Nanoscale* **2012**, *4*, 1996–2004.

(31) Saidi, W. a.; Feng, H.; Fichthorn, K. a. Binding of Polyvinylpyrrolidone to Ag Surfaces: Insight into a Structure-Directing Agent from Dispersion-Corrected Density Functional Theory. *J. Phys. Chem. C* **2013**, *117*, 1163–1171.

(32) Korte, K. E.; Skrabalak, S. E.; Xia, Y. Rapid Synthesis of Silver Nanowires through a CuCl- or CuCl2-Mediated Polyol Process. *J. Mater. Chem.* **2008**, *18*, 437.

(33) Guo, H.; Lin, N.; Chen, Y.; Wang, Z.; Xie, Q.; Zheng, T.; Gao, N.; Li, S.; Kang, J.; Cai, D.; et al. Copper Nanowires as Fully Transparent Conductive Electrodes. *Sci. Rep.* **2013**, *3*, 1–8.

(34) Abate, A.; Leijtens, T.; Pathak, S.; Teuscher, J.; Avolio, R.; Errico, M. E.; Kirkpatrik, J.; Ball, J. M.; Docampo, P.; McPherson, I.; et al. Lithium Salts as "Redox Active" P-Type Dopants for Organic Semiconductors and Their Impact in Solid-State Dye-Sensitized Solar Cells. *Phys. Chem. Chem. Phys.* **2013**, *15*, 2572–2579.

(35) Kato, Y.; Ono, L. K.; Lee, M. V.; Wang, S.; Raga, S. R.; Qi, Y. Silver Iodide Formation in Methyl Ammonium Lead Iodide Perovskite Solar Cells with Silver Top Electrodes. *Adv. Mater. Interfaces* **2015**, *2*, 2196–7350.

(36) Downing, J. H.; Deelay, P. D.; Fichte, R. Chromium and Chromium Alloys. *Ullmann's*

Encycl. Ind. Chem. **2000**.

(37) Kaltenbrunner, M.; Adam, G.; Głowacki, E. D.; Drack, M.; Schwödiauer, R.; Leonat, L.; Apaydin, D. H.; Groiss, H.; Scharber, M. C.; White, M. S.; et al. Flexible High Power-per-Weight Perovskite Solar Cells with Chromium Oxide–metal Contacts for Improved Stability in Air. *Nat. Mater.* **2015**, *14*, 1032–1039.

(38) Wang, C.; Zhao, D.; Grice, C.; Liao, W.; Yu, Y.; Cimaroli, A.; Shrestha, N.; Roland, P. J.; Chen, J.; Yu, Z.; et al. Low-Temperature Plasma-Enhanced Atomic Layer Deposition of Tin Oxide Electron Selective Layers for Highly Efficient Planar Perovskite Solar Cells. *J. Mater. Chem. A* **2016**, *4*, 12080.

(39) Chang, C.-Y.; Lee, K.-T.; Huang, W.-K.; Siao, H.-Y.; Chang, Y.-C. High-Performance, Air-Stable, Low-Temperature Processed Semitransparent Perovskite Solar Cells Enabled by Atomic Layer Deposition. *Chem. Mater.* **2015**, *27*, 5122.

(40) Seo, S.; Park, I. J.; Kim, M.; Lee, S.; Bae, C.; Jung, H. S.; Park, N.-G.; Kim, J. Y.; Shin, H. An Ultra-Thin, Un-Doped NiO Hole Transporting Layer of Highly Efficient (16.4%) Organic-Inorganic Hybrid Perovskite Solar Cells. *Nanoscale* **2016**, *8*, 11403.

(41) George, S. M. Atomic Layer Deposition: An Overview. *Chem. Rev.* **2010**, *110*, 111–131.

(42) Rathmell, A. R.; Nguyen, M.; Chi, M.; Wiley, B. J. Synthesis of Oxidation-Resistant Cupronickel Nanowires for Transparent Conducting Nanowire Networks. *Nano Lett.* **2012**, *12*, 3193–3199.

(43) Sun, Y.; Wang, Y. Monitoring of Galvanic Replacement Reaction between Silver Nanowires and HAuCl4 by In Situ Transmission X-Ray Microscopy. *Nano Lett.* **2011**, *11*, 4386–4392.

(44) Kim, A.; Lee, H.; Kwon, H.-C.; Jung, H. S.; Park, N.-G.; Jeong, S.; Moon, J. Fully Solution-Processed Transparent Electrodes Based on Silver Nanowire Composites for Perovskite Solar Cells. *Nanoscale* **2015**, *8*, 6308.

(45) Zhang, J.; Li, F.; Yang, K.; Veeramalai, C. P.; Guo, T. Low Temperature Processed Planar Heterojunction Perovskite Solar Cells Employing Silver Nanowires as Top

Electrode. *Appl. Surf. Sci.* **2016**, *369*, 308–313.

(46) Bailie, C. D.; Christoforo, M. G.; Mailoa, J. P.; Bowring, A. R.; Unger, E. L.; Nguyen, W. H.; Burschka, J.; Pellet, N.; Lee, J. Z.; Grätzel, M.; et al. Semi-Transparent Perovskite Solar Cells for Tandems with Silicon and CIGS. *Energy Environ. Sci.* **2014**, *8*, 956–963.

(47) Lee, M.; Ko, Y.; Min, B. K.; Jun, Y. Silver Nanowire Top Electrodes in Flexible Perovskite Solar Cells Using Titanium Metal as Substrate. *ChemSusChem* **2016**, *9*, 31–35.

(48) Guo, F.; Azimi, H.; Hou, Y.; Przybilla, T.; Hu, M.; Bronnbauer, C.; Langner, S.; Spiecker, E.; Forberich, K.; Brabec, C. J.; et al. High-Performance Semitransparent Perovskite Solar Cells with Solution-Processed Silver Nanowires as Top Electrodes. *Nanoscale* **2015**, *7*, 1642–1649.

Chapter 9

Conclusions

9.1 Summary of the key results

Organic-inorganic metal halide perovskite solar cells took a PV community by storm, recording unprecedented rise of power conversion efficiencies in the last three years, and showing realistic commercial prospects in the near future.[1–3]

The work presented in this thesis was primarily focused on the development of an efficient electron selective contact for perovskite solar cells. It delivered some important breakthroughs, pushing the technology closer to the commercial applications. The thesis covers some fundamental aspects of the device operation, shedding light on the existing limitations to the cell performance. Suitable engineering of the n-type contact enabled significant enhancements in power conversion efficiency of these devices. Another focus covered in this thesis was low temperature processing of the entire PV stack, including the development of a transparent electrode, which has been successfully presented.

In a typical n-i-p perovskite device architecture, where electron selective material is processed at the bottom of the device structure, nanocrystalline TiO_2 has been most commonly used as a hole blocking compact layer.[2,4,5] The processing of this layer typically involves 500 °C sintering step of the titania precursor, which allows the transformation of the amorphous phase of the metal oxide into a crystalline anatase.[6] In Chapter 4, pre-synthesised TiO_2 anatase nanoparticles were employed as the electron selective contact. High crystallinity of the nanoparticles yields in a good conductivity, which is an important factor for efficient charge transport. Furthermore, an addition of an organic ligand has facilitated interconnection between nanoparticles, enabling processing of the dense TiO_2 films at temperatures below 150 °C. Solar cells fabricated with these layers displayed enhanced PV performance, and importantly this work was one of the first demonstrations of fabrication the entire perovskite device at low temperature process.[7] It was a vital development which opened new avenues for perovskite applications, such as flexible solar cells, processed on polymer foils, or multi-junction architectures.

The interface between an electron selective contact and perovskite material has a strong influence on the device operation. In Chapter 5 it is shown that TiO_2 does not make a good electronic contact with the perovskite, and photogenerated charges are not efficiently extracted at that interface. Further evidence of the existence of an energetic barrier impeding the electron transfer are demonstrated in Chapter 6 *via* photoelectron spectroscopy study. In order to improve that contact, which was identified to be a limiting factor for the optimal device operation, a chemical interfacial modification was applied. A fullerene monolayer was self-assembled on the surface of TiO_2, which resulted in a favourable band alignment and enabled efficient charge extraction at the

n-type contact. Solar cells fabricated with the modified compact layer displayed dramatically enhanced power conversion efficiency.

Perovskite solar cells typically display an anomalous hysteresis in current-voltage characteristics, which varies between architectures and processing conditions.[8] The hysteresis phenomenon has been assigned to the migration of the ionic species, which are present in the perovskite film, and the existence of the electronic trap states.[9,10] Movement of the ions under the electric field causes a temporal polarisation of the perovskite material, which in turn affects the efficacy of charge extraction and the amount of interfacial recombination. In chapters 5-7 it is shown that good electronic contact at the charge selective interfaces can reduce the effect of this process, and the hysteretic behaviour can be largely suppressed. Fullerene-based materials act as a very efficient electron collection layer. Dramatic improvement of the device operation can be achieved both, by modifying the TiO_2 surface with a fullerene monolayer, as shown in Chapter 5, and by replacing the metal oxide with the fullerene material working as a sole compact layer, as presented in Chapter 6. Furthermore, C_{60} film can be easily solution-processed at temperatures below 100 °C. The photovoltaic performance of perovskite cells was further enhanced in the work presented in Chapter 7, where cross-linkable fullerene derivatives were used as an n-type contact. Solvent resistance of the crosslinked compact layer improves the morphology of the fullerene film in the solution-processed perovskite cell, which reduces shunting paths, and boosts up an open-circuit voltage and a stabilised power output. The work presented in this thesis constituted an important contribution to the understanding of the hysteresis phenomenon and helped the community advancing the technology further. Additionally, a new method for characterising photovoltaic performance of perovskite cells was developed throughout this work.[8] Introduction of the stabilised power output

(SPO) measurement, which is discussed in Chapter 5, allowed more reliable reporting of the power conversion efficiencies. Due to hysteretic effects a sole current-voltage scan does not accurately represent the photovoltaic performance of these devices. The SPO measurement was an important breakthrough, which allowed better comparison of the results published by different research labs.

Stability of the perovskite solar cells is one of the key challenges, which needs to be resolved before the technology can be successfully implemented in commercial applications. The ionic character of the material and sensitivity to the atmospheric conditions raise many doubts about the long-term performance. In Chapter 6, initial set of 500 hours stability test of the cells under load is presented. The devices were aged at the real operating conditions, which is the only viable way to investigate the sustainability of the device operation over a long period of time. The results revealed intrinsic TiO_2 instability, which has been assigned to the UV-induced degradation, in agreement with previous reports.[11,12] The cells employing organic fullerene contact displayed enhanced stability, preserving the photocurrent in the entire 500 hours time window. In Chapter 7, aging data under operational conditions of the cells employing crosslinked fullerenes is presented. Some devices exhibit very good stability within the first 200 hours. The data highlights the importance of the electronic contacts at the interfaces in long-term device operation.

Flexible photovoltaic applications constitute a rapidly growing PV niche market. Perovskite materials provide a very attractive technology to fulfil the requirements. In the previous chapters low temperature processing of the entire PV stack has been demonstrated, which enables the use of flexible plastic foils. One of the remaining challenges for this type of solar cells is transparent conductive electrodes. Indium tin oxide is the most commonly used transparent conductor processed on top of polymeric

substrates, but because of its brittleness and processing conditions, it is not well suited for flexible applications.[13,14] In Chapter 8, the development of room-temperature processed, highly conductive and flexible transparent electrodes based on silver nanowires is presented. The implementation of these electrodes into perovskite solar cells in different architectures so far has proven to be challenging. Possible solutions to the encountered incompatibility of the silver and halide perovskite have also been discussed.

9.2 Outlook

The thesis presents a number of conclusions paving the way for advancing the development of perovskite photovoltaics and provides a scope for promising future work. One of the persisting challenges, critical for the commercial success of the technology is the stability of these devices.[15] The choice of charge selective materials and precise control of the processes occurring at the contacts can certainly add value to the problem. The work presented in this thesis suggests that fullerene-based materials may be advantageous for the long-term performance. More research focused on the stability is required to find the optimal systems. The cross-linkable fullerene derivatives provide a very attractive route, which should be studied in more detail. Potentially, these materials could be functionalised with additional moisture-blocking moieties to further enhance the stability of perovskite cells.

Another important aspect for the future work is the reduction of non-radiative recombination, which could bring the perovskite device closer to an ideal mode of operation.[16] Large part of these losses come from interfacial recombination, due to number of defects present at the perovskite contacts.[17–19] N-type doping of the electron

transport material (fullerene-based or metal oxide layers investigated in this work) could improve this crucial operation. Perovskite properties and its defect density can also be influenced by the underlying material onto which the film is grown, as it was briefly highlighted in Chapter 6. The electroluminescence studies (EL mapping, EL quantum yield), potentially combined with high energy photoelectron spectroscopy could answer this problem and shed new light on the mechanism and amount of losses originating at that interface.

The work on silver nanowires highlighted a problem of chemical incompatibility of halide perovskites with silver electrode. Finding an effective barrier, which could prevent the halide ions from migration to the silver contact is an important subject for future research. The corrosive reaction of perovskites with different metals constitutes one of the major issues for the long-term stability of these cells.[20] Metallic silver, despite its reactivity when put in contact with perovskite layer, is the most commonly used top electrode, delivering a very good photovoltaic performance in short-term window.[21] Furthermore, it is probably the most viable metal choice from commercial point of view. Finding a solution to this instability would be a major leap forward in advancing the technology.

Lastly, the fabrication of truly flexible, highly efficient perovskite solar cells with documented well preserved long-term performance is, in the author's opinion, the ultimate goal for this technology. Delivering such solutions at a low cost would bring a widespread use of perovskite PV, thereby providing a very attractive tool in tackling the world's energy crisis.

9.3 References

(1) Green, M. A.; Ho-Baillie, A.; Snaith, H. J. The Emergence of Perovskite Solar Cells. *Nat. Photonics* **2014**, *8*, 506–514.

(2) Stranks, S. D.; Snaith, H. J. Metal-Halide Perovskites for Photovoltaic and Light-Emitting Devices. *Nat. Nanotechnol.* **2015**, *10*, 391–402.

(3) Shi, S.; Li, Y.; Li, X.; Wang, H. Advancements in All-Solid-State Hybrid Solar Cells Based on Organometal Halide Perovskite. *Mater. Horiz.* **2015**, *2*, 378–405.

(4) Shi, J.; Xu, X.; Li, D.; Meng, Q. Interfaces in Perovskite Solar Cells. *Small* **2015**, *11*, 2472–2486.

(5) Snaith, H. J. Perovskites: The Emergence of a New Era for Low-Cost, High-Efficiency Solar Cells. *J. Phys. Chem. Lett.* **2013**, *4*, 3623–3630.

(6) Kavan, L.; Graetzel, M. Highly Efficient Semiconducting TiO_2 Photoelectrodes Prepared by Aerosol Pyrolysis. *Electrochim. Acta* **1995**, *40*, 643–652.

(7) Wojciechowski, K.; Saliba, M.; Leijtens, T.; Abate, A.; Snaith, H. J. Sub-150 °C Processed Meso-Superstructured Perovskite Solar Cells with Enhanced Efficiency. *Energy Environ. Sci.* **2014**, *7*, 1142.

(8) Snaith, H. J.; Abate, A.; Ball, J. M.; Eperon, G. E.; Leijtens, T.; Noel, N. K.; Stranks, S. D.; Wang, J. T.; Wojciechowski, K.; Zhang, W. Anomalous Hysteresis in Perovskite Solar Cells. *J. Phys. Chem. Lett.* **2014**, *17*, 1511–1515.

(9) Tress, W.; Marinova, N.; Moehl, T.; Zakeeruddin, S. M.; Mohammad K., N.; Grätzel, M. Understanding the Rate-Dependent J-V Hysteresis, Slow Time Component, and Aging in $CH_3NH_3PbI_3$ Perovskite Solar Cells: The Role of a Compensated Electric Field. *Energy Environ. Sci.* **2015**, *8*, 995–1004.

(10) Reenen, S. Van; Kemerink, M.; Snaith, H. J. Modeling Anomalous Hysteresis in Perovskite Solar Cells. *J. Phys. Chem. Lett.* **2015**, *6*, 3808–3814.

(11) Leijtens, T.; Eperon, G. E.; Pathak, S.; Abate, A.; Lee, M. M.; Snaith, H. J. Overcoming

Ultraviolet Light Instability of Sensitized TiO_2 with Meso-Superstructured Organometal Tri-Halide Perovskite Solar Cells. *Nat. Commun.* **2013**, *4*, 2885.

(12) Pathak, S. K.; Abate, A.; Ruckdeschel, P.; Roose, B.; Gödel, K. C.; Vaynzof, Y.; Santhala, A.; Watanabe, S.-I.; Hollman, D. J.; Noel, N.; et al. Performance and Stability Enhancement of Dye-Sensitized and Perovskite Solar Cells by Al Doping of TiO_2. *Adv. Funct. Mater.* **2014**, *24*, 6046–6055.

(13) Krebs, F. C. Roll-to-Roll Fabrication of Monolithic Large-Area Polymer Solar Cells Free from Indium-Tin-Oxide. *Sol. Energy Mater. Sol. Cells* **2009**, *93*, 1636–1641.

(14) Olle Inganäs. Organic Photovoltaics: Avoiding Indium. *Nat. Photonics* **2011**, *5*, 201–203.

(15) Leijtens, T.; Eperon, G. E.; Noel, N. K.; Habisreutinger, S. N.; Petrozza, A.; Snaith, H. J. Stability of Metal Halide Perovskite Solar Cells. *Adv. Energy Mater.* **2015**, *5*, 1500963.

(16) Miller, O. D.; Yablonovitch, E.; Kurtz, S. R. Strong Internal and External Luminescence as Solar Cells Approach the Shockley–Queisser Limit. *IEEE J. Photovoltaics* **2012**, *2*, 303–311.

(17) Wojciechowski, K.; Stranks, S. D.; Abate, A.; Sadoughi, G.; Sadhanala, A.; Kopidakis, N.; Rumbles, G.; Li, C.; Friend, R. H.; Jen, A. K.; et al. Heterojunction Modification for Highly Efficient Organic-Inorganic Perovskite Solar Cells. *ACS Nano* **2014**, *8*, 12701–12709.

(18) Noel, N. K.; Abate, A.; Stranks, S. D.; Parrott, E. S.; Burlakov, V. M.; Goriely, A.; Snaith, H. J. Enhanced Photoluminescence and Solar Cell Performance via Lewis Base Passivation of Organic-Inorganic Lead Halide Perovskites. *ACS Nano* **2014**, *8*, 9815–9821.

(19) Wetzelaer, G.-J. a. H.; Scheepers, M.; Sempere, A. M.; Momblona, C.; Ávila, J.; Bolink, H. J. Trap-Assisted Non-Radiative Recombination in Organic-Inorganic Perovskite Solar Cells. *Adv. Mater.* **2015**, *27*, 1837.

(20) Kato, Y.; Ono, L. K.; Lee, M. V.; Wang, S.; Raga, S. R.; Qi, Y. Silver Iodide Formation

in Methyl Ammonium Lead Iodide Perovskite Solar Cells with Silver Top Electrodes. *Adv. Mater. Interfaces* **2015**, *2*, 2196–7350.

(21) Behrouznejad, F.; Shahbazi, S.; Taghavinia, N.; Wu, H.-P.; Diau, E. W.-G. A Study on Utilizing Different Metals as the Back Contact of $CH_3NH_3PbI_3$ Perovskite Solar Cells. *J. Mater. Chem. A* **2016**.

Appendix

Publications, conferences and posters

1. Publications

- Wojciechowski, K.; Saliba, M.; Leijtens, T.; Abate, A.; Snaith, H. J. Sub-150 °C processed meso-superstructured perovskite solar cells with enhanced efficiency, *Energy Environ. Sci.* **2014**, 7, 1142
- Wojciechowski, K.; Stranks, S. D.; Abate, A.; Sadoughi, G.; Sadhanala, A.; Kopidakis, N.; Rumbles, G.; Li, C.; Friend, R. H.; Jen, A. K.; Snaith, H. J. Heterojunction Modification for Highly Efficient Organic–Inorganic Perovskite Solar Cells, *ACS Nano* **2014**, 8, 12701
- Wojciechowski, K.; Leijtens, T.; Siprova, S.; Schlueter, C.; Hörantner, M.; Lee, T.-L.; Snaith, H. J. C60 as an efficient and stable n-type compact layer in perovskite solar cells, *J. Phys. Chem. Lett.* **2015**, 6, 2399
- Wojciechowski, K.; Ramirez, I.; Gorisse, T.; Dautel, O. J.; Dasari, R. R.; Sakai, N.; Song, S.; Marder, S. R.; Wantz, G.; Riede, M. K.; Snaith, H. J. Cross-linkable Fullerene Derivatives for Solution-processed n–i-p Perovskite Solar Cells, in preparation
- Snaith, H. J.; Abate, A.; Ball, J. M.; Eperon, G. E.; Leijtens, T.; Noel, N. K.; Stranks, S. D.; Wang, J. T.; Wojciechowski, K.; Zhang, W. Anomalous Hysteresis in Perovskite Solar Cells, *J. Phys. Chem. Lett.* **2014**, 17, 1511

- Carnie, M. J.; Charbonneau, C.; Davies, M. L.; Troughton, J.; Watson, T. M.; Wojciechowski, K.; Snaith, H.; Worsley, D. A. A One-Step Low Temperature Processing Route for Organolead Halide Perovskite Solar Cells. *Chem. Commun.* **2013**, 49, 7893
- Troughton, J.; Bryant, D.; Wojciechowski, K.; Carnie, M. J.; Snaith, H.; Worsley, D. A.; Watson, T. M. Highly efficient, flexible, indium-free perovskite solar cells employing metallic substrates, *J. Mater. Chem. A* **2015**, 3, 9141
- Bryant, D.; Greenwood, P.; Troughton, J.; Wijdekop, M.; Carnie, M.; Davies, M.; Wojciechowski, K.; Snaith, H. J.; Watson, T.; Worsley, D. A Transparent Conductive Adhesive Laminate Electrode for High-Efficiency Organic-Inorganic Lead Halide Perovskite Solar Cells, *Adv. Mater.* **2014**, 26, 7499
- Abate, A.; Saliba, M.; Hollman, D. J.; Stranks, S. D.; Wojciechowski, K.; Avolio, R.; Grancini, G.; Petrozza, A.; Snaith, H. J. Supramolecular Halogen Bond Passivation of Supramolecular Halogen Bond Passivation of Organic-Inorganic Halide Perovskite Solar Cells, *Nano Lett.* **2014**, 14, 3247
- Liu, J.; Pathak, S.; Stergiopoluos, T.; Leijtens, T.; Wojciechowski, K.; Schumann, S.; Kausch-Busies, N.; Snaith, H. J.; Employing PEDOT as the p-type Charge Collection Layer in Regular Organic-inorganic Perovskite Solar Cells, *J. Phys. Chem. Lett.* **2015**, 6, 1666
- Stranks, S. D.; Wood, S.; Wojciechowski, K.; Deschler, F.; Saliba, M.; Khandelwal, H.; Patel, J. B.; Elston, S. J; Herz, L. M.; Johnston, M. B.; Schenning, A. P. H. J.; Debije, M. G.; Riede, M. K.; Morris, S. M.; Snaith, H. J. Enhanced Amplified Spontaneous Emission in Perovskites using a Flexible Cholesteric Liquid Crystal Reflector, *Nano Lett.* **2015**, 15, 4935
- Hörantner, M.; Zhang, W.; Saliba, M.; Wojciechowski, K.; Snaith, H. J. Templated microstructural growth of perovskite thin films via colloidal monolayer lithography, *Energy Environ. Sci.* **2015**, 8, 2041

- Abate, A.; Pérez-Tejada, R.; Wojciechowski, K.; Foster, J. M.; Sadhanala, A.; Steiner, U.; Snaith, H. J.; Franco, S.; Orduna, J. Phosphonic anchoring groups in organic dyes for solid-state solar cells, *Phys. Chem. Chem. Phys.* **2015**, 17, 18780
- Leijtens, T.; Grancini, G.; Eperon, G. E.; Ball, J. M.; de Bastianni, M.; Wojciechowski, K.; Snaith, H. J.; Petrozza, A. Mapping Electric Field - Induced Switchable Poling and Structural Degradation in Hybrid Lead Halide Perovskite Thin Films, *Adv. Evergy Mater.* **2015**, 5, 1500962
- Pathak, S; Sakai, N.; Wisnivesky, F. R. R.; Stranks, S. D.; Liu, J.; Eperon, G. E.; Ducati, C.; Wojciechowski, K.; Griffiths, J. T.; Haghihgirad, A. A.; Pellaroque, A.; Friend, R. H.; Snaith, H. J. Perovskite Nano-crystals for Tuneable White Light Emission, Chem. Mater., **2015**, 27, 8066

2. Conferences

- Hybrid and Organic Photovoltaics Conference 2015, Rome, Italy, *Organic semiconductors replacing metal oxide compact layer in highly efficient and stable perovskite solar cells*, oral presentation
- MESO PV workshop 2015, Villars, Switzerland, *Heterojunction Modification for Highly Efficient Organic-Inorganic Perovskite Solar Cells*, oral presentation
- Science. Polish Perspectives 2014, Oxford, United Kingdom, *Perovskites – new solar revolution*, oral presentation

- SPIE Optics + Photonics 2014, San Diego, CA, United States, *Electron extraction layer for highly efficient perovskite solar cells*, oral presentation

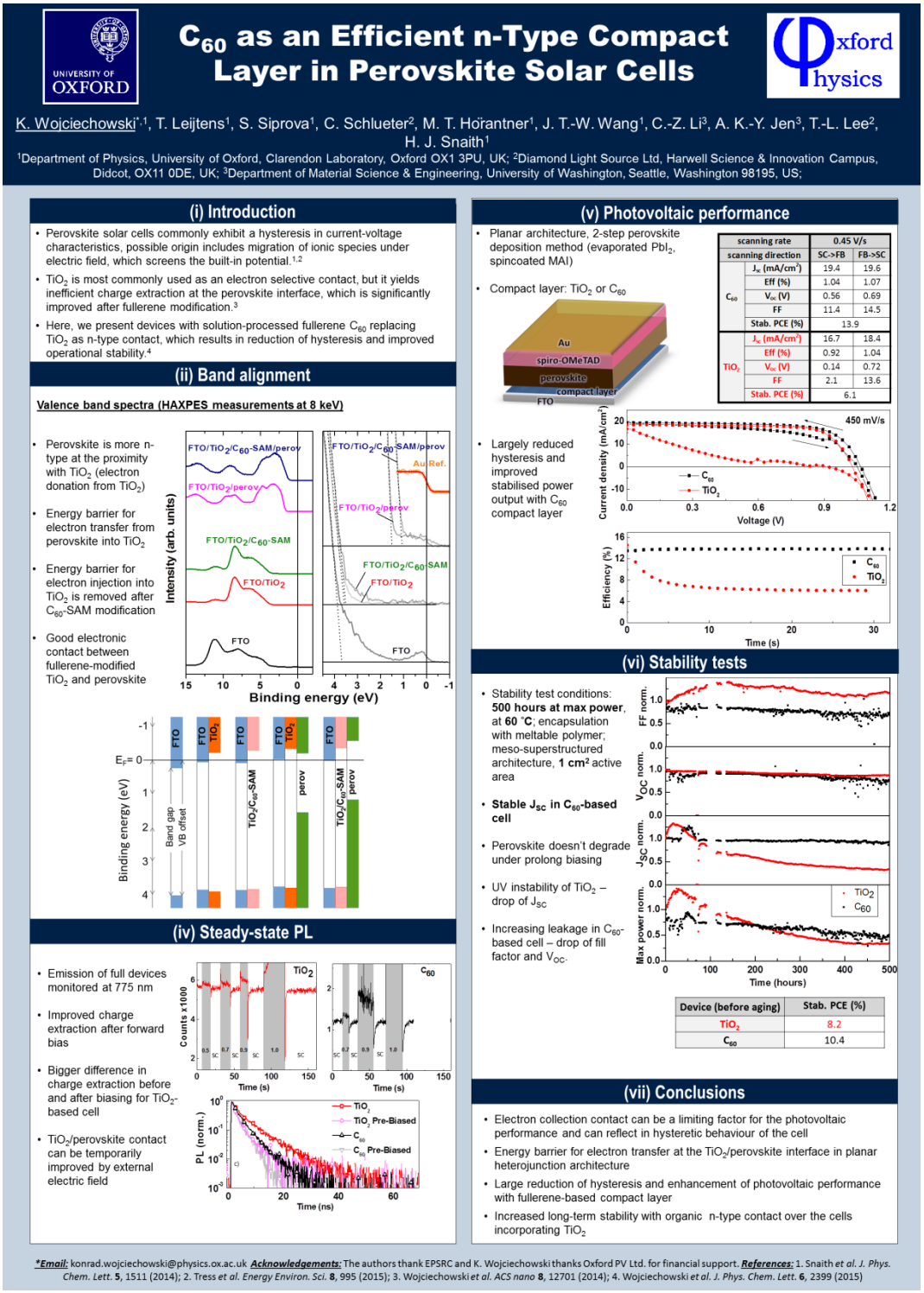
- International Conference on Perovskite Solar Cells and Optoelectronics 2015, Lausanne, Switzerland, *C60 as an efficient and stable n-type compact layer in perovskite solar cells*, poster presentation

- nanoGe - International Conference Solution processed Semiconductor Solar Cells 2014, Oxford, United Kingdom, *Modification of electron collection interface in perovskite solar cells*, poster presentation

- IOP Advances in Photovoltaics 2014, London, United Kingdom, *Modification of electron collection interface in perovskite solar cells*, poster presentation

- European Materials Research Society – Spring Meeting 2013, Strasbourg, France, *Transparent electrodes based on silver nanowires for solar cell applications*, poster presentation

3. Posters



scanning rate		0.45 V/s	
scanning direction		SC->FB	FB->SC
C60	Jsc (mA/cm2)	19.4	19.6
	Eff (%)	1.04	1.07
	Voc (V)	0.56	0.69
	FF	11.4	14.5
	Stab. PCE (%)	13.9	
TiO2	Jsc (mA/cm2)	16.7	18.4
	Eff (%)	0.92	1.04
	Voc (V)	0.14	0.72
	FF	2.1	13.6
	Stab. PCE (%)	6.1	

Device (before aging)	Stab. PCE (%)
TiO2	8.2
C60	10.4

Figure 1. PSCO 2015, Lausanne, poster

Modification of electron collection interface in perovskite solar cells

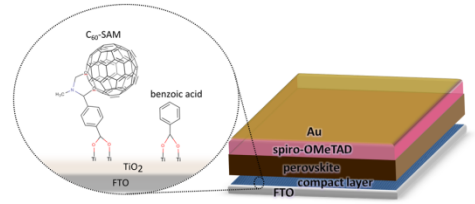
K. Wojciechowski*,1, S. D. Stranks[1], A. Abate[1], G. Sadoughi[1], A. Sadhanala[2], Chang-Zhi-Li[3], R. H. Friend[2], Alex K.-Y. Jen[3], H. J. Snaith
[1]Department of Physics, University of Oxford, Clarendon Laboratory, Oxford OX1 3PU, UK
[2]Department of Physics, University of Cambridge, Cavendish Laboratory, Cambridge, CB3 0EE, UK
[3]Department of Material Science & Engineering, University of Washington, Seattle, Washington 98195, US

(i) Introduction

- Anomalous hysteresis occurring in current-voltage characteristics remains to be the challenge in perovskite solar cells based on methylammonium lead halides[1]
- Better understanding of charge collection mechanism is required to address these issues and continue the progress of the technology
- Here we present enhancement of photovoltaic performance and reduction of hysteresis phenomenon through the suitable interface engineering

(ii) Self-assembled monolayer

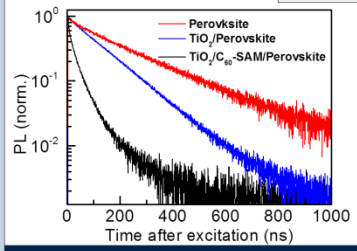
- TiO_2 electron-selective contact is modified with a monolayer anchored at the surface
- Planar heterojunction architecture



(iii) Electron extraction

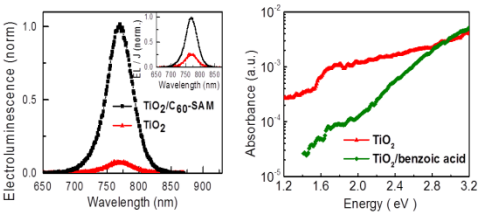
- Better **electronic coupling** between C_{60} and perovskite – efficient PL quenching

Sample	PLQE (%)
No quencher	7.6
TiO_2	3.8
TiO_2/C_{60}-SAM	0.5



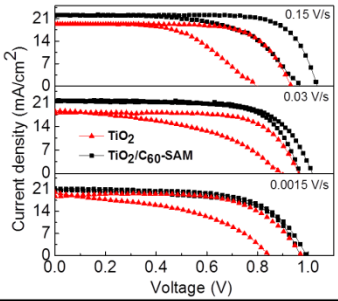
(iv) Trap-states passivation

- Effect of fullerene on perovskite
  - EL spectrum
- Effect of anchoring group on TiO_2
  - PDS spectrum



(v) Anomalous hysteresis

- Modified cells show no hysteresis at JV curves for slower scanning rates
- Passivation of interface trap-states reduces relaxation time
- Hysteresis influenced by the n-type interface



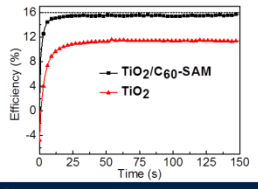
scanning rate		0.15 V/s		0.03 V/s		0.0015 V/s	
scanning direction		SC->FB	FB->SC	SC->FB	FB->SC	SC->FB	FB->SC
TiO_2/C_{60}-SAM	J_{sc} (mA/cm^2)	22.0	22.1	21.7	21.6	21.3	20.7
	Eff (%)	12.5	17.3	15.0	14.7	13.4	12.8
	V_{oc} (V)	0.97	1.04	1.02	0.97	0.99	0.97
	FF	0.59	0.75	0.67	0.70	0.63	0.63
TiO_2	J_{sc} (mA/cm^2)	19.3	19.3	18.6	18.0	20.1	18.7
	Eff (%)	8.5	12.7	7.6	12.1	7.5	12.2
	V_{oc} (V)	0.79	0.93	0.9	0.96	0.85	0.97
	FF	0.55	0.70	0.46	0.69	0.44	0.63

(vi) Photovoltaic performance

- Enhancement of all photovoltaic parameters upon C_{60}-SAM modification

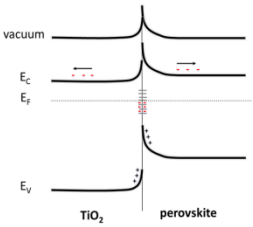
Device	No of devices	J_{sc} (mAcm^{-2})	V_{oc} (V)	FF	Efficiency (%)
TiO_2	57	17.8 ± 2.5	0.91 ± 0.05	0.68 ± 0.06	11.5 ± 2.3
TiO_2/C_{60}-SAM	55	20.0 ± 1.7	1.01 ± 0.03	0.73 ± 0.03	14.8 ± 1.7

- Stabilised power conversion Efficiencies (constant bias at max power point) reaching **15.7 %**



(vii) Conclusions

- Proposed mechanism: Fermi level pinning at short-circuit due to interface trap states – electrostatic barrier for electron collection
- 2-fold effect of C_{60}-SAM: facilitation of electron extraction and passivation of trap states at the n-type interface (both on TiO_2 and perovskite side)



Email: konrad.wojciechowski@physics.ox.ac.uk ***Acknowledgements:*** The authors thank EPSRC and K. Wojciechowski thanks Oxford PV Ltd. for financial support. ***References:*** 1. Snaith *et al. J. Phys. Chem. Lett.* **5**, 1511 (2014)

Figure 2. nanoGe 2014, Oxford, poster

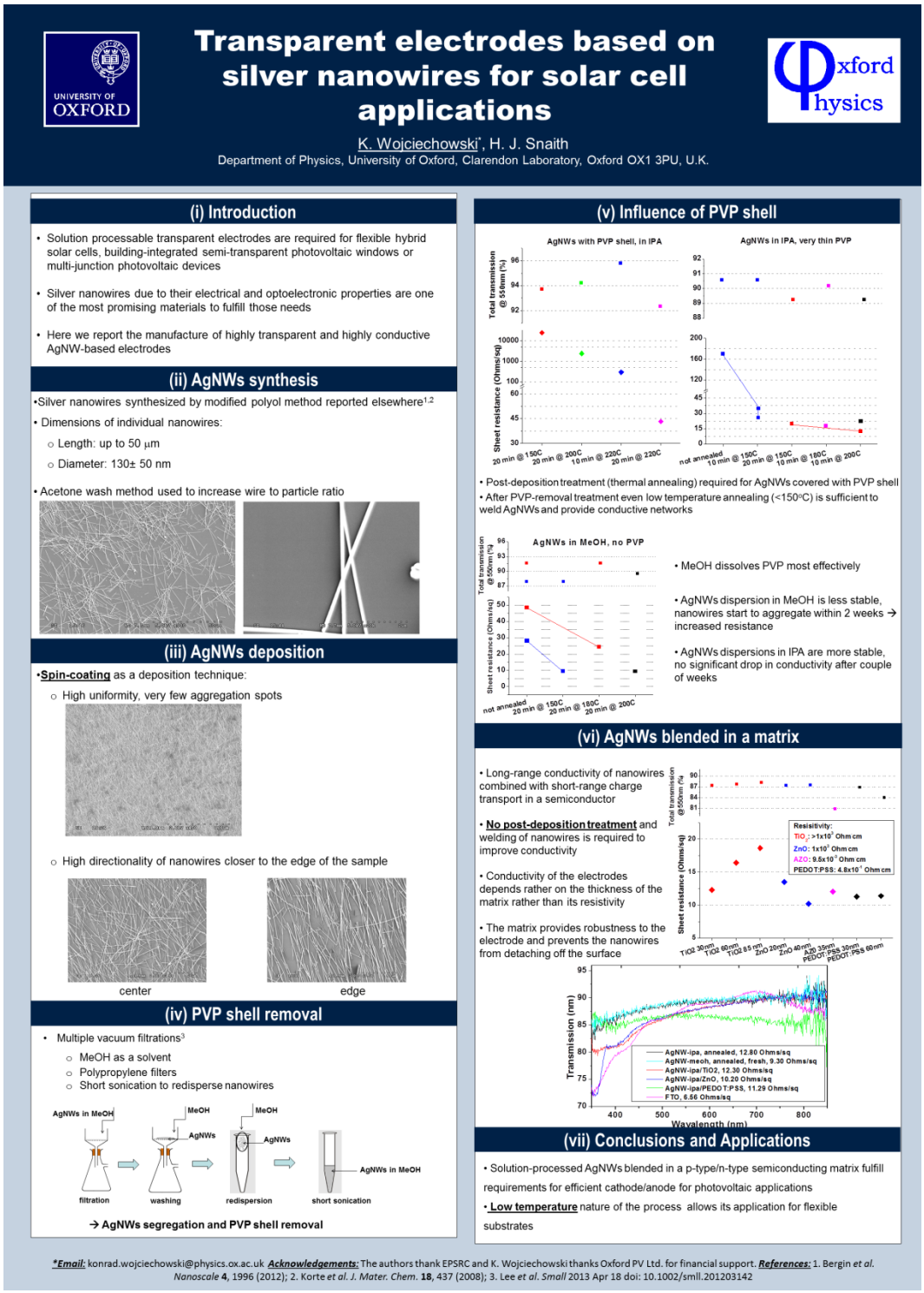


Figure 3. EMRS 2013, Strasbourg, poster